EVALUATING THE FREQUENCY, MAGNITUDE, AND BIOGEOCHEMICAL CONSEQUENCES OF UNDER-ICE PHYTOPLANKTON BLOOMS

A DISSERTATION
SUBMITTED TO THE DEPARTMENT OF EARTH SYSTEM SCIENCE
AND THE COMMITTEE ON GRADUATE STUDIES
OF STANFORD UNIVERSITY
IN PARTIAL FULFILLMENT OF THE REQUIREMENTS
FOR THE DEGREE OF
DOCTOR OF PHILOSOPHY

Courtney Michelle Payne
July 2023

This dissertation is online at: https://purl.stanford.edu/jv402ph9797

I certify that I have read this dissertation and that, in my opinion, it is fully adequate in scope and quality as a dissertation for the degree of Doctor of Philosophy.

Kevin Arrigo, Primary Adviser

I certify that I have read this dissertation and that, in my opinion, it is fully adequate in scope and quality as a dissertation for the degree of Doctor of Philosophy.

Karen Casciotti

I certify that I have read this dissertation and that, in my opinion, it is fully adequate in scope and quality as a dissertation for the degree of Doctor of Philosophy.

Leif Thomas

Approved for the Stanford University Committee on Graduate Studies.

Stacey F. Bent, Vice Provost for Graduate Education

This signature page was generated electronically upon submission of this dissertation in electronic format.

Abstract

The Arctic Ocean has changed substantially because of climate change. The loss of sea ice extent and thickness has increased light availability in the surface ocean during the ice-covered portion of the year. Sea ice loss has also been a factor in the observed increases in sea surface temperatures and likely impacts surface ocean nutrient inventories. These changing environmental conditions have substantially altered patterns of phytoplankton net primary production (NPP) across the Arctic Ocean. While NPP in the Arctic Ocean was previously considered insubstantial until the time of sea ice breakup and retreat, the observation of massive under-ice (UI) phytoplankton blooms in many of the Arctic seas reveals that the largest pulse of NPP may be produced prior to sea ice retreat. However, estimating how much NPP is generated during the UI part of the year is challenging, as satellite observations are hampered by sea ice cover and very few field campaigns have targeted UI blooms for study.

This thesis uses a combination of laboratory experiments, biogeochemical modeling, and an analysis of satellite remote sensing data to better understand how the magnitude and spatial frequency of UI phytoplankton blooms has changed over time in the Arctic Ocean, as well as to assess the likely biogeochemical consequences of these blooms. In Chapter 2, I present a one-dimensional ecosystem model (CAOS-GO), which I used to evaluate the magnitude of UI phytoplankton blooms in the northern Chukchi Sea (72°N) between 1988 and 2018. UI blooms were produced in all but four years over that period, accounted for half of total annual NPP, and were the primary drivers of interannual variability in NPP. Further, I found that years with large UI blooms had reduced rates of zooplankton grazing, leading to an intensification of the mismatch between phytoplankton and zooplankton populations.

In Chapter 3, I used the same model configuration to investigate the role of UI bloom variability in controlling sedimentary processes in the northern Chukchi Sea. I found that, as total annual NPP increased from 1988 to 2018, there were increases in particle export to the benthos, nitrification in the water column and the sediments, and sedimentary denitrification. These increases in particle export to the benthos and denitrification were driven by higher rates of NPP early in the year (January-June) and were highest in years where under-ice blooms dominate, indicating the importance of UI NPP as drivers of these biogeochemical consequences. Additionally, I tested the system's sensitivity

to added N, finding that, if N supply in the region increased, 30% of the added N would subsequently be lost to denitrification.

I subsequently deployed this model in the southern Chukchi Sea (68°N) to understand latitudinal differences in UI bloom importance across the region (Chapter 4). I found that UI blooms were far less important contributors to total NPP in the southern Chukchi Sea. Further, I found that their importance was waning over time; NPP generated in the UI period from 2013-2018 was only 34% of the 1988-1993 mean. This lower rate of UI NPP was driven by a far shorter UI period as sea ice retreated nearly six weeks earlier than in the northern Chukchi Sea. However, low UI NPP was associated with higher rates of both total NPP and sedimentary denitrification in the southern Chukchi Sea than in the north.

In Chapter 5, I used satellite remote sensing to determine how UI bloom frequency changed across the Arctic between 2003 and 2021. I found that UI blooms are a widespread feature and can be generated across 40% of the observable seasonal sea ice zone in the Arctic Ocean. While there was an increase in observable area as sea ice retreated, there was no change in UI area, driving a nearly 10% decline in the proportion of UI bloom prevalence. The Chukchi Sea was identified as both the region with the highest prevalence of UI blooms and the region most responsible for the decline in UI blooms.

Finally, to understand the functional relationship between co-limiting light and nutrient conditions on phytoplankton growth, I conducted a laboratory experiment (Chapter 6). Phytoplankton growth under co-limiting conditions, which is frequently observed in the field, is often modeled using one of two functional relationships, but these relationships produce vastly different predictions of phytoplankton bloom magnitude. Although this laboratory experiment aimed to quantify the functional relationship of light and nutrient limitation on phytoplankton growth, I faced challenges in quantifying the nitrogen (N) concentration and was unable to meaningfully distinguish between these two functional relationships. However, this work also demonstrated that there is little difference between these functional relationships in areas like the Arctic Ocean, where nutrient concentrations can be rapidly depleted, diminishing from non-limiting to scarce over just a few days.

Together, the results of this dissertation suggest that UI phytoplankton blooms can substantially contribute to total NPP, drive reductions in food availability, and change the rate of nitrogen loss. However, this work also demonstrates that UI blooms, which have likely been an important source of NPP across the Arctic since at least the 1980s, are likely an ephemeral feature, with their prevalence likely to decline in coming years as sea ice retreat shifts earlier.

Acknowledgments

When I told my parents, John and Lisa Payne, that I wanted to get a PhD in oceanography, they had a few questions: 1) who will pay for this, 2) what is oceanography, and 3) you're absolutely sure you'll get paid, right? In spite of their initial concerns, their support over the last six years has meant the world to me. From listening to me practice for my qualifying exam (even though I definitely noticed you sleeping, dad) to asking the important questions (why do we care about your work again?), they kept me grounded, lifted my spirits, and helped me remember to celebrate the milestones along the way. Without them, and the support of my sisters Stephanie and Rachael, I could not have made it to this point.

Over the past decade, I have had the incredible fortune of having two scientific mentors who saw my potential in spite of my complete lack of scientific knowledge or research experience. My first oceanography professor, Collin Roesler, helped me turn my haphazard fieldwork into a publishable paper and encouraged me to pursue research as a career, undoubtedly changing the trajectory of my life. Kevin Arrigo, my advisor at Stanford, gave me the freedom and support to practice asking (and answering) my own scientific questions and to try out most of the tools available to an oceanographer over the course of my PhD. He taught me how to turn data over repeatedly until I could understand the story it was telling us. Additionally, it would not occur to Kevin to treat a problem that one of his students encounters as beneath him to try to address. As a result, whenever I have run into a major obstacle or even a small stumbling block, I've always been able to turn to Kevin for help, and his delight at getting to break down equations or re-set the main goals of a project has been infectious, giving me the motivation to continue. Over the course of approximately 1,000 Treehouse burritos and tacos (plus a few hundred PB & Js), Kevin has demonstrated what great leadership and mentorship looks like; giving students any chunk of the pie they're interested in, listening to and supporting us through the challenges we face, and providing us with plenty of teasing and jokes along the way.

In addition to wonderful mentoring, I have been fortunate enough to land in one of the best possible lab groups. I arrived at Stanford eager to work on modeling projects but with minimal coding experience, something that typically would have made my research interests a non-starter. However, Gert van Dijken patiently sat with me for innumerable hours, helping me rout out countless

errors in my code. Later, when I decided to conduct a laboratory experiment, both Gert and Matt Mills helped me with everything from learning basic lab skills to improving my experimental design. I have also had the great fortune of overlapping with seven other graduate students in Kevin's lab: Ginny Selz, Kate Lewis, Hannah Joy-Warren, Casey Schine, Stephanie Lim, Claudette Proctor, and James Lauer. They patiently put up with my never-ending stories, helped me craft both big emails and small colorbars, and showed me how to critically think through scientific ideas and figures over countless lab meetings. Stephanie in particular put up with my irritatingly peppy early morning mood for three weeks straight when she brought me along on her research cruise. She showed me that true friendship sometimes means leaving the door unlocked while you shower in case your work colleague needs to vomit.

Finally, I am incredibly grateful to my bonus family. My friends - especially Antara Rao, Meghana Rao, Charlie Davies, and Claudia Villar Leeman - have helped me maintain my sanity for the past six the years through silly themed dinners, Halloween candy runs, and monthly phone calls. I am also thankful for my wonderful senior labrador, Lenora, who reminds me daily to take breaks to sniff, to leap into bodies of water with reckless abandon, and that cuddles can solve most problems. Last but certainly not least, my wife, Abi Vega, has been by my side throughout my time at Stanford. She let me talk my way through the myriad research and coding problems I encountered, edited countless first drafts of research proposals and papers, and even sent me snacks (delivered by Stephanie Lim) when I was trapped in the lab until 11pm. Abi has learned far more about phytoplankton than she ever desired to know, and in spite of that still feigns interest. If PhDs were granted fractionally, she would have earned a sizeable chunk of this one. In addition to all the ways she has tangibly supported my work, Abi has been my adventure buddy, (cautiously) joining me on every harebrained scheme I have come up with over the years. Our capers and mis-adventures - surfing waves that were quite a bit too big, 'biking' (also known as carrying our bikes) up and down a sand dune, and even bouldering a route once that left Abi sobbing before being rescued by a stranger - provided me with both much-needed comedic relief and the joy of accomplishing small things. I am so fortunate that we found and chose each other.

Contents

List of Tables

List of Figures

Chapter 1

Introduction

Phytoplankton are marine microorganisms that, despite accounting for less than 1% of the plant biomass on the planet, generate approximately half of the Earth's primary productivity and oxygen (*Field et al.*, 1998). These microscopic, largely single-celled algae both form the basis of the marine food web, providing food directly or indirectly to almost every marine organism (*Falkowski*, 2012). They also are critical drivers of global biogeochemical cycles, most notably for carbon (C) and nitrogen (N), because they fix C and utilize nutrients in the surface ocean before sinking to depth (*Volk and Hoffert*, 1985). Concerningly, phytoplankton net primary production (NPP) is projected to diminish by between 2 and 9% globally by 2080 because of anthropogenic climate change (*Bopp et al.*, 2013; *Cabré et al.*, 2015; *Krumhardt et al.*, 2017), with even larger changes anticipated in some regions. One of the few regions of the world where NPP is projected to increase, however, is the Arctic Ocean, where changes in NPP are projected to somewhat offset the globally declining trend (*Tagliabue et al.*, 2017). But estimates of future Arctic Ocean NPP are more uncertain than for any other region, with projections of regional NPP by 2100 ranging from a 20% decline to a 50% increase in NPP relative to the present (*Cabré et al.*, 2015; *Tagliabue et al.*, 2021; *Vancoppenolle et al.*, 2013). Before seeking to understand how Arctic Ocean NPP will change in the future, however, it is critical to assess how phytoplankton have responded to the substantial changes in the Arctic environment over the last century.

Phytoplankton growth rates are controlled by temperature (*Eppley*, 1972) and the interactions of light and nutrient availability, all three of which are projected to change substantially in the Arctic. Air temperatures in the region have warmed at a rate nearly four times faster than the global average (*Rantanen et al.*, 2022). Sea surface temperatures have also increased dramatically, with August temperatures warming by 1-7°C in 2019 relative to the 1982-2010 mean for four of the Arctic seas (ric, 2019). Increasing temperatures have both driven and exacerbated changes in sea ice extent (*Beer et al.*, 2020; *Screen and Simmonds*, 2010), which has declined at an accelerated rate over the last few decades (*Stroeve et al.*, 2014). These changes in sea ice cover have led to a far longer open

water period each summer (*Lewis et al.*, 2020). Sea ice in the Arctic is also substantially younger and thinner than it was in the past. Thick, multi-year sea ice covered nearly 60% of the seasonally sea ice-covered Arctic Ocean in 1988 (*Serreze and Stroeve*, 2015) but less than 30% of the Arctic Ocean by 2017 (*Kwok*, 2018). Mean sea ice thickness has declined by more than 2.0 m, resulting in a 66% loss of sea ice thickness and 75% loss in ice volume since 1958 (*Kwok*, 2018). This transition towards thinner, younger sea ice has led to the proliferation of melt ponds on the surface of the ice (*Webster et al.*, 2015), substantially increasing the light penetrating into the underlying water column (*Frey et al.*, 2011; *Light et al.*, 2015). Further, the Arctic is projected to experience large changes in N inventories in the near future, although the direction of change is uncertain. Some studies project that the increase in sea ice-free area, as well as more frequent storms and stronger winds, could enhance mixing and thus reduce N limitation (*Carmack and Chapman*, 2003; *Crawford et al.*, 2020; *Lewis et al.*, 2020; *Rainville and Woodgate*, 2009; *Tremblay et al.*, 2011; *Zhang et al.*, 2004). However, others postulate that sea ice loss and increases in precipitation and river outflow in the Arctic will further stratify the ocean (*McLaughlin and Carmack*, 2010; *Nummelin et al.*, 2015), preventing the entrainment of N-rich deep waters into the surface.

These changes in environmental conditions have substantially impacted phytoplankton productivity in the Arctic Ocean. Increases in temperature drive increases in phytoplankton growth rates (*Eppley*, 1972), particularly at inflow shelves *Ardyna and Arrigo* (2020), but may also drive a shift towards a change in community composition, with species typically observed in sub-polar ecosystems thriving in the Arctic (*Neukermans et al.*, 2018; *Oziel et al.*, 2020; *Polyakov et al.*, 2020). Changes in light and nutrient availability in the surface ocean have had even more radical impacts on Arctic NPP. As sea ice extent has diminished, open water area has expanded by nearly 30%, which has contributed to a 60% increase in Arctic NPP between 1998 and 2018 (*Lewis et al.*, 2020). However, *Lewis et al.* (2020) found that, since 2012, increases in NPP across the Arctic Ocean were driven not by changes in open water area but rather by increases in Chlorophyll *a*, which indicates that nutrient supply to the surface ocean may more directly control the increasing trend in NPP. Similarly, *Crawford et al.* (2020) found that increases in NPP in certain Arctic seas was correlated to increases in high-wind events during the summer, further supporting this link between changes in NPP and wind-driven mixing of nutrients into the surface ocean. Reduced sea ice coverage and increasing winds in the autumn may also have led to an increase in autumn blooms, which previously were only considered to form at lower latitudes *Ardyna et al.* (2014).

Perhaps the most notable change in scientific understanding of Arctic NPP, however, has been the increasing observation of under-ice phytoplankton blooms (UIB). Historically, sea ice algae were considered the only major source of NPP prior to sea ice retreat (*Arrigo*, 2003), with phytoplankton too light-limited during the sea ice-covered season to contribute substantially to annual NPP (*Perrette et al.*, 2011). However, observations of a massive UIB under 1 m thick, fully consolidated sea ice in the Chukchi Sea in 2011 (*Arrigo et al.*, 2012, 2014) upset this paradigm. Since these

initial observations, more than 30 UIBs have been identified (*Ardyna et al.*, 2020a). These blooms have been observed throughout the Arctic Ocean (*Arrigo et al.*, 2014; *Assmy et al.*, 2017; *Hill et al.*, 2018a; *Lalande et al.*, 2014; *Mayot et al.*, 2018; *Mundy et al.*, 2014; *Oziel et al.*, 2019) and in some cases have been found to produce $\sim$ 50% of the total annual NPP in the Arctic Ocean (*Arrigo et al.*, 2014; *Mayot et al.*, 2018; *Mundy et al.*, 2009; *Oziel et al.*, 2019). Despite the apparent importance of UIBs, basic questions remain about these blooms. For one, are UIBs a recent phenomenon, with under-ice light conditions preventing their generation prior to the 21st century? Sporadic observations of these blooms as early as the late 1950s (*Apollonio*, 1959; *Apollonio and Matrai*, 2011) indicate that perhaps they have been generated for quite some time even if their importance as an early source of NPP was not recognized. Further, questions of where these blooms are most commonly generated, as well as how their frequency has changed over time, both across the Arctic as a whole and in particular regions, are uncertain. For instance, *Horvat et al.* (2017) modeled changes in light penetration through sea ice and argued that UIBs became far more widespread in recent years, with <5% of the ice-covered Arctic Ocean permitting their development in 1986 but an increase to 30% of the Arctic by 2015. An inter-model comparison project (*Jin et al.*, 2016), however, indicates that the proportion of annual NPP produced by UIBs declined between 1980 and 2009. Finally, the role of UIBs in altering patterns of zooplankton grazing or biogeochemical cycling has not been assessed. Because UIBs are generated early in the year when water column temperatures are below 0°C (*Pacini et al.*, 2019), rates of zooplankton grazing on these blooms may be depressed (*Campbell et al.*, 2001; *Coyle et al.*, 2007; *Huntley and Lopez*, 1992), which could in turn intensify the mismatch in timing of the phytoplankton and zooplankton blooms (*Conover and Huntley*, 1991). As a result, C fixed by phytoplankton during the under-ice period may be disproportionately exported to the sediments, increasing benthic-pelagic coupling (*Honjo et al.*, 2010; *Lalande et al.*, 2020). On the Chukchi shelf, coupled partial nitrification-denitrification in the sediments drives high rates of both N recycling and N loss through denitrification (*Brown et al.*, 2015a). Consequently, 1-3% of the total loss of fixed N in the oceans is lost in the Chukchi Sea (*Chang and Devol*, 2009), a rate which could increase further if there is a substantial increase in phytoplankton production and particle export (*Baumann et al.*, 2013; *Chang and Devol*, 2009; *Fennel et al.*, 2009; *Fennel*, 2010; *Granger et al.*, 2011; *Horak et al.*, 2013; *Laurent et al.*, 2016; *Soetaert et al.*, 1996a, b).

This dissertation seeks to evaluate the frequency, magnitude, and biogeochemical consequences of UIBs. In Chapter 2, I present a new one-dimensional Nitrogen/Phytoplankton/Zooplankton/Detritus (NPZD) ecosystem model, CAOS-GO, that was parameterized for the northern Chukchi Sea. I use this model to assess the contributions of UIBs to total NPP between 1988 and 2018, as well as to assess the relationship between UIB magnitude and zooplankton grazing. In Chapter 3, I use CAOS-GO to quantify the impacts of UIBs on sedimentary nitrification and denitrification. Chapter 4 presents a comparison of CAOS-GO results in the northern (72°N) and southern (68°N) Chukchi Sea to quantify the relative importance of UIBs at different latitudes. In Chapter 5, I employ

satellite remote sensing to understand the distribution of UIBs on a pan-Arctic scale, identifying regions where they are likely most important and how their frequency changed between 2003 and 2021. Finally, Chapter 6 presents a laboratory experiment that aims to understand the functional relationship between phytoplankton growth and co-limitation by nutrient and light concentrations for the purpose of improving marine ecosystem models.

Chapter 2

Changes in Under-Ice Primary Production in the Chukchi Sea From 1988 to 2018

Courtney M. Payne, Gert L. van Dijken, Kevin R. Arrigo
Department of Earth System Science, Stanford University, Stanford, California, USA
Laura Bianucci
Institute of Ocean Sciences, Fisheries and Oceans Canada

A peer reviewed version of this chapter was published in AGU in the *Journal of Geophysical Research: Oceans*. To view the published open abstract: https://doi.org/10.1029/2021JC017483.

Payne, C. M., Bianucci, L., van Dijken, G. L., & Arrigo, K. R. (2021). Changes in under-ice primary production in the Chukchi Sea from 1988 to 2018. Journal of Geophysical Research: Oceans, 126. https://doi.org/10.1029/2021JC017483

Changes in sea ice thickness and extent have corresponded with substantial changes in net primary production (NPP) in the Arctic Ocean. In recent years, observations of massive phytoplankton blooms under sea ice have upended the previous paradigm that Arctic NPP was driven almost exclusively by growth in the marginal ice zone and open water periods. Here, a new 1-D biogeochemical model capable of simulating ice algal and phytoplankton dynamics both under the ice and in open waters is applied in the northern Chukchi Sea for the years 1988-2018. Over this period, substantial under-ice (UI) blooms were produced

in all but four years and were the primary drivers of interannual variation in total NPP. While NPP in the UI period was highly variable interannually due to fluctuations in ice thickness and the length of the UI period, UI NPP accounted for nearly half of total NPP between 1988 and 2018. Further, years with high UI NPP had reduced annual zooplankton grazing, indicating an intensification in the mismatch between phytoplankton and zooplankton populations and possibly altering the partitioning of food between benthic and pelagic ecosystems. These results demonstrate that the often-overlooked ice covered period can be highly productive in the Arctic Ocean, and that the northern Chukchi Sea has been amenable to UIB formation since at least 1988.

2.1 Introduction

As a result of the amplified effects of anthropogenic climate change in the polar regions (*Screen and Simmonds*, 2010), the Arctic is warming more rapidly than anywhere else in the world (*Stocker et al.*, 2013). These rising temperatures have contributed to the changing sea ice conditions observed in the Arctic over the past several decades. Sea ice extent has diminished markedly and the rate of change is accelerating; between 1997 and 2014, sea ice coverage shrank at a rate four times greater than that between 1979 and 1996 (*Serreze and Stroeve*, 2015). Additionally, sea ice thickness has declined across the Arctic basin; between 2003 and 2012, the thickness of the sea ice pack decreased by an average of 7.5 cm yr^{-1} (*Laxon et al.*, 2013). Part of this reduction in thickness is due to the loss of multi-year ice at a rate of 15-17% per decade between 1979 and 2011 (*Comiso*, 2012). By 2014, only one quarter of the areal coverage of 5+ year-old sea ice observed in the 1980s remained (*Serreze and Stroeve*, 2015). Thinner and younger sea ice has also led to the proliferation of melt ponds on the surface of the ice (*Webster et al.*, 2015) and substantially reduced Arctic albedo (*Perovich and Polashenski*, 2012).

Sea ice loss has already had large-scale impacts on Arctic Ocean ecosystems. As sea ice extent declined between 1998 and 2018, open water area increased by 27%, contributing to a 57% increase in net primary production (NPP) during the open water period (*Lewis and Arrigo*, 2020). As sea ice formation shifts later in the year, wind-driven mixing has allowed autumn blooms to form (*Ardyna et al.*, 2014). There is even substantial evidence that the ice-covered part of the year, a period historically assumed to be too light-limited to allow for much phytoplankton productivity, can support massive under-ice blooms (UIBs). For instance, phytoplankton biomass exceeded 1291 mg chlorophyll *a* (Chl *a*) m^{-2} in a UIB observed in the Chukchi Sea in the western Arctic Ocean (*Arrigo et al.*, 2012, 2014). While UIBs have been sporadically noted throughout the Arctic Ocean (*Apollonio and Matrai*, 2011; *English*, 1961; *Fortier et al.*, 2002; *Strass and Nöthig*, 1996; *Yager et al.*, 2001), observations of these blooms have become more frequent in recent years (*Arrigo et al.*, 2012, 2014; *Assmy et al.*, 2017; *Boles et al.*, 2020; *Hill et al.*, 2018b; *Leu et al.*, 2011; *Mundy et al.*, 2009,

2014; *Oziel et al.*, 2019; *Randelhoff et al.*, 2020), perhaps suggesting that changing ice conditions may be more amenable to UIB formation. The thinner, melt pond-covered sea ice that now dominates much of the Arctic Ocean can transmit substantially more light into the underlying water column (*Light et al.*, 2015; *Webster et al.*, 2015). *Horvat et al.* (2017) found that, largely due to thinning sea ice, up to 30% of the Arctic Ocean had sufficient light to support a UIB between 2006 and 2015. Increasing under-ice light penetration may substantially increase the probability of UIB formation and thus the magnitude of carbon (C) fixed under the ice. These earlier blooms may further enhance the mismatch between phytoplankton and zooplankton populations in cold Arctic waters (*Conover and Huntley*, 1991).

Here we present a new 1-D nitrogen, phytoplankton, zooplankton, and detritus (NPZD) biogeochemical model, which we refer to as the Coupled Arctic Ocean System (CAOS) model. CAOS is coupled to an existing physical model (GOTM; *Burchard et al.*, 1999) and a sedimentary chemistry model (OMEXDIA; *Soetaert et al.*, 1996a) to determine if changing atmospheric and sea ice conditions between 1988 and 2018 have altered annual NPP in the northern Chukchi Sea where the massive UIB was observed (*Arrigo et al.*, 2012, 2014). In this study, we assess the relative magnitude of NPP during the under-ice, marginal ice zone, and open water periods from 1988 to 2018 and evaluate which environmental variables are the most important in controlling the magnitude of under-ice NPP.

2.2 Methods

2.2.1 Study site

The three coupled 1-D models (Figure 2.1) were forced with both satellite-derived and reanalysis data for 72.16°N and 166.60°W (Figure 2.2). This location is in the midst of the massive phytoplankton bloom observed on the Chukchi shelf in 2011 (*Arrigo et al.*, 2014). It is located along a major flowpath of Anadyr and Bering Shelf water advected through the Bering Strait and is 107 km from the shelf break (Figure 2.2; shelf break = 200 m isobath), so the influence of physical processes associated with the shelf break is likely to be minimal.

2.2.2 Physical model

The 1-D General Ocean Turbulence Model (GOTM, version 5.4; *Burchard et al.*, 1999) was used to generate hourly temperature, salinity, buoyancy frequency, and turbulent diffusion coefficient timeseries. GOTM was run with a water column composed of 50 vertical layers of 1 m thickness and timesteps of 1 hr.

GOTM does not directly include a dynamic ice model. To account for the effects of sea ice cover on heat flux, GOTM was modified such that when satellite-derived sea ice concentration surpassed

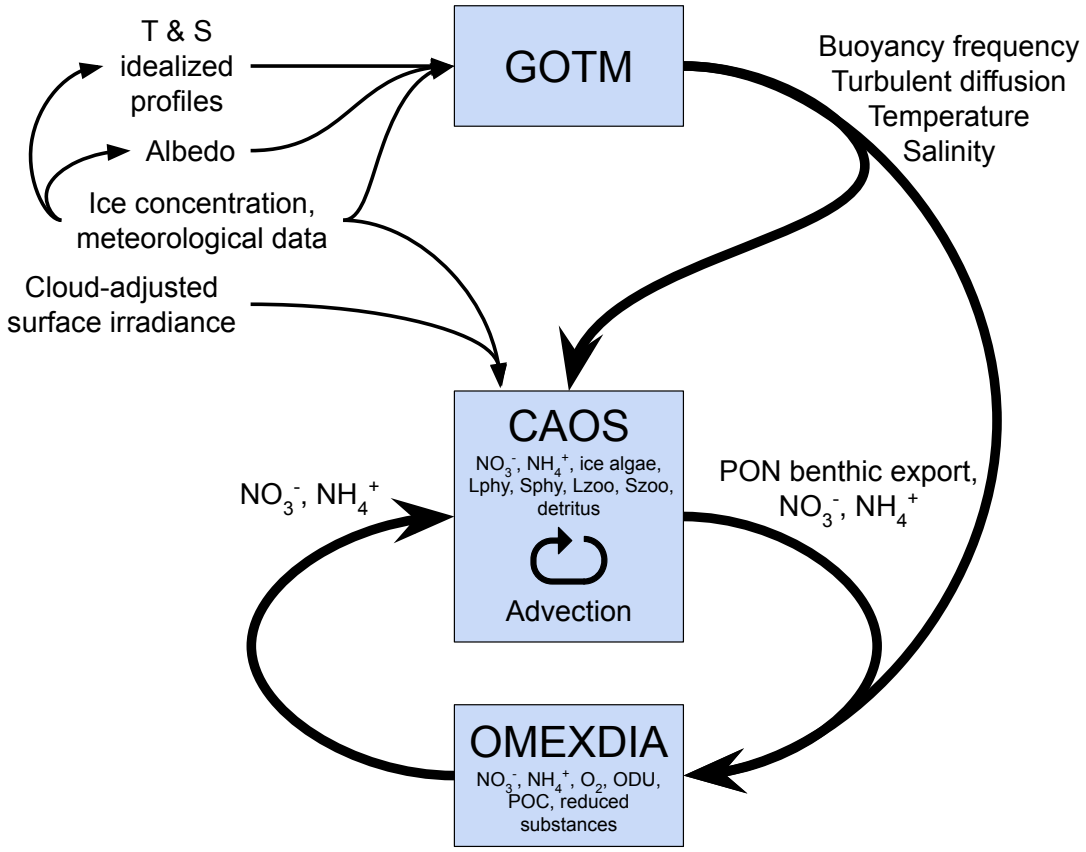

Figure 2.1: An overview of the inputs and outputs shared between the 3 models (GOTM, CAOS, and OMEXDIA). Thick lines represent flows between models, while thin lines represent external inputs to the models. State variables are listed in small text for the CAOS and OMEXDIA models.

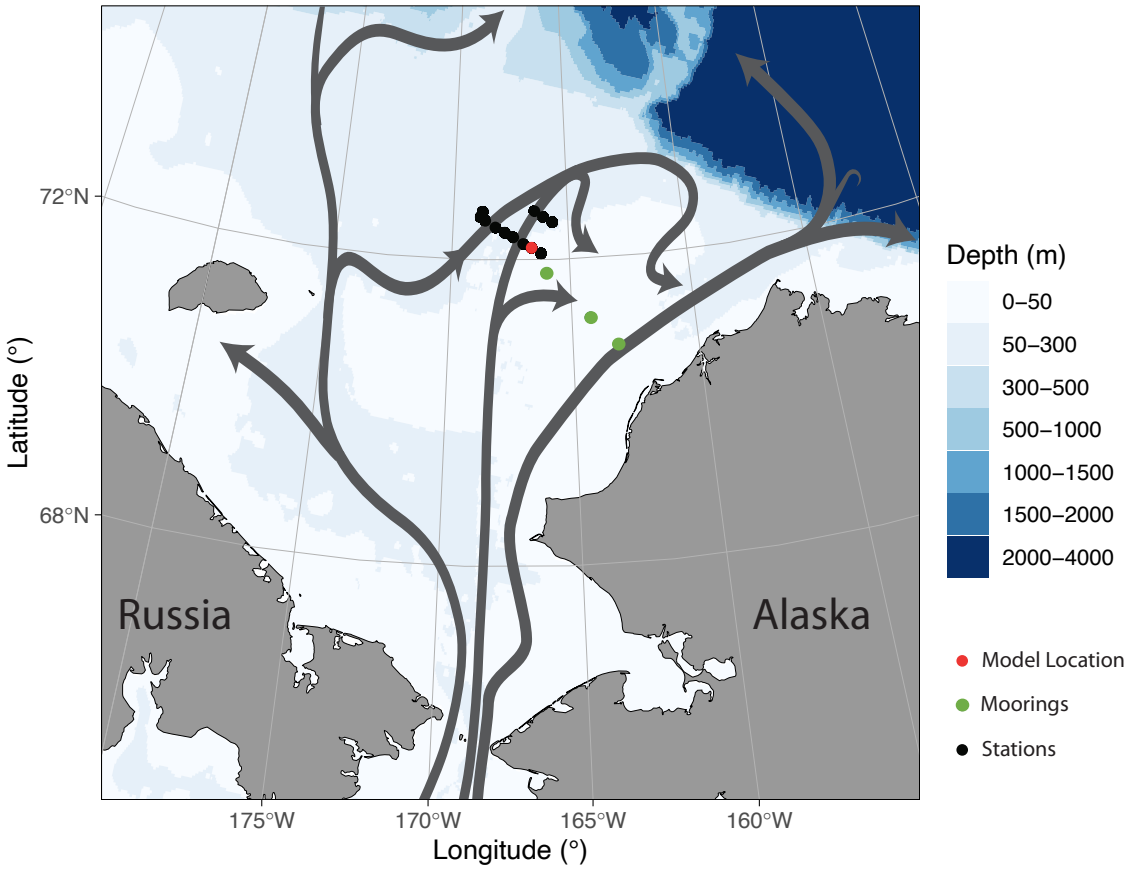

Figure 2.2: Bathymetric map of the Chukchi Sea including schematic flow paths of advected water (grey lines, after *Corlett and Pickart*, 2017). Points represent the location of the model (red), ICESCAPE 2011 stations used to create idealized profiles (black), and moorings used to evaluate model performance (green; *Mordy et al.*, 2020).

90% (see section 2.2.5), the heat flux across the air-sea boundary was set to zero and surface water temperatures remained at the salinity-dependent freezing point of seawater (where the freezing point of water in °C is -0.0575 times the salinity, or -1.90 °C at the wintertime surface salinity). The effect of sea ice cover on wind momentum flux to the surface ocean was simulated as described by *Schulze and Pickart* (2012), who found that wind momentum was transmitted through fully consolidated pack ice at a reduced rate when compared to open-water conditions, but that partial coverage resulted in an increase in wind momentum flux. As a result, when sea ice concentration is ≥90%, the model transmits 76% of wind momentum to the ocean; at sea ice concentrations of >10% and <90%, the model transmits 126% of the momentum to the ocean; and when sea ice concentration is ≤10%, 100% of the momentum is transmitted to the ocean (*Schulze and Pickart*, 2012). See section 2.2.5 for details on the sea ice concentration input.

GOTM was further modified to reflect the effects of surface type (ice, snow, and melt pond coverage) on albedo and thus shortwave radiative heating of the surface ocean. Different albedo time series were used for each year of the model run to simulate changes in snow, ice, and melt pond conditions. Albedo for different surface types and rates of change of albedo in the Chukchi Sea (Figure A1) were adapted from *Perovich and Polashenski* (2012), while timings matched those of the prescribed ice conditions, described in section 2.2.5. See supplementary text A.1.1 for more details on modifications to albedo.

To compensate for processes not included in our modified version of GOTM (including horizontal advection, precipitation, and sea ice melt), modeled temperature and salinity were relaxed towards several idealized profiles (see supplementary text A.1.2) on a timescale of 5 d for salinity and 15 d for temperature. Idealized temperature and salinity profiles (Figure A.2) were created using remote sensing products and cruise data from 2011 and 2014 (*Pacini et al.*, 2019). The mixed layer temperature of the idealized profiles was set using satellite-derived sea surface temperature (SST) when not ice-covered. CTD data collected at ICESCAPE 2011 stations (4-5 July and 8 July, 2011) and SUBICE stations (16 May to 20 June 2014) were used to determine the mixed layer depth and the thickness of the thermocline. To reflect annual differences in freshwater input to the water column, the salinity in the mixed layer for each year's idealized profiles was scaled from the 2011 profiles depending on the length of the sea ice melt period. Although increasing river runoff and meltwater has altered the salinity of the Arctic Ocean (*Mauritzen*, 2012; *Woodgate et al.*, 2005, 2012), our model does not account for these changes. See supplementary text A.1.2 for more details on idealized profiles.

2.2.3 Biogeochemical model

The CAOS model is a modified version of a nitrogen (N) based biogeochemical model for the Ross Sea, Antarctica (*Arrigo*, 2003). CAOS uses GOTM-derived temperature, buoyancy frequency (for determining mixed layer depth), and turbulent diffusion (which is added to a background turbulent

diffusivity of $5 \cdot 10^{-4}$ m^2 s^{-1} - *Rainville and Winsor*, 2008) as physical inputs (see Section 2.2.2). Surface spectral irradiance is determined using the radiative transfer model of (*Gregg and Carder*, 1990), adjusted for cloud cover (*Dobson and Smith*, 1988). CAOS then computes transmission of spectral photosynthetically available and usable radiation (PAR and PUR, respectively) through the sea ice and into the water column (*Arrigo et al.*, 1991, 1998a; *Morel*, 1978; *Perovich et al.*, 1986) using seasonally variable absorption coefficients (*Bricaud et al.*, 1995; *Lewis et al.*, 2020) according to Beer's law (see supplementary text A.2.1 for radiative transfer equations).

CAOS dynamically models ice algae, large and small phytoplankton, large and small zooplankton (*Ashjian et al.*, 2003; *Sherr et al.*, 2008, 2009), detritus, and two inorganic N pools, nitrate (NO_3^-) and ammonium (NH_4^+; Figure 2.3 - see supplementary text A.2.2-2.7 for all model equations). The model calculates PON export to the benthos, which is used as input for the sediment model OMEXDIA (see Section 2.2.4). The CAOS model is run with a 15 minute timestep.

In order to run the model for multiple years in the Chukchi Sea, which is characterized by the northward advection of NO_3^--replete waters through the Bering Strait, horizontal advection must be included. The effects of advection are simulated by relaxing all state variables towards prescribed profiles. Often, this is done by using observational data. However, there are not sufficiently high-quality observational data to provide prescribed profiles of all state variables between 1988 and 2018. Instead, we took advantage of the fact that water advects from the south in the Chukchi Sea; sea ice cover of this advecting water diminishes earlier, allowing an earlier start to phytoplankton growth. This was accomplished by running the model twice; model profiles generated for Day+1 (first run) were used as prescribed profiles for Day+0 (second run). NO_3^- profiles were further modified following day of year (DOY) 300 so that NO_3^- concentrations were gradually restored to 16 mmol m^{-3} throughout the water column (see supplementary text A.2.7). In the first run only, state variables were reset to the initial conditions on 1 January each year. While this relaxation was necessary to approximate the typical seasonal cycle of NO_3^-, the strength of the relaxation and length of time of the offset were chosen to minimize impacts on other state variables. For example, large phytoplankton blooms simulated with and without advection were statistically comparable (slope=1.0023, R^2=0.997, p<0.001).

2.2.4 Sediment model

The sedimentary component of our model is OMEXDIA, the early diagenetic model by *Soetaert et al.* (1996a), implemented dynamically in R using the ReacTran (*Soetaert and Meysman*, 2012) and deSolve (*Soetaert et al.*, 2010) packages. The model has six state variables, including one fast- and one slow-remineralizing organic matter class, oxygen (O_2), NO_3^-, NH_4^+, and reduced substances (which included both POC removed as solid substances, such as through pyritization or manganese carbonate formation, and dissolved organic C that diffused through the sediments). The model calculates rates of oxic and anoxic mineralization, nitrification, denitrification, and the production

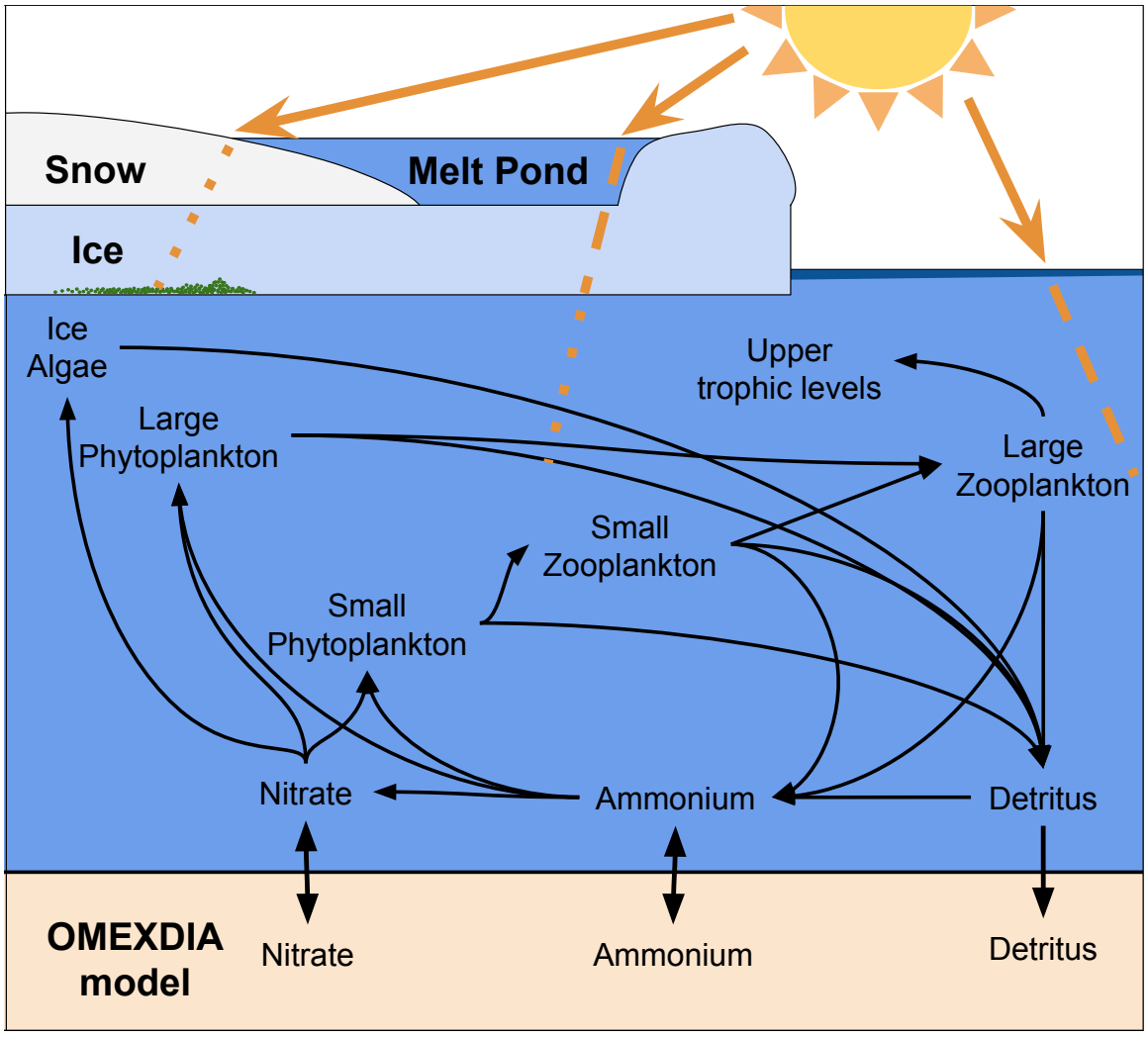

Figure 2.3: A diagram of the CAOS model. Light passes through snow, ice, and/or melt ponds depending on ice conditions. Black arrows represent N exchange between state variables (text). Upper trophic levels are not explicitly modeled, but mortality of zooplankton is assumed to contribute to upper trophic levels. Detritus and the bottom layer concentrations of two inorganic nitrogen state variables (nitrate and ammonium) are also used as input for the sediment model, OMEXDIA.

of solid inorganic C-containing minerals in ocean sediments. For full details of the OMEXDIA model equations, see *Soetaert et al.* (1996a).

OMEXDIA was run with a time step of one day over the top 0.5 m of the sediments, with 100 layers of a thickness increasing exponentially from 0.1 mm at the surface to 20 mm at the deepest layer (according to $y=0.094e^{0.568x}$, where y is the layer thickness and x is the layer number). The model uses as input daily mean bottom water salinity and temperature from GOTM, as well as daily mean bottom water NO_3^- and NH_4^+ concentrations and a daily summed PON benthic export (converted to C export) from CAOS.

2.2.5 Model forcing

Meteorological conditions (wind, air temperature, pressure, relative humidity, and cloud cover) were set using the National Centers for Environmental Prediction (NCEP) North American Regional Reanalysis (NARR; 32 km resolution used in this model configuration) products, provided by the NOAA/OAR/ESRL PSL, Boulder, Colorado, USA from their website at: `ttps://psl.noaa.gov/data/gridded/`. Additionally, as mentioned in section 2.2.2, GOTM temperatures were nudged towards idealized profiles, with temperatures over the mixed layer set using NOAA OISST version 2.1 (0.25° latitude and longitude resolution) (*Reynolds et al.*, 2007) data, provided by the NOAA/OAR/ESRL PSL, Boulder, Colorado, USA, from their Web site at `https://psl.noaa.gov/`.

Snow and melt pond thickness were computed using the mean of two Arctic Ocean snow depth models, SnowModel-LG (*Liston et al.*, 2020; *Stroeve et al.*, 2020, 25 km resolution, ERA5 forcing) and CPOM (*Zhou et al.*, 2021, 12.5 km resolution). Sea ice thickness was derived from ice age (*Tschudi et al.*, 2019, 62.5 km resolution, ERA-Interim forcing) by fitting a compilation of average spring (February-March 2004-2008) ice thickness by age (*Tschudi et al.*, 2016). Melt pond areal coverage was also estimated based on satellite-derived ice age (*Tschudi et al.*, 2019), with a more rapid increase and higher maximum in melt pond areal coverage for first-year sea ice (1.39% d^{-1}, up to 54% areal coverage) than for multi-year ice (0.64% d^{-1}, up to 38% areal coverage), as in *Webster et al.* (2015). See supplementary text A.3.1-A.3.3 for more details on deriving ice, snow, and melt pond layer thicknesses and melt pond areal coverage from satellite observations.

The onset of snow melt was set using the mean National Snow and Ice Data Center (NSIDC) snow melt onset date (*Anderson et al.*, 2019, 75 km resolution; see supplementary text A.3.4 for more details on the snow melt date). Sea ice began to melt (and melt ponds began to form) on the first 24-hr period when the mean NCEP NARR 2 m air temperature exceeded 0°C at the model location. Following the ice melt date, melt pond thickness increased to its maximal thickness (90% of the maximum snow thickness) by the start of sea ice retreat. Over this same period, sea ice thickness decreased by 0.0073 m d^{-1}, or 50% of the total ice melt necessary to produce the idealized salinity profiles. For the duration of sea ice retreat, sea ice and melt pond thickness remained fixed. The timing of the start and end of sea ice retreat and advance were set based on the sea

ice concentration (75 km resolution), provided by the NOAA/NSIDC Climate Data Record sea ice concentration (*Meier et al.* 2019; *Peng et al.* 2013). Sea ice retreat starts when satellite-derived ice cover diminished below 90% and ends when ice concentration decreased below 10%. Between these dates, sea ice extent diminishes linearly. Following ice retreat, open water persisted until the start of ice advance, the date at which satellite-derived ice concentration increased above 10%. Sea ice concentration then increased linearly until the date when satellite-derived concentration surpassed 90%.

2.2.6 Initialization and parameterization

The models are spun up for one year using the same input data for the first two years before proceeding to subsequent years; the first year is excluded from further analysis. State variables for each model run are initialized with identical concentrations in all layers of the water column (Table 2.1). For both phytoplankton and zooplankton size classes, these initial values are also minimum values - state variables are not allowed to diminish below these values.

Table 2.1: CAOS model state variables and initial values. All are in units of mmol N m^{-3}. * indicates that the initial value is also a minimum value.

State Variable	Description	Initial Value
IA	Ice algae	0.0
Sphy	Small phytoplankton functional group	0.05 *
Lphy	Large phytoplankton functional group	0.05 *
Szoo	Small zooplankton functional group	0.01 *
Lzoo	Small phytoplankton functional group	0.01 *
Detri	Detritus functional group	0.0
NO_3^-	Dissolved nitrate concentration	16.0
NH_4^+	Dissolved ammonium concentration	0.0

GOTM parameters used in the standard run matched those used in the OWS Papa test case (`https://gotm.net/cases/ows_papa/`), with the exception of those used to control meteorological fluxes, which were calculated using the formulation of *Kondo* (1975). For a full list of GOTM model equations and parameters, see *Burchard et al.* (1999). Parameters for the standard run of CAOS are listed in Table 2.2. Parameters for the standard run of OMEXDIA that differ from those used in *Soetaert et al.* (1996a) are listed in Table 2.3. For a full list of OMEXDIA model parameters, see *Soetaert et al.* (1996b) and *Soetaert et al.* (1996a). For a description of methods used to evaluate model performance, including comparing modeled and satellite NPP (*Arrigo et al.* 2008; *Lewis et al.* 2020; *Pabi et al.* 2008) and modeled and observed NO_3^- (*Arrigo et al.* 2017; *Lowry et al.* 2015; *Mordy et al.* 2020) and sensitivity analysis, see supplementary section A.4.1 and A.4.2. For a description of the evaluation of model performance and sensitivity analysis, see supplementary section A.5.1-A.5.3.

Table 2.2: CAOS model parameters: parameter descriptions, values, units, and sources of parameters used.

Parameter	Description	Value	Unit	Source
IA_L	Maximum ice algal Chl *a* concentration	30	mg Chl *a* m^{-2}	a
IA_{x_0}	Sigmoid midpoint for logistical curve describing ice algal growth	14	d	b
IA_k	Ice algal logistical growth rate	0.4	mg Chl *a* m^{-2} d^{-1}	b
$IA_{comp.irrad.}$	Compensation irradiance for ice algae	2.0	μmol photons m^{-2} s^{-1}	c
$loss_{IA}$	Disassociation rate of ice algae	0.05	d^{-1}	d
E_{k_Lphy}	Observed photoacclimation parameter, E_k, for large phytoplankton	54.9-67.6	μmol photons m^{-2} s^{-1}	e, *
μ_{0_Lphy}	Specific growth rate for large phytoplankton at 0°C	1.78	d^{-1}	e, **
$mort_{Lphy}$	Death and loss rate of large phytoplankton	0.065	d^{-1}	d
$K_{s\_NO3\_Lphy}$	Half-saturation constant for NO_3^- uptake by large phytoplankton	0.9	mmol N m^{-3}	-
$K_{s\_NH4\_Lphy}$	Half-saturation constant for NH_4^+ uptake by large phytoplankton	0.7	mmol N m^{-3}	-
C/N_{Lphy}	Carbon to nitrogen ratio of large phytoplankton	106/14	mol:mol	f,g
C/Chl_{Lphy}	Carbon to Chl *a* ratio of large phytoplankton	60	g:g	g
E_{k_Sphy}	Observed photoacclimation parameter, E_k, for small phytoplankton	100	μmol photons m^{-2} s^{-1}	h, *
μ_{0_Sphy}	Specific growth rate for small phytoplankton at 0°C	1	d^{-1}	e, **
$mort_{Sphy}$	Death and loss rate of small phytoplankton	0.045	d^{-1}	d
$K_{s\_NO3\_Sphy}$	Half-saturation constant for NO_3^- uptake by small phytoplankton	0.3	d^{-1}	-
$K_{s\_NH4\_Sphy}$	Half-saturation constant for NH_4^+ uptake by small phytoplankton	0.1	mmol N m^{-3}	-
C/N_{Sphy}	Carbon to nitrogen ratio of small phytoplankton	106/16	mol:mol	i
C/Chl_{Sphy}	Carbon to Chl *a* ratio of small phytoplankton	100	g:g	j
$Sphy_{scarce}$	Sphy scarcity threshold: Szoo consumption is adjusted by Sphy/$Sphy_{scarce}$	0.5	mmol N m	-
$mort_{zoo}$	Zooplankton mortality rate	0.05	d^{-1}	d
ex_{zoo}	Zooplankton excretion rate	0.1	d^{-1}	d
γ	Zooplankton unassimilated grazing fraction	0.25	d^{-1}	d
$K_{s\_Sphy\_Szoo}$	Half-saturation constant for small phytoplankton uptake by small zooplankton	0.5	mmol N m^{-3}	-
$K_{s\_Lphy\_Lzoo}$	Half-saturation constant for large phytoplankton uptake by large zooplankton	0.5	mmol N m^{-3}	-
$K_{s\_Szoo\_Lzoo}$	Half-saturation constant for small zooplankton uptake by large zooplankton	0.5	mmol N m^{-3}	-
$Remin_{Det\rightarrow NH4}$	Remineralization rate of detritus to NH_4^+	0.2	mmol N m^{-3}	k
w_{det}	Detrital sinking rate	5	m d^{-1}	b
C/N_{det}	Carbon to nitrogen ratio of detritus	106/15.8	mol:mol	j
$Nitr\_m_{NH4\rightarrow NO3}$	Slope for the depth-dependent nitrification rate	0.5824	mmol N m^{-4}	l
$Nitr\_b_{NH4\rightarrow NO3}$	Y-intercept for the depth-dependent nitrification rate (values below 0 = 0)	-3.4313	mmol N m^{-3}	l

a *Arrigo* (2017), *b* *Welch and Bergmann* (1989), *c* *McMinn et al.* (1999), *d* *Arrigo et al.* (2014),
e *Fasham et al.* (1990), *f* *Brzezinski* (1985); *Lomas et al.* (2019), *g* ICESCAPE 2011 data,
h *Lewis et al.* (2019), *i* *Redfield* (1958), *j* *Sakshaug* (2004), *k* *Davis and Benner* (2007), *l* SUBICE 2014 data

∗ Reported E_k values were measured for PAR. Since phytoplankton functional groups were modeled using PUR, these values were modified in the model to reflect that only 38.3% of photosynthetron-produced light is usable by phytoplankton.

∗∗ Reported growth rates of 0.89 and 1.6 d^{-1} were observed at -1.6 °C. These values were adjusted using the *Eppley* (1972) temperature/growth relationship to calculate specific growth rates at 0 °C.

Table 2.3: Parameters used in the OMEXDIA model that differ from those in *Soetaert et al.* (1996a).

Parameter	**Description**	**Value**	**Unit**	**Source**
F_{fast}	Flux of fast-decaying detritus	(*)	g C m^{-2} yr^{-1}	a
F_{slow}	Flux of slow-decaying detritus	(*)	g C m^{-2} yr^{-1}	a
p_{fast}	Proportion of fast-decaying detritus	0.5	d^{-1}	b
R_{fast}	Decay rate for the fast-decaying detritus	0.18	d^{-1}	c
R_{slow}	Decay rate for the slow-decaying detritus	0.005	d^{-1}	b
$k_{in}(O_2$ denit)	Half saturation conc. for O_2 inhibition in denitrification	15	mmol O_2 m^{-3}	d
$k_{in}(NO_3^-$ anox)	Half saturation conc. for NO_3^- inhibition in anoxic mineralization	1	mmol NO_3^- m^{-3}	d
$k_{in}(O_2$ anox)	Half saturation conc. for O_2 inhibition in anoxic mineralization	1	mmol NO_3^- m^{-3}	d
C/N_{fast}	Carbon to nitrogen ratio of fast-decaying detritus	106/14.18	mol:mol	a
C/N_{slow}	Carbon to nitrogen ratio of slow-decaying detritus	106/12.1	mol:mol	e
ϕ_0	Porosity at the sediment-water interface	0.915	-	d
$coeff_\phi$	Coefficient for exponential porosity changes	4	-	b
Db_0	Constant bioturbation coefficient in the bioturbated layer	2	cm^2 yr^{-1}	f
x_b	Depth below which bioturbation decays exponentially	3	cm	f
O_2_bw	Oxygen concentration of the bottom water NO_3^-	300	mmol N m^{-3}	**
NO_3^-_bw	Daily mean bottom-water NO_3^-	(*)	mmol N m^{-3}	a
NH_4^+_bw	Daily mean bottom-water NH_4^+	(*)	mmol N m^{-3}	a
w	Sedimentation rate	0.35	cm y^{-1}	e, g
Temperature	Daily mean bottom-water temperature	(*)	°C	a
Salinity	Daily mean bottom-water salinity	(*)	-	a

(*) Variable conditions produced by GOTM or the CAOS model.
** Mean oxygen concentration for the stations closest to the model location for ICESCAPE 2011.
a from CAOS model. *b* *Soetaert et al.* (1996a). *c* *Davis and Benner* (2007). *d* *Soetaert et al.* (1996b).
e *Cooper and Grebmeier* (2018). *f* *Teal et al.* (2008). *g* *Darby et al.* (2009).

2.2.7 Primary production

Ice algal (IA) NPP was computed from the daily change in modeled ice algal Chl *a* concentration, using an algal C:Chl ratio of 35 (*Cota and Horne*, 1989, see supplementary text A.2.2 for ice algal equations). IA NPP extended from bloom initiation (when light reached the compensation irradiance, 2.0 μmol photons m^{-2} s^{-1}, in the bottom layer of the ice) until the start of ice melt and meltpond formation, and was integrated annually. Daily phytoplankton NPP was integrated with respect to depth over three different time periods based on sea ice conditions. The under-ice (UI) period extended from the initiation of phytoplankton growth (the date when daily phytoplankton NPP increases above 0.05 g C m^{-2} d^{-1}) until the start of sea ice retreat. The marginal ice zone (MIZ) period extended from the start until the end of ice retreat. Finally, the open water (OW) period was initiated at the end of ice retreat. The OW period ended on the earliest date when light was reduced in the water column: either when the sea ice advanced in the autumn, or when light diminished below 1% the maximum value reached in the mixed layer (DOY 300±6). NPP was also integrated both daily and monthly, and zooplankton grazing of both phytoplankton classes was integrated monthly, annually, and within the UI, MIZ, and OW periods.

NPP was further divided into new, regenerated, surface, and subsurface production. All NO_3^--based NPP was considered new production, while NH_4^+-based NPP was considered regenerated production. To determine if production was located in the surface or subsurface, for each day of the model run, large phytoplankton biomass for each layer (z) of the water column below 10 m was compared to the layer above (z-1). If the lower layer (z) had >110% of the biomass in the layer above (z-1), that layer was considered to be the upper boundary of the subsurface Chl *a* maximum (SCM). Total NPP above that depth was then defined as surface NPP, while NPP at or below that depth was defined as NPP within the SCM. If no obvious SCM existed (z was always < 110% of z-1), water column NPP was integrated and was considered to be surface NPP.

2.2.8 Statistics

Multiple linear regression was used to assess the relative importance of ice and snow layer thicknesses and changing ice condition dates in controlling NPP. Ice variables were assessed for collinearity using the variance inflation factor (VIF). VIF was <3 for all ice variables, indicating only moderate correlation among layer thickness and ice condition date variables. The multiple linear regression that best fit data was identified using backward selection by sequentially eliminating the variable with the highest p-value until only statistically significant variables ($p<0.05$) remained. Regressions were visually inspected to ensure that the relationships between independent and dependent variables were linear. Regressions were also checked to ensure that the residuals were normally distributed using the Shapiro-Wilk test and thorough visual inspection of histograms and Quantile-Quantile plots. The relative importance of each variable in the multiple linear regression model was calculated using the 'relaimpo' package in R.

Annual cycles of daily NPP were clustered using k-means clustering based on NPP in the UI and MIZ periods. The optimal k value was determined using the gap statistic. ANOVA and post hoc Tukey's honest significant difference (HSD) tests were then used on the clusters to assess the relationship between ice conditions and annual cycle type. All statistical analysis was conducted in R.

2.3 Results

In most years (such as the standard run year, 2011; Figure 2.4), sea ice algae begin to grow at the bottom of the ice in the spring and draw down NO_3^- from surface waters. As air temperatures increase and sea ice and snow begin to melt, the ice algal bloom sloughs off the bottom of the ice and sinks through the water column to the sea floor. The remineralization of this organic matter allows NH_4^+ to accumulate in surface waters (in concentrations of 0.4 mmol m^{-3} Figure 2.4b), where little NH_4^+ is nitrified. Soon thereafter, the biomass of large phytoplankton in the mixed layer increases rapidly beneath the sea ice as light in the water column increases, reaching an average maximum of 29.8 mg Chl a m^{-3} (Figure 2.4c). This phytoplankton bloom rapidly takes up NO_3^- and NH_4^+ over the upper 30 m (Figure 2.4a and b). Concentrations of large phytoplankton in the upper water column start to diminish around the time of sea ice retreat as NO_3^- is depleted. At the same time, NH_4^+ accumulates below the mixed layer (0.6 mmol m^{-3}; Figure 2.4b) as detritus is remineralized, and nitrification in the water column and sediments allows bottom-water concentrations of NO_3^- to reach an autumn maximum of 32.9 mmol m^{-3}.

During the OW period in the summer and autumn, large phytoplankton biomass accumulates below the mixed layer where NO_3^- is still available, reaching mean concentrations of 13 mg Chl a m^{-3}. Small phytoplankton also accumulate near the base of the mixed layer in the late summer and autumn, but at concentrations of only 0.4 mg Chl a m^{-3} (Figure 2.4d). Concentrations of large and small zooplankton rapidly increase once water column temperatures exceed 0°C and reach peak concentrations (of 0.11 and 0.02 mmol N m^{-3}, Figures 2.4e and f for large and small zooplankton, respectively) in the late summer. These increases occur after large phytoplankton have descended to the SCM. As ice advances in the autumn, NO_3^- concentrations are slowly restored to the winter concentration of 16 mmol m^{-3}.

2.3.1 Interannual changes in ice conditions

Several satellite-derived snow and ice conditions changed significantly between 1988 and 2018 at the model location in the Chukchi Sea, while others showed no trend with time. The snow melt date advanced by 12.4 days per decade earlier over this period (R^2=0.139, p=0.039; Figure 2.5d). The start and end dates of sea ice retreat were earlier by 8.8 (R^2=0.327, p<0.001; Figure 2.5f) and 9.3 (R^2=0.267, p=0.0034; Figure 2.5g) days per decade, respectively. The date of ice advance, on the

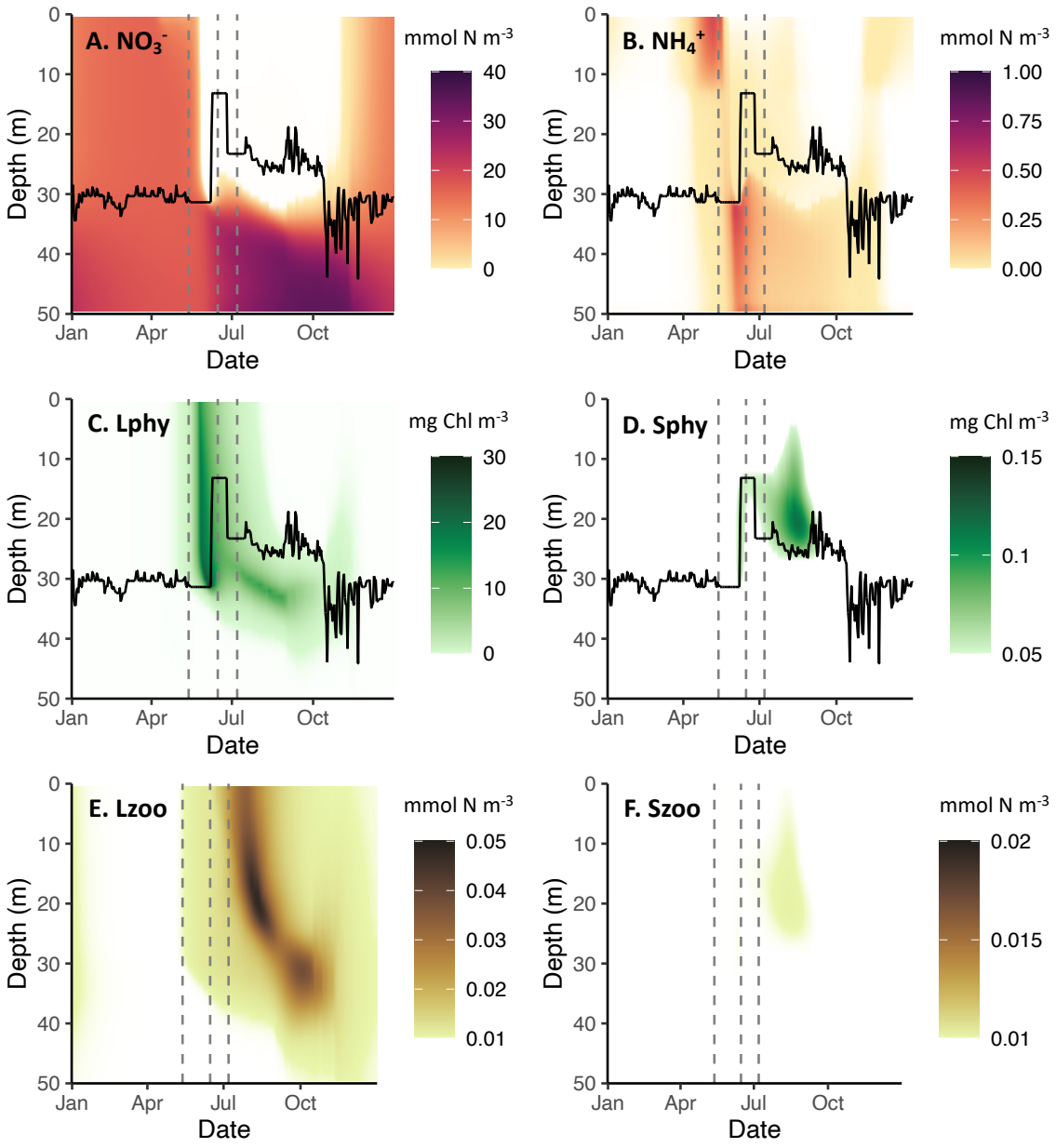

Figure 2.4: Annual depth vs. time plots of (A) nitrate (NO_3^-), (B) ammonium (NH_4^+), (C) large phytoplankton (Lphy), (D) small phytoplankton (Sphy), (E) large zooplankton (Lzoo), and (F) small zooplankton (Szoo) for 2011, the standard run year. Black lines (A-D) represent the mixed layer depth, calculated based on GOTM-derived buoyancy frequency. Grey dashed lines on each subplot represent, from left to right, the date of ice melt, the start of ice retreat (which marks the end of the UI period and start of the MIZ period), and the end of ice retreat (marking the end of the MIZ period and beginning of the OW period).

other hand, was delayed by 12.1 days per decade (R^2=0.265, p=0.0036; Figure 2.5a). Snow thickness diminished by 2.4 cm per decade (R^2=0.206, p=0.0103; Figure 2.5c). The sea ice melt date (Figure 2.5e) showed no statistically significant trend with time. Likewise, mean spring ice age (between March 1st and the start of ice retreat - see supplementary text A.1; Figure 2.5a) and age-derived thickness (Figure 2.5b) also showed no trend with time.

2.3.2 Interannual changes in total annual NPP

Between 1988 and 2018, total (ice algal + phytoplankton) annual NPP ranged from 74.7 to 100.1 g C m^{-2} yr^{-1}, increasing annually by 0.34 g C m^{-2} yr^{-1} (R^2=0.148, p=0.033; Figure 2.6a). New production ranged from 59.7 to 76.6 g C m^{-2} yr^{-1} (mean=68.2±4.7 g C m^{-2} yr^{-1}), with higher total annual NPP associated with higher new production (R^2=0.852, p<0.001). Multiple linear regression revealed that 78.2% of the variance (p<0.001) in total annual NPP is controlled by a combination of sea ice thickness (R^2=0.353, p=0.001), the length of the OW period (R^2=0.223, p<0.001), and the length of the UI period (R^2=0.206, p=0.013).

2.3.3 Contributions by ice algae, UI, MIZ, and OW NPP to total NPP

To assess the relative contribution by ice algae and phytoplankton to annual NPP, we divided the annual cycle into four periods: the ice algal (IA), the under-ice (UI), the marginal ice zone (MIZ), and the open water (OW) periods (see section 2.2.7). Between 1988 and 2018, the IA period varied in length from 0 to 76 days, beginning between DOY 69 and 157 and ending between DOY 120 and 161. The length of the IA period increased by 1.1 d yr^{-1} (R^2=0.168, p=0.024), driven by changes in the start of the IA period, which became earlier by 1.4 d yr^{-1} (R^2=0.224, p=0.008). The UI period varied in length from 6 to 91 days with no significant trend between 1988 and 2018. The UI period began between DOY 101 and 170 (mean=137±21). Both the start and end of the UI period shifted earlier, by 1.1 d yr^{-1} (R^2=0.238, p=0.005) and 0.9 d yr^{-1} (R^2=0.327, p<0.001), respectively. The MIZ period varied in length from 9 to 45 days over the study period, with the exception of 1988 when the MIZ period length was 98 days because sea ice never fully retreated. There was no significant interannual change in MIZ period between 1988 and 2018. The OW period varied in length 50 to 128 days between 1989 and 2018 but was 0 days long in the anomalous sea ice year 1988. Between 1988 and 2018, the length of the OW period increased by 15.1 days per decade (R2=0.309, p<0.001) due to both earlier ice retreat and later ice advance.

Annual sea ice algal NPP averaged 1.7±1.5 g C m^{-2} yr^{-1} and was highly variable interannually, ranging between 0 and 4.4 g C m^{-2} yr^{-1} (Figure 2.6a). Between 1988 and 2018, IA NPP increased annually by 0.05 g C m^{-2} yr^{-1} (R^2=0.101, p=0.082) and accounted for 0-4.5% of total (phytoplankton + ice algae) annual NPP (mean=1.9±1.6%; Table 2.4). Multiple linear regression revealed that 93.1% of the variance (p<0.001) in annual NPP by ice algae is controlled by the length of the

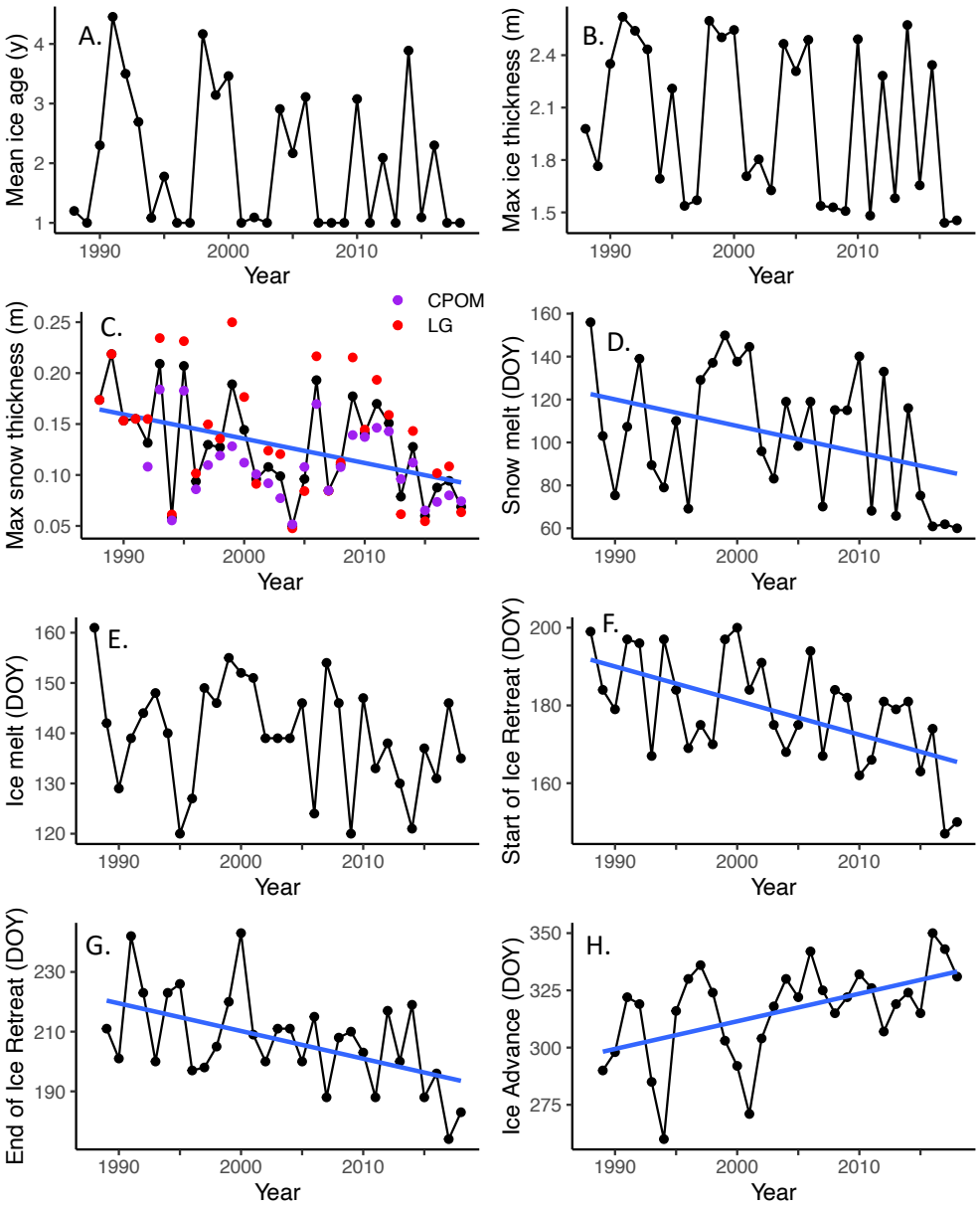

Figure 2.5: Ice and snow conditions between 1988 and 2018: (A) mean ice age (y); (B) maximum ice thickness (m); (C) maximum snow thickness (m); (D) snow melt date (DOY); (E) ice melt date (DOY); (F) the date when sea ice retreat starts (DOY), (G) the date when sea ice retreat ends (DOY), and (H) the date when sea ice advances (DOY). Blue lines are used when linear regressions are statistically significant. For snow thickness, the mean (black) of two models, CPOM (purple) and SnowModel-LG (red), is used.

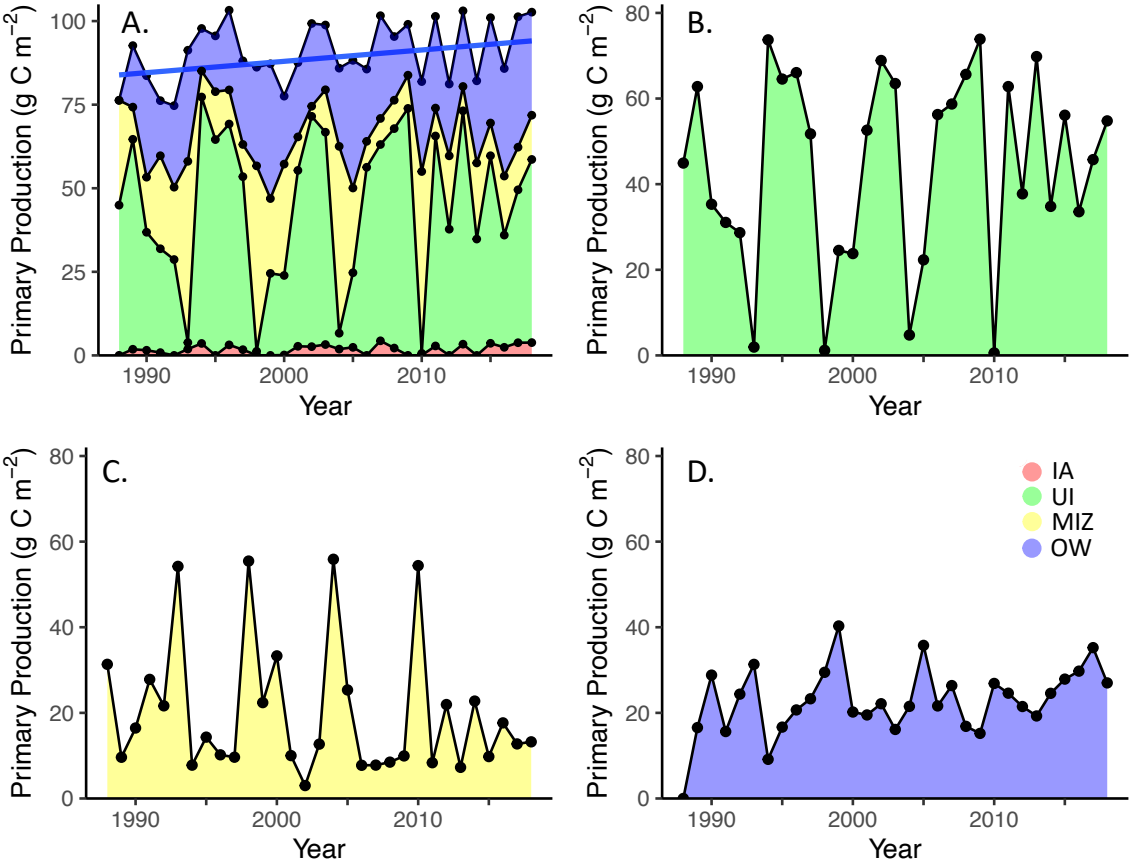

Figure 2.6: (A) Total annual NPP (upper black line) and its component parts, (B) annual UI NPP, (C) annual MIZ NPP, and (D) annual OW NPP between 1988 and 2018. Total annual NPP is composed of ice algal (IA) NPP (red), UI NPP (green), MIZ NPP (yellow), and OW NPP (blue). A blue line is used to indicate the statistically significant increase in total annual NPP.

snow melt period (R^2=0.462, p<0.001), ice thickness (R^2=0.252, p<0.001), and snow thickness (R^2=0.216, p<0.001).

NPP during the UI period varied from 0.6 to 73.9 g C m^{-2} yr^{-1} (mean=44.3±22.6 g C m^{-2} yr^{-1}; Figure 2.6b), with no significant trend between 1988 and 2018. The UI period accounted for a mean of 48.7±22.0% of total annual NPP (range=0.7%-78.2%; Table 2.4), the highest proportion among the four different periods. It also was the most important period for new production, with a mean of 35.8 g C m^{-2} yr^{-1} of new production (mean=84.4% of UI NPP was new; Table A.2). Surface waters were highly productive, with only 1.9% of UI NPP associated with an SCM (Table A.3). One of the primary drivers of variation in UI NPP was UI period length; years with longer UI periods were associated with higher UI NPP (R^2=0.818, p<0.001; Figure 2.7a). Multiple linear regression revealed that 94.7% of the variance in UI NPP (p<0.001) is controlled by the length of the UI period

Table 2.4: Bloom type, % Ice Algal (IA), % UI, % MIZ, % OW, and Total NPP (g C m^{-2} yr^{-1}) for each year. Annual cycles of NPP were separated into 3 clusters (Bloom Types): UI-dominated (UI), mixed dominance (Mix), and MIZ-dominated (MIZ). Means and standard deviation of the magnitude of total NPP (g C m^{-2} yr^{-1}) and NPP within the UI, MIZ, and OW periods for each of the three clusters are listed at the bottom of the table.

Year	Bloom Type	% IA	% UI	% MIZ	% OW	Total
1988	Mix	0.0	58.9	41.1	0.0	76.3
1989	UI	2.0	69.1	10.6	18.2	90.8
1990	Mix	1.9	43.0	20.0	35.1	82.1
1991	Mix	1.1	41.2	37.0	20.7	75.4
1992	Mix	0.0	38.4	29.0	32.6	74.7
1993	MIZ	2.1	2.1	60.7	35.0	89.4
1994	UI	3.8	78.2	8.3	9.7	94.2
1995	UI	0.0	67.5	15.0	17.4	95.6
1996	UI	3.1	66.0	10.2	20.7	100.1
1997	UI	2.0	59.9	11.2	27.0	86.4
1998	MIZ	0.0	1.4	64.4	34.2	86.2
1999	Mix	0.0	28.1	25.7	46.2	87.2
2000	Mix	0.2	30.7	43.0	26.1	77.4
2001	UI	3.2	62.0	11.8	23.0	84.9
2002	UI	2.7	71.3	3.1	22.9	96.7
2003	UI	3.4	66.4	13.3	16.9	95.6
2004	MIZ	2.2	5.7	66.5	25.6	84.0
2005	Mix	2.8	26.0	29.5	41.7	85.8
2006	UI	0.0	65.7	9.1	25.2	85.6
2007	UI	4.5	60.4	8.0	27.1	97.2
2008	UI	2.4	70.5	9.1	18.1	93.2
2009	UI	0.0	74.6	10.0	15.4	99.0
2010	MIZ	0.0	0.7	66.4	32.8	81.9
2011	UI	2.9	63.7	8.5	24.9	98.6
2012	Mix	0.0	46.5	27.0	27.5	81.1
2013	UI	3.4	70.0	7.3	19.3	99.7
2014	Mix	0.0	42.4	27.7	29.9	82.1
2015	UI	3.7	57.6	10.0	28.6	97.4
2016	Mix	2.9	40.2	21.2	35.7	83.4
2017	UI	3.9	46.9	13.1	35.7	83.4
2018	UI	3.9	55.4	13.4	27.3	98.8
Mean	UI	2.6±1.4	65.0±7.6	10.1±2.8	22.2±6.2	94.8±5.0
Mean	Mix	0.9±1.2	39.5±9.7	30.1±7.8	29.4±12.8	80.6±4.4
Mean	MIZ	1.1±1.2	2.5±2.2	64.5±2.7	31.9±4.3	85.4±3.2

(R^2=0.545, p<0.001), ice thickness (R^2=0.347, p<0.001), and the length of the snow melt period (R^2=0.055, p<0.001). Variation in UI NPP was the most important driver of interannual changes in total annual NPP (R^2=0.424, p<0.001).

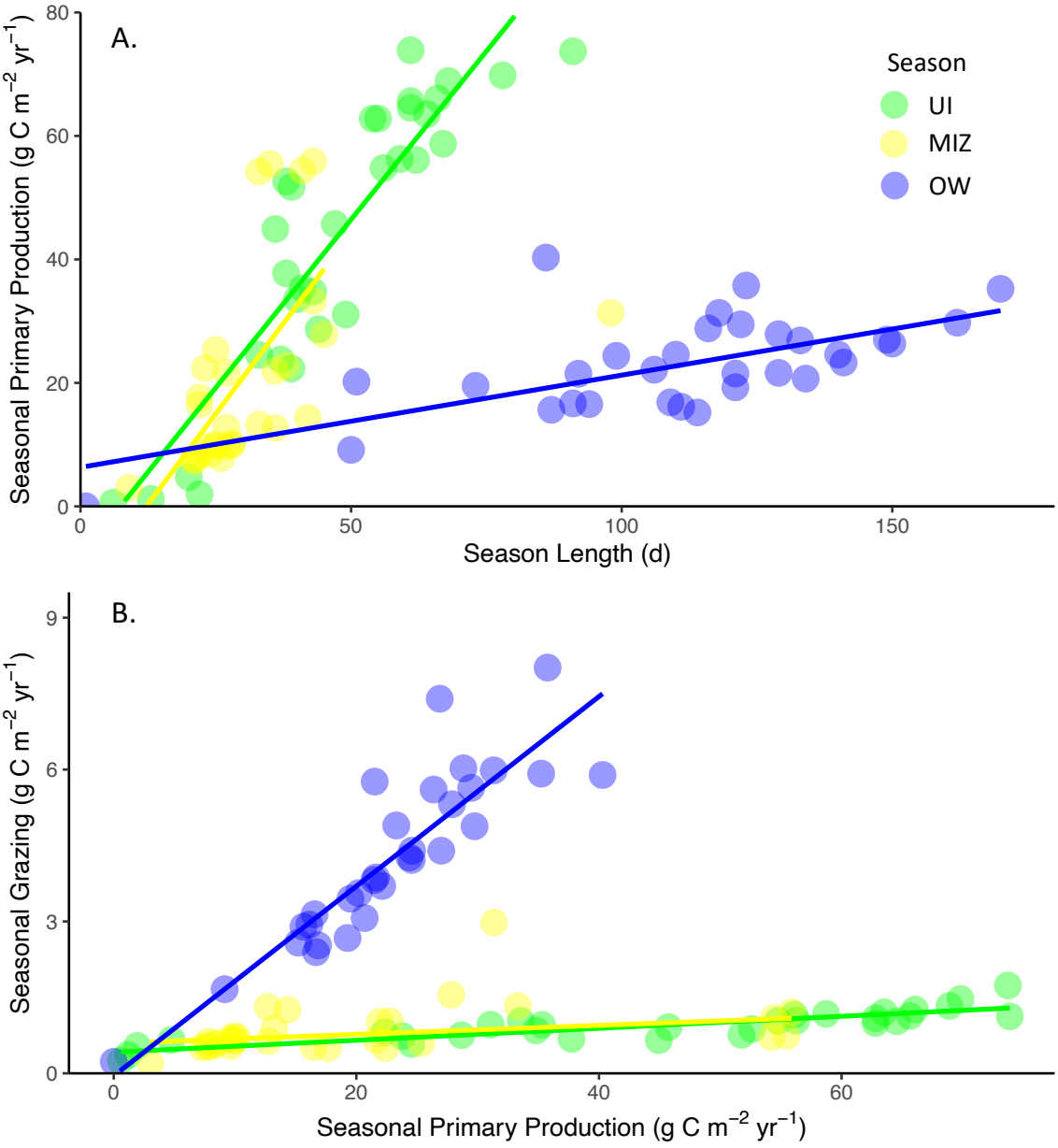

Figure 2.7: Scatterplots of A) length of period (d) vs. NPP (g C m^{-2} yr^{-1}) and B) NPP vs. grazing (g C m^{-2} yr^{-1}) for the UI (green), MIZ (yellow), and OW (blue) periods. Lines (in the period color) are used when linear regressions are statistically significant.

In the MIZ period, NPP ranged from 3.0 to 55.9 g C m^{-2} yr^{-1} (mean=20.1±15.6 g C m^{-2} yr^{-1}; Figure 2.6c) and accounted for 3.1%-66.5% of total annual NPP (mean=23.6±19.1%; Table 2.4), with no interannual trend. The MIZ period was responsible for the smallest proportion of new production of the three periods, accounting for only 13.6 g C m^{-2} yr^{-1} (mean=60.0% of MIZ NPP was new; Table A.2). During this period, the depth of maximum NPP transitioned from surface waters to the SCM, which accounted for 54.0% of MIZ NPP (Table A.3). For all years except 1988 (when ice never retreated), the MIZ period length was significantly correlated with variation in MIZ NPP, accounting for 40.4% of the variance in MIZ NPP ($p<0.001$; Figure 2.7a). Multiple linear regression for all years except 1988 revealed that 78.9% of the variance ($p<0.001$) in annual NPP in the MIZ is controlled by the lengths of the UI ($R^2=0.540$, $p<0.001$) and MIZ periods ($R^2=0.248$, $p=0.002$). MIZ NPP was the second most important driver of interannual changes in annual NPP ($R^2=0.273$, $p=0.003$).

NPP in the OW period varied from 9.1 to 40.3 g C m^{-2} yr^{-1} (mean=23.6±2.9 g C m^{-2} yr^{-1}; Figure 2.6d) in the years when sea ice retreated (all years except 1988). OW NPP made up 9.7-46.2% of annual NPP (mean=26.7±8.2%, Table 2.4) but showed no interannual trend for years in which there was an OW period (1989-2018, $p=0.185$). New production in the OW period averaged 17.4 g C m^{-2} yr^{-1} (mean = 77.2% of OW NPP was new production; Table A.2). Most NPP during this period (mean=94.4% of phytoplankton NPP) was associated with the SCM (Table A.3). Variation in the length of the OW period was significantly correlated to the magnitude of OW NPP, accounting for 47.4% of the variance in OW NPP ($p<0.001$; Figure 2.7a). Multiple linear regression revealed that 70.0% of the variance ($p<0.001$) in OW NPP was controlled by the lengths of the OW ($R^2=0.268$, $p<0.001$), UI ($R^2=0.237$, $p=0.042$), and MIZ ($R^2=0.081$, $p=0.027$) periods and by sea ice thickness ($R^2=0.114$, $p=0.024$). Variation in OW NPP did not significantly drive variation in total annual NPP.

Monthly integrated NPP also changed substantially between 1988 and 2018 (Figure 2.8), increasing annually by 0.005 g C m^{-2} yr^{-1} in March ($R^2=0.262$, $p=0.003$), by 0.05 g C m^{-2} yr^{-1} in April ($R^2=0.213$, $p=0.009$), and by 1.0 g C m^{-2} yr^{-1} in May ($R^2=0.190$, $p=0.014$). In contrast, during the summer and autumn seasons, NPP decreased between 1988 and 2018. July NPP decreased by 0.41 g C m^{-2} yr^{-1} ($R^2=0.134$, $p=0.043$) and September NPP by 0.09 g C m^{-2} yr^{-1} ($R^2=0.118$, $p=0.059$). NPP during June, August, October, and November showed no significant trend over time.

2.3.4 Zooplankton grazing

Zooplankton grazing of total annual NPP ranged from 4.9 to 11.1 g C m^{-2} yr^{-1} (mean=7.5±1.4 g C m^{-2} yr^{-1}) and showed no trend with time.

During the UI period, grazing of NPP averaged 1.4±0.5 g C m^{-2} yr^{-1} (ranging between 0.3 and 2.5 g C m^{-2} yr^{-1} between 1988 and 2018), or 7.8±13.5% of UI NPP. Although there was no change in UI grazing between 1988 and 2018, it was significantly correlated to UI NPP, with 78.8% of variance

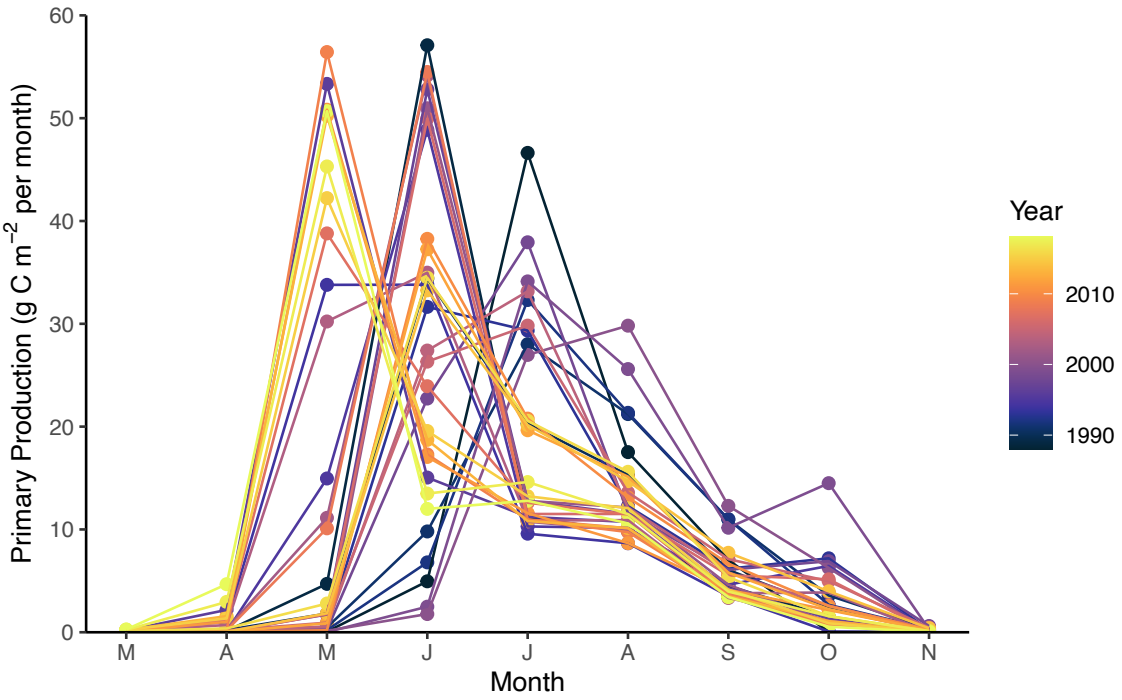

Figure 2.8: Monthly integrated water column NPP (g C m^{-2} per month) for March-November from 1988 to 2018 (colorbar).

in UI grazing attributable to annual changes in UI NPP ($p<0.001$, slope=0.02 g C m^{-2} yr^{-1} yr^{-1}; Figure 2.7b). However, because high UI NPP depressed NPP in the MIZ and OW periods, UI NPP was negatively correlated with annual zooplankton grazing ($R^2=0.404$, $p<0.001$, slope=-0.040).

Grazing by zooplankton during the MIZ period averaged 1.1±0.6 g C m^{-2} yr^{-1} (ranging between 0.3 to 3.5 g C m^{-2} yr^{-1}), consuming 6.7±3.1% of MIZ NPP. 25.5% of the variance in zooplankton grazing during the MIZ period can be attributed to annual changes in MIZ NPP ($p=0.004$, slope=0.01 g C m^{-2} yr^{-1} yr^{-1}; Figure 2.7b). MIZ NPP was also correlated with total annual zooplankton grazing ($R^2=0.220$, $p=0.008$, slope=0.043).

Zooplankton grazing during the OW period varied between 1.7 and 9.0 g C m^{-2} yr^{-1} between 1989 and 2018 (mean=5.1±1.7 g C m^{-2} yr^{-1}), or 21.4±3.5% of OW NPP, and didn't change significantly over time. OW NPP was significantly correlated with both grazing in the OW period ($R^2=0.784$, $p<0.001$, slope=0.21 g C m^{-2} yr^{-1} yr^{-1}; Figure 2.7b) and annual grazing ($R^2=0.643$, $p<0.001$, slope=0.144).

2.3.5 Water column bloom types

Clustering analysis demonstrated that the annual cycle of NPP for each year could be separated into one of three different temporal patterns (Table 2.4) based on the periods defined above: years where the UI bloom dominated total annual NPP (17 of 31 years; Figure 2.9a), years when the MIZ bloom dominated NPP (4 of 31 years; Figure 2.9c), and "mixed" years when both the UI and MIZ blooms were dominant (10 of 31 years; Figure 2.9b). For annual depth vs. time plots for each of these three bloom types, see supplementary section A.5.4 and supplementary Figures A.6-A.8.

These bloom dominance types were associated with different magnitudes of total annual NPP and annual zooplankton grazing. UI-dominated blooms led to years with higher total annual NPP (94.8±5.0 g C m^{-2} yr^{-1}) than mixed (80.6±4.4 g C m^{-2} yr^{-1}, $p<0.001$) or MIZ-dominated blooms (85.4±3.2 g C m^{-2} yr^{-1}, $p=0.003$). Total new production was also significantly higher in years dominated by UI blooms (71.3±3.4 g C m^{-2} yr^{-1}) than for mixed (64.5±3.2 g C m^{-2} yr^{-1}, $p<0.001$) or MIZ-dominant years (64.2±2.0 g C m^{-2} yr^{-1}, $p=0.001$). There was no significant difference between peak daily NPP rate in UI-dominated blooms (5.1±1.6 g C m^{-2} d^{-1}) and mixed UI-MIZ blooms (4.1±0.7 g C m^{-2} d^{-1}). However, mixed dominance blooms had, on average, lower peak production rates than MIZ-dominated blooms (6.3±1.4 g C m^{-2} d^{-1}, $p=0.028$). Bloom type also affected the magnitude of annual zooplankton grazing ($p=0.007$); UI-dominant years featured far less annual zooplankton grazing (7.1±1.1 g C m^{-2} yr^{-1}) than years with MIZ-dominant blooms (9.4±0.8 g C m^{-2} yr^{-1}). There was no difference in annual zooplankton grazing between mixed-dominance (7.6±1.6 g C m^{-2} yr^{-1}) and UI- or MIZ-dominant blooms.

There were no interannual trends in bloom type from 1988-2018, but environmental variables affected bloom type. The annual cycle was dominated by UI blooms under thinner ice conditions (1.68±0.28 m), while thicker ice resulted in either MIZ (2.40±0.19 m, $p<0.001$) or mixed-dominance blooms (2.50±0.07 m, $p<0.001$). MIZ blooms dominated in years where ice retreated earlier (DOY 166.8±3.4 d), while mixed-dominance blooms formed when ice retreated later (DOY 187.9±10.7 d, $p=0.019$).

2.4 Discussion

Despite its short growing season, the Chukchi Sea is a highly productive coastal ecosystem. Our model estimated a rate of total annual NPP ranging between 75 and 100 g C m^{-2} yr^{-1} between 1988 and 2018, values on the higher end of the 55 to 105 g C m^{-2} yr^{-1} of annual NPP previously reported for the Chukchi Sea (*Arrigo et al.*, 2014; *Hill and Cota*, 2005; *Lee et al.*, 2007). However, NPP in the Chukchi Sea can be patchy. Rates can surpass 170 g C m^{-2} yr^{-1} *Hansell et al.* (1993); *Hill et al.* (2018a) along the NO_3^--rich major advective pathways near our model study region but are typically much lower near the coast in the NO_3^--deplete Alaska Coastal Current. *Stabeno et al.* (2020) argue that the high productivity of the Chukchi shelf is due to the existence of Multiple

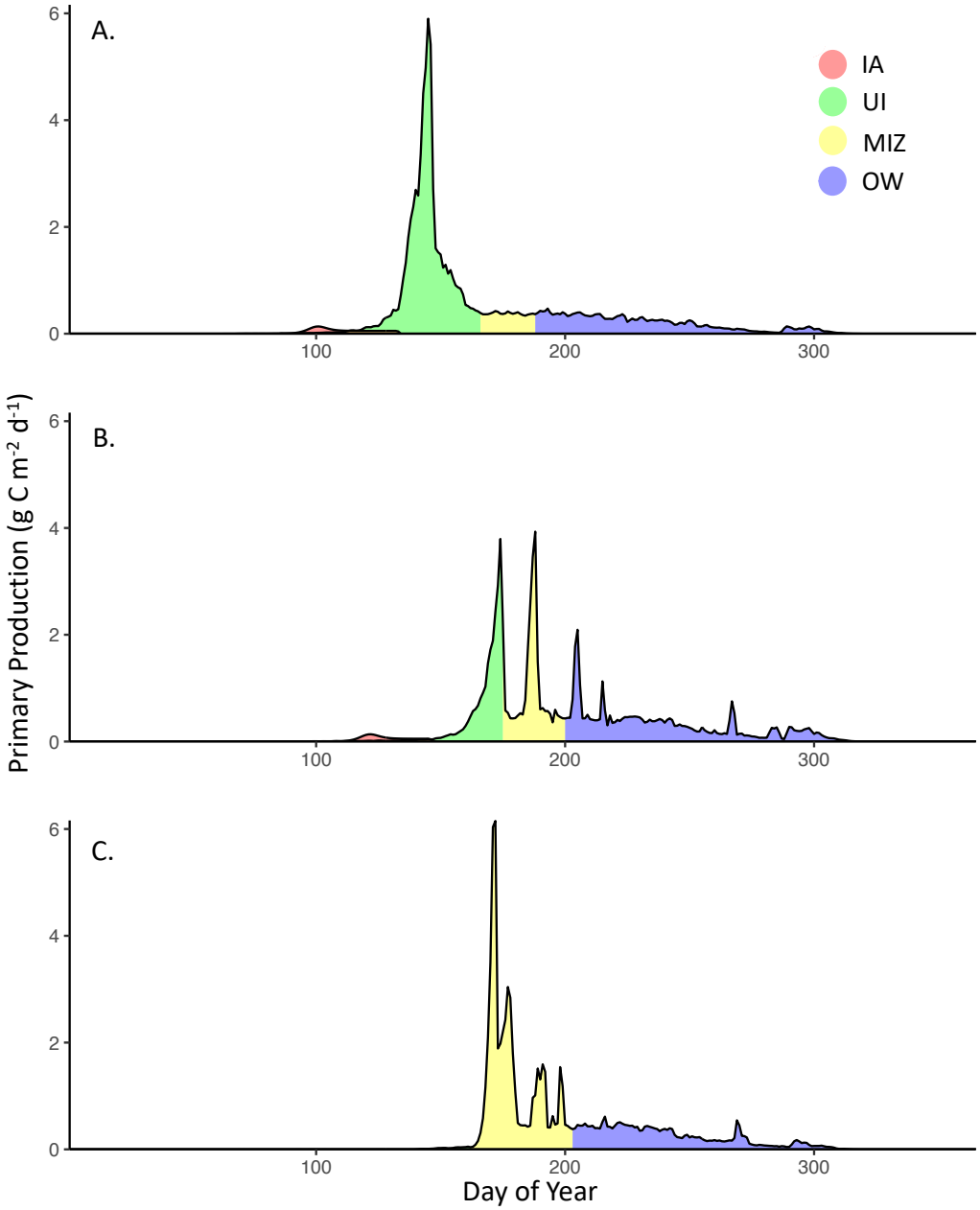

Figure 2.9: Example annual cycles of daily NPP (g C m^{-2} d^{-1}) for (A) a UI-dominant year (2013), (B) a year with mixed UI and MIZ dominance (2005), and (C) an MIZ-dominant year (2010). Red shading represents production by ice algae while green, yellow, and blue shading represent production during UI, MIZ, and OW periods, respectively.

Productive Layers (the MPL hypothesis), whereby ice algae and phytoplankton contribute to high regional NPP in distinct surface and subsurface layers. Our study also partitions annual NPP, not by

different layers, but rather into four periods of production in the Chukchi Sea: microalgae growing within sea ice and phytoplankton that bloom under sea ice, in the MIZ, and during the open water period.

Sea ice microalgae form the first source of NPP each year, and as a result, are a critical source of food to pelagic organisms (*Arrigo*, 2017; *Fortier et al.*, 2002; *Gradinger*, 2009; *Søreide et al.*, 2010) at a time of year when other sources of food are scarce (*Assmy et al.*, 2013; *Bradstreet and Cross*, 1982). When light returns to the Chukchi Sea following the polar night, ice-associated algae are able to use their stable position atop the water column to take advantage of increasing under-ice light and high water column NO_3^- concentrations. Ice algal concentrations can surpass 300 mg Chl *a* m^{-2}, although concentrations more typically range between 4 and 30 mg Chl *a* m^{-2} in the Chukchi Sea (*Arrigo et al.*, 2017; *Gradinger*, 2009; *Selz et al.*, 2018) and range between 0 and 30 mg Chl *a* in our model. These dense assemblages can substantially diminish the transmission of light through the ice, reducing light available to phytoplankton growing in the water column and further delaying the initiation of water column NPP. Ice algae modeled as a part of this study were able to grow under lower light conditions than phytoplankton, with algal blooms beginning on average 28 days earlier (and as much as 45 days earlier) than phytoplankton blooms. In addition to their importance as an early food source, ice algal assemblages are typically dominated by diatoms and can substantially contribute to annual C export (*Boetius et al.*, 2013; *Fahl and Nöthig*, 2007) because their siliceous cell walls and large cell size cause them to sink rapidly through the water column (*Smetacek*, 1999). As a result, ice algal NPP is often thought to contribute substantially to the food available to benthic organisms (*Campbell et al.*, 2009). In areas such as the central Arctic, ice algal NPP is thought to comprise more than 50% of total annual NPP. However, despite their importance to pelagic and benthic grazers and to C export, ice algae are probably minor contributors to total annual NPP in more productive parts of the Arctic, including the continental shelf of the Chukchi Sea. Mean annual ice algal NPP calculated in our model averaged 1.7 g C m^{-2} yr^{-1}, in line with previous observations of 1-2 g C m^{-2} (*Gradinger*, 2009) in the Chukchi Sea. As a result, modeled ice algal NPP contributed 0-5% of total annual NPP in the Chukchi Sea, similar to the 2-10% contribution estimated on Arctic continental shelves (*Arrigo*, 2017; *Dupont*, 2012; *Gosselin et al.*, 1997; *Jin et al.*, 2012).

The second period of production evaluated here, phytoplankton production in the under-ice period, was historically thought to be too light-limited to contribute substantially to annual NPP (*Hameedi*, 1978; *Perrette et al.*, 2011). However, data from the ICESCAPE program (*Arrigo et al.*, 2012, 2014) demonstrated that massive phytoplankton blooms can form beneath the sea ice. Light transmission through sea ice gradually increases as snow melts, sea ice thins, ice algae slough off the bottom of the sea ice, and melt ponds proliferate on the surface of the ice (*Light et al.*, 2015; *Perovich and Polashenski*, 2012). Phytoplankton, largely centric diatoms (*Laney and Sosik*, 2014) with high maximum photosynthetic rates and photosynthetic efficiencies (*Lewis et al.*, 2019), are primed to bloom as light limitation lifts. Massive blooms have been reported in the UI period, with

particularly extraordinary observations during the ICESCAPE 2011 cruise, where depth-integrated Chl *a* averaged a remarkable 840 mg m^{-2} over hundreds of km^2 of fully consolidated, 1 m thick sea ice (*Arrigo et al.*, 2012, 2014). These high Chl *a* concentrations were also associated with high rates of NPP. During the ICESCAPE 2011 cruise, the UI period alone was found to contribute nearly 70 g C m^{-2} yr^{-1} (*Arrigo et al.*, 2014), comparable to our modeled annual rates of UI NPP, which were 62.8 g C m^{-2} yr^{-1} in 2011 and the maximum for the time series, 73.9 g C m^{-2} yr^{-1} in 2009. Our model results further suggest that UI NPP accounted for nearly half of total annual NPP between 1988 and 2018, and years in which UI blooms dominated saw, on average, higher total annual NPP. The importance of the UI period to annual NPP is supported by a number of recent studies, which have found that NPP associated with UIBs was of equal or greater magnitude to NPP in the rest of the year (*Arrigo et al.*, 2014; *Lowry et al.*, 2014; *Mayot et al.*, 2018; *Mundy et al.*, 2009; *Oziel et al.*, 2019). Despite growing evidence of the high rates of NPP during the UI period, the fate of UI NPP remains under-studied. Because the mixed layer remains cold (<-1.5°C) during the UI period, previous studies have found that zooplankton species were unable to graze effectively (*Campbell et al.*, 2001; *Coyle et al.*, 2007; *Huntley and Lopez*, 1992), possibly leading to a mismatch in phytoplankton and zooplankton annual cycles (*Conover and Huntley*, 1991). Our results indicate that UI-period zooplankton grazing scarcely increased in years with high UI NPP, indicating that low temperatures prevented zooplankton from taking advantage of increased food availability in the UI period. Further, years with high UI NPP were associated with reduced annual zooplankton grazing. Consequently, increasing NPP in the UI period may intensify the mismatch in phytoplankton and zooplankton (*Conover and Huntley*, 1991), increasing organic matter export to the sediments (*Lalande et al.*, 2020) and thus decreasing food availability to pelagic-feeding fish, birds, and mammals (*Bradstreet and Cross*, 1982; *Loeng et al.*, 2005).

More frequent observations of UIBs in recent years (*Ardyna et al.*, 2020b) and model results by *Horvat et al.* (2017) lend credence to the hypothesis that changing ice conditions have led to an increased incidence of UIBs in recent years (*Arrigo et al.*, 2014). However, our model demonstrates that, as early as 1988, conditions in the northern Chukchi Sea were amenable to UIB formation. The UI period was, in fact, the most productive period in 17 of the 31 years modeled as a part of this study and was only insubstantial (UI NPP of < 5 g C m^{-2} yr^{-1}) in four years with thick sea ice cover. While our study found a substantial increasing trend in total annual NPP during spring (1.1 g C m^{-2} yr^{-1}) between 1988 and 2018, we found no evidence of increasing NPP associated with the UI period over this timeframe. This is likely a function of the location we chose to model, which is a region where multi-year ice is present in some years but not others. The associated high degree of interannual variability in sea ice age and thickness resulted in highly variable NPP during the UI period, which swamped any secular trend over time. Had we elected to model a region further to the south that was dominated by first year ice, rather than the site of the massive UIB observed during ICESCAPE 2011 (*Arrigo et al.*, 2012), we likely would have observed an increase in UI NPP

between 1988 and 2018.

The MIZ period, representing the third source of production evaluated as a part of our study, has been historically associated with the highest rates of NPP in Arctic waters (*Niebauer*, 1991; *Perrette et al.*, 2011; *Sakshaug*, 2004). As ice breaks up and retreats within the MIZ, the mixed layer shoals substantially, dramatically increasing light available in the water column and allowing for rapid phytoplankton growth (*Sakshaug and Skjoldal*, 1989) that strips nutrients from the mixed layer (*Perrette et al.*, 2011). Using satellite observations, *Perrette et al.* (2011) noted that high Chl *a* concentrations can be found in a narrow band (20-100 km) along the ice edge, moving northward as ice retreats. Although the MIZ blooms only last 20 days following sea ice retreat in the analysis of *Perrette et al.* (2011), their study estimates that rates of MIZ NPP were up to twice as high as during the OW period. However, our study found that, while the MIZ period could contribute substantially to total annual NPP in years with particularly thick multi-year sea ice, on average it accounted for the smallest proportion (less than 24%) of total NPP between 1988 and 2018 of the three pelagic sources of NPP evaluated. Further, we found that this period accounted for a mere 10% of total NPP in years characterized by large UIBs. During most years from 1988-2018, the MIZ period represented a transition as NPP shifted from NO_3^--depleted surface waters down to the SCM. As a result, the MIZ period generated a smaller proportion of new production than either the UI or the OW periods. Much of the discrepancy between our findings and those of *Perrette et al.* (2011) can be attributed to the fact that *Perrette et al.* (2011) assumed that all Chl *a* observed in the 20 days following sea ice retreat was generated in the MIZ, ignoring the possibility of UI generation of production. *Lowry et al.* (2014) considered locations in the Chukchi Sea to host MIZ blooms if Chl *a* increased following ice retreat, but were likely to host UIBs if Chl *a* concentrations decreased. Their study suggested that UIBs covered an area 2.5-fold higher than blooms generated in the MIZ. While NPP in the MIZ period is more easily studied than in the UI period, our study found that the MIZ period is likely not as important in driving annual NPP in the Chukchi Sea as the UI period.

During the OW period, the fourth NPP source evaluated here, phytoplankton productivity is largely confined to the SCM (*Arrigo et al.*, 2014; *Brown et al.*, 2015b; *Hill and Cota*, 2005; *Martin et al.*, 2010). UI and MIZ NPP leaves surface waters devoid of NO_3^-, preventing substantial surface NPP in the OW period (*Codispoti et al.*, 2005, 2009; *Mills et al.*, 2018). As a result, most phytoplankton biomass in this period is concentrated in a layer just below the mixed layer, where NO_3^- concentrations remain elevated and light is still available (*Brown et al.*, 2015b; *Hill and Cota*, 2005). While diatoms dominate community composition in the SCM (*Hill and Cota*, 2005), small flagellates can become abundant in surface waters following NO_3^- depletion (*Li et al.*, 2009). Our study showed that greater than 90% of OW NPP was located within the SCM. In a study of SCMs in the Chukchi Sea between 2002 and 2012, *Brown et al.* (2015b) found that SCMs developed up to one month prior to ice retreat, and gradually deepen to ∼30 m by the summer. Consistent with these observations, we find that SCMs can be generated as much as 34 days before ice retreat in

years with UIBs. The generation of an SCM during the UI period supports the hypothesis, first put forth by *Palmer* (2013) and *Brown et al.* (2015b), that phytoplankton growing in the low-light conditions of the UI period are better photophysiologicaly acclimated to grow once they descend to the SCM.

While the MIZ and OW periods have historically been presumed to be far more productive on Arctic continental shelves than the ice-covered portion of the year, our study demonstrates that UI production makes up the greatest proportion of total annual NPP in the northern Chukchi Sea and is the most critical period in driving interannual variability. Relying on cruise and satellite data exclusively from the MIZ and OW periods has historically caused us to drastically underestimate NPP in parts of the Arctic that host UIBs. A satellite-based survey by *Arrigo and Van Dijken* (2011), for example, estimated that annual NPP between 1998 and 2008 was only 5 g C m^{-2} yr^{-1} at the location of this model, more than an order of magnitude lower than both the *Arrigo et al.* (2014) NPP estimates based on nitrate drawdown and our modeled estimates of total annual NPP. Incorporation of new technologies that allow us to better estimate the relative importance of UIBs to total annual NPP, such as moorings, floats, or AUVs with bio-optical or biogeochemical sensors, are more likely to produce accurate estimates of regional NPP.

Further, our study finds that conditions in the Chukchi Sea have likely been amenable to the formation of UIBs since at least the late 1980s. Indeed, observations of UIBs dating back to at least 1957 (*English*, 1961) indicate that UIBs have been generated sporadically for decades. However, as thinner, younger sea ice has come to dominate much of the Arctic Ocean in recent years (*Laxon et al.*, 2013; *Serreze and Stroeve*, 2015), observations of UIBs have grown to include most of the Arctic Ocean (*Ardyna et al.*, 2020b). It is quite likely that continued changes in sea ice cover will only make UIBs more widespread in the Arctic Ocean in the future (*Horvat et al.*, 2017), further demonstrating the critical importance of better understanding NPP under sea ice.

2.5 Acknowledgments

Analysis for the SUBICE program was supported by the National Science Foundation (NSF) grant PLR-1304563 to KRA. Model code and all data are available at `https://purl.stanford.edu/gc896jc5127`.

Chapter 3

Increases in Benthic Particulate Export and Sedimentary Denitrification in the Northern Chukchi Sea Tied to Under-Ice Primary Production

Courtney M. Payne, Kevin R. Arrigo
Department of Earth System Science, Stanford University, Stanford, California, USA

A peer reviewed version of this chapter was published in AGU in the *Journal of Geophysical Research: Oceans*. To view the published open abstract: https://doi.org/10.1029/2021JC018110.

Payne, C. M., & Arrigo, K. R. (2022). Increases in benthic particulate export and sedimentary denitrification in the northern Chukchi Sea tied to underice primary production. Journal of Geophysical Research: Oceans, 127. https://doi.org/10.1029/2021JC018110.

Changing sea ice conditions have led to increases in net primary production (NPP) in the northern Chukchi Sea, driven in part by massive under-ice phytoplankton blooms. These blooms increase the particle export to the sediments and could affect the rate of sedimentary denitrification. We use a 1-D coupled ecosystem model forced with satellite-derived

sea ice conditions to quantify changes in particle export, nitrification, and denitrification on the northern Chukchi shelf. Between 1988 and 2018, increases in annual NPP drove secular increases in particle export to the benthos (1.8±0.8 mmol m^{-2} yr^{-1}), water-column and sedimentary nitrification (1.2±0.4 and 1.1±0.4 mmol m^{-2} yr^{-1}, respectively), and sedimentary denitrification rates (1.3±0.5 mmol m^{-2} yr^{-1}). Increased annual export to the benthos and denitrification were driven by higher rates early in the year (from January-June) and are highest in years where under-ice blooms dominate. Greater denitrification rates in the northern Chukchi Sea would likely reduce NPP in downstream regions such as the Greenland Sea and promote greater N_2 fixation in the North Atlantic. We also evaluated how changes in wintertime nitrogen (N) concentrations in the northern Chukchi Sea due to sea ice loss or changes in advection might impact rates of denitrification. Through N sensitivity experiments, we found that 30% of all added N was lost through denitrification, diminishing the N supply available downstream of the Chukchi Sea. Thus, increased particle export associated with under ice blooms has the potential to markedly alter the N cycle both in the northern Chukchi Sea and in adjacent waters.

3.1 Introduction

The Chukchi Sea, located north of the Bering Strait, is one of the most productive regions in the Arctic Ocean. Mean estimates of annual net primary production (NPP) for the region typically range between 55 and 105 g C m^{-2} yr^{-1} (*Arrigo et al.*, 2014; *Hill and Cota*, 2005; *Lee et al.*, 2007). Along major advective pathways, however, particularly high nutrient concentrations can spur rates of NPP that surpass 170 g C m^{-2} yr^{-1} (*Hansell et al.*, 1993; *Hill et al.*, 2018a). This high NPP supports substantial zooplankton, fish, seabird, and marine mammal populations (*De Robertis et al.*, 2017; *Ershova et al.*, 2015; *Kuletz et al.*, 2015; *Logerwell et al.*, 2015; *Moore and Kuletz*, 2019) as well as rich benthic communities (*Grebmeier et al.*, 1988; *Grebmeier*, 2006; *Grebmeier et al.*, 2015; *Lalande et al.*, 2007).

In recent decades, earlier onset of sea ice melt and retreat as well as later sea ice advance in the Chukchi Sea (*Stroeve et al.*, 2014) have contributed to a 34% increase in the length of the ice-free period between 1998 and 2018 (*Lewis et al.*, 2020). The sea ice in the region has also thinned substantially in recent decades; *Kwok* (2018) found a nearly 50% decline in ice thickness in the northern Chukchi Sea between 1958 and 1997 (from 2 to 1 m), and a further 40% decline in ice thickness between 1997 and 2017 (from 1 to 0.6 m). *Serreze and Stroeve* (2015) use ice age as a proxy for thickness but come to a similar conclusion, finding that only 5% of the Arctic was covered in ice more than 5 years old in 2014, as compared to nearly 30% in 1988.

Changes in sea ice coverage have affected Chukchi Sea ecosystems. As sea ice extent diminished between 1998 and 2018, satellite-derived observations indicate that the Chukchi Sea has experienced

a 30% increase in open water area and a 97% increase in annual NPP (*Lewis et al.*, 2020). The delay in ice advance in autumn led to a 35% increase in the incidence of remotely-sensed autumn blooms in the Chukchi Sea between 1998 and 2012 (*Ardyna et al.* 2014). Further, substantial phytoplankton blooms have been observed under fully consolidated ice cover in the Chukchi Sea (*Arrigo et al.*, 2012; 2014; *Hill et al.*, 2018a). Model results by *Horvat et al.* (2017) found that these under-ice blooms (UIBs), likely a rare feature in the Arctic Ocean prior to 1990 (*Ardyna et al.*, 2020a), could have formed over as much as 30% of the Arctic Ocean between 2006 and 2015 as younger, thinner sea ice dominated the region. More frequent observations of UIBs throughout the Arctic Ocean in recent years (*Arrigo et al.*, 2012; 2014; *Assmy et al.*, 2017; *Boles et al.*, 2020; *Hill et al.*, 2018b; *Leu et al.* 2011; *Mundy et al.* 2009; 2014; *Oziel et al.*, 2019; *Randelhoff et al.*, 2020) indicate that these blooms may be becoming more frequent as sea ice conditions change.

Furthermore, climate change is likely to either diminish or enhance nutrient supply to the surface of the Arctic Ocean, thus changing annual NPP (*Lewis et al.* 2020; *Li et al.*, 2009). Observations in the early 2010s indicated that nutrient entrainment in the surface ocean decreased due to an increase in precipitation, ice melt, and river outflow (*McLaughlin and Carmack*, 2010; *Nummelin et al.* 2016), causing smaller phytoplankton species to proliferate (*Li et al.*, 2009). However, recent evidence indicates that substantial increases in NPP since 2012 (*Henley et al.*, 2020; *Lewis et al.* 2020) have largely been promoted by an increase in nutrient supply (*Lewis et al.*, 2020; *Mordy et al.* 2020; *Randelhoff et al.*, 2019, 2020). These increases are likely a result of sea ice loss, as the greater open water area leads to more mixing events (*Zhang et al.* 2010), more storms (*Yang* 2004), enhanced upwelling near shelf breaks (*Carmack and Chapman*, 2003; *Tremblay and Gagnon* 2009; *Tremblay et al.* 2011), and the generation of internal waves (*Rainville and Woodgate* 2009). In the Chukchi Sea, where the northward advection of NO_3^--replete waters through the Bering Strait predominates (*Woodgate et al.* 2005), changes in transport may also lead to changes in nutrient concentrations. Between 1990 and 2015, a strengthening of the Pacific-Arctic pressure head (*Peralta-Ferriz and Woodgate*, 2017) led to an increase in transport through the Bering Strait of 0.01 Sv yr^{-1} (*Woodgate*, 2018), corresponding to a 30% increase in transport over the climatology. High transport of Pacific waters into the Arctic Ocean has been associated with ship-based and mooring observations of higher nutrient concentrations in the Chukchi Sea (*Mordy et al.*, 2020), indicating that nutrient concentrations may increase in the Chukchi Sea if this increase in transport continues.

Altered sea ice conditions and NPP could have substantial impacts on the marine nitrogen (N) cycle in the Chukchi Sea and further downstream (*Arrigo et al.*, 2014; *Arrigo and Van Dijken*, 2015). Phytoplankton blooms in the under-ice (UI) period are dominated by diatoms (*Laney and Sosik*, 2014) which sink rapidly and contribute disproportionately to global particulate organic carbon (POC) export due to their highly silicified cell walls and large cell size (*Smetacek* 1999). If NPP during the UI period is substantial, reduced grazing pressure due to cold water temperatures (*Campbell et al.* 2001; *Coyle et al.*, 2007; *Huntley and Lopez*, 1992) is likely to increase POC

and particulate organic N (PON) export to the sediments (*Payne et al.*, 2021). Observations in the northern Chukchi Sea indicate that algal export during the UI period can be high (with daily chlorophyll (Chl) *a* export to the benthos of up to 5 mg m^{-3} d^{-1}), is almost entirely diatom-dominated (93-100%), and has increased over time (*Lalande et al.*, 2007, 2020; *Szymanski and Gradinger*, 2016). This observed increase in organic matter export to the sediments should substantially increase benthic-pelagic coupling (*Honjo et al.*, 2010; *Lalande et al.*, 2020) and could have implications for regional N loss. Coupled partial nitrification-denitrification in the sediments of the shallow Chukchi shelf (*Brown et al.*, 2015a) drives both high N recycling and high rates of fixed-N loss in the sediments. As a result, the Chukchi Sea accounts for 1-3% of the global sink of fixed N in the oceans (*Chang and Devol*, 2009). Both observational studies (*Baumann et al.*, 2013; *Horak et al.*, 2013; *Granger et al.*, 2011; *Townsend and Cammen*, 1988) and models (*Chang and Devol*, 2009; *Fennel et al.*, 2009; *Fennel*, 2010; *Laurent et al.*, 2016; *Soetaert et al.*, 1996b, a) indicate that increases in particle export can lead to increases in sedimentary denitrification when other controls on denitrification (namely, bottom-water oxygen and N concentrations and water column depth; *Soetaert et al.*, 1996b, a) are constant. A further increase in sedimentary denitrification could also have some downstream impacts, potentially limiting NPP downstream of the Chukchi Sea (*Arrigo and Van Dijken*, 2015) but increasing rates of N_2 fixation in the North Atlantic (*Yamamoto-Kawai et al.*, 2006).

To investigate the impacts of changing patterns of NPP in the Chukchi Sea between 1988 and 2018 on the regional N cycle, we use a coupled ecosystem model, CAOS-GO (the Coupled Arctic Ocean Sediment model with GOTM and OMEXDIA; *Payne et al.*, 2021), composed of interconnected biogeochemical (the Coupled Arctic Ocean System model, or CAOS; *Payne et al.*, 2021), physical (the General Ocean Turbulence Model, or GOTM, version 5.4; *Burchard et al.*, 1999), and sedimentary chemistry (OMEXDIA; *Soetaert et al.*, 1996b, a) models. We evaluate the impact of interannual changes in sea ice conditions and increasing annual NPP (*Payne et al.*, 2021) on the export rate of PON from surface waters to the benthos and whether this export has stimulated or inhibited water column and sedimentary nitrification and denitrification. Further, we quantify the sensitivity of annual NPP, PON export, nitrification, and denitrification to changes in the N inventory of the Chukchi Sea.

3.2 Methods

The coupled CAOS-GO model (Figure 3.1) was implemented at 72.16°N and 166.60°W (Figure 3.2) in the northern Chukchi Sea for the period 1988 to 2018, as in *Payne et al.* (2021). GOTM (*Burchard et al.*, 1999) and CAOS ((*Payne et al.*, 2021) require as input temporal changes in sea ice concentration, atmospheric conditions (e.g. 10 m wind, air temperature, pressure, relative humidity, and cloud cover), albedo, idealized temperature and salinity profiles, and cloud-adjusted surface

irradiance (*Dobson and Smith*, 1988; *Gregg and Carder*, 1990). GOTM produces hourly profiles of temperature, salinity, buoyancy frequency, and turbulent diffusion coefficients, while CAOS dynamically simulates the vertical behavior of N-based state variables, including sea ice algae, small and large phytoplankton, small and large zooplankton, nitrate (NO_3^-), ammonium (NH_4^+), and detritus. The sediment model, OMEXDIA (*Soetaert et al.*, 1996a, b), requires input of bottom-water concentrations of NO_3^- and NH_4^+ and rates of PON export to the benthos from CAOS, as well as bottom-water temperature and salinity from GOTM. OMEXDIA simulates daily changes in fast- and slow-remineralizing organic matter, oxygen (O_2), NO_3^-, NH_4^+, N_2, and a reduced substances state variable (which included both POC removed as solid substances, such as through pyritization or manganese carbonate formation, and dissolved organic C that diffused through the sediments). OMEXDIA also calculates rates of oxic and anoxic remineralization (where PON is converted to NH_4^+), nitrification, and denitrification, as well as vertical fluxes of NO_3^- and NH_4^+ between the sediments and the water column which are subsequently used by CAOS. While *Soetaert et al.* (1996a) use ammonia (NH_3) to represent the combined pools of NH_4^+ and NH_3, here we will use the term NH_4^+ throughout because this molecule is dominant at the typical ocean pH. Additionally, we report concentrations and rates taking place in thin layers in the sediments in nmol cm^{-3} but in mmol m^{-3} in the water column and for depth-integrated sedimentary processes (both units are equivalent). For more complete model details, see *Payne et al.* (2021).

Satellite-derived and reanalysis data were used as inputs for CAOS-GO. Atmospheric conditions were determined using the National Centers for Environmental Prediction (NCEP) North American Regional Reanalysis (NARR; 32 km resolution used in this model configuration) products, which were provided by NOAA/OAR/ESRL PSL, Boulder, Colorado, USA from their website at `https://psl.noaa.gov/data/gridded/`. Idealized temperature profiles used in GOTM were determined using NOAA OISST version 2.1 (0.25° latitude and longitude resolution) data (*Reynolds et al.*, 2007), provided by the NOAA/OAR/ESRL PSL, Boulder, Colorado, USA, from their website at `https://psl.noaa.gov/`. The mean of two Arctic Ocean snow depth models, SnowModel-LG (*Liston et al.*, 2020; *Stroeve et al.*, 2020; 25 km resolution) and CPOM (*Zhou et al.*, 2021; 12.5 km resolution), was used to compute snow and melt pond thicknesses. Ice age (*Tschudi et al.*, 2019; 62.5 km resolution) was used to calculate sea ice thickness and melt pond areal coverage (*Webster et al.*, 2015). The National Snow and Ice Data Center (NSIDC) snow melt onset date (*Anderson et al.*, 2019; 75 km resolution) provided the start date of snow melt each year. Sea ice began melting (and melt ponds began to form) on the first day when daily average NCEP NARR 2 m air temperature rose above 0°C at the model location. The timing of sea ice retreat and advance were set using sea ice concentration data (75 km resolution), provided by the NOAA/NSIDC Climate Data Record mean sea ice concentration (*Meier et al.*, 2019; *Peng et al.*, 2013). See supplementary text B.1 and B.2 for methods and results of sensitivity analyses.

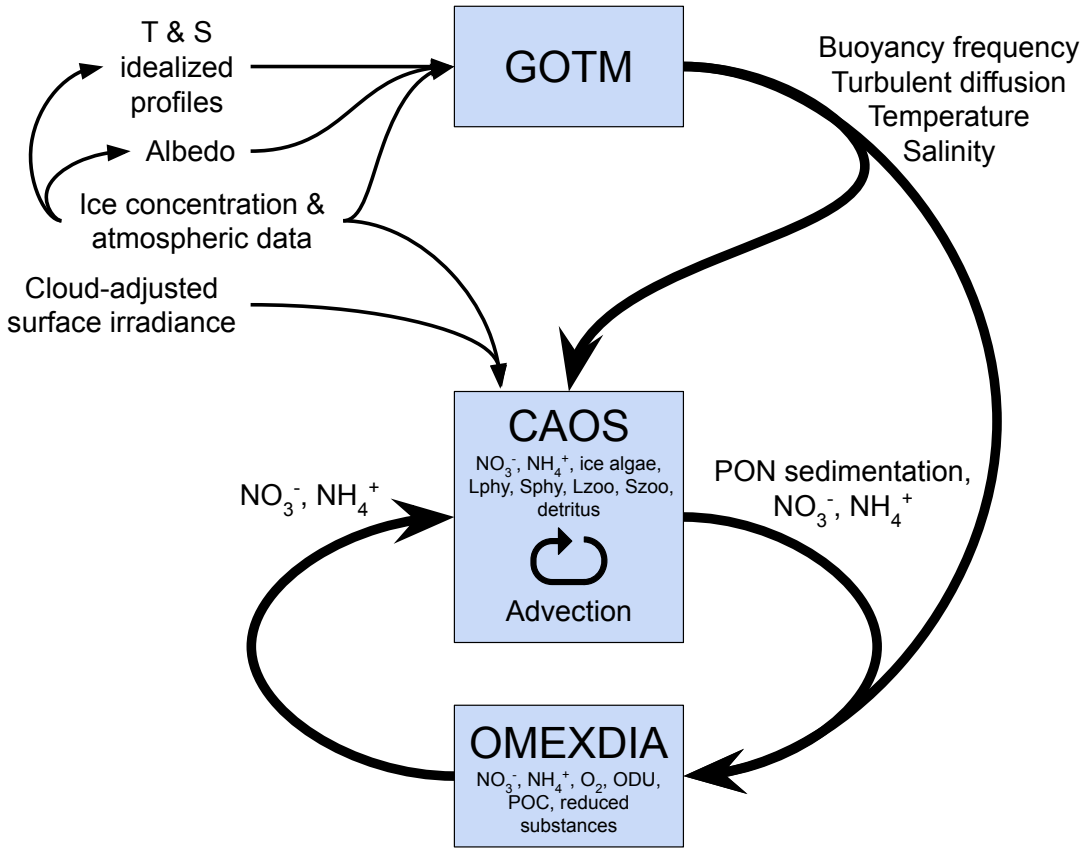

Figure 3.1: An overview of the inputs and outputs shared between the 3 coupled models (GOTM, CAOS, and OMEXDIA) in CAOS-GO. Thick lines represent flows between models, while thin lines represent external inputs to the models. State variables are listed in small text for the CAOS and OMEXDIA models. *Lphy, Sphy, Lzoo, and Szoo* are abbreviations for the CAOS model state variables of large phytoplankton, small phytoplankton, large zooplankton, and small zooplankton, respectively. *ODU* is an abbreviation for the OMEXDIA model state variable of oxygen demand units. From *Payne et al.* (2021).

3.2.1 Under-ice, marginal ice zone, and open water periods

As in *Payne et al.* (2021), we divided the annual cycle into the UI, marginal ice zone (MIZ), and open water (OW) periods. The UI bloom period extended from the initiation of exponential phytoplankton growth (when phytoplankton N assimilation exceeded 0.5 mmol N m^{-2} d^{-1}) and lasted until the start of sea ice retreat, when satellite-derived sea ice concentration diminished below 90%. The MIZ period extended from the start of sea ice retreat until its conclusion, when sea ice concentrations diminished below 10%. Finally, the OW period began at the conclusion of ice retreat and terminated on the earliest date when either ice advanced in the autumn or light diminished below 1% the maximum value reached in the mixed layer, or on DOY 300±6.

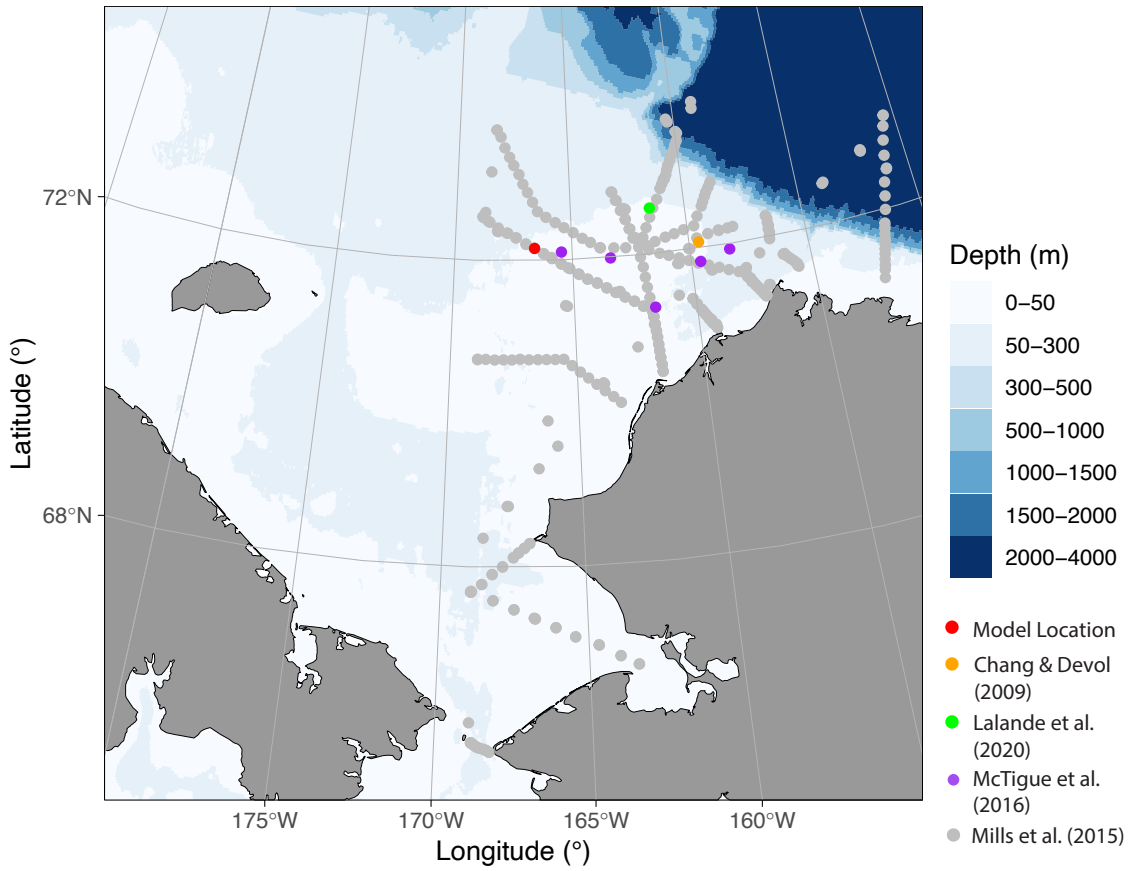

Figure 3.2: Bathymetric map of the Chukchi Sea. Points represent the location of the model (red) in relationship to observational data collected by *Chang and Devol* (2009, orange), *Lalande et al.* (2020, green), *McTigue et al.* (2016, purple), and *Mills et al.* (2015, grey).

3.2.2 Winter Nitrate Inventory Experiment

Wintertime NO_3^- concentration shows minimal spatial variability across the Chukchi shelf; surface NO_3^- concentrations averaged 14.0±1.91 mmol m^{-3} across the region in 2014 (*Arrigo et al.*, 2017). To test the effect of pre-bloom winter NO_3^- concentration on rates of sedimentary denitrification, we ran the model for the year 2011, a year with a moderate UIB (*Payne et al.*, 2021), under different initial (wintertime) NO_3^- conditions. To represent the range of wintertime NO_3^- concentrations observed in the Chukchi Sea (*Mordy et al.*, 2020), we progressively altered the wintertime NO_3^- concentration by ±2 mmol m^{-3} in a series of simulations, resulting in initial NO_3^- concentrations ranging from 10 to 26 mmol m^{-3} (or depth-integrated NO_3^- concentrations of 500 to 1300 mmol m^{-2}). These were used to test how much successive 100 mmol NO_3^- m^{-2} additions (2 mmol m^{-3} over 50 m) impacted N assimilation by microalgae, PON export to the benthos, nitrification, and denitrification at different

initial NO_3^- concentrations.

3.2.3 Statistics

Multiple linear regression was used to evaluate the importance of environmental conditions (e.g. ice thickness, length of UI period) on PON export to the sediments and denitrification rates. First, we checked for collinearity by using the variance inflation factor (VIF). Variables were only moderately correlated (VIF was <3 for all variables) and should have minimal impact on the correlations. Multiple linear regression variables were identified using backward selection, whereby the variable with the highest p-value was sequentially eliminated until only statistically significant variables ($p<0.05$) remained. These regressions were subsequently checked using the Shapiro-Wilk test and visual inspection of histograms, quantile-quantile plots, and plots of the independent and dependent variables. Linear regressions are reported with the standard error, and plots with linear regressions include a confidence interval of 95%.

To cluster annual cycles of daily NPP into distinct types, k-means clustering was used based on NPP in the UI and MIZ periods. The gap statistic was used to determine the optimal k value. The annual cycle of N assimilation by microalgae each year was separated into one of three different temporal patterns based on the relative amount of assimilation during the UI and MIZ periods: years dominated by blooms in the UI period (17 of 31 years), years dominated by bloms in the MIZ period (4 of 31 years), or "mixed" years when both the UI and MIZ blooms were approximately equal (10 of 31 years; Table 3.1). To quantify the relationship between annual nitrification and denitrification rates and the annual bloom type, ANOVA and post hoc Tukey's honest significant difference (HSD) tests were used. All statistical analyses were conducted in R version 4.1.0, including the relative importance of each variable in multiple linear regressions, which was assessed using the 'relaimpo' package version 2.2-6 (*Grömping*, 2006).

3.3 Results

As water column NPP increased in the spring, particle export to the benthos increased shortly afterwards, subsequently leading to changes in sedimentary processes. For example, in 2011, a year with a moderate UIB, (Table 3.1, *Payne et al.*, 2021), the phytoplankton bloom began on DOY 113 and peaked during the UI period (on DOY 147) at 352.0 mmol PON m^{-2}. PON export to the benthos peaked eight days later (on DOY 155; Figure 3.3a) at 6.5 mmol m^{-2} d^{-1}. PON export to the benthos diminished below 0.1 mmol N m^{-2} d^{-1} on DOY 326, when N assimilation by microalgae was 0.1 mmol m^{-2} d^{-1}.

As PON was exported to the benthos, sedimentary concentrations of O_2, NO_3^-, and NH_4^+ underwent rapid changes. O_2, which maintained a concentration of 300 nmol cm^{-3} in the top 0.01 cm of the sediments, dropped to near-zero below the top 3 cm (Figure 3.3b). Within six days of

Table 3.1: Modeled dominant bloom type (UI-dominant, MIZ-dominant, or mixed dominance), winter ice thickness (m), winter snow thickness (m), length of the under-ice (UI) period (d), length of the marginal ice zone (MIZ) period (d), length of the open water (OW) period (d), annual N assimilation (mmol N m^{-2} yr^{-1}), benthic PON export (mmol N m^{-2} yr^{-1}), water column nitrification (WC Nitr.; mmol N m^{-2} yr^{-1}), sedimentary nitrification (S. Nitr.; mmol N m^{-2} yr^{-1}), and sedimentary denitrification (S Denit.; mmol N m^{-2} yr^{-1}) for 1988 to 2018.

Year	Dominant bloom	Winter ice thick.	Winter snow thick.	UI period	MIZ period	OW period	N Assim.	PON Export	WC Nitr.	S. Nitr.	S. Denit.
1988	Mix	2.0	0.17	36	98	0	850.4	240.0	464.9	146.5	168.0
1989	UI	1.8	0.22	54	27	94	1012	313.4	456.5	185.0	227.3
1990	Mix	2.4	0.15	41	22	116	915.5	259.8	496.3	173.3	196.5
1991	Mix	2.6	0.16	49	45	87	840.1	229.4	466.7	143.3	152.2
1992	Mix	2.5	0.13	44	27	99	832.6	227.3	451.9	147.4	160.8
1993	MIZ	2.4	0.21	22	33	118	996.2	299.2	479.6	176.5	210.3
1994	UI	1.7	0.06	91	26	50	1050	331.7	464.0	199.8	249.7
1995	UI	2.2	0.21	61	42	91	1065	340.0	495.8	204.4	249.9
1996	UI	1.5	0.09	66	28	134	1116	366.4	493.0	226.8	284.6
1997	UI	1.6	0.13	39	23	141	963.0	288.1	466.3	180.8	220.6
1998	MIZ	2.6	0.13	13	35	122	960.5	282.1	466.1	173.3	205.5
1999	Mix	2.5	0.19	33	23	86	972.1	285.9	504.6	175.5	201.5
2000	Mix	2.5	0.14	37	43	51	863.1	240.0	462.8	157.3	177.0
2001	UI	1.7	0.10	38	25	73	946.1	279.9	464.4	178.2	214.1
2002	UI	1.8	0.11	68	9	106	1077	343.3	474.4	202.4	250.6
2003	UI	1.6	0.10	64	36	111	1065	338.0	479.9	202.9	253.2
2004	MIZ	2.5	0.05	20	43	121	936.7	272.0	464.4	177.5	210.0
2005	Mix	2.3	0.10	39	25	123	956.8	274.6	497.9	175.8	201.5
2006	UI	2.5	0.19	59	21	129	954.6	280.8	492.7	170.8	200.6
2007	UI	1.5	0.08	67	21	150	1084	343.6	501.1	208.0	258.1
2008	UI	1.5	0.11	61	24	109	1039	328.1	457.3	203.4	252.1
2009	UI	1.5	0.18	61	28	114	1104	367.4	450.3	211.0	270.6
2010	MIZ	2.5	0.14	6	41	133	912.8	260.8	444.8	176.2	207.0
2011	UI	1.5	0.17	55	22	140	1099	356.2	483.9	212.1	264.2
2012	Mix	2.3	0.15	38	36	92	904.9	259.7	487.1	168.7	195.0
2013	UI	1.6	0.08	78	21	121	1111	363.0	488.5	213.1	266.6
2014	Mix	2.6	0.13	43	38	110	915.5	260.9	504.8	178.1	199.9
2015	UI	1.7	0.06	62	25	129	1086	345.9	510.1	199.7	246.7
2016	Mix	2.3	0.09	40	22	162	929.6	267.8	499.8	180.0	207.4
2017	UI	1.4	0.09	47	27	170	1087	343.3	535.7	209.7	256.1
2018	UI	1.5	0.07	56	33	149	1102	355.4	521.8	221.5	272.6

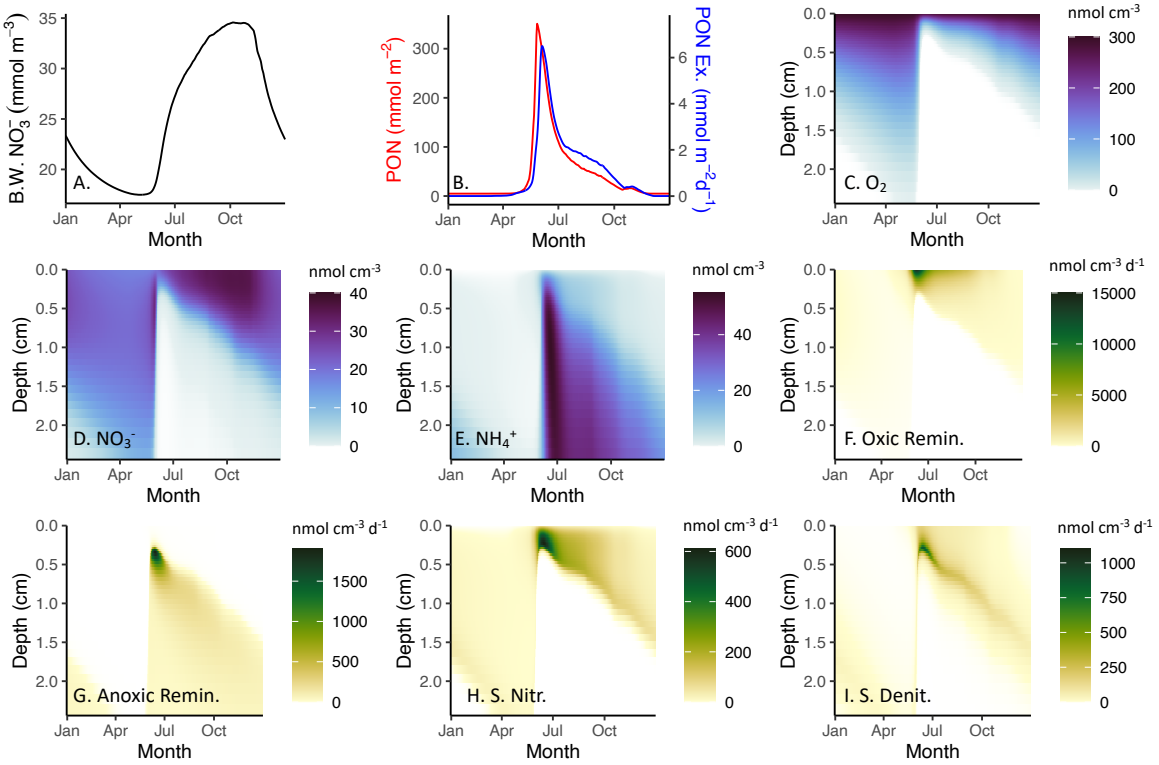

Figure 3.3: Modeled annual cycles of state variables for the standard run year, 2011. A) Bottom-water NO_3^- concentration (mmol N m^{-3}, B) Depth-integrated phytoplankton PON (mmol N m^{-2} d^{-1}; red) and PON exported to the sediments (mmol N m^{-2} d^{-1}; blue), and C) O_2 (mmol N m^{-3}), D) NO_3^- (mmol N m^{-3}), E) NH_4^+ (mmol N m^{-3}), F) oxic remineralization (nmol N cm^{-3} d^{-1}), G) anoxic remineralization (nmol N cm^{-3} d^{-1}), H) sedimentary nitrification (nmol N cm^{-3} d^{-1}), and I) sedimentary denitrification (nmol N cm^{-3} d^{-1}) for the top 2.5 cm of the sediments.

the peak in deposition of PON to the sediments (DOY 161), oxic remineralization and, to a lesser extent, nitrification and the oxidation of reduced substances, drove down the O_2 concentration to $\leq$1 nmol cm^{-3} below the top 0.3 cm of the sediments (Figure 3.3e). Oxic remineralization peaked at the surface of the sediments at a rate of 15000 nmol cm^{-2} d^{-1}. The oxic remineralization of organic N generates NH_4^+, the depth-integrated concentrations of which peaked 12 days after the peak in PON export (DOY 167), with concentrations increasing to 55 nmol cm^{-3} over the top 5 cm of the sediments (Figure 3.3d). Two other processes, anoxic remineralization and nitrification, both peaked at this same time (DOY 167). Anoxic remineralization (Figure 3.3f) is inhibited by both O_2 and NO_3^- concentrations (such that concentrations of 1 nmol cm^{-3} of either substance reduces anoxic remineralization by 50%) and peaked at a rate of 1890 nmol cm^{-2} d^{-1} at a depth of 0.4 cm on DOY 165. Nitrification (Figure 3.3g), the process by which NH_4^+ is oxidized to NO_3^-, peaked at a rate of 600 nmol cm^{-2} d^{-1} on DOY 165 in the top 0.2 cm. Because O_2 concentrations diminished

as nitrification rates increased and because high bottom-water NO_3^- concentrations drove diffusion into the sediments, almost all NO_3^- produced through sedimentary nitrification was subsequently denitrified. As a result, sedimentary NO_3^- concentrations diminished, reaching their lowest concentration on DOY 163, as nitrification intensified, driving higher diffusion of NO_3^- into the sediments. Denitrification (Figure 3.3g) dominated in a very thin layer at a depth of 0.3 cm and peaked on DOY 166, one day after the peaks in anoxic remineralization and nitrification and 11 days after the maximal PON export to the benthos.

In the months following the peak in PON export to the benthos, concentrations of O_2 and NO_3^- gradually increased at depths between 0.3 and 3 cm in the sediments, while NH_4^+ concentrations diminished over this same period. As a result, processes that were highly concentrated in the top 0.4 cm of the sediments during peak PON export to the benthos happened over a more diffuse layer of the sediments (the top ~3 mm) in the autumn and winter. As expected, oxic processes (oxic remineralization and nitrification) closely resembled the distribution of O_2 (and thus NO_3^-) in the sediments throughout the year, while anoxic processes (anoxic remineralization and denitrification) were inversely related to O_2 concentration (and thus the distribution of NH_4^+).

3.3.1 Interannual variance in phytoplankton bloom timing and PON export to the benthos

Between 1988 and 2018, the phytoplankton bloom began on average in mid-May (DOY 137±21), shifting earlier by 1.1 d each year (R^2=0.238, p=0.005). Biomass typically peaked in mid-June during the under-ice period (8.4±17.4 days prior to the start of ice retreat, or on DOY 170±20), and this peak shifted earlier by 1.0 d yr^{-1} (R^2=0.187, p=0.015) between 1988 and 2018. Blooms peaked at a concentration of 292.6±57.4 mmol PON m^{-2} and daily N assimilation by microalgae (phytoplankton and sea ice algae) peaked at 54.9±16.5 mmol N m^{-2} d^{-1}. The phytoplankton bloom ended when microalgal N assimilation dropped below 0.5 mmol N m^{-2} d^{-1} on DOY 294±13. PON export to the benthos increased above 0.1 mmol N m^{-2} d^{-1} on DOY 135±27 and the onset of PON export shifted earlier by 1.3 d y^{-1} (R^2=0.183, p=0.016). Particle export peaked on average at a rate of 5.1±1.3 mmol PON m^{-2} d^{-1} on DOY 181±23. PON export diminished below 0.1 mmol N m^{-2} d^{-1} on average on DOY 321±11.

There was substantial interannual variability in the annual magnitude of PON exported to the benthos, which ranged from 227.3 to 367.4 mmol N m^{-2} yr^{-1} between 1988 and 2018 (mean=301.4±44.5 mmol N m^{-2} yr^{-1}; Figure 3.4a), increasing annually by 1.8±0.8 mmol N m^{-2} yr^{-1} (R^2=0.130, p=0.047; Figure 3.4a). Annual PON export averaged 30.2±1.8% of the magnitude of annual N assimilation by microalgae, or 46.0±3.6% of annual NO_3^- assimilation. The annual peak in daily PON export ranged from 2.9 in 1991 to 6.9 mmol N m^{-2} d^{-1} in 2009 (mean=5.1±1.3 mmol N m^{-2} d^{-1}; Figure 3.5a). Multiple linear regression revealed that 76.5% of the variance (p<0.001) in annual PON export to the benthos was controlled by a combination of sea ice thickness (R^2=0.419, p<0.001), the length of

Table 3.2: Modeled linear regressions of time (1988-2018) versus monthly benthic PON export, water column nitrification, sedimentary nitrification, and sedimentary denitrification (units of mmol N m^{-2} per month yr^{-1}). R^2, p-value, and slope is listed for each statistically significant ($p<0.05$) month.

Process	Month	R^2	p-value	Slope
Benthic export	March	0.132	0.045	9.82E-4
Benthic export	April	0.245	0.005	1.36E-3
Benthic export	May	0.291	0.002	5.50E-3
Benthic export	June	0.167	0.022	1.73E-2
Water column nitrification	February	0.152	0.030	5.87E-5
Water column nitrification	March	0.255	0.004	1.24E-3
Water column nitrification	April	0.208	0.010	1.11E-2
Water column nitrification	May	0.243	0.005	6.77E-2
Water column nitrification	June	0.144	0.035	9.86E-2
Sedimentary nitrification	March	0.132	0.045	9.83E-4
Sedimentary nitrification	April	0.245	0.005	1.36E-3
Sedimentary nitrification	May	0.292	0.002	5.50E-3
Sedimentary nitrification	June	0.167	0.022	1.73E-2
Sedimentary denitrification	January	0.129	0.048	1.54E-3
Sedimentary denitrification	February	0.130	0.046	1.36E-3
Sedimentary denitrification	March	0.136	0.041	1.26E-3
Sedimentary denitrification	April	0.193	0.013	1.48E-3
Sedimentary denitrification	May	0.301	0.001	5.23E-3
Sedimentary denitrification	June	0.151	0.031	2.58E-2
NH_4^+ flux	April	0.215	0.009	-6.45E-3
NH_4^+ flux	May	0.240	0.005	-6.45E-1

the UI period (R^2=0.229, p=0.025), and the length of the OW period (R^2=0.117, p=0.006). These same three factors were most influential in determining the amount of N assimilated by microalgae each year, explaining 75.2% of the variance ($p<0.001$) in annual N assimilation. Indeed, PON export to the sediments was highly correlated with annual N assimilation by microalgae, which explained 99.1% of the variance in PON export ($p<0.001$, slope=0.538, Figure 3.4b). Variation in N assimilation by UI microalgae accounted for 47.8% of the variance ($p<0.001$) in annual PON export, which is substantially more than that explained by N assimilation during the MIZ (R^2=0.295, p=0.002) or OW (not statistically significant) periods.

The timing of PON export to the benthos also changed between 1988 and 2018 (Figure 3.5a). Organic matter exported to the sediments peaked between 6 and 36 days after the peak in phytoplankton biomass (mean=11.2±7.8 after the biomass peak, or on DOY 181±23) with the peak coming earlier by 1.2 d yr^{-1} (R^2=0.200, p=0.012; Figure 3.5a). Additionally, PON export increased significantly between 1988 and 2018 in the months of March-June (Table 3.2, Figure 3.5a), but showed no significant trends in other months.

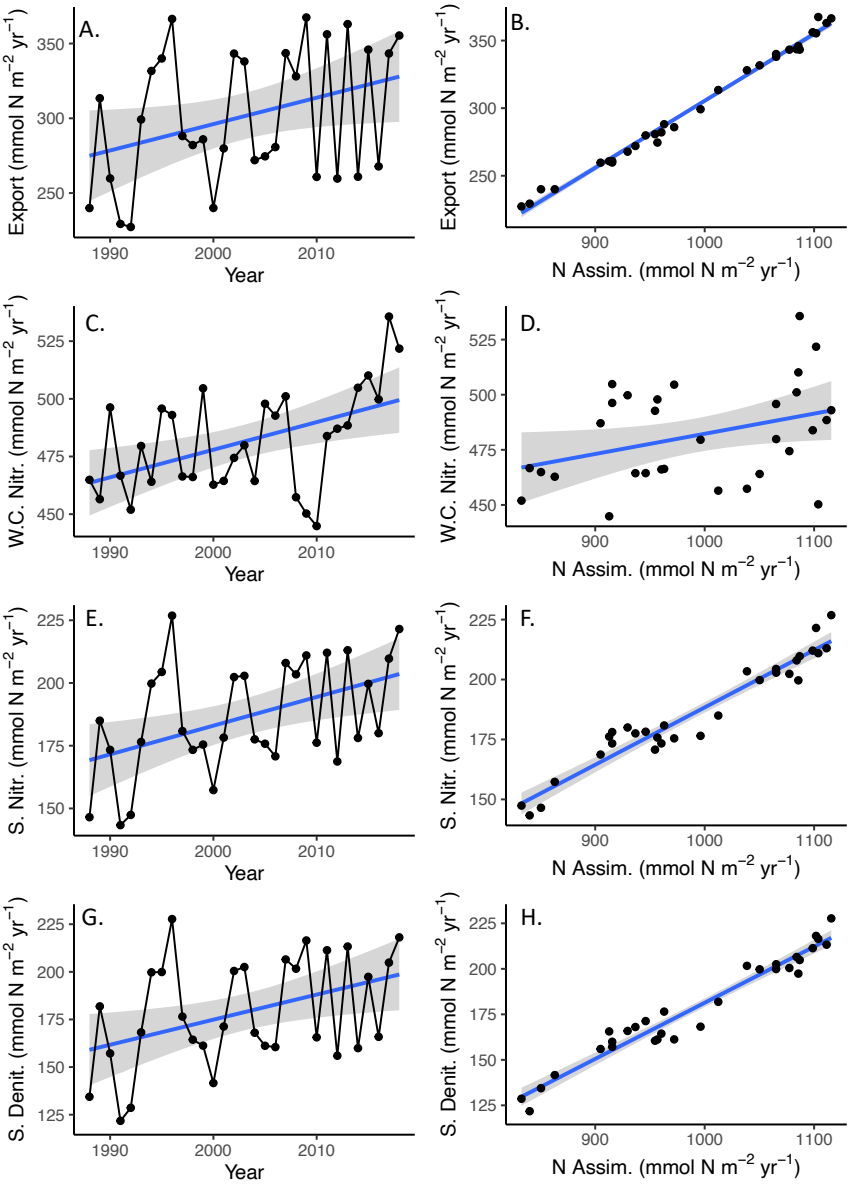

Figure 3.4: Modeled interannual trends for 1988 to 2018 in A) PON export to the benthos (mmol N m^{-2} yr^{-1}), C) water column (WC) nitrification (mmol N m^{-2} yr^{-1}), E) sedimentary nitrification (mmol N m^{-2} yr^{-1}), and G) sedimentary denitrification (mmol N m^{-2} yr^{-1}). Scatterplots of annual N Assimilation ("Assim.") vs. B) PON export to the benthos (mmol N m^{-2} yr^{-1}), D) water column (WC) nitrification (mmol N m^{-2} yr^{-1}), F) sedimentary nitrification (mmol N m^{-2} yr^{-1}), and H) sedimentary denitrification (mmol N m^{-2} yr^{-1}). Blue line indicates statistically significant linear regressions and grey shading represents the 95% confidence interval for these regressions.

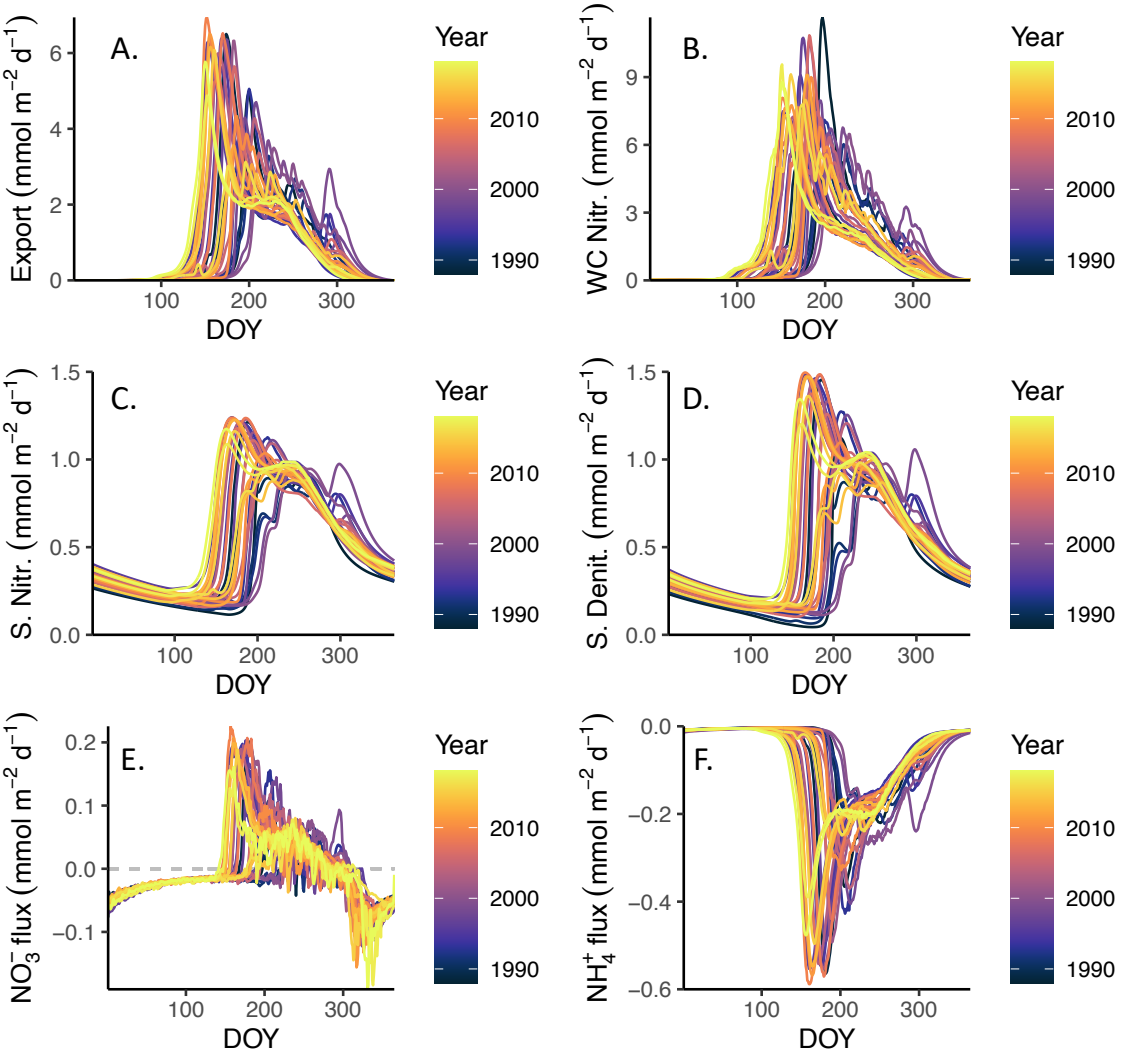

Figure 3.5: Modeled interannual differences in A) PON export to the benthos (mmol N m^{-2} d^{-1}), B) water column (WC) nitrification (mmol N m^{-2} d^{-1}), C) sedimentary nitrification (mmol N m^{-2} d^{-1}), D) sedimentary denitrification (mmol N m^{-2} yr^{-1}), E) NO_3^- flux into the sediments (mmol N m^{-2} yr^{-1}), and F) NH_4^+ flux into the sediments (mmol N m^{-2} yr^{-1}) for each day of the year (DOY) between 1988 and 2018 (colorbar). One year (1999, purple) had a large fall bloom following a mixing event in early October and this increase in N assimilation subsequently drove an anomalous spike in all other processes on DOY ∼300.

3.3.2 Nitrification and denitrification

Daily water column nitrification rates ranged between a minimum of 0.01±0.004 mmol N m^{-2} d^{-1} and an average peak of 8.3±1.3 mmol N m^{-2} d^{-1} (Figure 3.3b) between 1988 and 2018. Water column nitrification rates typically peaked on DOY 177.5±18.9, and this peak shifted earlier by 0.9 d yr^{-1}

between 1988 and 2018 (R^2=0.204, p=0.011). Annual depth-integrated water column nitrification rates ranged from 444.8 to 535.7 mmol N m^{-2} yr^{-1} (mean=481.5±22.3 mmol N m^{-2} yr^{-1}; Figure 3.4c), equivalent to 48.9±4.2% of annual N assimilation by microalgae. The annual rate of water-column nitrification increased by 1.2±0.4 mmol N m^{-2} yr^{-1} (R^2=0.239, p=0.005) between 1988 and 2018. Annual water-column nitrification was weakly but significantly correlated with annual N assimilation by microalgae (R^2=0.135, p=0.042; Figure 3.4d). Multiple linear regression revealed that 29.2% of the variance (p<0.001) in annual water column nitrification was controlled by the length of the snow melt period. Because N assimilation by microalgae during the OW period was concentrated at the depth of the subsurface Chl *a* maximum (*Payne et al.* 2021) and water-column nitrification rate increased with depth in the CAOS model, variation in OW N assimilation accounted for 28.5% of the variance in water column nitrification (p=0.002), while variation in UI and MIZ N assimilation showed no statistically significant relationship with water column nitrification.

Daily sedimentary nitrification rates ranged from a minimum of 0.19±0.03 mmol m^{-2} d^{-1} to a mean peak daily rate of 1.1±0.1 mmol m^{-2} d^{-1} (Figure 3.5c). Annual sedimentary nitrification rates were much lower than those in the water column, ranging from 143.3 to 226.8 mmol N m^{-2} yr^{-1} (mean=186.4±22.2 mmol N m^{-2} yr^{-1}; Figure 3.4e) and nitrifying on average 18.8±0.8% of annual N assimilated by microalgae and 62.1±3.0% of exported PON. Similar to water column nitrification, annual sedimentary nitrification increased by 1.1±0.4 mmol N m^{-2} yr^{-1} each year between 1988 and 2018 (R^2=0.220, p=0.008). Multiple linear regression revealed that 77.7% of the variance (p<0.001) in annual sedimentary nitrification was controlled by a combination of sea ice thickness (R^2=0.388, p<0.001), the length of the OW period (R^2=0.200, p<0.001), and the length of the UI period (R^2=0.189, p=0.041). Annual N assimilation by microalgae was highly correlated with annual sedimentary nitrification, explaining 93.1% of the interannual variance (p<0.001; Figure 3.4f). Variation in N assimilation by microalgae during the UI period drove more of the variance in annual sedimentary nitrification (40.0%) than the other two periods (p<0.001).

Because of high water column O_2 concentrations, denitrification was limited to the sediments. Average daily denitrification rates ranged from 0.14±0.04 to 1.2±0.2 mmol m^{-2} d^{-1} (Figure 3.5d), while annual denitrification ranged from 121.8 to 227.7 mmol N m^{-2} yr^{-1} between 1988 and 2018 (mean=178.8±28.3 mmol N m^{-2} yr^{-1}; Figure 3.4c). Sedimentary denitrification removed a mean of 17.9±1.4% of the annual N assimilated by microalgae, 59.3±2.3% of the PON exported to the sediments, and 95.5±4.3% of the NO_3^- produced through sedimentary nitrification. Annual denitrification increased annually over this period by 1.3±0.5 mmol N m^{-2} yr^{-1} (R^2=0.179, p=0.018). Multiple linear regression revealed that 76.1% (p<0.001) of the variance in annual denitrification was controlled by a combination of sea ice thickness (R^2=0.616, p<0.001) and the length of the OW period (R^2=0.145, p=0.004). Denitrification was highly correlated with both annual N assimilation by microalgae (Figure 3.4d), which explained 94.9% of the variance in denitrification rates (p<0.001;

Figure 3.4d), and with PON export to the benthos, which explained 95.4% of the variance in denitrification ($p<0.001$). Variation in N assimilation by microalgae during the UI period drove more of the variance in annual denitrification than the two other periods, accounting for 44.1% ($p<0.001$).

Increases in annual rates of nitrification and denitrification between 1988 and 2018 were driven by increases in these processes between January and June (Figure 3.5b, c and d). Water-column nitrification increased significantly in February-June while sedimentary nitrification increased in March-June (Table 3.2). Denitrification increased significantly over a longer time period, from January-June (Table 3.2). There was no statistically significant change during July-December in either sedimentary process, or in January and February for sedimentary nitrification.

3.3.3 Sediment-water exchange of NO_3^- and NH_4^+

NO_3^- and NH_4^+ fluxes across the sediment-water interface in the OMEXDIA model vary depending on the bottom-water salinity, temperature, and NO_3^- and NH_4^+ concentrations (*Soetaert et al.*, 1996a, b). The sediments were typically a net source of NO_3^- to the overlying water column, supplying 2.3±1.9 mmol m^{-2} yr^{-1}. NO_3^- diffused out of the sediments in the early part of the year at a rate of 0.05 mmol m^{-2} d^{-1} due to lower NO_3^- concentrations in the water column. However, this pattern reversed on 176±24 when NO_3^- began to diffuse into the sediments, peaking on DOY 199±36 at a rate of 0.14±0.06 mmol m^{-2} d^{-1} (Figure 3.5e). In autumn, the sediments once again became a net source of NO_3^- to the water column, peaking at a rate of 0.10±0.03 mmol m^{-2} d^{-1} on DOY 319±60. While there was no secular trend in either the annual net NO_3^- flux from the sediments to the water column, the peak timing, or the peak magnitude, there was a slight increase in the magnitude in the peak flux rate of NO_3^- out of the sediments in the autumn between 1988 and 2018 (R^2=0.243, p=0.005, slope=-0.002).

In contrast to the sediment-water flux of NO_3^-, which could represent either a source to or sink of water-column NO_3^-, the sediments consistently acted as a source of NH_4^+ to the water column at an average rate of 29.8±5.1 mmol NH_4^+ m^{-2} yr^{-1}. In general, the supply of NH_4^+ to the water column peaked at a rate of 0.42±0.13 mmol m^{-2} d^{-1} on DOY 190±24 (Figure 3.5f). While the magnitude of the peak NH_4^+ flux did not change over time, the peak shifted earlier by 1.1 d yr^{-1} (R^2=0.180, p=0.018) from 1988 to 2018.

3.3.4 Water column bloom types

Of the 31 years between 1988 and 2018, 17 years were dominated by UIBs, 4 by NPP in the MIZ period, and 10 featured a mix of both UI and MIZ blooms (Table 3.1). Years when UI blooms were dominant had higher annual N assimilation by microalgae (1056.5±55.5 mmol N m^{-2} yr^{-1}) than either MIZ-dominant (951.6±35.6 mmol N m^{-2} yr^{-1}, p=0.003) or mixed-dominance (898.1±49.1 mmol N m^{-2} yr^{-1}, $p<0.001$) years. In years with high N assimilation by microalgae in the UI period, PON export to the benthos (334.4±28.2 mmol N m^{-2} yr^{-1}) was also greater than in years with either

MIZ (278.5±16.3 mmol N m^{-2} yr^{-1}, $p<0.001$) or mixed-dominance blooms (254.5±19.6 mmol N m^{-3} yr^{-1}, $p<0.001$). While nitrification in the water column showed no significant differences with bloom type, there were significant differences in sedimentary nitrification, with UI-dominant years having higher rates of sedimentary nitrification (201.7±15.2 mmol N m^{-2} yr^{-1}) than either mixed-dominance years (164.6±14.5 mmol N m^{-2} yr^{-1}, $p<0.001$) or MIZ-dominant years (175.9±1.8 mmol N m^{-2} yr^{-1}, $p=0.007$). As a result, UI-dominant years also had higher sedimentary denitrification rates (199.4±17.7 mmol N m^{-2} yr^{-1}) than either mixed-dominance years (148.8±15.8 mmol N m^{-2} yr^{-1}, $p<0.001$) or MIZ-dominant years (166.6±1.9 mmol N m^{-2} yr^{-1}, $p<0.003$).

3.3.5 Sensitivity to initial NO_3^- concentration

To test how a change in the wintertime NO_3^- concentration (which might be caused by a change in advection from the Bering to the Chukchi Sea) could impact water column and sedimentary N biogeochemistry, we increased initial wintertime NO_3^- concentration in successive runs by 100 mmol m^{-2} (2 mmol m^{-3} over the 50 m water column), resulting in final concentrations ranging from 600 to 1300 mmol m^{-2} (12 to 26 mmol m^{-3}; Table 3.3). Results indicate that the N cycle in the Chukchi Sea is quite sensitive to the addition of new NO_3^- to the system, with most (79-86%) of the incremental 100 mmol m^{-2} NO_3^- additions being assimilated by phytoplankton by the end of the year (Table 3.3). Most of this increase is driven by higher NO_3^- assimilation during the UI period (61-66 mmol m^{-2} yr^{-1}), with a sizeable proportion also assimilated during the OW period (17-21 mmol m^{-2} yr^{-1}). Almost none of the added NO_3^- was assimilated within the MIZ.

This 79-86 mmol m^{-2} yr^{-1} increase in N assimilation by phytoplankton in response to a 100 mmol m^{-2} incremental increase in wintertime NO_3^- translated to a 24-34 mmol m^{-2} yr^{-1} increase in PON export (Table 3.3). As a result, rates of nitrification in the water column and the sediments increased by 54-58 and 7-14 mmol m^{-2} yr^{-1}, respectively, and the sedimentary denitrification rate increased by 26-32 mmol m^{-2} yr^{-1}. Finally, each 100 mmol m^{-2} increase in wintertime NO_3^- increased the NO_3^- flux from the sediments to the water column by 3-4 mmol m^{-2} yr^{-1} and decreased the flux of NH_4^+ by 4-5 mmol m^{-2} yr^{-1}.

Interestingly, as initial NO_3^- concentration was increased from 600 to 1300 mmol m^{-2}, each incremental 100 mmol m^{-2} increase in water column NO_3^- had a diminishing effect on many N-cycle processes such as NO_3^- assimilation, PON export to the benthos, sedimentary nitrification, and NH_4^+ flux out of the sediments (Table 3.3). Conversely, the same 100 mmol m^{-2} increase in water column NO_3^- enhanced the mean water-column NO_3^- concencentration, water-column nitrification, sedimentary denitrification, and NO_3^- flux from the sediments (Table 3.3).

Table 3.3: The impact of a 100 mmol m^{-2} increase in modeled wintertime NO_3^- concentration at a variety of initial NO_3^- concentrations (with final concentrations changing from 12-26 mmol m^{-3}, or 600-1300 mmol m^{-2}). Impact is assessed through the change in NO_3^- assimilation (mmol m^{-2} yr^{-1}), benthic PON export (mmol m^{-2} yr^{-1}), mean water-column NO_3^- concentration (mmol m^{-2}), water-column nitrification (WC Nitr.; mmol m^{-2} yr^{-1}), sedimentary nitrification (S. Nitr.; mmol m^{-2} yr^{-1}), sedimentary denitrification (S. Denit.; mmol m^{-2} yr^{-1}), NO_3^- and NH_4^+ fluxes across the sediment-water boundary, and the change in magnitude of N assimilation during the UI, MIZ, and OW periods (mmol N m^{-2} yr^{-1}).

Range Init. NO_3^-	**Δ Init. NO_3^-**	**Δ NO_3^- assim.**	**Δ UI NO_3^- assim.**	**Δ MIZ NO_3^- assim.**	**Δ OW NO_3^- assim.**	**Δ N export**	**Mean Δ NO_3^-**	**Δ WC nitr.**	**Δ S. nitr.**	**Δ S. denit.**	**Δ NO_3^- flux**	**Δ NH_4^+ flux**
500 - 600	100	85.8	65.5	-0.9	21.1	34.4	81.8	54.3	14.2	25.6	3.3	-4.7
600 - 700	100	83.2	65.3	-1.2	19.2	32.4	82.9	53.9	13.0	31.8	3.4	-4.8
700 - 800	100	83.2	65.6	-0.8	18.4	31.1	83.5	54.8	11.5	30.8	3.6	-4.9
800 - 900	100	81.7	65.7	-1.2	17.2	29.9	84.0	54.5	10.3	30.1	3.8	-4.9
900 - 1000	100	81.6	65.6	-0.2	16.2	28.4	84.8	55.6	9.2	29.3	3.9	-4.8
1000 - 1100	100	82.1	64.8	0.0	17.2	27.7	85.4	56.6	8.6	29.2	4.1	-4.8
1100 - 1200	100	79.1	60.4	1.3	17.5	24.5	86.7	57.0	7.4	27.5	4.0	-4.3
1200 - 1300	100	79.2	60.5	1.2	17.6	23.8	87.0	57.5	6.9	27.4	4.1	-4.3

3.4 Discussion

The Chukchi Sea accounts for 0.2% of global ocean surface area but 1-3% of global fixed N loss in the oceans (*Chang and Devol*, 2009) due to the coupled partial nitrification-denitrification processes that predominate in the shallow continental shelf sediments (*Brown et al.*, 2015a). Despite the outsize importance of this region to global fixed N loss, field measurements of denitrification rates in the Chukchi Sea are sparse and largely confined to areas near Hanna Shoal in the northern Chukchi Sea (see Figure 3.2). Measured rates of sedimentary denitrification on the 50 m deep continental shelf of the northern Chukchi Sea ranged from 0.76-1.58 mmol m^{-2} d^{-1} in the summer of 2004 (*Chang and Devol*, 2009) and from 0.14-0.98 mmol m^{-2} d^{-1} in August of 2013 (*McTigue et al.*, 2016). Our CAOS-GO model produced mean annual denitrification rates of 0.41 to 0.78 mmol m^{-2} d^{-1} and maximum rates of 0.82-1.50 mmol m^{-2} d^{-1} between 1988 and 2018. Rates of fixed N loss through denitrification have also been estimated from excess N measurements taken throughout the Chukchi Sea. Assuming non-Redfield uptake by phytoplankton, fixed N loss in the Chukchi Sea was calculated as 1.9±2.3 and 4.1±7.1 mmol m^{-3} in 2010 and 2011, respectively (*Mills et al.*, 2015). CAOS-GO produced excess N in line with these values, ranging from 2.4 to 4.6 mmol m^{-3} between 1988 and 2018 (3.6±0.6 mmol m^{-3}). Further, our results indicate that denitrification rates increased annually by 1.3 mmol m^{-2} yr^{-1} over this timeframe, indicating that the sediments of the northern Chukchi Sea may contribute even more to global N loss than previously projected.

Much of this modeled increase in denitrification was attributable to the increase in annual NPP (*Payne et al.*, 2021) and PON exported to the benthos. A 3.8 mmol m^{-2} yr^{-1} increase in N assimilation by microalgae between 1988 and 2018 corresponded to a 1.8 mmol m^{-2} yr^{-1} increase in PON export to the benthos. This trend was also observed in sediment traps deployed in the Hanna Shoal area by *Lalande et al.* (2020), who found that 2016 rates of Chl *a* export were substantially higher than previous measurements made in 2004 (*Lalande et al.*, 2007). CAOS-GO produced a mean rate of POC export to the benthos of 29.2±4.3 g C m^{-2} yr^{-1} between 1988 and 2018, comparable to the 29.7 g C m^{-2} yr^{-1} average export reported for the Chukchi Sea (*Chang and Devol*, 2009). A mooring deployed at 37 m depth (8 m above the seafloor) by *Lalande et al.* (2020) recorded a mean export rate of 3 to 5 mg Chl *a* m^{-2} d^{-1} from surface waters during a UIB in June-July 2016, similar to our modeled export rate for this same period of 3 to 4.8 mg Chl *a* m^{-2} d^{-1}.

The CAOS-GO model showed that particle export to the benthos and sedimentary nitrification and denitrification rates were all tightly coupled to the magnitude of annual NPP, which explained 93-99% of the variance in these three rates. The high correlation between NPP and sedimentary processes is not surprising. For example, *Townsend and Cammen* (1988) argued that changes in the magnitude and seasonality of pelagic NPP directly affected the quantity and quality of the organic matter that arrives at the sediment surface, thus influencing benthic productivity. In the Arctic Ocean specifically, a study by *Fu et al.* (2016) used nine Earth system models to assess how climate change would impact Arctic NPP and export over time. While these climate models projected

a reduction in nutrient inventories resulting from an increase in stratification due to surface-ocean warming and freshening, which opposes most recent observations of nutrient inventories in the Arctic (*Henley et al.*, 2020; *Lewis et al.*, 2020; *Mordy et al.*, 2020; *Randelhoff et al.*, 2018, 2019), a decline in NPP between the 1990s and 2090s was tightly coupled to a decline in particle export to the benthos. The correlation between PON exported to the benthos and rates of coupled partial nitrification-denitrification in the sediments has similarly been widely observed (*Baumann et al.*, 2013; *Horak et al.*, 2013; *Granger et al.*, 2011) and assumed in models (*Chang and Devol*, 2009; *Fennel et al.*, 2009; *Fennel*, 2010; *Laurent et al.*, 2016; *Soetaert et al.*, 1996b, a) used to calculate denitrification rates.

Sea ice algae and under-ice phytoplankton are considered to be efficient exporters of organic matter (*Boetius et al.*, 2013; *Fahl and Nöthig*, 2007) because of their silicified cell walls (*Smetacek*, 1999) and because they face less grazing pressure than algae growing during warmer times of the year (*Campbell et al.*, 2001; *Conover and Huntley*, 1991; *Coyle et al.*, 2007; *Huntley and Lopez*, 1992). Indeed, previous work with the CAOS-GO model (*Payne et al.*, 2021) demonstrated that zooplankton grazing was on average 3.5 times greater during the OW than the UI periods, even though the OW period generated only half the phytoplankton biomass. The temperature dependence of zooplankton grazing suggests that massive UIBs observed in the northern Chukchi Sea would likely be disproportionately exported, as was hypothesized by *Arrigo et al.* (2014), and might subsequently fuel increases in denitrification (*Townsend and Cammen*, 1988). This appears to be supported by CAOS-GO results, which indicates that secular increases in particulate export to the benthos and denitrification were driven by NPP generated early in the year (and thus mostly in the UI period) and by years where NPP was dominated by large UIBs.

However, the CAOS-GO model demonstrates that export efficiency is also closely tied to the depth over which phytoplankton production is generated. Ice algal and UI NPP modeled here were exported at a higher rate, but at a lower export efficiency, than NPP generated during the MIZ and OW periods when phytoplankton are concentrated within a subsurface Chl *a* maximum. This was because ice algal and UI blooms developed higher in the water column (at an average depth of 0 m and ∼15m), and thus descended a longer distance and over a longer time period (at 5 m d^{-1}, or on average over 10 and 7 days, respectively) than MIZ and OW blooms (which were generated at a depth of 30 m on average and as a result sunk over 4 days). The longer period of sinking for IA and UI biomass allowed much more PON to be remineralized before reaching the sediments. At the 0.2 d^{-1} remineralization rate used in the CAOS-GO model, only 11% and 26% of the biomass produced in the IA and UI blooms, as compared to 41% of the MIZ/OW biomass, reached the sediments. Thus, the model indicates that the higher PON export and sedimentary denitrification rates associated with UIBs is due to their higher annual NPP, rather than a greater export efficiency.

The secular increases in annual NPP, PON export to the benthos, and denitrification in the northern Chukchi Sea likely have large ramifications downstream. Satellite analysis of NPP in the

Arctic Ocean (*Arrigo and Van Dijken*, 2015) revealed that an increase in Chukchi Sea NPP, likely driven by changing sea ice cover, was followed by a significant decline in NPP in the Greenland Sea the following year. *Arrigo and Van Dijken* (2015) hypothesized that phytoplankton in the Chukchi Sea were able to consume a greater proportion of available NO_3^-, reducing both NO_3^- availability and NPP in the N-limited Greenland Sea (*Krisch et al.*, 2020). Reductions in NPP in regions downstream of the Chukchi Sea could substantially limit food available to zooplankton, pelagic fish, marine mammals, and seabirds (*Hamilton et al.*, 2021; *Joiris*, 2011; *Munk*, 2003; *Rysgaard et al.*, 1999). Additionally, the Chukchi shelf has some of the lowest N^* values (a measure of N excess relative to phosphorus; *Gruber and Sarmiento*, 1997) in the global ocean (*Deutsch and Weber*, 2012), driven by high sedimentary denitrification (*Brown et al.*, 2015a; *Chang and Devol*, 2009; *Devol et al.*, 1997; *Mills et al.*, 2015). A study by *Yamamoto-Kawai et al.* (2006) found that the excess phosphate relative to N in waters downstream of the Chukchi Sea stimulated N_2 fixation in the surface waters of the North Atlantic. Although N_2 fixation was previously considered only feasible in warm, N-deplete waters (*Sohm et al.*, 2011), recent work has found ample evidence of both N_2 fixers (*Blais et al.*, 2012; *Díez et al.*, 2012; *Fernández-Méndez et al.*, 2016; *Moisander et al.*, 2010) and N_2 fixation (*Baer et al.*, 2017; *Blais et al.*, 2012; *Mulholland et al.*, 2012; *Sipler et al.*, 2017) in the Arctic Ocean. Higher rates of denitrification in the northern Chukchi Sea would further diminish the N^* values of waters in the region, which in turn could spur an increase in N_2 fixation in both the Arctic (*Tremblay and Gagnon*, 2009) and the North Atlantic oceans (*Yamamoto-Kawai et al.*, 2006). Rates of nitrogen fixation in the Arctic may already offset as much as 27% of the Arctic denitrification-driven N deficit (*Sipler et al.*, 2017), further demonstrating the importance of this region in regulating the global N budget.

The CAOS-GO model showed secular increases in denitrification between 1988 and 2018 without any change in modeled N inventory. However, climate change has increased NO_3^- inventory in the Chukchi Sea through both the increase in advection of NO_3^--rich Pacific waters into the Arctic Ocean (*Mordy et al.*, 2020; *Peralta-Ferriz and Woodgate*, 2017; *Woodgate*, 2018) and consequences of sea ice loss, including more frequent winter storms (*Zhang et al.*, 2010; *Yang*, 2004), enhanced upwelling near shelf breaks (*Carmack and Chapman*, 2003; *Tremblay and Gagnon*, 2009; *Tremblay et al.*, 2011), and the generation of internal waves. Satellite analysis reveals that an increase in NO_3^- concentration and phytoplankton biomass has largely driven the increase in NPP in the Chukchi Sea since 2009 (*Lewis et al.*, 2020). Our sensitivity analysis showed that by increasing the modeled wintertime NO_3^- concentration, 82% of the added NO_3^- was assimilated by phytoplankton, with most of this increase driven by assimilation during the UI period. However, NO_3^- additions also contributed to increases in particulate export to the benthos, sedimentary nitrification, and sedimentary denitrification; 30% of the added NO_3^- was subsequently exported to the benthos and lost through denitrification. As a result, CAOS-GO suggests that, while an increase in NO_3^- concentration will contribute to higher NPP both in the Chukchi Sea and in downstream ecosystems,

one third of added N will subsequently be lost through coupled partial nitrification-denitrification in the northern Chukchi Sea.

The UI period can be critically important to the ecology and biogeochemistry of the northern Chukchi Sea. Our CAOS-GO model found that UIBs on average generated nearly 50% of annual NPP between 1988 and 2018 (*Payne et al.*, 2021) and that the secular increase in NPP was driven largely by increases in the spring and thus largely during the UI period. Higher NPP subsequently led to increases in PON export to the benthos and sedimentary nitrification and denitrification. Thus, it appears that a period historically thought to support little phytoplankton growth (*Hameedi*, 1978; *Perrette et al.*, 2011) is disproportionately important in the northern Chukchi Sea. In addition to impacting downstream regions (*Arrigo and Van Dijken*, 2015; *Krisch et al.*, 2020; *Tremblay and Gagnon*, 2009; *Yamamoto-Kawai et al.*, 2006), massive UIBs are altering northern Chukchi Sea ecosystems. By removing fixed N from the surface waters during a part of the year with low zooplankton growth (*Sherr et al.*, 2008, 2009), UIBs enhance the phytoplankton-zooplankton timing mismatch (*Conover and Huntley*, 1991). Our model demonstrates that years when production was dominated by UIBs featured 25% less zooplankton grazing than years with blooms only in the MIZ period (*Payne et al.*, 2021) but that UI-dominant years have 15% more sedimentary nitrification and 20% more denitrification than MIZ-dominant years, indicating an increase in benthic-pelagic coupling. This likely negatively impacts the many fish, seabird, and marine mammal populations that rely on pelagic production in the northern Chukchi Sea (*De Robertis et al.*, 2017; *Kuletz et al.*, 2015; *Logerwell et al.*, 2015; *Moore and Kuletz*, 2019). For example, fin whales, which time their migration to arrive as zooplankton abundance increases during the OW period (*Tsujii et al.*, 2016), might encounter far fewer food sources in areas with large UIBs. While UIBs lead to reduced pelagic grazing, they could also substantially enhance benthic production (*Townsend and Cammen*, 1988) in a region that already supports rich benthic communities (*Grebmeier et al.*, 1988; *Grebmeier*, 2006; *Grebmeier et al.*, 2015; *Lalande et al.*, 2007). While our model did not include changes in benthic macrofaunal communities, a field study by *McTigue et al.* (2016) indicates that high bioturbation and bioirrigation may enhance denitrification in the northern Chukchi Sea, indicating that our model results may even under-predict possible changes over time in sedimentary denitrification. However, our results should not be extrapolated across the Chukchi Sea or the Arctic Ocean as a whole. A remote sensing study estimating the frequency of MIZ and UI blooms in the Chukchi Sea by *Lowry et al.* (2014) seems to indicate that the southern Chukchi Sea experiences fewer MIZ blooms than the northern Chukchi Sea, and that UIBs are diminishing in spatial coverage over time. In contrast, a modeling study by *Horvat et al.* (2017) indicates that changing sea ice conditions is gradually making more regions of the Arctic Ocean amenable to UIB formation. Future studies (and especially field sampling campaigns) should investigate the spatial variability of UIBs as well as their biogeochemical and ecological ramifications.

3.5 Acknowledgements

The authors would like to thank Gert van Dijken, Matthew Mills, Stephanie Lim, and Casey Schine for providing input on analysis. Model code and all data are available at `https://purl.stanford.edu/xc612sy7581`.

Chapter 4

North-South Differences in Under-Ice Primary Production in the Chukchi Sea From 1988 to 2018

Courtney M. Payne, Gert L. van Dijken, Kevin R. Arrigo
Department of Earth System Science, Stanford University, Stanford, California, USA

This chapter was submitted to *Elementa: Science of the Anthropocene* in May 2023.

Payne, C. M., van Dijken, G. L., & Arrigo, K. R. (2022). North-south differences in under-ice primary production in the Chukchi Sea from 1988 to 2018. Journal of Geophysical Research: Oceans, 127. https://doi.org/10.1029/2022JC018431

As Arctic sea ice has thinned and begun to retreat earlier in the year, there have been substantial changes in the timing and magnitude of regional net primary production (NPP). Most notably, field-based, remote sensing, and model-based studies have demonstrated that massive under-ice phytoplankton blooms (UIBs) contribute substantially to annual NPP and can even drive increases in sedimentary nitrogen recycling and loss through coupled partial nitrification-denitrification. In this study, we used a 1-D biogeochemical model (CAOS-GO) to compare the magnitude of NPP associated with UIBs in the northern and southern Chukchi Sea between 1988 and 2018. While UIBs were critical in driving interannual variation and secular increases in annual NPP and sedimentary nitrification and denitrification in the northern Chukchi Sea, UIBs were far less important at our southern site. As the length of the under-ice period diminished between 1988 and

2018, there was a decrease in the amount of NPP produced during the under-ice period. Despite higher rates of both annual NPP and denitrification at the southern site, there were no secular trends in these rates over time. Our results indicate that, as sea ice continues to retreat earlier, the impact of UIBs on the biogeochemistry of the Chukchi Sea is likely to diminish.

4.1 Introduction

A substantial decline in sea ice extent and thickness has been observed throughout the Arctic Ocean (*Kwok*, 2018; *Serreze and Stroeve*, 2015). Air and sea surface temperatures (SSTs) in the Arctic are warming disproportionately compared to the global average (*Stocker et al.*, 2013). This is especially true in the Chukchi Sea, which extends westward from the coast of Alaska to Russia and is warming more rapidly than most of the Arctic Ocean (ric, 2019), contributing to a 33 day increase in the length of the Chukchi Sea open water (OW) period between 2009 and 2018 (*Lewis et al.*, 2020). Model projections indicate that the OW period will increase to 6-7 months by 2040 in the southern Chukchi Sea, representing a 100% increase from the present 3-4 months (*Wang and Overland*, 2015). Additionally, the Arctic Ocean has experienced significant declines in multi-year ice, which covered nearly 60% of the Arctic Ocean in 1988 (*Serreze and Stroeve*, 2015) but less than one third of the Arctic Ocean by 2017 (*Kwok*, 2018). Much of the Chukchi Sea is now covered by far thinner first-year ice; between 1958 and 2017, average sea ice thickness declined by 70%, from 2 m to 0.6 m (*Kwok*, 2018).

The increasing length of the OW period and the thinner sea ice cover have had substantial effects on primary producers in the Chukchi Sea. Net primary production (NPP) increased by 96% between 1998 and 2018 thanks in part to the increase in the length of the OW period (*Lewis et al.*, 2020). Further, a satellite study by *Ardyna et al.* (2014) indicates that between 1998 and 2012 there was a 35% increase in the incidences of autumn blooms in the Chukchi Sea, although this effect was patchy across the region. In addition to changes in NPP during the OW period, the observation of massive under-ice blooms (UIBs; *Arrigo et al.*, 2012, 2014; *Hill et al.*, 2018b) in the Chukchi Sea has upset the paradigm that most Arctic Ocean NPP is generated in the marginal ice zone (MIZ; *Perrette et al.* 2011). Phytoplankton biomass can exceed 1000 mg chlorophyll *a* (Chl *a*) m^{-2} (*Arrigo et al.*, 2014) during the under-ice (UI) period even under fully consolidated 1 m thick sea ice. Satellite analysis and modeling studies indicate that Chukchi Sea UIBs are more common than MIZ-generated blooms (*Lowry et al.*, 2014) and could have been a feature of the Arctic Ocean since at least the late 1980s (*Clement Kinney et al.*, 2020; *Horvat et al.*, 2017; *Jin et al.*, 2016; *Payne et al.*, 2021; *Zhang et al.* 2015).

Changes in sea ice conditions and the timing and magnitude of annual NPP likely impact the marine nitrogen (N) cycle in the Chukchi Sea and in downstream ecosystems (*Arrigo et al.*, 2014;

Arrigo and Van Dijken, 2015). The diatom blooms that predominate in the Chukchi Sea (*Laney and Sosik*, 2014) can sink rapidly to the seafloor due to the large cell size and silicified cell walls (*Smetacek*, 1999), disproportionately exporting particulate organic carbon (POC) out of the surface ocean. But UIBs might allow even higher rates of POC export to the sediments because of the low grazing rates (*Campbell et al.*, 2001; *Sherr and Sherr*, 2009; *Sherr et al.*, 2009) associated with the cold water temperatures (-1.5°C) found during this period. As NPP has increased in the northern Chukchi Sea, particulate export to the sediments has likely increased (*Payne and Arrigo*, 2022). On the broad continental shelf of the Chukchi Sea, coupled partial nitrification-denitrification in the sediments leads to high N recycling and loss (*Brown et al.*, 2015a), causing the region to contribute 1-3% of the total N lost in the world's oceans (*Chang and Devol*, 2009). An increase in the rate of POC export can subsequently lead to increases in the loss of fixed N from the system (*Payne and Arrigo*, 2022), reducing the amount of N available to primary producers downstream (*Arrigo and Van Dijken*, 2015).

Here, we use the Coupled Arctic Ocean Sediment model with GOTM and OMEXDIA (CAOS-GO; Figure C.1) to assess how changes in NPP and the N cycle may have differed between the northern and southern Chukchi Sea from 1988 to 2018. The model is composed of interconnected physical, biogeochemical, and sedimentary chemistry models. CAOS-GO was previously implemented in the northern Chukchi Sea (*Payne et al.*, 2021; *Payne and Arrigo*, 2022), at a location where UIBs were observed by *Arrigo et al.* (2014). This northern site was located 100 km south of the northern edge of the Chukchi Shelf and was covered by multi-year ice in some years and first-year ice in others (*Payne et al.*, 2021). However, first-year ice dominates over much of the rest of the Chukchi Sea and sea ice retreats earlier in the year in the south than it does in the north (ric, 2019). As a result of the very different ice conditions, SSTs in the southern Chukchi Sea have changed substantially more rapidly than to the north, increasing to as high as 11°C in the southern Chukchi Sea in August of 2018 (*Osborne et al.*, 2018). Here, we compare the NPP previously projected in the northern Chukchi Sea (*Payne et al.*, 2021) to the southern Chukchi Sea and identify the environmental variables that control NPP during the UI, MIZ, and OW periods. In addition, we evaluate how export of particulate organic N (PON) to the benthos, nitrification in the water column and sediments, and sedimentary denitrification may have changed between 1988 and 2018 in the southern Chukchi Sea and how this compares to the northern Chukchi Sea (*Payne and Arrigo*, 2022).

4.2 Methods

4.2.1 Modeling Configuration

The coupled CAOS-GO model (Figure C.1) was implemented in the southern Chukchi Sea at 67.78°N and 168.24°W (station 3.7 of the Distributed Biological Observatory; *Moore and Grebmeier*, 2018)

and in the northern Chukchi Sea at 72.16°N and 166.60°W (Figure 4.1; *Payne et al.* 2021; *Payne and Arrigo* 2022) for the years 1988 to 2018. Hereafter, we refer to the northern model location as the north and the southern model location as the south.

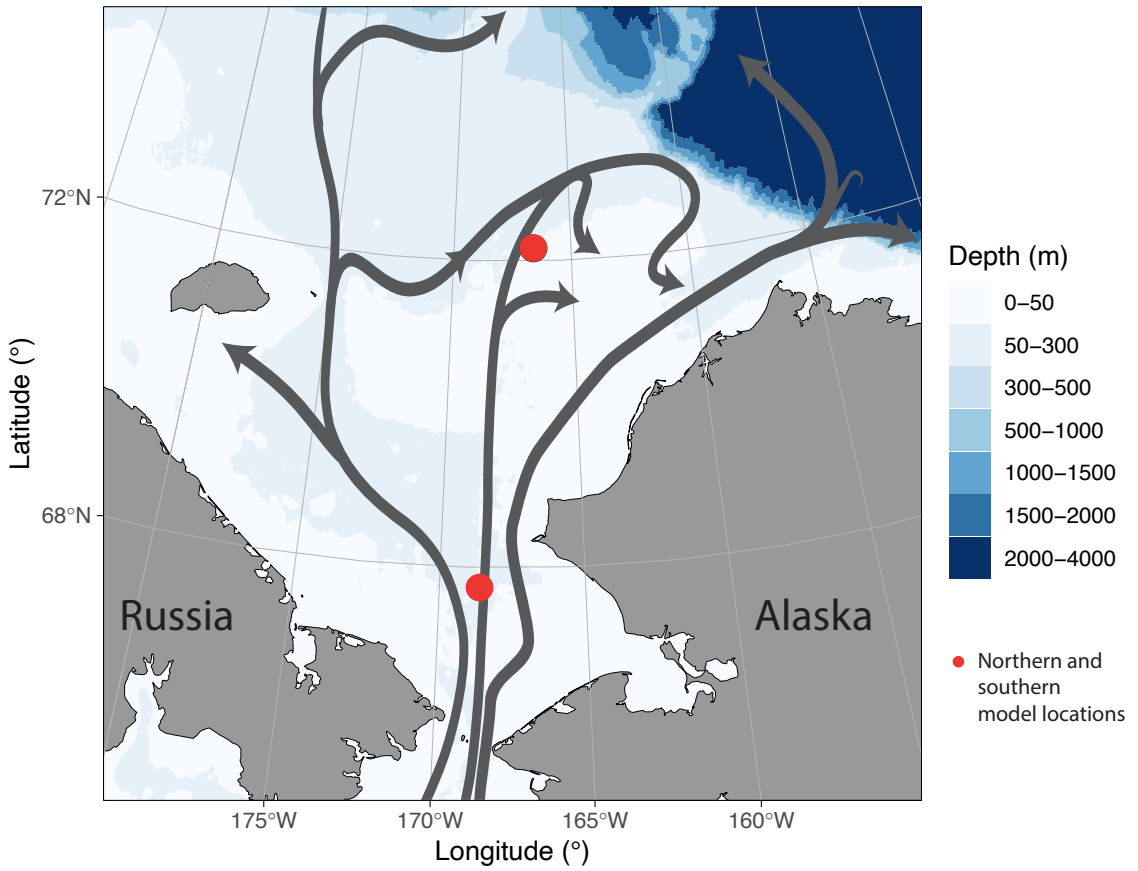

Figure 4.1: Bathymetric map of the Chukchi Sea including schematic flow paths of advected water (gray lines, after *Corlett and Pickart* 2017). Points represent the southern (red) and northern (black) model locations.

The physical component of CAOS-GO, the General Ocean Turbulence Model (GOTM, version 5.4; *Burchard et al.* 1999), was used to produce hourly profiles of temperature, salinity, buoyancy frequency, and turbulent diffusion coefficients. The biogeochemical model, CAOS (*Payne et al.* 2021), dynamically simulates the vertical behavior of N-based state variables in sea ice and over a 50 m water column, including ice algae, small and large phytoplankton (representing flagellates and diatoms, respectively), small and large zooplankton (representing phagotrophic protists and large copepods, respectively), nitrate (NO_3^-), ammonium (NH_4^+), and detritus. Initial concentrations of these N-based state variables are described in Table 4.1, while the effects of advection are simulated by relaxing all N-based state variables towards prescribed profiles. Because water in the

Chukchi Sea advects from the south, where sea ice cover diminishes earlier, phytoplankton growth in these advecting waters begins earlier and will have slightly higher phytoplankton and lower nutrient concentrations than at our model location. We generated these prescribed profiles by running the model twice. As in *Payne et al.* (2021), model profiles generated for Day+1 (first run) were used as prescribed profiles for Day+0 (second run). NO_3^- profiles were further modified following DOY 300 to gradually increase back to the initial NO_3^- concentration (Table 4.1). The sediment model, OMEXDIA (*Soetaert et al.*, 1996a, b), calculates changes in fast- and slow-remineralizing organic matter, oxygen (O_2), NO_3^-, NH_4^+, N_2, and a reduced substances state variable (which included both POC removed as solid substances, such as through pyritization or manganese carbonate formation, and dissolved organic C that diffused through the sediments). Inputs to OMEXDIA include bottom-water NO_3^- and NH_4^+ concentrations and rates of particulate organic N (PON) export to the benthos from CAOS and inputs of bottom-water temperature and salinity from GOTM. OMEXDIA calculates rates of nitrification and denitrification as well as the fluxes of NO_3^- and NH_4^+ between the sediments and the water column that are used as inputs to CAOS.

Table 4.1: CAOS model state variables and initial values. All are in units of mmol N m^{-3}. * indicates that the initial value is also a minimum value. From *Payne et al.* (2021).

State Variable	**Description**	**Initial Value**
IA	Ice algae	0.0
Sphy	Small phytoplankton functional group	0.05 *
Lphy	Large phytoplankton functional group	0.05 *
Szoo	Small zooplankton functional group	0.01 *
Lzoo	Small phytoplankton functional group	0.01 *
Detri	Detritus functional group	0.0
NO_3^-	Dissolved nitrate concentration	16.0
NH_4^+	Dissolved ammonium concentration	0.0

Table 4.2: Parameters used in the OMEXDIA model that differ from those in *Soetaert et al.* (1996a). From *Payne et al.* (2021).

Parameter	**Description**	**Value**	**Unit**	**Source**
F_{fast}	Flux of fast-decaying detritus	(*)	g C m^{-2} yr^{-1}	a
F_{slow}	Flux of slow-decaying detritus	(*)	g C m^{-2} yr^{-1}	a
p_{fast}	Proportion of fast-decaying detritus	0.5	d^{-1}	b
R_{fast}	Decay rate for the fast-decaying detritus	0.18	d^{-1}	c
R_{slow}	Decay rate for the slow-decaying detritus	0.005	d^{-1}	b
$k_{in}(O_2$ denit)	Half saturation conc. for O_2 inhibition in denitrification	15	mmol O_2 m^{-3}	d
$k_{in}(NO_3^-$ anox)	Half saturation conc. for NO_3^- inhibition in anoxic mineralization	1	mmol NO_3^- m^{-3}	d
$k_{in}(O_2$ anox)	Half saturation conc. for O_2 inhibition in anoxic mineralization	1	mmol NO_3^- m^{-3}	d
C/N_{fast}	Carbon to nitrogen ratio of fast-decaying detritus	106/14.18	mol:mol	a
C/N_{slow}	Carbon to nitrogen ratio of slow-decaying detritus	106/12.1	mol:mol	e
ϕ_0	Porosity at the sediment-water interface	0.915	-	d
$coeff_\phi$	Coefficient for exponential porosity changes	4	-	b
Db_0	Constant bioturbation coefficient in the bioturbated layer	2	cm^2 yr^{-1}	f
x_b	Depth below which bioturbation decays exponentially	3	cm	f
O_2_bw	Oxygen concentration of the bottom water NO_3^-	300	mmol N m^{-3}	**
NO_3^-_bw	Daily mean bottom-water NO_3^-	(*)	mmol N m^{-3}	a
NH_4^+_bw	Daily mean bottom-water NH_4^+	(*)	mmol N m^{-3}	a
w	Sedimentation rate	0.12	cm y^{-1}	e
Temperature	Daily mean bottom-water temperature	(*)	°C	a
Salinity	Daily mean bottom-water salinity	(*)	-	a

(*) Variable conditions produced by GOTM or the CAOS model.
** Mean oxygen concentration for the stations closest to the model location for ICESCAPE 2011.
a from CAOS model. *b* *Soetaert et al.* (1996a). *c* *Davis and Benner* (2007). *d* *Soetaert et al.* (1996b).
e *Cooper and Grebmeier* (2018). *f* *Teal et al.* (2008).

Model inputs for CAOS-GO include both satellite-derived and reanalysis data that characterize atmospheric conditions, albedo, idealized temperature and salinity profiles, sea ice concentration and age, and cloud-adjusted surface irradiance. For further details on model inputs, see *Payne et al.* (2021). See supplemental sections C.2 and C.3 for details about model validation at the southern model location.

4.2.2 Physical Model Configuration

As in *Payne et al.* (2021), our GOTM setup did not include horizontal advection, precipitation, and sea ice melt directly. Instead, modeled salinity and temperature profiles were relaxed towards idealized profiles (on timescales of 5 and 15 d, respectively) to compensate for these processes. These idealized profiles were created for each year by using remote sensing products and cruise data collected between 2010 and 2018 (*Arrigo et al.*, 2014; *Grebmeier*, 2017; *Pacini et al.*, 2019; *Peralta-Ferriz and Woodgate*, 2015) as well as modeled fields (*Maslowski et al.*, 2004). The same idealized wintertime temperature and salinity profiles were used each year (*Pacini et al.*, 2019). Subsequently, to reflect interannual differences in the timing of sea ice retreat, idealized temperature profiles in the spring and summer varied based on sea ice concentration as well as satellite-derived sea surface temperature (SST). The salinity in the mixed layer for each year's idealized profiles was scaled depending on the length of the sea ice melt period to reflect annual differences in freshwater input to the water column. As in *Payne et al.* (2021), local sea ice melt generated 50% of the salinity changes in these idealized profiles, with the remaining 50% presumed to be generated by horizontal advection of sea ice melt, precipitation, and runoff. For more details, see supplemental section C.1.

4.2.3 Primary production

The annual cycle of microalgal primary production was divided into four periods: the ice algal (IA), UI, MIZ, and OW periods. The IA period extended from the initiation of the IA bloom, when under-ice light increased above a compensation irradiance of 2 μmol photons m^{-2} s^{-1} (*McMinn et al.*, 1999) until the ice melt date (when air temperatures rose above 0°C for 24 hrs - see *Payne et al.*, 2021), when ice algae began to slough off the bottom of the sea ice. The UI period extended from the initiation of phytoplankton growth (defined as the date when daily phytoplankton NPP exceeded 0.05 g C m^{-2} d^{-1}) until the start of sea ice retreat (when satellite-derived sea ice concentration diminished below 90%). The MIZ period extended from the start to the end of sea ice retreat (when sea ice concentrations diminished below 10%). The OW period extended from the end of sea ice retreat to either the date that sea ice began to advance in the autumn or when average mixed layer light diminished below 1.5 μmol photons m^{-2} s^{-1}, whichever was earliest.

NPP was further divided into new, regenerated, surface, and subsurface production. NPP fueled by NO_3^- was considered new production and NPP fueled by NH_4^+ was considered regenerated production. To calculate the proportion of NPP in the surface or subsurface, large phytoplankton

biomass for each layer (z) of the water column below 10 m was compared to the layer above (z-1). If the lower layer (z) had >110% of the biomass in the layer above (z-1), that layer was considered to be the upper boundary of the subsurface Chl *a* maximum (SCM). Total NPP above that depth was then defined as surface NPP, while NPP at or below that depth was defined as NPP within the SCM. If no obvious SCM existed (z was always < 110% of z-1), water column NPP was integrated and was considered to be surface NPP.

4.2.4 Statistics

To evaluate the importance of environmental conditions (e.g. ice thickness, length of UI period) on NPP, PON export, and nitrification and denitrification, we used multiple linear regression. We checked for collinearity among predictor variables by using the variance inflation factor (VIF), but found only moderate correlation (VIF was <3.5 for all variables). Backward selection was used to identify multiple linear regressions. In backward selection, the variable with the highest p-value was sequentially eliminated until only statistically significant ($p<0.05$) variables remained. Regressions were subsequently checked using visual inspection of histograms, quantile-quantile plots, and plots of the independent and dependent variables and the Shapiro-Wilk test. Linear regressions are reported with the standard error, and plots with linear regressions include a confidence interval of 95%. Relative importance of each variable in multiple linear regressions was assessed using the 'relaimpo' statistical package in R, version 2.2-6 (*Grömping*, 2006).

Annual cycles of daily NPP were clustered into distinct water column bloom types using *k*-means clustering based on NPP in the UI and MIZ periods. The optimal *k* value was determined using the gap statistic. To quantify the relationship between water column bloom type and NPP, PON export to the benthos, nitrification, and denitrification, ANOVA and post hoc Tukey's honest significant difference (HSD) tests were used. Statistical analyses were all conducted in R version 4.1.0.

4.3 Results

4.3.1 Snow and ice conditions

Satellite-derived snow and ice conditions differed significantly between the southern and northern Chukchi Sea. While the north typically featured multi-year sea ice, the south exclusively hosted thinner first-year ice with a snow cover that was only two-thirds as thick as that in the north (Figure 4.2a-c and Table 4.3). Snow started melting four weeks earlier in the south, allowing ice algal blooms to start one month earlier (in mid-March) and last three weeks longer than in the north (Figure 4.2d, Figure 4.3a, and Table 4.3). Sea ice retreat also started 40 days earlier and ended 53 days earlier in the south (typically stretching from mid-May to early June between 1988 and 2018) than in the north (where sea ice retreat lasted from the end of June to the end of July; Figure 4.2f

Table 4.3: Average sea ice and snow conditions and biogeochemistry at the northern and southern Chukchi Sea model locations for 1988 to 2018, with standard deviation and p-values.

Variable	North	South	P-value
Ice age (yr)	1.5±1.1	0.45±0.05	<0.001
Ice thickness (m)	2.0±0.4	1.5±0.1	<0.001
Snow thickness (cm)	12.9±4.8	8.7±3.1	<0.001
Snow melt date (DOY)	104±30	77±19	<0.001
UI period start (DOY)	137±21	111±10	<0.001
Ice melt date (DOY)	140±11	132±15	0.026
Ice retreat start (DOY)	178±14	138±13	<0.001
Ice retreat end (DOY)	210±22	157±12	<0.001
Ice advance (DOY)	320±20	336±16	<0.001
IA period (d)	31.5±24.8	53.8±21.4	<0.001
UI period (d)	41.8±18.1	27.9±13.6	<0.001
MIZ period (d)	31.3±15.0	18.4±7.6	<0.001
OW period (d)	109.7±38.4	152.3±13.1	<0.001
Annual NPP (g C m^{-2} yr^{-1})	89.0±8.0	109.0±8.9	<0.001
IA NPP (g C m^{-2} yr^{-1})	1.7±1.5	3.0±1.3	<0.001
UI NPP (g C m^{-2} yr^{-1})	44.3±22.6	18.4±17.2	<0.001
MIZ NPP (g C m^{-2} yr^{-1})	20.1±15.6	24.3±16.0	0.3
OW NPP (g C m^{-2} yr^{-1})	22.8±8.0	63.3±11.6	<0.001
Annual Grazing (g C m^{-2} yr^{-1})	7.5±1.4	19.1±2.8	<0.001
UI Grazing (g C m^{-2} yr^{-1})	1.4±0.5	1.2±0.4	0.039
MIZ Grazing (g C m^{-2} yr^{-1})	1.1±0.6	0.5±0.2	<0.001
OW Grazing (g C m^{-2} yr^{-1})	4.9±1.9	17.2±3.0	<0.001
Export to benthos (mmol N m^{-2} yr^{-1})	301.4±44.5	401.9±53.0	<0.001
WC Nitrification (mmol N m^{-2} yr^{-1})	481.5±22.3	573.7±49.3	<0.001
S. Nitrification (mmol N m^{-2} yr^{-1})	186.4±22.2	224.5±16.3	<0.001
S. Denitrification (mmol N m^{-2} yr^{-1})	178.8±28.3	262.4±24.6	<0.001

and g, Table 4.3). This early sea ice retreat in the southern Chukchi Sea caused both shorter UI and MIZ periods than in the north by 14 and 13 days, respectively (Figure 4.3b and c, Table 4.3). In both the south and the north, ice retreat shifted to earlier in the year between 1988 and 2018 (Table 4.4). This resulted in a UI period in the southern Chukchi Sea that shortened by 7.0 d per decade between 1988 and 2018. Sea ice advance began later over time in both the south and the north (Table 4.4), advancing on average 16 days later in the south than in the north (Figure 4.2h and Table 4.3). The south typically had a 42 day longer OW period than the north (Figure 4.3d and Table 4.3), although this diminished over time, since the OW period lengthened more rapidly in the north than in the south (Table 4.4).

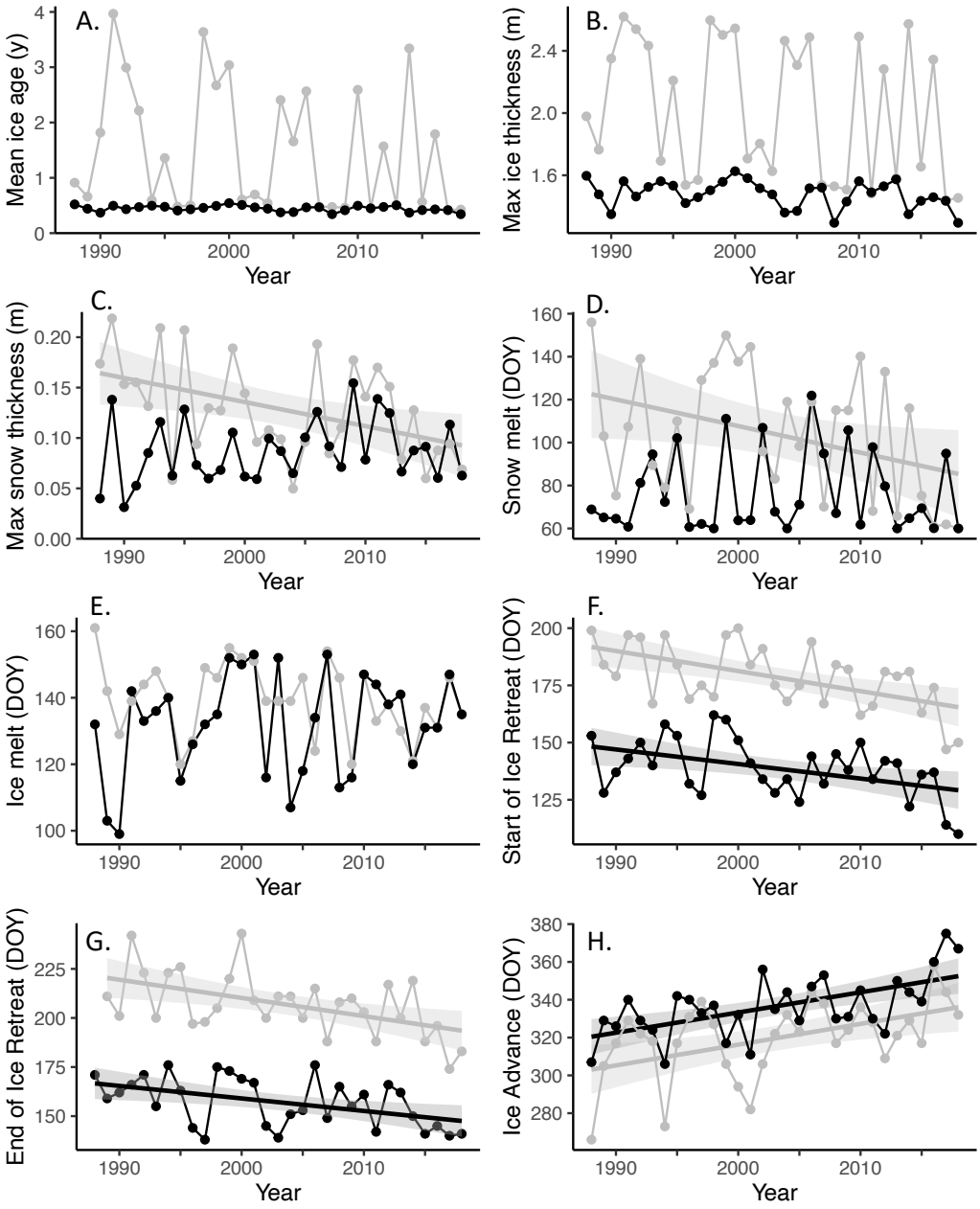

Figure 4.2: Ice and snow conditions between 1988 and 2018: A) mean ice age (y), B) maximum ice thickness (m), C) maximum snow thickness (m), D) snow melt date (DOY), E) ice melt date (DOY), F) the date when ice retreat starts (DOY), G) the date when ice retreat ends (DOY), and H) the date when ice advances (DOY), for the southern (black) and northern (grey) model locations. Lines are used when regressions are significant and grey shading represents the 95% confidence interval for these regressions.

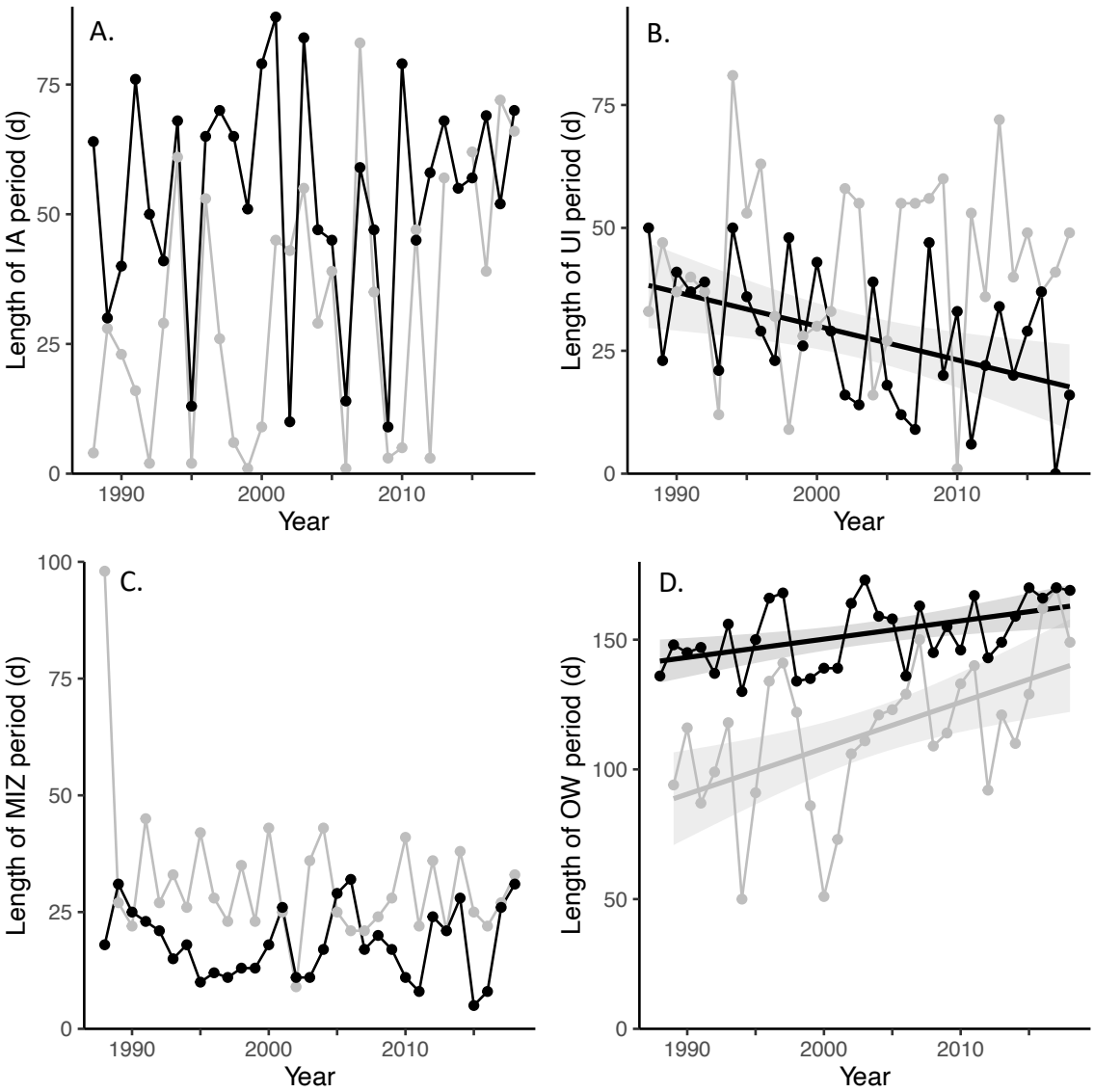

Figure 4.3: Lengths between 1988 and 2018 of the A) IA period (d), B) UI period (d), C) MIZ period (d), and D) OW period (d), for the southern (black) and northern (grey) model locations. Lines are used when linear regressions are statistically significant and grey shading represents the 95% confidence interval for these regressions.

Table 4.4: Secular trends for the northern (N.) and southern (S.) Chukchi Sea in snow thickness (cm yr^{-1}), the dates of ice condition transitions (d yr^{-1}); the lengths of the UI and OW periods (d yr^{-1}); annual and UI NPP (g C m^{-2} yr^{-1} yr^{-1}); grazing during the UI and OW periods (g C m^{-2} yr^{-1} yr^{-1}); and N cycle processes (mmol N m^{-2} yr^{-1} yr^{-1}). Linear regressions, R^2, and p-values are listed.

Variable	N. trend	N. R^2	N. p-value	S. trend	S. R^2	S. p-value
Snow thickness	-0.24	0.206	0.010	-	-	-
Snow melt date	-1.2	0.139	0.039	-	-	-
UI period start	-1.1	0.231	0.006	-	-	-
Ice retreat start	-0.88	0.327	<0.001	-0.64	0.211	0.009
Ice retreat end	-1.4	0.315	0.001	-0.64	0.219	0.008
Ice advance	1.1	0.244	0.005	0.99	0.367	<0.001
UI period	-	-	-	-0.71	0.221	0.008
OW period	2.5	0.345	<0.001	0.71	0.242	0.005
Annual NPP	0.34	0.148	0.033	-	-	-
UI NPP	-	-	-	-0.80	0.177	0.019
UI grazing	-	-	-	-0.02	0.179	0.018
OW grazing	-	-	-	0.12	0.127	0.050
Export to benthos	1.8	0.130	0.046	-	-	-
WC nitrification	1.2	0.239	0.005	-2.8	0.262	0.003
S. nitrification	1.1	0.220	0.008	-0.7	0.171	0.021
S. denitrification	1.3	0.179	0.018	-	-	-

4.3.2 Interannual changes in annual NPP

In the south, annual NPP (ice algal + phytoplankton) averaged 109.0±8.9 g C m^{-2} yr^{-1} (Figure 4.4a) and was 25.8% higher than in the north (Table 4.3). New production in the south averaged 87.3±8.0 g C m^{-2} yr^{-1}, 28.0% higher than in the north. Different environmental controls drove interannual variability in annual NPP in the northern and southern Chukchi Sea. While ice thickness and the length of the UI period explained much of the variance in annual NPP in the north (*Payne et al.* 2021), variation in annual NPP in the south was better explained by snow conditions, with years with a longer ice algal period (R^2=0.382, p<0.001) or thinner snow (R^2=0.243, p=0.005) yielding higher NPP.

Interannual variability in southern Chukchi Sea NPP was driven not by NPP during the UI, MIZ, and OW periods, but rather by a reduction in autumn NPP between 1988 and 2018 (Figure 4.5a). Over this 31-year period, modeled September and October NPP diminished by 0.21 g C m^{-2} yr^{-1} (R^2=0.186, p=0.015) and 0.25 g C m^{-2} yr^{-1} (R^2=0.127, p=0.049), respectively. The frequency of autumn blooms did not diminish at our model location in the satellite record between 2003 and 2018, where there were no significant changes in NPP. However, due to the low solar angle in the autumn, ocean color data were not available following September 21 each year, making it impossible to evaluate changes in integrated NPP in September and October from the satellite record. However, modeled NPP in September and October was negatively correlated with both the satellite-derived

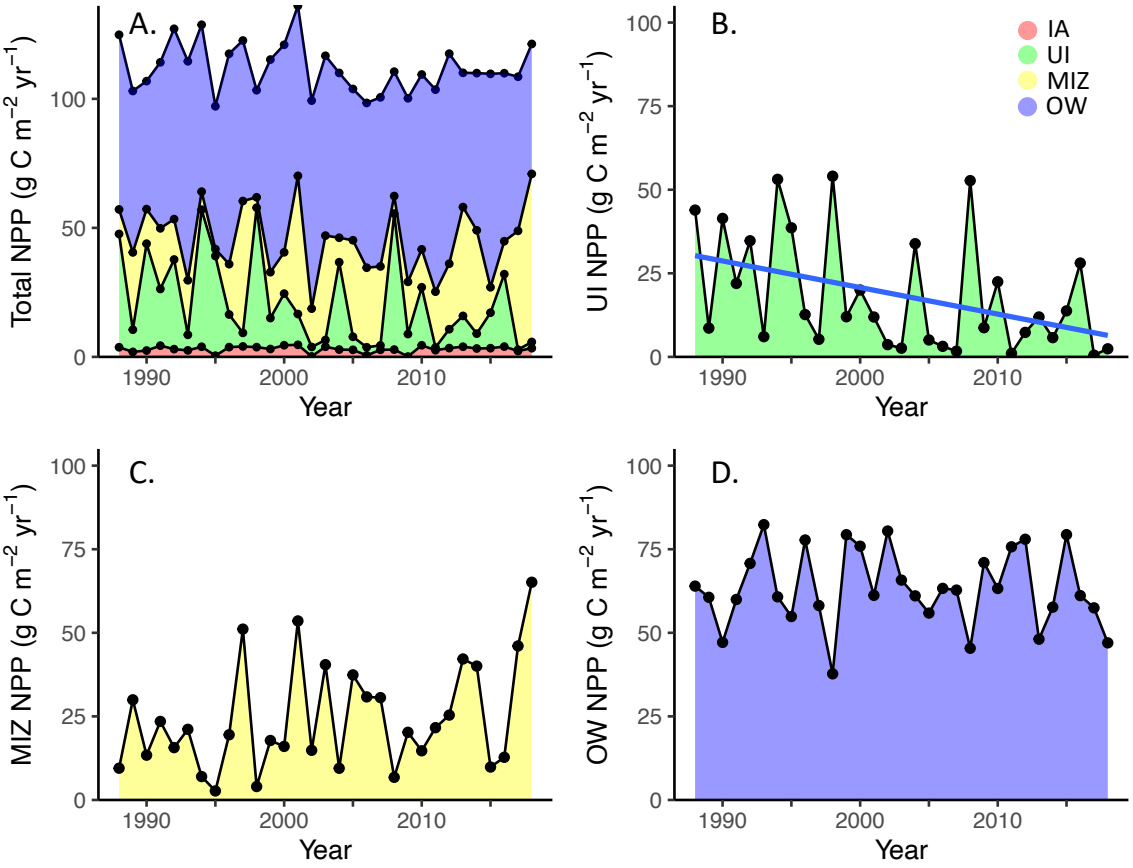

Figure 4.4: (A) Annual NPP (upper black line) in the southern Chukchi Sea and its component parts, ice algal (IA) NPP (red), B) annual UI NPP (green), C) annual MIZ NPP (yellow), and D) annual OW NPP (blue) between 1988 and 2018. A blue line is used to indicate the statistically significant decline in UI NPP.

maximum SST (R^2=0.231, p=0.006 and R^2=0.209, p=0.010, respectively) and the date when the modeled MLD dropped below 35 m (R^2=0.655, p<0.001 and R^2=0.153, p=0.030, respectively). While satellite-derived SST has not changed significantly in September, SST increased by 1.8°C in October (R^2=0.294, p=0.002) and by 1.6°C in November (R^2=0.275, p=0.002) between 1988 and 2018. Further, NPP in September and October were both negatively correlated with satellite-derived SSTs during those months (R^2=0.207, p=0.010 and R^2=0.273, p=0.003 for September and October, respectively). These correlations indicate that in years when summer SSTs were higher, there was stratification until later in the year, preventing the entrainment of new nutrients in the water column and reducing the incidences of autumn blooms.

4.3.3 NPP and zooplankton grazing in the IA, UI, MIZ, and OW periods

NPP during the sea ice algal (IA) period averaged 3.0±1.3 g C m^{-2} yr^{-1} between 1988 and 2018 in the southern Chukchi Sea (Figure 4.4a), accounting for 2.6±1.0% of annual NPP (Table 4.5). These annual rates for ice algae were 76.5% higher than those in the northern Chukchi Sea (Table 4.3). 90.0% of the variance (p<0.001) in annual NPP by ice algae was controlled by the length of the snow melt period (R^2=0.660, p<0.001), with a longer period of snow melt yielding higher NPP by ice algae.

The UI period accounted for nearly half of annual NPP in the northern Chukchi Sea (Table 4.3) but a mere 16.3±15.4% of annual NPP in the south (18.4±17.2 g C m^{-2} yr^{-1}; Figure 4.4b) between 1988 and 2018. While this period had the highest proportion of new production (89.9±2.9% new production) of any period in the southern Chukchi Sea, it accounted for only 16.3 g C m^{-2} yr^{-1} of total new production, a rate that was lower than both the MIZ and OW periods. Furthermore, NPP in the UI period diminished by 0.8 g C m^{-2} yr^{-1} (Figure 4.4b, Table 4.4) between 1988 and 2018. Interannual variance in NPP during the UI period (R^2=0.860, p<0.001) was controlled primarily by the length of the UI period (R^2=0.798, p<0.001; Figure 4.6a), but also by the length of the ice algal period (R^2=0.062, p=0.002), with a longer UI period and shorter snow melt period yielding more NPP during the UI period.

NPP in the MIZ period was not significantly different between the north and south (Table 4.3). In the south, NPP during the MIZ period reached an average of 24.3±16.0 g C m^{-2} yr^{-1} (Figure 4.4c) and accounted for 21.6±13.5% of annual NPP (Table 4.5). On average, 77.7% of the annual NPP during the MIZ period was new production, contributing 19.9±13.4 g C m^{-2} yr^{-1} in the southern Chukchi Sea. In the north, NPP transitioned from surface waters to the subsurface chlorophyll maximum (SCM; *Payne et al.*, 2021) during the MIZ period. In contrast, in the south, 87.3% of the NPP during the MIZ period was generated in surface waters. Multiple linear regression revealed that 77.0% of the variance (p<0.001) in NPP during the MIZ period in the southern Chukchi Sea was controlled by the length of the UI period (R^2=0.390, p<0.001), the length of the MIZ period (R^2=0.224, p<0.001; Figure 4.6a), and the length of the ice algal period (R^2=0.156, p<0.001).

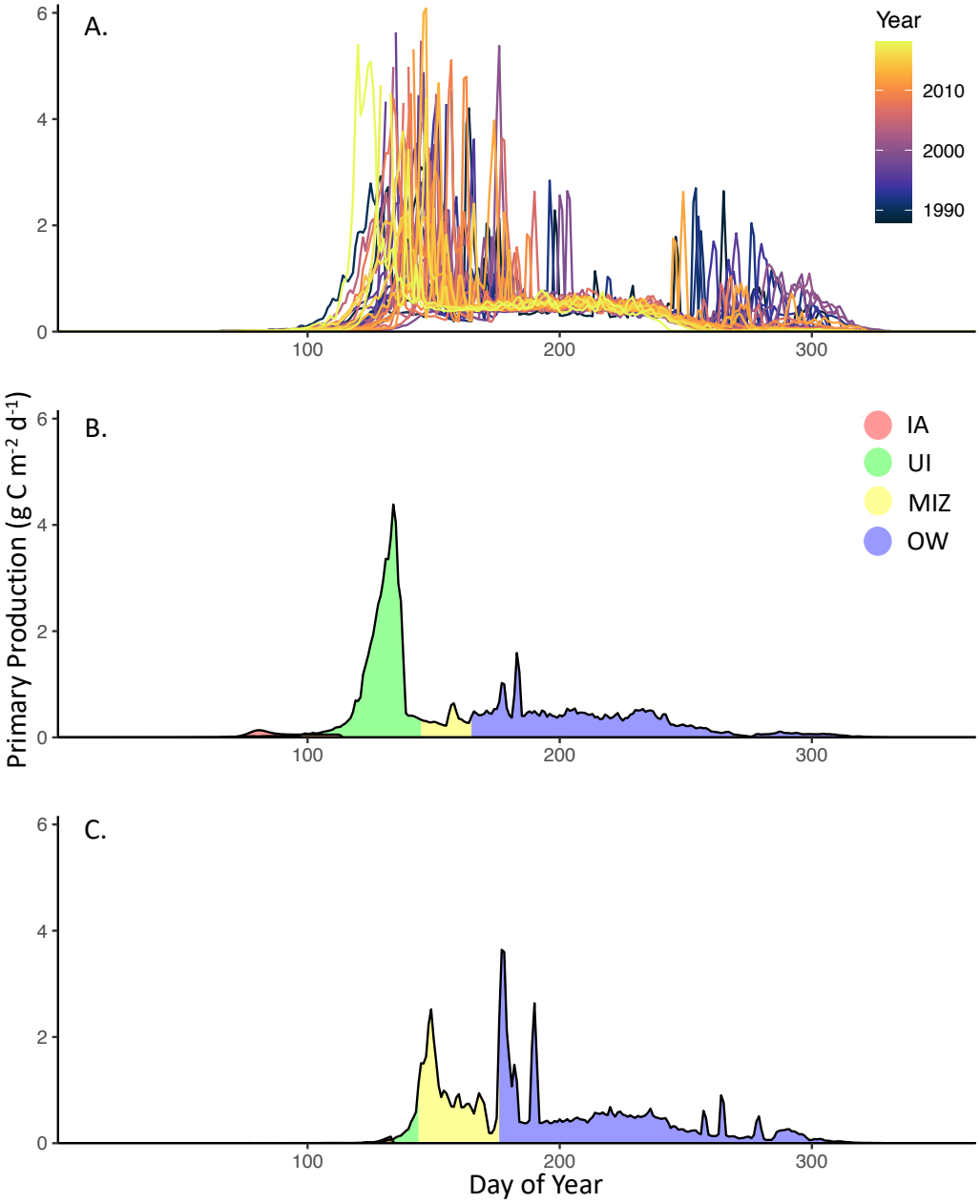

Figure 4.5: A) Daily water-column NPP for 1988 to 2018 in the southern Chukchi Sea, and example annual cycles of daily NPP (g C m^{-2} d^{-1}) for B) a year with a UIB (2008), and C) a year without a UIB (2006). Red shading represents production by ice algae while green, yellow, and blue shading represent production during UI, MIZ, and OW periods, respectively.

Table 4.5: Bloom type, % IA, % UI, % MIZ, % OW, and annual NPP (g C m^{-2} yr^{-1}) for each year in the southern Chukchi Sea. Annual cycles of NPP were separated into two clusters (Bloom Types): years with UIBs (UIB) and years without UIBs (N). Means and standard deviation of annual NPP (g C m^{-2} yr^{-1}) and NPP within the UI, MIZ, and open water (OW) periods (%) for both of the clusters are listed at the bottom of the table.

Year	Bloom Type	% IA	% UI	% MIZ	% OW	Annual
1988	UIB	3.1	36.3	7.8	52.8	121.1
1989	N	1.9	7.1	24.7	50.1	101.1
1990	UIB	2.4	34.2	11.1	38.9	104.4
1991	N	4.0	18.1	19.4	49.5	109.8
1992	UIB	2.4	28.7	12.9	58.4	124.2
1993	N	2.3	5.0	17.4	68.0	112.0
1994	UIB	3.2	43.9	5.8	50.2	124.8
1995	UIB	0.5	31.9	2.2	45.3	96.7
1996	N	3.3	10.5	16.1	64.2	113.7
1997	N	3.4	4.3	42.2	48.0	118.6
1998	UIB	3.8	44.6	3.3	31.2	99.6
1999	N	2.7	9.9	14.7	65.5	112.2
2000	N	3.9	16.5	13.2	62.7	116.4
2001	N	3.6	9.8	44.2	50.5	131.4
2002	N	0.2	3.0	12.3	66.4	99.1
2003	N	3.5	2.2	33.4	54.3	112.8
2004	UIB	2.6	28.0	7.8	50.4	107.2
2005	N	2.7	4.2	30.9	46.2	101.1
2006	N	0.6	2.6	25.5	52.3	97.8
2007	N	2.8	1.4	25.3	51.8	97.8
2008	UIB	2.6	43.5	5.6	37.5	107.7
2009	N	0.1	7.2	16.7	58.6	100.1
2010	UIB	4.3	18.6	12.1	52.2	104.9
2011	N	2.6	0.9	17.8	62.5	101.0
2012	N	3.0	6.0	21.0	64.4	114.1
2013	N	3.7	9.9	34.8	39.7	106.1
2014	N	3.0	4.8	33.1	47.6	106.7
2015	N	3.2	11.4	8.1	65.5	106.3
2016	UIB	3.8	23.2	10.5	50.5	105.9
2017	N	2.1	0.4	38.0	47.4	106.3
2018	N	2.9	2.0	53.8	38.8	117.9
Mean	UIB	2.9±1.1	36.9±10.3	8.7±4.0	51.5±7.7	109.6±10.1
Mean	N	2.6±1.1	7.2±5.3	28.6±12.3	61.6±11.2	108.7±8.5

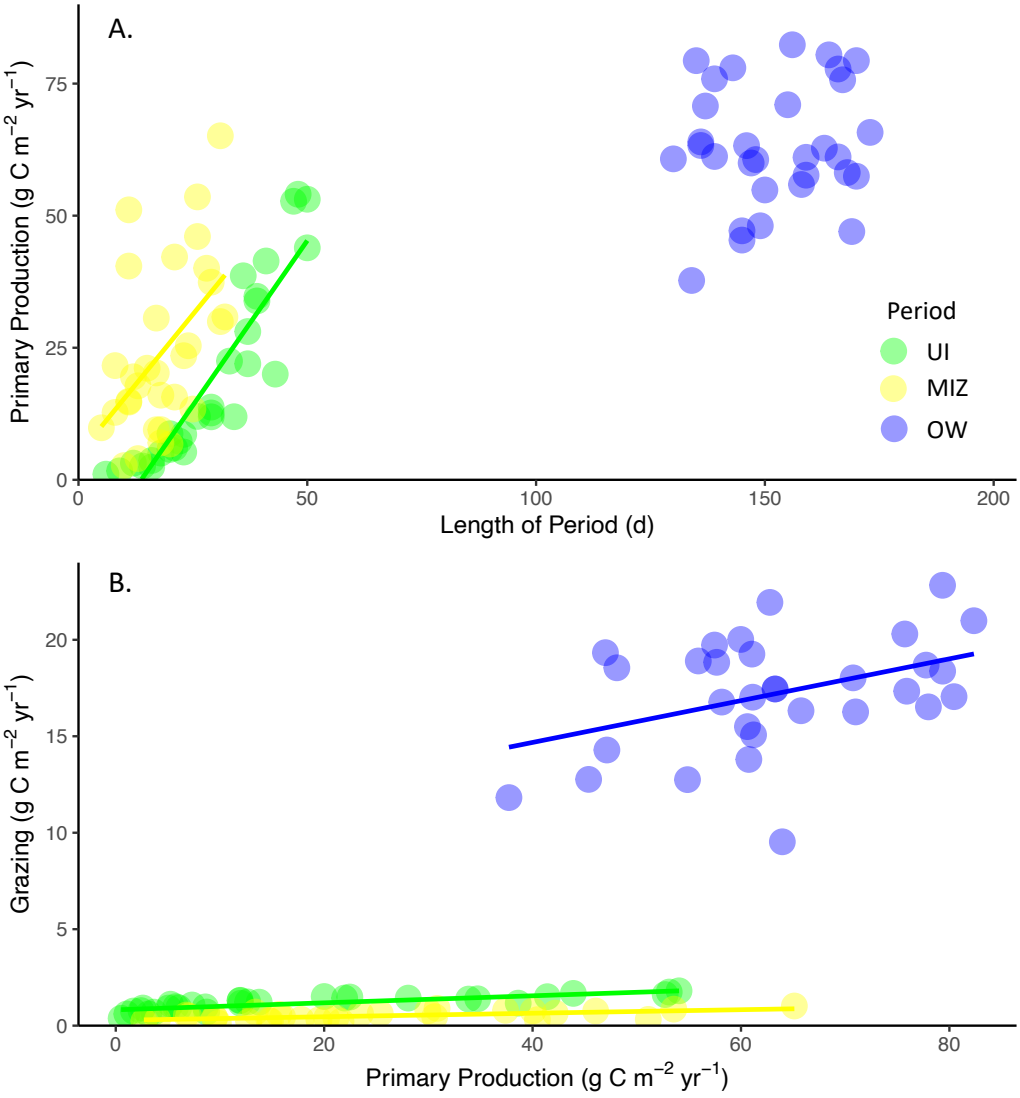

Figure 4.6: Scatterplots for the southern Chukchi Sea of A) the length of the period (d) versus seasonal NPP (g C m^{-2} yr^{-1}) and B) seasonal NPP versus seasonal grazing (g C m^{-2} yr^{-1}) for the UI (green), MIZ (yellow), and OW (blue) periods. Lines (in the season color) are used when linear regressions are significant ($p<0.05$) and grey shading represents the 95% confidence interval for these regressions.

Shorter UI periods and longer MIZ periods yielded more NPP during the MIZ period, while a shorter ice algal period was correlated with a longer and more productive UI period and thus was associated with reduced NPP during the MIZ period.

Between 1988 and 2018, NPP in the southern Chukchi Sea during the OW period averaged 63.3±11.6 g C m^{-2} yr^{-1} (Figure 4.4d), nearly three times higher than NPP in the OW period in the north (Table 4.3). The OW period accounted for most (56.9±11.1%) of the annual NPP in the southern Chukchi Sea (Table 4.5), and 71.2% of all NPP during the OW period was new production (45.5±9.0 g C m^{-2} yr^{-1}). Most of the NPP during this period (81.2±16.2%) was associated with the SCM. Variation in the length of the OW period was not significantly correlated to the magnitude of NPP during OW period ($p<0.001$; Figure 4.6a). 31.0% of the variance ($p=0.006$) in NPP during the OW period was controlled by snow thickness ($R^2=0.167$, $p=0.014$) and the length of the MIZ period ($R^2=0.143$, $p=0.022$). Due to the very long OW period (152.3±13.1 d), NPP was not correlated with the length of the OW period in the southern Chukchi (Figure 4.6a) and was instead greatest when thick snow prevented NPP during the UI period and a short MIZ period prevented NPP during the MIZ period.

Zooplankton grazed phytoplankton at an average rate of 19.1±2.8 g C m^{-2} yr^{-1} between 1988 and 2018 (17.2±2.9% of annual NPP), 1.5 times greater than in the north (Table 4.3). During the UI period, grazing by zooplankton in the southern Chukchi Sea averaged 1.2±0.4 g C m^{-2} yr^{-1}, consuming 15.8±16.7% of NPP in the UI period. Zooplankton grazing during the MIZ period in the south averaged 0.5±0.2 g C m^{-2} yr^{-1} (0.4±0.2% of NPP in the MIZ period) or less than half of the grazing during the MIZ period in the north. Southern Chukchi Sea zooplankton consumed 17.2±3.0 g C m^{-2} yr^{-1} during the OW period (or 27.7±5.6% of OW period NPP), 2.5 times more biomass than was typically consumed in the north (Table 4.3). While southern Chukchi Sea grazing diminished by 0.02 g C m^{-2} yr^{-1} yr^{-1} during the UI period ($R^2=0.179$, $p=0.018$), grazing increased by 0.12 g C m^{-2} yr^{-1} in the OW period ($R^2=0.127$, $p=0.050$). NPP during the UI, MIZ, and OW periods was significantly correlated with grazing during that period (Figure 4.6b).

4.3.4 PON export to the benthos

The amount of PON exported to the benthos averaged 401.9±53.0 mmol N m^{-2} yr^{-1} in the southern Chukchi Sea, a rate 33.3% higher than that to the north (Table 4.3). 33.0±1.7% of the annual N assimilated by microalgae (and 42.7±3.1% of the total annual NO_3^- assimilation by microalgae) was exported to the benthos. Daily PON export peaked on average at 5.2±1.5 mmol N m^{-2} d^{-1} (Figure 4.7a). As in *Payne and Arrigo* (2022), PON export to the sediments was highly correlated with annual N assimilation by microalgae, which in the south explained 97.4% of the variance in PON export ($p<0.001$). In addition, interannual variance in PON export could be explained by snow thickness ($R^2=0.242$, $p=0.005$) and the length of the snow melt period ($R^2=0.239$, $p=0.005$), the primary drivers of variance in annual NPP. Between 1988 and 2018, PON export increased

marginally in August but diminished in September and October (Table 4.6, Figure 4.7a) due to the reduction in N assimilated by microalgae during the autumn.

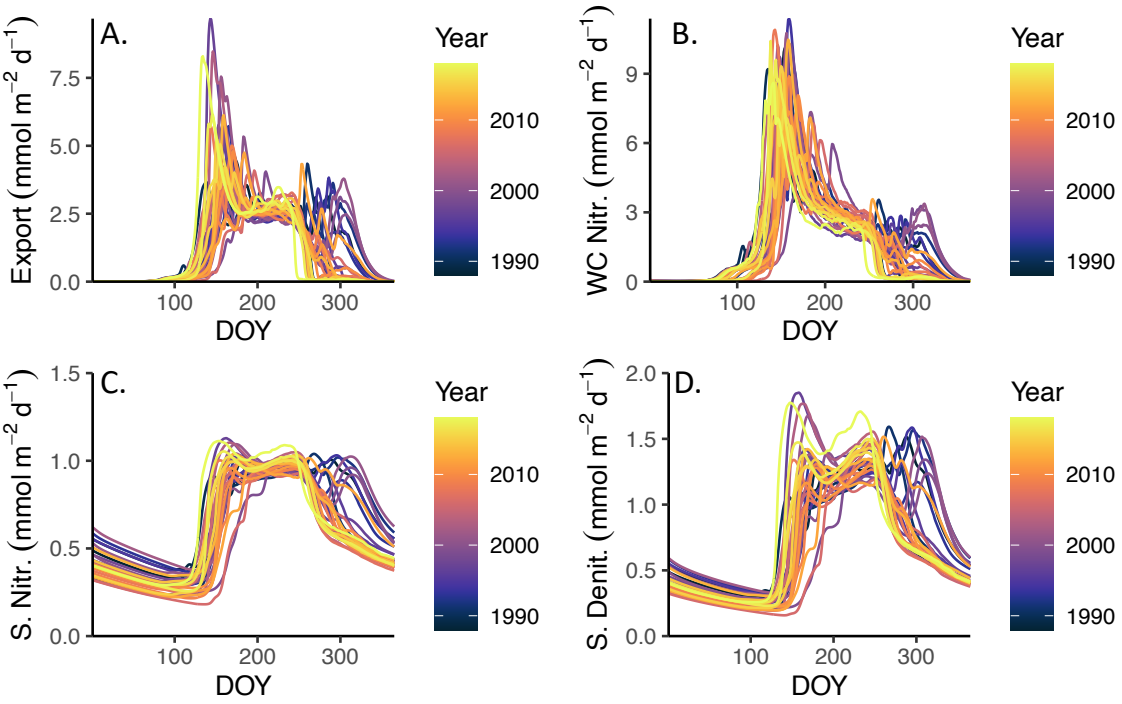

Figure 4.7: Rates of A) PON export to the benthos (mmol N m^{-2} d^{-1}), B) water column nitrification (WC Nitr., mmol N m^{-2} d^{-1}), C) sedimentary nitrification (S. Nitr., mmol N m^{-2} d^{-1}), and D) sedimentary denitrification (S. Denit., mmol N m^{-2} d^{-1}) for each day of the year (DOY) between 1988 and 2018 (colorbar) in the southern Chukchi Sea.

4.3.5 Nitrification and Denitrification

Between 1988 and 2018, daily depth-integrated water column nitrification rates in the south ranged from 0.01±0.004 to 8.9±1.3 mmol N m^{-2} d^{-1} (Figure 4.7b), peaking in early June (on DOY 155.4±12.5). Annual nitrification rates averaged 573.7±49.3 mmol N m^{-2} yr^{-1} in the southern Chukchi Sea, equivalent to 46.1±3.3% of annual N assimilation by microalgae. These annual water column nitrification rates diminished by 2.8 mmol N m^{-2} yr^{-1} (R^2=0.262, p=0.003) between 1988 and 2018 but were still 19.1% higher than rates to the north (Table 4.3). 72.2% of the variance (p<0.001) in annual water column nitrification was controlled by the length of the OW (R^2=0.468, p<0.001) and UI periods (R^2=0.254, p=0.025). Furthermore, changes in annual N assimilation by microalgae explained 40.0% of the interannual variance in water column nitrification (p<0.001). Variation in N assimilation during the UI period accounted for 30.5% of the variance in water column nitrification (p=0.001), more than N assimilation in the IA (R^2=0.167, p=0.023), MIZ (R^2=0.135, p=0.042), or

Table 4.6: Linear regressions for changes between 1988 and 2018 in the southern Chukchi Sea in monthly benthic PON export (mmol N m^{-2} per month), water column nitrification (mmol N m^{-2} per month), sedimentary nitrification (mmol N m^{-2} per month), and sedimentary denitrification (mmol N m^{-2} per month). R^2, p-value, and slope is listed for each statistically significant ($p<0.05$) month.

Process	**Month**	**R^2**	**P-value**	**Slope**
Benthic export	August	0.158	0.027	1.11E-2
Benthic export	September	0.223	0.007	-2.79E-2
Benthic export	October	0.210	0.009	-4.52E-2
Water column nitrification	January	0.137	0.040	-2.68E-4
Water column nitrification	February	0.227	0.007	-2.28E-4
Water column nitrification	September	0.214	0.009	-2.44E-2
Water column nitrification	October	0.213	0.009	-3.52E-2
Sedimentary nitrification	January	0.144	0.035	-2.95E-3
Sedimentary nitrification	February	0.143	0.036	-2.61E-3
Sedimentary nitrification	March	0.145	0.035	-2.35E-3
Sedimentary nitrification	April	0.159	0.026	-2.22E-3
Sedimentary nitrification	September	0.188	0.015	-1.44E-3
Sedimentary nitrification	October	0.265	0.003	-7.49E-3
Sedimentary nitrification	November	0.156	0.038	-6.98E-3
Sedimentary nitrification	December	0.160	0.026	-3.96E-3
Sedimentary denitrification	January	0.139	0.039	-2.62E-3
Sedimentary denitrification	February	0.147	0.033	-2.29E-3
Sedimentary denitrification	March	0.151	0.031	-2.05E-3
Sedimentary denitrification	April	0.164	0.024	-1.95E-3
Sedimentary denitrification	August	0.141	0.038	2.31E-3
Sedimentary denitrification	October	0.260	0.003	-1.35E-2
Sedimentary denitrification	November	0.144	0.035	-1.04E-2
Sedimentary denitrification	December	0.137	0.040	-3.97E-3

OW (no statistically significant relationship) periods. Decreases in annual water column nitrification in the southern Chukchi Sea between 1988 and 2018 were driven by decreases during January, February, September, and October (Figure 4.7b, Table 4.6) due to lowered incidences of autumn blooms.

Daily sedimentary nitrification rates in the southern Chukchi Sea ranged from 0.29±0.05 to 1.0±0.04 mmol m^{-2} d^{-1} (Figure 4.7c) between 1988 and 2018. Annual rates were substantially lower than rates in the water column, averaging 224.5±16.3 mmol N m^{-2} yr^{-1} and were 20.4% higher than corresponding rates in the north (Table 4.3). Nitrification in the sediments accounted for an average of 18.5±1.2% of annual N assimilated by microalgae in the southern Chukchi Sea and 56.4±5.3% of the exported PON. Rates of sedimentary nitrification diminished by 0.7 mmol N m^{-2} yr^{-1} each year between 1988 and 2018 (R^2=0.171, p=0.021). The variability in annual sedimentary nitrification was controlled primarily by the amount of N assimilated by microalgae (R^2=0.481, p<0.001) and subsequently exported to the benthos (R^2=0.503, p<0.001). Sedimentary nitrification variance could be explained by snow thickness (R^2=0.242, p=0.005), the primary driver of variance in both annual N assimilation by microalgae and PON export to the benthos. Decreases in annual sedimentary nitrification between 1988 and 2018 were driven by decreases in January-April and September-December (Figure 4.7c, Table 4.6) caused by the reduction in PON exported to the benthos in the autumn.

Because of relatively high concentrations of O_2 in the water column, our model configuration assumes no denitrification occurs in the water column. However, modeled sedimentary denitrification rates could be substantial, ranging from 0.26±0.04 to 1.5±0.2 mmol N m^{-2} d^{-1} (Figure 4.7d). Annual denitrification rates were 46.8% higher than those to the north (Table 4.3), averaging 262.4±24.6 mmol N m^{-2} yr^{-1} between 1988 and 2018, and did not change significantly over time. Sedimentary denitrification in the southern Chukchi Sea removed 21.6±1.2% of the annual N assimilated by microalgae, 65.7±4.6% of the PON exported to the sediments, and 116.8±4.3% of the NO_3^- produced through sedimentary nitrification. Denitrification was closely correlated with N assimilation by microalgae (R^2=0.668, p<0.001) and PON export to the benthos (R^2=0.743, p<0.001), and thus shared the same environmental drivers of interannual variability (snow thickness, with R^2=0.239 and p=0.005, and the length of the snow melt period, with R^2=0.140 and p=0.038). Annual sedimentary denitrification showed no trend over time, but sedimentary denitrification diminished in January-April and October-December and increased in August (Figure 4.7d, Table 4.6), driven by changes in PON export and sedimentary nitrification due to a reduction in autumn bloom incidence.

In addition to an increase in sedimentary nitrification and denitrification in the southern Chukchi Sea relative to the north, there was a difference in the balance between the processes. In the north, 62% and 59% of the PON exported to the benthos was subsequently nitrified and denitrified, respectively. As a result, there was slightly more nitrification than denitrification in the sediments (7.6

mmol m^{-2} yr^{-1} more; Table 4.3). However, in the south, only 56% of the PON exported to the benthos was nitrified, but the relative amount of exported PON that was denitrified increased to 65%. This shifted the balance between sedimentary nitrification and denitrification to favor denitrification, which on average removed 37.9 mmol N m^{-2} yr^{-1} more than was converted to NO_3^- through sedimentary nitrification (Table 4.3). As a result, denitrification in the southern Chukchi Sea relied on more NO_3^- that had diffused across the sediment-water interface as substrate. The balance between nitrification and denitrification was controlled (R^2=0.969, p<0.001) by the location (R^2=0.515, p<0.001) and the amount of PON exported to the benthos (R^2 = 0.454, p<0.001; Figure 4.8a). The differences between the north and south arise because of differences in phenology, with the amount of N assimilation during the OW period controlling more of the variance in the nitrification-denitrification balance (R^2=0.760, p<0.001; Figure 4.8b) than any other metrics of phenology (lengths of the period of production and N assimilation during each period). The rate of PON export to the benthos controlled the balance of nitrification and denitrification because it drove higher oxygen utilization in the surface layers sediments. In the south, the higher rates of PON export to the benthos corresponded to a far thinner oxic layer, allowing denitrification higher in the sediments (mean depth of 5 mm between June and November) than to the north (mean depth of 9 mm).

4.3.6 Water column bloom types

In order to characterize patterns of bloom evolution in the southern Chukchi Sea, we performed clustering analysis that categorized years based on NPP during the UI and MIZ periods. In the north, this resulted in three different types of annual cycles: 17 years dominated by NPP in the UI period (where NPP in the UI period accounted for a mean of 65.0±7.6% of annual NPP), 4 MIZ-dominant years (where NPP in the MIZ period averaged 64.5±2.7% of annual NPP), and 10 mixed-dominance years (where NPP during the UI and MIZ periods averaged 39.5±9.7% and 30.1±7.8% of annual NPP, respectively; *Payne et al.*, 2021). In the south, only two distinct annual cycles were produced through our analysis (Table 4.5). Because OW blooms dominated annual NPP every year, the major distinguishing feature between years was whether a UIB was present (10 of 31 years; Figures 4.5b and C.4a, c, and e) or absent (21 of 31 years; Figures 4.5c and C.4b, d, and f). The years with UIBs had nearly five times more NPP in the UI period but less NPP in the MIZ (30.7% of non-UIB years) and OW periods (85.0% of non-UIB years; Table 4.7). Years that were categorized as having UIBs also had lower peak rates of NPP, less annual zooplankton grazing, and 7.2% higher annual water-column nitrification rates than years without UIBs. There were no significant differences in annual NPP, ice algal NPP, PON export to the benthos, sedimentary nitrification, or sedimentary denitrification between the two bloom patterns.

Environmental conditions determined whether a UIB was generated each year. While ice thickness did not significantly vary between the two bloom types, years with UIBs had thinner snow cover than years without UIBs (Table 4.7). Years characterized by moderate UIBs also had UI periods

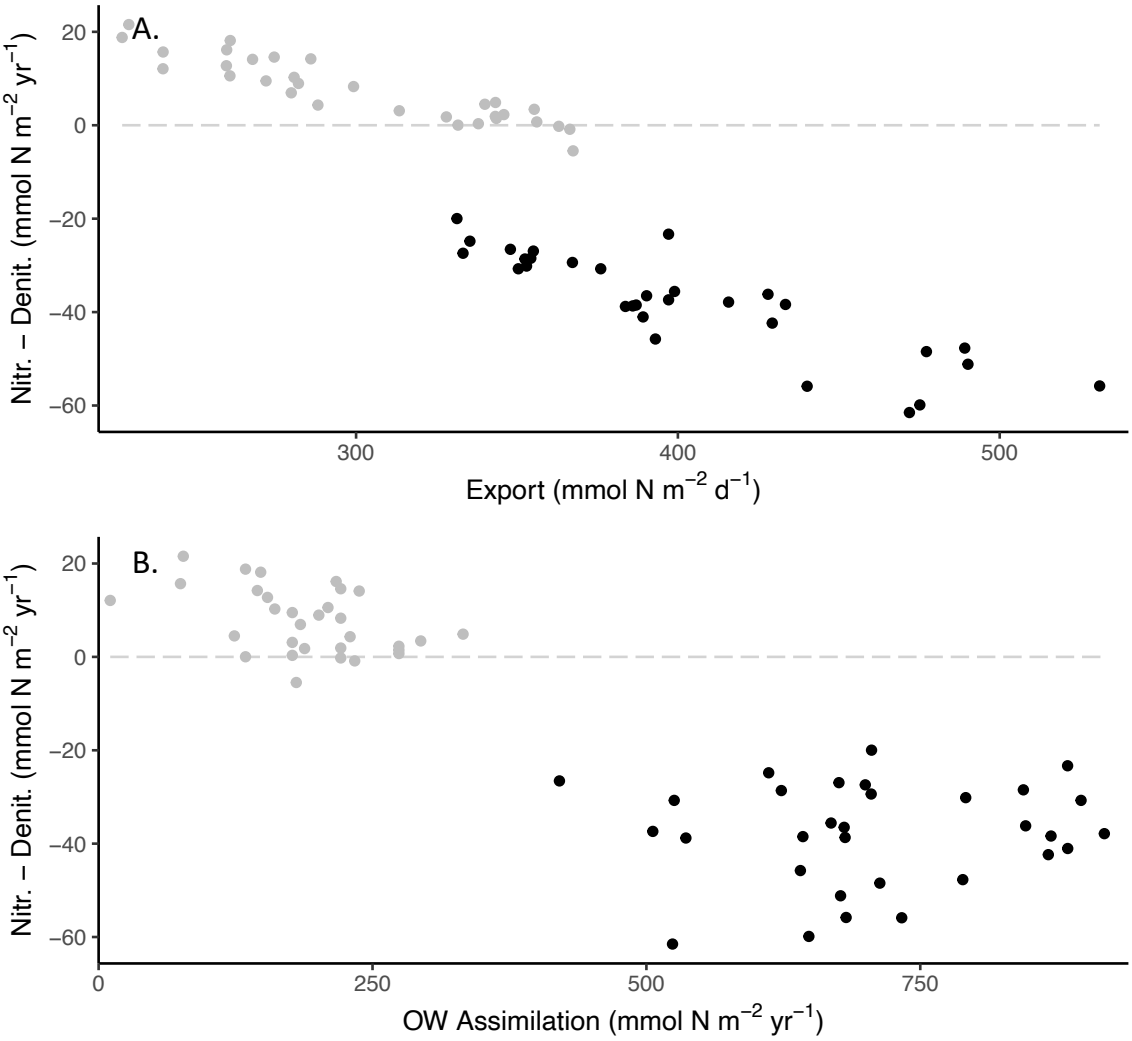

Figure 4.8: Scatterplots comparing the balance between nitrification and denitrification (mmol N m^{-2} yr^{-1}) to A) PON export (mmol m^{-2} yr^{-1}) and B) OW assimilation (mmol N m^{-2} yr^{-1}) for the northern (grey) and southern (black) Chukchi Sea.

Table 4.7: Differences in environmental drivers and consequences of water column bloom pattern in the southern Chukchi Sea. Averages (and standard deviations) are listed for years with and without UIBs, as well as p-values.

Variable	UIB years	Non-UIB years	P-value
Snow thickness (cm)	6.9±2.6	9.6±3.0	0.023
UI period (d)	42.0±6.2	21.1±10.7	<0.001
UI NPP (g C m^{-2} yr^{-1})	44.3±22.6	7.8±6.0	<0.001
MIZ NPP (g C m^{-2} yr^{-1})	9.6±4.5	31.3±14.6	<0.001
OW NPP (g C m^{-2} yr^{-1})	56.6±10.2	66.6±11.0	0.023
Peak Daily NPP (g C m^{-2} d^{-1})	3.9±0.6	6.0±2.7	0.021
Annual Grazing (g C m^{-2} yr^{-1})	16.9±3.1	20.2±2.0	<0.001
WC Nitrification (mmol N m^{-2} yr^{-1})	601.2±47.2	560.6±45.7	0.029

that ran nearly twice as long as years without UIBs, although the lengths of other periods (IA, MIZ, and OW periods) were not significantly different.

4.4 Discussion

4.4.1 Ice conditions and primary production

The southern Chukchi Sea, long observed to be dominated by thin first-year ice, is currently experiencing a five month-long ice-free period, an event that is not expected in the northern Chukchi Sea until 2040 (*Wang and Overland*, 2015). At present, sea ice retreats in the southern Chukchi Sea more than one month earlier and advances two weeks later than in the northern Chukchi Sea (*Serreze et al.*, 2016). While the resulting north-south gradient in sea ice concentration is certainly in part a function of latitudinal differences in solar forcing and air temperature, it is also driven by the increasing amount of heat transported through the Bering Strait (*Shimada et al.*, 2006; *Serreze et al.*, 2016; *Woodgate et al.*, 2012; *Woodgate*, 2018). Across the Chukchi Sea, 67% of the variance in the timing of both ice retreat and advance between 1979 and 2014 was explained by the amount of heat advected through the Bering Strait (*Serreze et al.*, 2016). These heat fluxes through the Bering Strait have increased substantially since the 1990s, driven by a 0.01 Sv yr^{-1} increase in the transport of Pacific waters into the Arctic Ocean (*Woodgate et al.*, 2012; *Woodgate*, 2018). These differences in the timing of sea ice advance and retreat between the northern and southern Chukchi are projected by CMIP models to extend through at least 2090, with the north remaining ice-covered two months longer than our model location in the south (*Wang and Overland*, 2015).

The differences in the timing of sea ice loss between the north and the south result in distinctly different growing conditions for sea ice microalgae and phytoplankton in the Chukchi Sea. The earliest source of NPP each year is sea ice microalgae (*Arrigo et al.*, 2017; *Fortier et al.*, 2002). As light increases in the late winter and early spring, microalgae suspended in the bottom 5-10 cm of

the sea ice are primed to take advantage of the high water-column NO_3^- concentrations (*Arrigo*, 2017; *Bradstreet and Cross*, 1982; *Fortier et al.*, 2002; *Gradinger*, 1996). Ice algal blooms can be generated more than one month earlier than water column blooms (*Payne et al.*, 2021) and provide a critical early burst of NPP to a pelagic ecosystem lacking in food sources (*Arrigo et al.*, 2017; *Assmy et al.*, 2013; *Bradstreet and Cross*, 1982; *Fortier et al.*, 2002; *Gradinger*, 2009; *Søreide et al.*, 2010). Ice algal NPP in our study averaged 3.0 g C m^{-2} yr^{-1} in the southern Chukchi Sea, in line with rates observed on other shallow Arctic continental shelves (*Arrigo*, 2017; *Dupont*, 2012; *Gosselin et al.*, 1997; *Gradinger*, 2009; *Jin et al.*, 2012). Further, this rate was significantly higher than in the north, driven by a three-week longer growing season.

As melt ponds form on the surface of sea ice in the Chukchi Sea, UI phytoplankton blooms can form a second pulse of NPP. Although the sea ice-covered period has historically been considered to be too light-limited to allow for significant phytoplankton growth (*Hameedi*, 1978; *Perrette et al.*, 2011), observations of massive under-ice phytoplankton blooms in the Chukchi Sea (*Arrigo et al.*, 2012, 2014; *Hill et al.*, 2018a; *Lowry et al.*, 2014) demonstrated that this period can contribute substantially to annual NPP. It has been estimated that, due to their inability to observe UIBs, satellite-derived NPP is underestimated by more than an order of magnitude in the northern Chukchi Sea (*Arrigo and Van Dijken*, 2011; *Arrigo et al.*, 2014). *In situ* observations of UIBs have demonstrated that this period can account for more than half of total NPP (*Arrigo et al.*, 2014; *Lowry et al.*, 2014; *Mayot et al.*, 2018; *Mundy et al.*, 2009; *Oziel et al.*, 2019), and modeling work by *Payne et al.* (2021) showed that in the north, the UI period accounted for nearly half of annual NPP and drove most of the interannual variability. However, the massive UIBs that can be supported in the northern Chukchi Sea appear in other modeling studies to not be reproduced uniformly across the Chukchi Sea. *Zhang et al.* (2015) found that while 46% of the Chukchi Sea supported UIBs between 1988 and 2013, massive UIBs covered only 8% of the area over the same period, and that these blooms were largely concentrated in the northern Chukchi Sea near the shelf break. Results from our southern location support this broader trend modeled across the Chukchi Sea - the earlier start of sea ice retreat and shorter UI period caused the UI period to only contribute 16% towards annual NPP. As a result, NPP during the MIZ and OW periods was much higher and annual NPP estimated by CAOS-GO was much more in line with satellite-derived (MODIS) estimates than in the north (with mean satellite-derived and modeled 2003-2018 NPP of 110.1±35.1 and 105.9±5.6 g C m^{-2} yr^{-1}, respectively; Figure C.3, *Lewis et al.*, 2020; *Lewis and Arrigo*, 2020).

Furthermore, we found that the contributions of the UI period to annual NPP was reduced by more than 20 g C m^{-2} between 1988 and 2018 in the southern Chukchi Sea, dropping in the last five years of our record to an average of 34% the annual NPP estimated in the first five years. A satellite-based analysis of the prevalence of UIBs and MIZ blooms throughout the Chukchi Sea similarly revealed that the area that likely supported UIBs shrunk between 1998 and 2012 (*Lowry et al.*, 2014), indicating that the shelf region as a whole may be seeing a reduction in the prevalence

of UIBs over time. As the Chukchi Sea is predicted to experience a continued decrease in sea ice coverage (*Wang and Overland*, 2015) and loss of multi-year ice (*Serreze and Stroeve*, 2015; *Serreze et al.*, 2016), the decreasing trend modeled here indicates that the UIBs that contribute so substantially to annual NPP in the northern Chukchi Sea (*Arrigo et al.*, 2012, 2014) may diminish in importance in the future. Model intercomparison work by *Jin et al.* (2016) indicates this may be an Arctic-wide trend. While all three models in their study found that an increase in open-water area is driving an Arctic-wide increase in NPP, the importance of UIBs differed spatially, with NPP during the UI period increasing in some regions due to the increase in light transmission into the ocean but diminishing in regions with high rates of sea ice loss.

The MIZ period has long been considered to be responsible for the highest rates of NPP and the largest contributor to annual NPP in Arctic waters (*Niebauer*, 1991; *Perrette et al.*, 2011; *Sakshaug*, 2004). However, our results suggest that this was not the case in the northern Chukchi Sea, where the MIZ contributed less to annual NPP than both the UI and OW periods because of both nutrient depletion in surface waters during the UI period and the short length of the MIZ period (*Payne et al.*, 2021). While the southern Chukchi Sea had an MIZ period that was, on average, 40% shorter than in the north, NPP during the MIZ period was not significantly different between the two regions. Instead, low NO_3^- utilization during the UI period in the south allowed for substantially higher rates of NPP in surface waters during the MIZ period. While there are no known *in situ* measurements of NPP during the MIZ period near the southern model location, observations at the beginning of the OW period during ICESCAPE 2011 indicate that phytoplankton biomass and NPP were highest in the top 20 m of the water column (*Arrigo et al.*, 2014). Similarly, several remote sensing studies (*Lowry et al.*, 2014; *Perrette et al.*, 2011) have observed MIZ blooms at our southern model location, indicating that NPP increased in the mixed layer following sea ice retreat. These observations, paired with our model results, indicate that the loss of sea ice in the early spring allows the MIZ period to contribute a disproportionate 22% towards annual NPP relative to its short duration (18 days) in the southern Chukchi Sea.

Because NPP during the UI and MIZ periods consumes most of the nutrients in the surface waters of the Chukchi Sea, NPP during the OW period is dominated by phytoplankton growing at the SCM (*Arrigo et al.*, 2014; *Brown et al.*, 2015a; *Hill and Cota*, 2005; *Martin et al.*, 2010). As the OW period throughout the Chukchi Sea has increased (by 37 days between 1998 and 2018), satellite-derived estimates of NPP in the Chukchi Sea have nearly doubled (*Lewis et al.*, 2020). While NPP during the OW period contributed minimally to total NPP (26%) in the northern Chukchi Sea, it generated more than half of the annual NPP in the south. The far larger OW blooms in the southern Chukchi Sea are expected to support much larger zooplankton populations than in the north. In both locations, zooplankton grazed more during the warmer waters of the OW period when growth was less constrained by cold temperatures (*Campbell et al.*, 2001; *Huntley and Lopez*, 1992; *Payne et al.*, 2021). However, the far higher rates of annual grazing in the south and the increase in grazing

over time indicate that the longer OW period and higher SSTs in the south (ric, 2019) might allow for richer pelagic ecosystems than in the northern location.

Although our model did not produce a change in NPP during the OW period at either location between 1988 and 2018, there was a 14.3 g C m^{-2} yr^{-1} decrease in NPP during September and October in the southern Chukchi Sea. Remote sensing studies of the Arctic Ocean (*Ardyna et al.* 2014) and of the Chukchi and Bering Seas (*Waga and Hirawake*, 2020) indicate that autumn blooms have increased in many sectors of the Arctic Ocean, including in the southern Chukchi Sea, between 1998 and 2017. However, these studies also demonstrate the patchy nature of autumn blooms, and both studies find a low incidence of autumn blooms at our model location. Our model results suggest that the lack of autumn blooms in some parts of the southern Chukchi Sea may be attributable to a greater degree of stratification than at similar latitudes in the Arctic. We found that, as SSTs increased over time at our southern location (*Osborne et al.*, 2018), rising to 11°C by 2018, the water column remained stratified until later in the year. This finding is supported by satellite observations - at our model location in the southern Chukchi Sea, SSTs have increased by an average of 1.7 °C in both October and November. Our model results indicate that this increased stratification could prevent the entrainment of deep NO_3^- into the upper water column in the autumn (see the depth vs. time plots for a year with and without an autumn bloom in Figure C.4a-d) and prevent the formation of autumn phytoplankton blooms. Due to the patchy nature of fall blooms, these model results may not be representative of the entire Chukchi shelf. However, they highlight that increasing SSTs may prevent mixing in the fall and may lead to a reduction in incidences of autumn blooms as the Arctic warms further in the future.

4.4.2 Particulate export and fixed N loss

Because of the shallow continental shelf and high rates of NP of the Chukchi Sea, particle export to the benthos can be substantial. In the northern Chukchi Sea, CAOS-GO produced an average POC export rate of 29.2±4.3 g C m^{-2} yr^{-1} between 1988 and 2018, similar to the Chukchi Sea-wide estimate of 29.7 g C m^{-2} yr^{-1} (*Chang and Devol*, 2009). Similarly, Chl *a* export rates derived from moorings deployed above the seafloor by *Lalande et al.* (2020); *Nishino et al.* (2016) compare favorably with modeled Chl *a* export rates to the benthos. For instance, in the northern Chukchi Sea, a mooring deployed at 37 m depth (8 m above the seafloor) observed a mean export rate of 3 to 5 mg Chl *a* m^{-2} d_{-1} during a UIB in June-July 2016, while CAOS-GO produced an export rate of 3 to 4.8 mg Chl *a* m^{-2} d^{-1} during this same period. In the southern Chukchi Sea, a mooring deployed by *Nishino et al.* (2016) between 2012 and 2014 captured a sudden increase in exported Chl *a* during the UI period in mid-May of 2013, peaking in mid-June, remaining high (1-15 mg Chl *a* m^{-3}) until mid-July, and finally dropping below 1 mg Chl *a* m^{-3} in mid-October. Similarly, CAOS-GO found that, at a depth of 45 m, Chl *a* began to rapidly increase on 15 May and peaked on 9 June 2013. Following a bloom of 3 weeks, Chl *a* remained elevated until the beginning of July,

when it diminished to around 1 mg Chl *a* until late September, when Chl *a* concentrations started to drop. While the phenology of exported Chl *a* between the mooring and our model are in good agreement, the magnitude of the bloom observed by the fluorometer on the *Nishino et al.* (2016) mooring near the end of its 10 month long deployment was substantially larger, reaching as high as 30 mg Chl *a* m^{-3}.

The amount of NPP produced during the four distinct microalgal bloom periods has important consequences on the regional N cycle of the Chukchi Sea. High rates of NPP provide more biomass for export to the benthos, which on the Chukchi shelf is associated with a loss of fixed N through coupled partial nitrification-denitrification (*Brown et al.*, 2015a). The Chukchi Sea accounts for a disproportionately large amount of global N loss in the oceans as a result of its high export production and shallow continental shelf (*Chang and Devol*, 2009). While observational studies have yet to compare denitrification rates near our model locations, limited *in situ* observations indicate that sedimentary oxygen utilization in the south is twice as high as in north (*Granger et al.* 2018; *Grebmeier*, 2012; *Reeve et al.*, 2019), which is evidence of enhanced supply of C and N to the benthos and higher denitrification in the south. Consistent with these observations, we found that the south featured higher rates of PON export to the benthos than the north, contributing to a nearly 50% higher loss of fixed N through denitrification in the south. Further, we found that denitrification outweighed nitrification in the sediments of the southern Chukchi Sea. Our model found that the balance between nitrification and denitrification was controlled by the phenology of NPP and the rate of PON export to the benthos, with years with more NPP later in the year and higher total PON export seeing more denitrification than nitrification. While no studies that we are aware of have captured the annually-integrated balance between sedimentary nitrification and denitrification, this finding highlights that, because denitrification can use NO_3^- diffused across the sediment-water boundary, denitrification rates can exceed the supply of NO_3^- produced locally in the sediments through nitrification.

More importantly, our results demonstrate that the drivers of interannual variation in the N cycle differ substantially between the northern and the southern Chukchi Sea. In the north, the UI period dominated annual production in most years (17 of 31), with an average of 65% of annual NPP generated during the UI period in those years. UI-dominated years had 16% higher annual NPP, 28% more PON export to the benthos, 20% more sedimentary nitrification, and 30% more denitrification than in years with more MIZ production (*Payne et al.*, 2021; *Payne and Arrigo*, 2022). However, in the south, only 10 years featured moderate UIBs, and even in those years, the OW period contributed more to annual NPP. Instead, NPP during the far-longer OW period (∼5 months) drove the much higher rates of annual NPP, PON export to the benthos, and sedimentary nitrification and denitrification observed in the south. Moreover, while annual NPP, PON export to the benthos, and sedimentary nitrification and denitrification all decreased over time in the northern Chukchi Sea, there were no secular changes between 1988 and 2018 in the south. Instead,

interannual variation in PON export to the benthos and sedimentary nitrification and denitrification were driven by a decline in NPP in the autumn (September and October) as a result of enhanced autumn stratification between 1988 and 2018.

4.4.3 The Future Chukchi Sea

Both the trends in sea ice cover observed over the past 40 years (*Kwok*, 2018; *Lewis et al.*, 2020; *Serreze and Stroeve*, 2015; *Serreze et al.*, 2016) and modeling studies (*Wang and Overland*, 2015) indicate that the Arctic Ocean is shifting to a state more like the southern Chukchi Sea of today, with thin, first-year ice that melts early, allowing a long OW period each summer. Pan-Arctic modeling studies indicate that thus far, a longer OW period has corresponded to an increase in NPP (*Clement Kinney et al.*, 2020; *Jin et al.*, 2016; *Zhang et al.*, 2015). As the Chukchi Sea experiences a longer OW period, our results indicate that annual NPP in the north could increase by over 25%, which could result in ∼50% more sedimentary denitrification. Even though the Chukchi Sea has historically been responsible for 1-3% of the global loss of fixed N in the oceans (*Chang and Devol*, 2009), our results indicate that a transition to a much longer ice-free period in the region will increase the rate of denitrification in the sediments, resulting in a greater loss of fixed N. As larger phytoplankton blooms take up a greater proportion of the available NO_3^- in the Chukchi Sea, the amount of NO_3^- available in N-limited waters downstream will be reduced (*Arrigo and Van Dijken*, 2015). This may already be happening; satellite analysis revealed that in years following unusually high NPP in the Chukchi Sea, there was a significant reduction in NPP downstream in the Greenland Sea (*Arrigo and Van Dijken*, 2015).

A reduction in the NPP of ecosystems downstream of the Chukchi Sea could reduce the abundance of zooplankton, fish, marine mammals, and seabirds that rely on phytoplankton blooms as a food source (*Hamilton et al.*, 2021; *Joiris*, 2011; *Munk*, 2003; *Rysgaard et al.*, 1999). Additionally, increasing N removal through denitrification in the Chukchi Sea would exacerbate the low ratio of available N:P (phosphorus) found on the Chukchi shelf (*Deutsch and Weber*, 2012; *Devol et al.*, 1997; *Gruber and Sarmiento*, 1997; *Mills et al.*, 2015). The Chukchi shelf currently contains some of the world's lowest values of N^* (a measure of excess N relative to phosphorus; *Gruber and Sarmiento*, 1997) in the global ocean (*Deutsch and Weber*, 2012). *Yamamoto-Kawai et al.* (2006) found that high rates of N_2 fixation in the surface waters of the North Atlantic were stimulated by the lower N:P ratios emanating from upstream in the Chukchi Sea, indicating that higher rates of NPP and greater denitrification in the future might further increase rates of N_2 fixation in waters downstream of the Chukchi Sea. Finally, there is increasing evidence that low N^* values may even stimulate N_2 fixation in the Arctic Ocean (*Blais et al.*, 2012; *Díez et al.*, 2012; *Fernández-Méndez et al.*, 2016; *Moisander et al.*, 2010; *Mulholland et al.*, 2012; *Tremblay and Gagnon*, 2009). Although data are sparse, *Sipler et al.* (2017) found that rates of N_2 fixation in the Arctic Ocean may currently offset up to 27% of the N deficit driven by denitrification in Arctic sediments.

While our results demonstrate that a shift towards a longer, more productive OW season could enhance denitrification, they also highlight that the UI period may not remain dominant in the northern Chukchi Sea in the future. Modeling efforts to assess the importance of UIBs have demonstrated that these blooms have increased in magnitude in the northern Chukchi Sea by 2% per year between 1988 and 2013 (*Zhang et al.*, 2015) and by over 5% per year between 1980 and 2018 in the central Arctic (*Clement Kinney et al.*, 2020). The radiative transfer model of *Horvat et al.* (2017) further indicates that between 2006 and 2015, 30% of the Arctic Ocean received sufficient light to allow for under-ice phytoplankton growth for at least three days in July. However, in comparing three other models, *Jin et al.* (2016) found that the proportion of NPP generated in UIBs diminished between 1980 and 2009 on a pan-Arctic scale due to declines in sea ice cover over this period, suggesting a shift towards more Subarctic ecosystems. The impacts of a shift away from UIBs would likely be substantial. When these massive blooms are generated, they can strip the surface ocean of nutrients at a time when water temperatures are below -1.5°C (*Arrigo et al.* 2012, 2014) and when zooplankton grazing is minimal (*Campbell et al.*, 2001; *Huntley and Lopez*, 1992; *Payne et al.*, 2021). This may substantially reduce pelagic food availability for the fish, birds, and mammals that feed in the Chukchi Sea (*Bradstreet and Cross* 1982; *Loeng et al.*, 2005) while simultaneously increasing benthic-pelagic coupling, benthic production, and enhancing sedimentary denitrification and fixed N loss. However, the waning magnitude of UIBs in the south suggests that these blooms may only affect the biogeochemistry the Chukchi Sea and downstream waters for a few more decades.

4.5 Acknowledgements

The authors would like to thank Matthew Mills and Stephanie Lim for providing input on analysis. All model input and output data are available at https://purl.stanford.edu/nz800dp6262.

Chapter 5

Pan-Arctic analysis of the frequency of under-ice phytoplankton blooms, 2003-2021

Courtney M. Payne, Gert L. van Dijken, Kevin R. Arrigo

A peer reviewed version of this chapter was published in AGU in the *Journal of Geophysical Research: Oceans*. To view the published open abstract: https://doi.org/10.1029/2022JC018431

Department of Earth System Science, Stanford University, Stanford, California, USA

Under-ice (UI) phytoplankton blooms have been observed in most of the marginal seas of the Arctic Ocean and are often found to contribute substantially to total primary production. However, because remote sensing studies cannot directly measure UI blooms and limited in situ observations prevent analysis of their frequency across the region as a whole, their distribution has not previously been characterized across the Arctic Ocean. Here, we use remote sensing data to discern which parts of the Arctic Ocean demonstrate evidence of UI blooms and whether UI bloom frequency changed between 2003 and 2021. Results suggest that UI blooms were generated nearly as frequently as marginal ice zone (MIZ) blooms, with evidence of UI blooms over nearly 40% of the observable seasonally ice-free Arctic Ocean while MIZ blooms covered 60% in any given year. However, while there was no significant change in the UI bloom area over the study period, there was a nearly 10% decline in the proportion of UI area in the seasonal sea ice zone. This decline was driven largely by declines in the Chukchi

Sea, where UI blooms were also most prevalent. Our analysis demonstrates the need for increased observational studies of UI blooms and their ecological and biogeochemical consequences throughout the Arctic Ocean.

5.1 Introduction

Historically, phytoplankton in the Arctic Ocean were presumed to contribute to total annual net primary production (NPP) only after sea ice retreat, when shallow mixed layers and the alleviation of light limitation allowed blooms to form (*Niebauer*, 1991; *Perrette et al.*, 2011; *Sakshaug and Skjoldal*, 1989). These marginal ice zone (MIZ) blooms, which could rapidly strip surface waters of macronutrients (*Niebauer*, 1991), accounted for up to 65% of annual NPP in the Barents Sea and on the Bering Shelf (*Sakshaug*, 2004). However, observations of a massive phytoplankton bloom generated under fully consolidated 1 m thick first-year ice (*Arrigo et al.*, 2012) demonstrated that phytoplankton NPP could be substantial during the sea ice-covered portion of the year. These under-ice (UI) phytoplankton blooms have been observed in most of the Arctic and sub-Arctic seas (*Arrigo et al.*, 2014; *Assmy et al.*, 2017; *Hill et al.*, 2018a; *Lalande et al.*, 2014; *Mayot et al.*, 2018; *Mundy et al.*, 2014; *Oziel et al.*, 2019) since at least the late 1950s (*Apollonio*, 1959; *Apollonio and Matrai*, 2011; *Fortier et al.*, 2002; *Gosselin et al.*, 1997; *Mundy et al.*, 2009; *Strass and Nöthig*, 1996; *Yager et al.*, 2001). UI blooms can substantially contribute to total NPP, accounting for ∼50% of total annual NPP in the Canadian Arctic (*Mundy et al.*, 2009; *Oziel et al.*, 2019) and in the Chukchi (*Arrigo et al.*, 2014) and Greenland (*Mayot et al.*, 2018) seas. Further, these UI blooms likely have large biogeochemical implications, including reducing zooplankton grazing (*Payne et al.*, 2021), which in turn leads to an increase in carbon export flux and nitrogen (N) loss through sedimentary denitrification (*Payne and Arrigo*, 2022).

Quantifying NPP during the UI period, as well as identifying where in the Arctic Ocean these blooms are generated and how their frequency has changed over time, is critical to understanding how Arctic phytoplankton are responding to the rapid changes to the Arctic environment (*Ardyna and Arrigo*, 2020). A study modeling light penetration through sea ice (*Horvat et al.*, 2017) suggested that, due to diminishing sea ice thickness across the Arctic (*Kwok*, 2018), under-ice light has substantially increased, possibly leading to an increase in UI bloom frequency over time. Modeling work by *Clement Kinney et al.* (2020) similarly indicated that in the Central Arctic, half of all NPP is generated in sea ice-covered waters, and that regional NPP has increased by 20% since 1980. However, modeling work in the southern Chukchi Sea (*Payne et al.*, 2022) and across the entirety of the Arctic Ocean (*Jin et al.*, 2016) indicates that increasingly early sea ice loss has led to a reduction in the magnitude of NPP during the UI period.

Because efforts to quantify total annual NPP using satellite remote sensing cannot capture NPP generated under sea ice, remote sensing estimates can differ from observational estimates of NPP

by an order of magnitude in areas with large UI blooms (*Arrigo et al.*, 2014). However, *Lowry et al.* (2014) used daily chlorophyll *a* (Chl) concentrations around the time of sea ice retreat to identify parts of the Chukchi Sea that likely hosted UI blooms between 1998 and 2012. *Lowry et al.* (2014) relied on a conceptual model that assumed that if Chl concentrations increased after sea ice retreat, this was evidence of the alleviation of light limitation and thus an MIZ bloom (Figure 5.1, yellow line). If, however, Chl concentrations were initially high but diminished following sea ice retreat (due presumably to nutrient exhaustion during the UI period), this was evidence of a previous UI bloom (Figure 5.1, green line). Here, we present work extending the conceptual model of *Lowry et al.* (2014) from the Chukchi Sea to the entire Arctic Ocean (Figure 5.2a). We quantify how prevalent UI and MIZ blooms are across the Arctic, identify regions that support the highest proportion of UI blooms, and assess whether there has been a change in the prevalence of UI blooms over time.

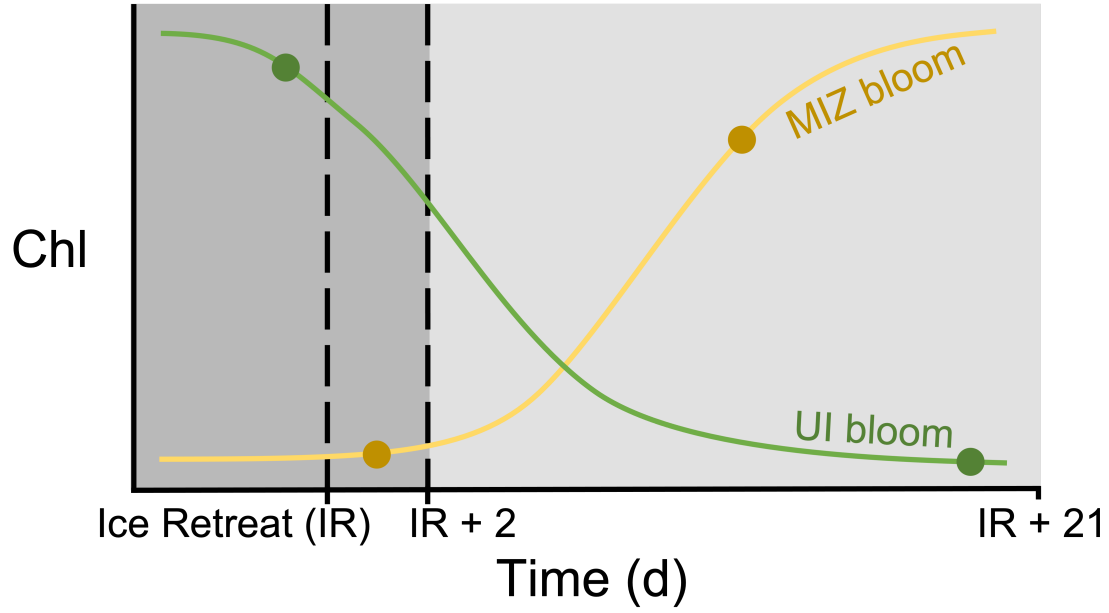

Figure 5.1: **Conceptual diagram for identifying UI and MIZ blooms. Chl retrievals for each pixel around the time of ice retreat (when ice concentration diminished below 10%) were classified as indicating a UI (green) or an MIZ bloom (yellow).**

5.2 Methods

5.2.1 Remote Sensing Data

Daily sea ice concentration was generated from the Climate Data Record (CDR) of sea ice concentration from passive microwave data (version 4.0; *Meier et al.* 2021) provided by the National

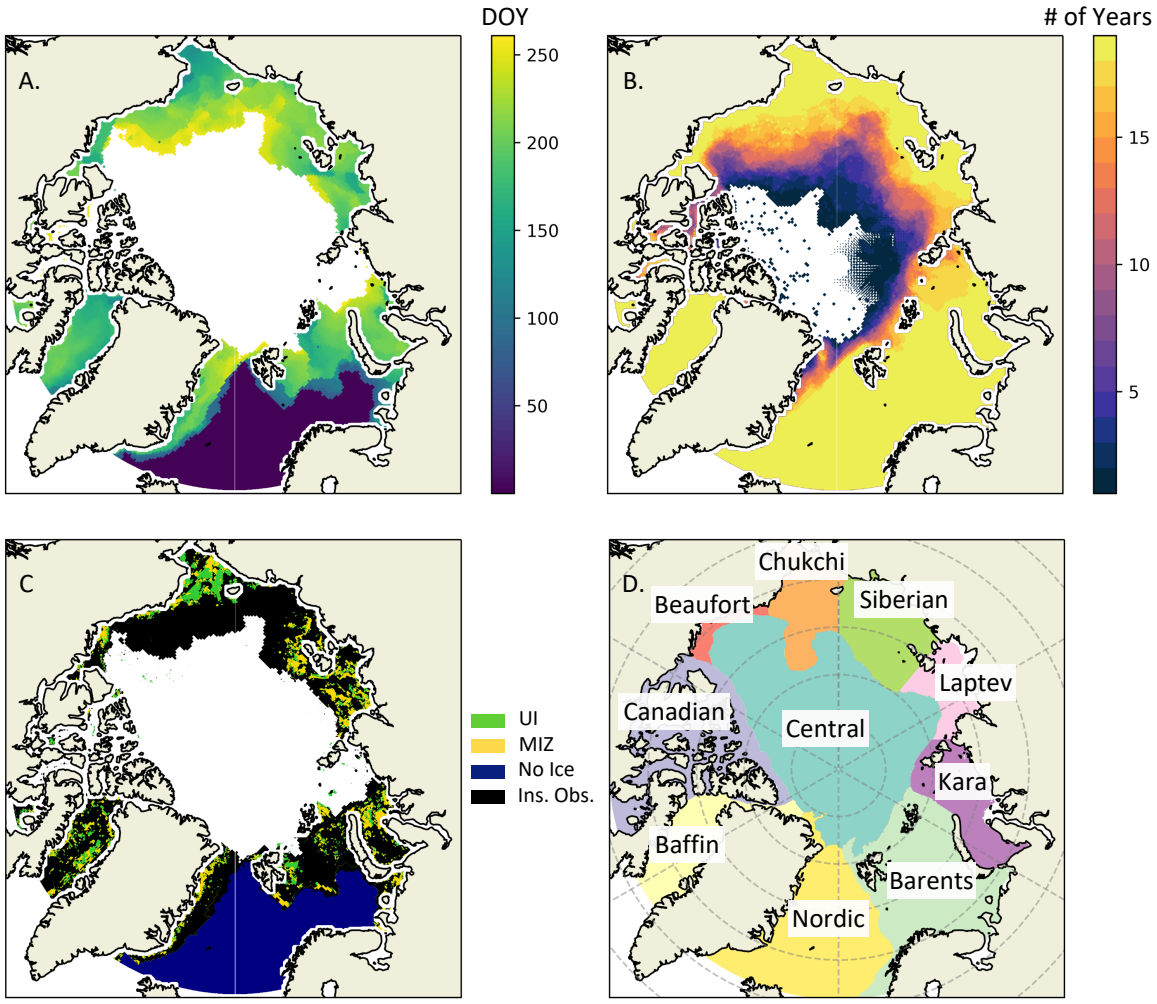

Figure 5.2: **Examples of sea ice retreat and bloom classification, 2003.(A) Arctic Ocean regions used for regional analysis, with 5° latitude bands and 60° longitude bands demarcated using dashed gray lines. Only the area north of the Arctic Circle (66.5°N) was analyzed. (B) Day of Year (DOY) of sea ice retreat (10% sea ice concentration threshold) for 2003. (C) UI bloom (green), MIZ bloom (yellow), and no ice cover (navy) pixels were separated from pixels with insufficient observations ('Ins. Obs'; black) for 2003. (D) OW bloom (blue) pixels were separated from pixels that did not support OW blooms (Not OW; grey) for 2003.**

Snow and Ice Data Center (NSIDC) in the polar stereographic projection (25 km resolution) for 1998-2021. These data were subsequently regridded to 4 km resolution to allow comparison with Chl data.

Daily Chl concentrations (4 km resolution) were generated from satellite retrievals of remote sensing reflectance (R_{RS}) using the Arctic Ocean-specific algorithm of *Lewis and Arrigo* (2020). This algorithm, developed using 501 coincident *in situ* measurements from 25 cruises, better accounts for the unique bio-optical properties of Arctic waters than the standard empirical NASA-Chl algorithm, such as greater pigment packaging and higher chromophoric dissolved organic matter concentrations (CDOM; *Ben Mustapha et al.*, 2012; *Huot et al.*, 2013; *Fichot et al.*, 2013; *Matsuoka et al.*, 2007, 2011, 2017). Daily Level 3 binned R_{RS} data were acquired from the NASA Ocean Color website (`https://oceancolor.gsfc.nasa.gov/`) from MODIS-Aqua for the years 2003-2021 (Reprocessing R2018.0). Pixels outside of the Arctic Circle (<66.5°N) were excluded from analysis, as were pixels within 50 km of the coast.

5.2.2 Pixel Classification, Analysis, and Statistics

For each year from 2003 to 2021, each pixel in the Arctic Ocean (Figure 5.2a) was classified as being ice free or as experiencing either a UI or MIZ bloom based on Chl observations near the time of sea ice retreat. If sea ice concentration was below 10% on the date of maximum sea ice extent for the Arctic Ocean for that year, the pixel was considered ice free. If sea ice concentration was greater than 10%, we calculated the date of sea ice retreat by finding the first date when sea ice concentration diminished below 10% for any given pixel (Figure 5.2b). We then computed the maximum Chl concentration over two separate periods in the weeks surrounding sea ice retreat. Period one extended from the first Chl observation at that pixel until 2 days after the date of sea ice retreat. Period two extended from 3 to 21 days after sea ice retreat (Figure 5.1). If sea ice never diminished below the sea ice retreat threshold but there was at least one Chl retrieval, the pixel was considered to have experienced a UI bloom. Pixels were also considered to host a UI bloom if the maximum Chl concentration during period one exceeded the maximum Chl concentration observed during period two. The pixel was classified as hosting an MIZ bloom if the maximum Chl concentration was higher during period two than period one (Figure 5.1). If there were not at least one Chl observation in each of these periods, the pixel was considered to have insufficient observations to classify it as hosting either an MIZ or UI bloom. To estimate the areal coverage of UI and MIZ blooms by region and for the Arctic Ocean as a whole, we assumed that the relative frequency of UI and MIZ blooms observed in each region would be maintained across the pixels with insufficient observations to be classified.

This technique of classifying pixels relies on a comparison of Chl concentration from a minimum of two Chl retrievals. When Chl concentrations for those retrievals are similar (0-1 mg Chl m^{-3} difference between periods one and two), there is a potential to mis-classify blooms. However, we

found that the number of pixels where the difference between the Chl retrievals was <1 mg Chl m^{-3} was approximately equal for pixels classified as MIZ and UI blooms, indicating that mis-classification should affect both blooms equally. Further, this analysis does not rely on a Chl threshold to classify Chl observations as UI or MIZ blooms. UI blooms can generate high biomass in surface waters, but due to nutrient depletion, surface Chl can diminish substantially by the time of sea ice retreat (*Arrigo et al.*, 2014; *Brown et al.*, 2015b), meaning that satellite-derived Chl concentrations in the days surrounding sea ice retreat may not be reflective of the original magnitude of the bloom. A previous study by *Lowry et al.* (2014) that relied upon a Chl threshold of 2.5 mg m^{-3} found that most pixels (59.9%) never reached the Chl threshold in the weeks surrounding sea ice retreat, and we consequently decided against applying a Chl threshold to identify UI blooms.

In addition to classifying the area that supported UI and MIZ blooms, we quantified the area that supported open water (OW) blooms. We considered a pixel to have generated an OW bloom if Chl exceeded 1 mg m^{-2} in the period from 22 days after ice retreat until the sea ice minimum extent day in any given year. Because UI blooms can substantially deplete the nutrients in surface waters prior to sea ice retreat, Chl concentrations at the time of sea ice retreat should not be compared to the maximum Chl concentration reached over the OW period. Consequently, we evaluated whether any given pixel supported an MIZ or UI bloom around the time of sea ice retreat and separately evaluated whether it supported an OW bloom later in the year (>22 days after retreat).

Following classification (Figure 5.2c and d), pixels in each category were summed spatially over different areas of interest, including the entire Arctic Ocean, ten geographic regions (Figure 5.2a), 5° latitudinal bands, and within geographic regions by 5° latitude band. We used linear regression to assess trends in the absolute area or proportion of total area classified as one of the three categories between 2003 and 2021. A significance threshold of $p<0.05$ was used for the statistical tests presented in this study. All analyses were conducted in Python version 3.8.8.

Additionally, we evaluated how sensitive our analysis was to two parameters: the sea ice retreat concentration threshold (10% in the primary analysis) and the length of time between ice retreat and the end of period one (2 d in the primary analysis). We ran our bloom classification analysis using four different sea ice retreat concentration thresholds (50%, 25%, 15%, and 10%) with three distinct definitions of the end of period one (ice retreat + 2 d, 4 d, and 6 d). For each of these 12 runs, we compared the average areal coverage and trends over the time series across the Arctic for the MIZ and UI bloom categories.

5.3 Results

5.3.1 Pan-Arctic trends

Excluding areas within 50 km of the coastline, the Arctic Ocean covers an area of 1.1×10^7 km^2. Between 2003 and 2021, we analyzed a mean of 7.5×10^6 km^2 of the Arctic Ocean because the

remainder was covered in sea ice year-round. As sea ice retreated over a larger area over time, our area of analysis increased by 7.4×10^3 km^2 yr^{-1} (R^2=0.692, p<0.001). However, the presence of sea ice and cloud cover prevented the analysis of an average of 3.9×10^6 km^2 (Figure 5.2c, black area). Consequently, our analysis was based on the 3.5×10^6 km^2 of the Arctic Ocean that was classifiable as being ice free or as supporting UI or MIZ blooms, and the size of this classifiable region did not change between 2003 and 2021 across the Arctic Ocean as a whole. Each year, an average of 2.2×10^6 km^2 of the Arctic Ocean was classified as being ice free (or 62.9±3.1% of the classifiable area; Figures 5.4c and 5.3), and this area increased over time by 2.7×10^4 km^2 yr^{-1} (R^2=0.345, p=0.008). A further 8.0×10^5 km^2 of Arctic surface waters experienced MIZ blooms (covering 22.3±2.0% of the classifiable area; Figure 5.4b), and these blooms did not change significantly by proportion or areal coverage between 2003 and 2021 (Figure 5.3). Finally, an area of 5.0×10^5 km^2 supported UI blooms (covering 14.3±2.3% of the classifiable area, Figure 5.4a). While there was no significant change in the area supporting a UI bloom in any year, there was a 0.3% yr^{-1} decline in the relative proportion of UI bloom area as a function of total classifiable area between 2003 and 2021 (R^2=0.381, p=0.005; Figure 5.3). On average, MIZ and UI blooms covered 61.6% and 38.4%, respectively, of the classifiable seasonally ice-free portion of the Arctic Ocean. UI blooms also declined proportionally within the classifiable seasonally ice-free Arctic, declining from 43.4% coverage in 2003 to 32.2% by 2021 (-0.5% yr^{-1}, R^2=0.419, p=0.003).

OW blooms covered 2.5×10^6 km^2 (Figure 5.4d) and they increased their areal coverage by 5.2×10^4 km^2 yr^{-1} (R^2=0.752, p<0.001). OW blooms were rarely generated in areas that had insufficient observations during the sea ice retreat period, covering only 12.0% of the insufficiently observed area. Regions that supported UI and MIZ blooms infrequently went on to generate OW blooms, which covered a mere 18.8% of UI bloom area and only 25.9% of MIZ bloom area. However, OW blooms were commonly generated in regions that were always ice free and covered 77.7% of the ice free region, on average.

5.3.2 Trends by Latitude

At the most southerly latitude band of 66.5-70°N (9.0×10^5 km^2 classifiable area), ice free waters were most common, covering 75.1% of the total classifiable area (Figure 5.5a). An increase in classifiable area between 2003 and 2021 was largely driven by a sizable increase in ice free area between 2003 and 2021 (Table 5.1). UI blooms accounted for an average of 10.7% of the classifiable area in this latitude band, but these blooms declined by both proportion and area (Table 5.1). MIZ blooms, which covered 14.0% of the classifiable area between 66.5 and 70°N, did not change significantly between 2003 and 2021.

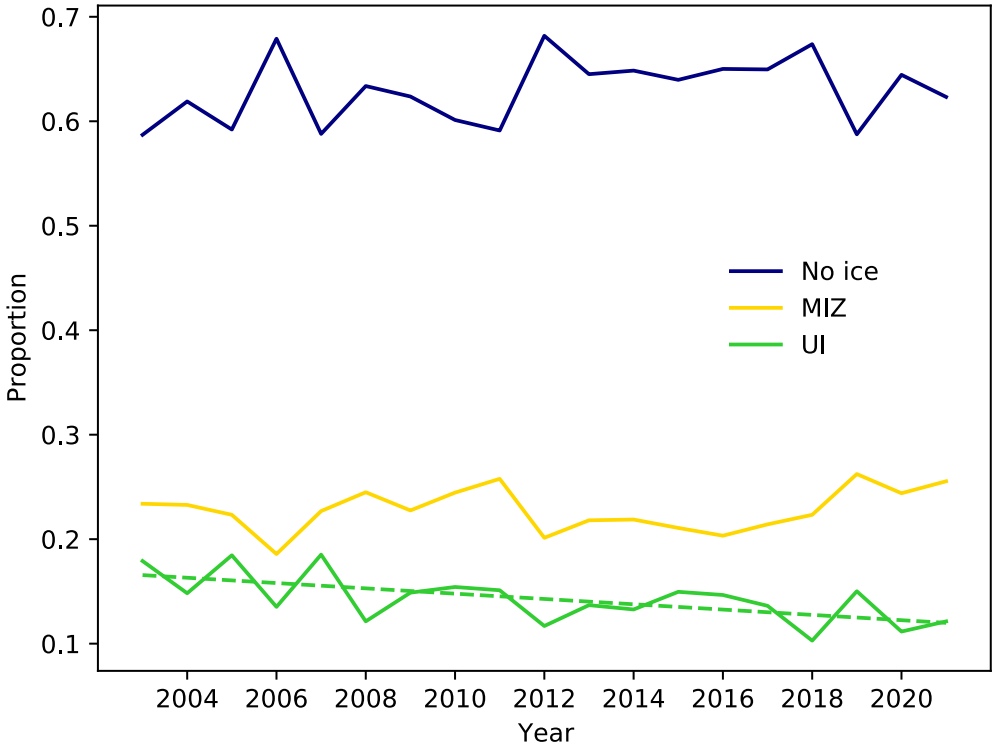

Figure 5.3: **Trends in the proportion of ice-free, UI bloom, and MIZ bloom area for the Arctic Ocean, 2003-2021.** Dashed lines indicate significant trends.

Table 5.1: **Significant trends in total classifiable area or trends in UI, MIZ, or Ice Free area or proportional coverage for regions and latitude bands between 2003 and 2021.**

Location	Class	Slope	R^2	*p*-value
66.5-70°N	Classifiable	2.1×10^3 km^2 yr^{-1}	0.210	0.049
66.5-70°N	Ice Free	2.8×10^3 km^2 yr^{-1}	0.317	0.012
66.5-70°N	UI	-0.2% yr^{-1}	0.288	0.018
66.5-70°N	UI	-1.7×10^3 km^2 yr^{-1}	0.238	0.034
70-75°N	Ice Free	7.6×10^3 km^2 yr^{-1}	0.280	0.020
75-80°N	MIZ	5.1×10^3 km^2 yr^{-1}	0.241	0.047
75-80°N	UI	-0.4% yr^{-1}	0.365	0.006
80-85°N	Classifiable	2.4×10^3 km^2 yr^{-1}	0.227	0.039
80-85°N	UI	-0.4% yr^{-1}	0.365	0.006
Central	Classifiable	1.6×10^4 km^2 yr^{-1}	0.259	0.003

Central	UI	-1.2 yr^{-1}	0.249	0.030
Central, 75-80°N	Classifiable	2.2×10^3 km^2 yr^{-1}	0.289	0.017
Central, 75-80°N	MIZ	1.7×10^3 km^2 yr^{-1}	0.278	0.020
Baffin	MIZ	0.7% yr^{-1}	0.277	0.021
Baffin	UI	-0.5% yr^{-1}	0.245	0.031
Baffin, 75-80°N	MIZ	1.6% yr^{-1}	0.396	0.004
Baffin, 75-80°N	UI	-1.6% yr^{-1}	0.396	0.004
Baffin, 75-80°N	UI	-8.0×10^2 km^2 yr^{-1}	0.403	0.003
Chukchi	MIZ	1.1% yr^{-1}	0.379	0.005
Chukchi	UI	-1.1% yr^{-1}	0.381	0.005
Chukchi	UI	-3.3×10^3 km^2 yr^{-1}	0.260	0.026
Chukchi, 66.5-70°N	MIZ	1.2% yr^{-1}	0.274	0.022
Chukchi, 66.5-70°N	UI	-1.2% yr^{-1}	0.274	0.022
Chukchi, 66.5-70°N	UI	-1.3×10^3 km^2 yr^{-1}	0.213	0.047
Chukchi, 70-75°N	UI	-1.3% yr^{-1}	0.320	0.012
Laptev	Classifiable	5.0×10^3 km^2 yr^{-1}	0.271	0.022
Laptev	MIZ	0.7% yr^{-1}	0.234	0.036
Laptev	UI	-0.7% yr^{-1}	0.234	0.036
Laptev, 70-75°N	Classifiable	4.8×10^3 km^2 yr^{-1}	0.282	0.019
Laptev, 70-75°N	MIZ	0.9% yr^{-1}	0.308	0.014
Laptev, 70-75°N	UI	-0.9% yr^{-1}	0.308	0.014
Laptev, 70-75°N	UI	-5.6×10^2 km^2 yr^{-1}	0.255	0.027
Laptev, 75-80°N	MIZ	2.9×10^3 km^2 yr^{-1}	0.227	0.004
Kara	Classifiable	7.1×10^3 km^2 yr^{-1}	0.483	0.012
Kara, 80-85°N	Classifiable	2.4×10^3 km^2 yr^{-1}	0.529	<0.001
Kara, 80-85°N	MIZ	2.0% yr^{-1}	0.254	0.028
Kara, 80-85°N	MIZ	4.0×10^2 km^2 yr^{-1}	0.483	<0.001
Kara, 80-85°N	UI	-2.0% yr^{-1}	0.254	0.028
Barents, 66.5-70°N	Classifiable	5.2×10^2 km^2 yr^{-1}	0.211	0.048
Barents, 70-75°N	Classifiable	3.3×10^3 km^2 yr^{-1}	0.221	0.042
Barents, 80-85°N	Classifiable	1.4×10^3 km^2 yr^{-1}	0.362	0.006
Barents, 80-85°N	UI	-2.1% yr^{-1}	0.238	0.034
Nordic	Ice Free	0.2% yr^{-1}	0.440	0.002
Nordic	Ice Free	7.3×10^5 km^2 yr^{-1}	0.412	0.003
Nordic	MIZ	-0.1% yr^{-1}	0.224	0.041
Nordic	UI	-0.1% yr^{-1}	0.412	0.003
Nordic	UI	-1.5×10^3 km^2 yr^{-1}	0.382	0.005

Nordic, 66.5-70°N	Ice Free	0.2% yr^{-1}	0.402	0.003
Nordic, 66.5-70°N	Ice Free	3.1×10^3 km^2 yr^{-1}	0.286	0.018
Nordic, 66.5-70°N	MIZ	-0.1% yr^{-1}	0.310	0.013
Nordic, 66.5-70°N	MIZ	-5.8×10^2 km^2 yr^{-1}	0.286	0.018
Nordic, 66.5-70°N	UI	-0.1% yr^{-1}	0.305	0.014
Nordic, 66.5-70°N	UI	-3.8×10^2 km^2 yr^{-1}	0.307	0.014
Nordic, 70-75°N	Classifiable	3.2×10^3 km^2 yr^{-1}	0.250	0.029
Nordic, 70-75°N	Ice Free	0.2% yr^{-1}	0.311	0.013
Nordic, 70-75°N	Ice Free	4.1×10^3 km^2 yr^{-1}	0.319	0.012
Nordic, 70-75°N	MIZ	-0.2% yr^{-1}	0.305	0.014
Nordic, 70-75°N	MIZ	-8.0×10^2 km^2 yr^{-1}	0.258	0.026
Nordic, 75-80°N	UI	-0.3% yr^{-1}	0.280	0.020
Nordic, 75-80°N	UI	-7.0×10^2 km^2 yr^{-1}	0.242	0.032
Nordic, 80-85°N	Classifiable	4.0×10^2 km^2 yr^{-1}	0.281	0.020
Nordic, 80-85°N	UI	-3.3×10^2 km^2 yr^{-1}	0.367	0.006

For the 70-75°N latitude band (1.8×10^6 km^2 classifiable area, or twice the size of the next largest latitude band), most of the classifiable area (65.7%) was ice free (Figure 5.5b). MIZ and UI blooms were proportionally higher than to the south, covering 21.1% and 13.3% of the classifiable area, respectively. Over this latitude band, ice-free area increased its areal coverage between 2003 and 2021 (Table 4.4).

Between 75 and 80°N (7.7×10^5 km^2 classifiable area), ice free area still dominated, covering 46.3% of the classifiable area (Figure 5.5c). MIZ blooms, however, covered a larger proportion of the classifiable area than at lower latitudes, accounting for 35.7% of classifiable area, and their areal coverage increased over time (Table 5.1). Meanwhile, UI blooms, which covered an average of 18.1% of classifiable area, declined by 7.6% between 2003 and 2021 (Table 5.1).

The northernmost latitude band, from 80-85°N, had a far smaller classifiable area (only 6.1×10^4 km^2 on average) than more southerly latitudes due to greater sea ice coverage. The classifiable area nearly doubled over time at this latitude band (Table 5.1) as sea ice retreated at higher latitudes. UI blooms covered an average of 51.3% of the classifiable area (Figure 5.5d), but because UI bloom area did not change over time as classifiable area expanded, there was a decline in UI bloom area between 2003 and 2021 (Table 5.1). MIZ blooms accounted for 38.5% of classifiable pixels across this latitude band, while ice-free area covered 10.2% of the classifiable area. There were no trends over time in the proportion or total area of MIZ bloom or ice-free coverage.

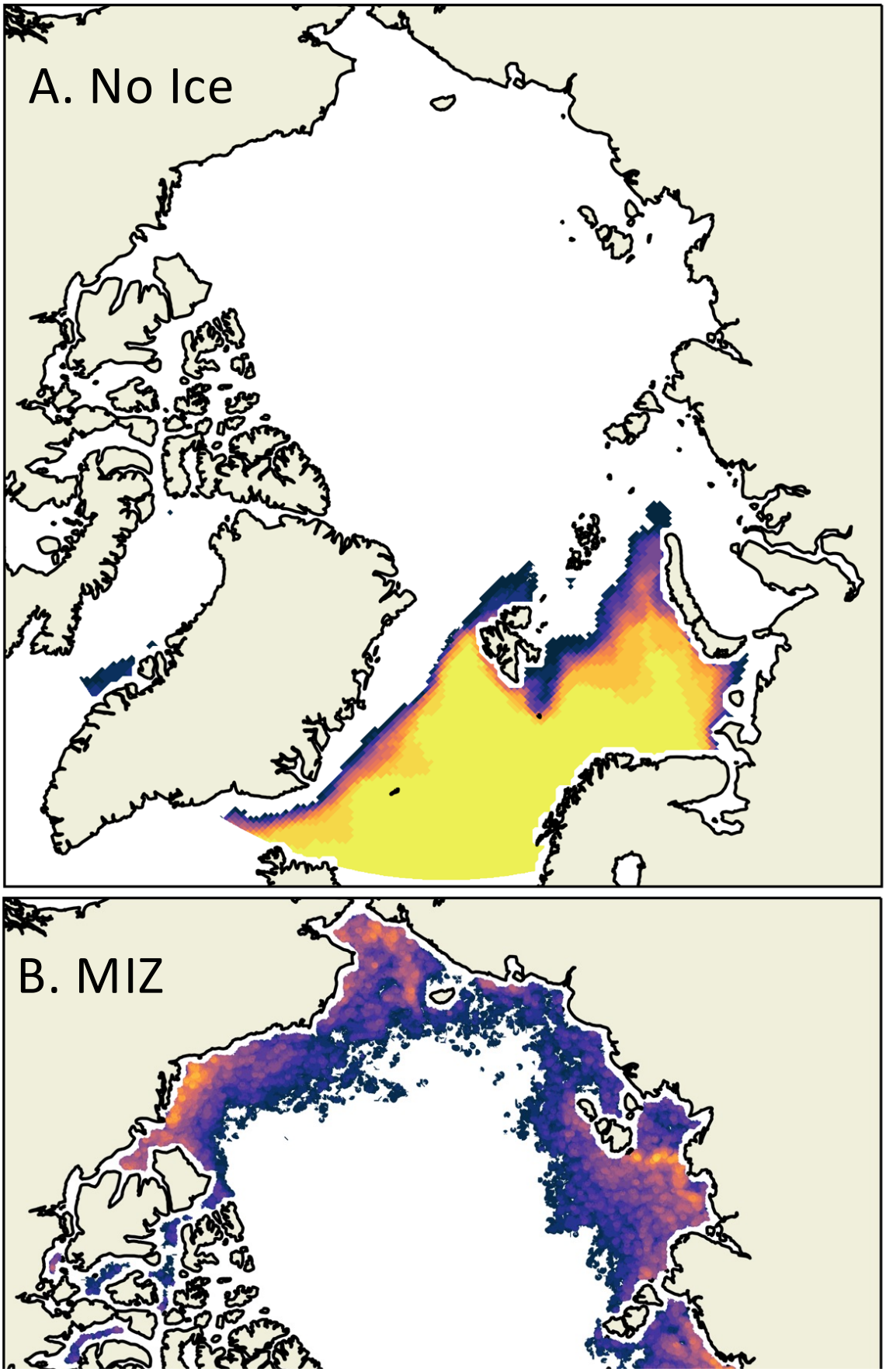
A. No Ice
B. MIZ

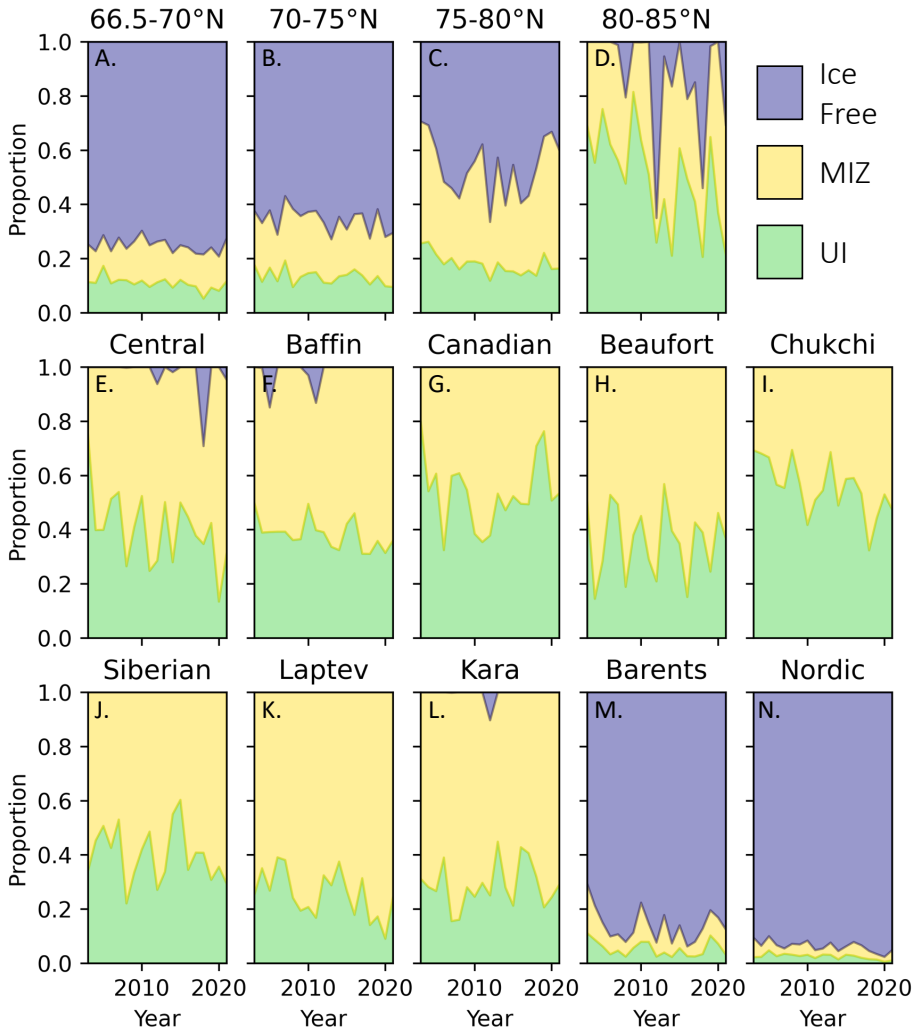

Figure 5.5: **Bloom classification by latitude and region, 2003-2021.** Proportion of pixels that were identified as UI blooms (green), MIZ blooms (yellow), or that were ice free (blue) for the latitude bands A) 66.5-70°N, B) 70-75°N, C) 75-80°N, and D) 80-85°N, and for the E) Central Arctic, F) Baffin Bay, G) Canadian Archipelago, H) Beaufort Sea, I) Chukchi Sea, J) Siberian Sea, K) Laptev Sea, L) Kara Sea, M) Barents Sea, and I) Nordic Sea.

5.3.3 Regional trends

In the Central Arctic, an increase in ice free area drove an increase in classifiable area between 2003 and 2021 (Table 5.1). UI blooms covered 38.1% of the classifiable seasonally ice-free of this region (Figure 5.5e), but UI bloom area diminished by 1.2% yr^{-1} between 2003 and 2021 (Table 5.1). Most of the Central Arctic (88.6%) had insufficient Chl observations to be classified as supporting either MIZ or UI blooms, but the Central Arctic was estimated to support greater MIZ and UI bloom areal coverage than any other regions (Table 5.2).

Baffin Bay had the second highest mean area of MIZ blooms (Figure 5.5f, Table 5.2). Baffin Bay also hosted the second highest areal coverage of UI blooms of any of the regions (Figure 5.5f, Table 5.2). However, while UI blooms covered nearly 40% of the classifiable area of Baffin Bay (Figure 5.5f), UI blooms declined by 0.5% yr^{-1} between 2003 and 2021 as a proportion of total classifiable area (Table 5.1) and were replaced by MIZ blooms. These changes were largely driven by changes in the 75-80°N latitude band (Table 5.1).

While the Canadian Archipelago had the second smallest classifiable area after the Beaufort Sea, the region had the second highest proportion of UI bloom area (53.6% of classifiable area, 3.3×10^4 km^2; Figure 5.5g). There were no significant trends in UI or MIZ bloom area or proportion over time.

UI blooms were most prevalent in the Chukchi Sea, accounting for the highest proportion of classifiable area (55.6%; Figure 5.5i) and covering both the largest area and second largest estimated area of all the regions of the Arctic Ocean (Figure 5.4a, Table 5.2). However, the region also saw large-scale declines in UI bloom areal extent, which fell by nearly 50% from 1.3×10^5 km^2 in 2003 to 6.6×10^4 km^2 by 2021 (Table 5.1). UI blooms declined and MIZ blooms expanded as a proportion of classifiable area at a rate of 1.1% yr^{-1} (Table 5.1). This change in UI bloom proportion was observed evenly between the 66.5-70°N and 70-75°N latitude bands (Table 5.1).

In the Laptev Sea (Figure 5.5k), there was an increase in the classifiable area between 2003 and 2021, driven almost entirely by sea ice loss in the 75-80°N latitude band (Table 5.1). UI blooms on average covered less of the classifiable seasonally ice free area of the Laptev Sea than in any other regions (24.7%; Table 5.2) and these blooms declined and were replaced by MIZ blooms (0.7% yr^{-1}; Table 5.1), driven largely by changes in the southernmost portion of the region (70-75°N latitude band).

MIZ blooms were prevalent in the Kara Sea, covering 70.6% of the classifiable part of the region (Figure 5.4b, Figure 5.5l, Table 5.2). In the 80-85°N latitude band, a small increase in MIZ bloom coverage drove a 2.0% yr^{-1} transition from UI bloom to MIZ bloom area (Table 5.1).

The Barents and Nordic Seas were dominated by ice-free area, (86.1% and 937% of classifiable area, respectively; Figure 5.4c, Figure 5.5m and n, Table 5.2). While only observed over a small percentage of classifiable area, UI and MIZ blooms still had sizeable areal coverage (Table 5.2). In the Barents Sea, UI blooms did not change in frequency across the region as a whole, but declined

Table 5.2: 2003-2021 mean areal coverage (km^2) of insufficient observations, ice free, MIZ, and UI blooms by region, as well as the relative frequency ('freq.') of UI blooms and the estimated ('Est.') UI and MIZ areal coverage by region.

Region	**Ins. Obs.**	**Ice Free**	**MIZ**	**UI**	**UI freq.**	**Est. UI**	**Est. MIZ**
Central	9.7×10^5	2.7×10^3	7.6×10^4	4.7×10^4	0.381	4.1×10^5	6.7×10^5
Baffin	2.9×10^5	3.6×10^3	1.4×10^5	8.8×10^4	0.390	2.0×10^5	3.1×10^5
Canadian	9.3×10^4	0	3.0×10^4	3.3×10^4	0.525	8.2×10^4	7.4×10^4
Beaufort	3.4×10^4	0	3.7×10^4	1.9×10^4	0.344	3.1×10^4	5.9×10^4
Chukchi	4.7×10^5	0	8.3×10^4	1.0×10^5	0.554	3.6×10^5	2.9×10^5
Siberian	6.6×10^5	0	5.3×10^4	3.6×10^4	0.400	3.0×10^5	4.5×10^5
Laptev	2.4×10^5	0	1.0×10^5	3.3×10^4	0.247	9.1×10^4	2.8×10^5
Kara	3.9×10^5	1.0×10^3	1.4×10^5	5.6×10^4	0.283	1.7×10^5	4.2×10^5
Barents	4.9×10^5	8.9×10^5	8.5×10^4	5.3×10^4	0.382	2.4×10^5	3.9×10^5
Nordic	3.0×10^5	1.3×10^6	5.4×10^4	3.5×10^4	0.394	1.5×10^5	2.4×10^5
Total	3.9×10^6	2.2×10^6	8.0×10^5	5.0×10^5	0.384	2.0×10^6	3.2×10^6

by 2.2% yr^{-1} from 80-85°N between 2003 and 2021 (Table 5.1). MIZ blooms were also not prevalent as a proportion of classifiable area in the Barents Sea (8.6%; Figure 5.5m), but again had substantial areal coverage (Table 5.2). In the Nordic Sea, ice free area expanded substantially from 2003-2021 driven by ice loss from 70-75°N (Table 5.1), driving a decline in UI bloom area and in the proportion of UI and MIZ blooms across the classifiable area (Table 5.1).

5.3.4 Sensitivity Analysis

We tested the sensitivity of our analysis to two parameters - the sea ice concentration threshold (%) where we considered sea ice to have retreated and the number of days between sea ice retreat and the end of period one. Ice retreat thresholds of 10-25% resulted in little change in the areal coverage of UI and MIZ blooms, nor in the trends in UI area from 2003-2021 (Table 5.3). However, an ice retreat threshold of 50% resulted in insufficient observations for most pixels to be classified, reducing the classifiable area in the seasonally sea ice-covered Arctic Ocean by 56%. This drove a $\sim 3.5 \times 10^5$ km^2 decline in both UI and MIZ area, representing a reduction in area of 33-68% for each of these bloom types. Due to the very low proportion of analyzable area classified as supporting UI or MIZ blooms, there were no trends in the proportion of UI bloom area at the 50% ice retreat threshold, but there was an increasing trend in MIZ areal coverage over time (Table 5.3). Our analysis was also relatively insensitive to changes in the length of time between ice retreat and the end of period one. Added days disproportionately increased UI bloom area but had little effect on trends in UI or MIZ blooms (Table 5.3).

5.4 Discussion

In the Arctic Ocean, water column NPP is partitioned between three distinct periods defined by sea ice cover - the UI, MIZ, and OW periods. While NPP during the UI period was historically considered negligible (*Hameedi*, 1978; *Perrette et al.*, 2011), observations of massive UI phytoplankton blooms in recent years (*Arrigo et al.*, 2012, 2014; *Mayot et al.*, 2018; *Mundy et al.*, 2009; *Oziel et al.*, 2019) demonstrate that this period can be highly productive. Changes in sea ice conditions, particularly the thinning of sea ice and the proliferation of melt ponds on the surface of the ice (*Kwok*, 2018; *Webster et al.*, 2015), have substantially changed UI light availability (*Light et al.*, 2015), possibly increasing areal coverage (*Horvat et al.*, 2017) or productivity (*Zhang et al.*, 2015) of UI blooms. The MIZ period, on the other hand, has long been considered responsible for the largest pulse of NPP in the Arctic Ocean (*Niebauer*, 1991; *Perrette et al.*, 2011; *Sakshaug and Skjoldal*, 1989; *Sakshaug*, 2004). Following the MIZ and UI periods, nutrients are stripped from the surface ocean and NPP during the OW period typically is concentrated in a subsurface Chl maximum (*Arrigo et al.*, 2014; *Brown et al.*, 2015a; *Hill and Cota*, 2005; *Martin et al.*, 2010). The OW period may be gaining in importance; increases in NPP across the Arctic Ocean appear to be driven in part by increases in

Table 5.3: Analysis sensitivity to the ice retreat threshold (IR) and the length of time between IR and the end of period one (+ Days).

IR (%)	**+ Days (d)**	**UI (10^5 km^2)**	**MIZ (10^5 km^2)**	**UI slope**	**UI R^2**	**UI *p*-val**	**MIZ slope**	**MIZ R^2**	**MIZ *p*-val**
10	2	5.0	8.1	-0.25% yr^{-1}	0.381	0.005	-	-	-
10	4	6.5	8.5	-0.28% yr^{-1}	0.364	0.006	-	-	-
10	6	8.0	8.5	-0.27% yr^{-1}	0.316	0.012	-	-	-
15	2	5.0	8.0	-0.25% yr^{-1}	0.375	0.005	-	-	-
15	4	6.5	8.5	-0.27% yr^{-1}	0.359	0.007	-	-	-
15	6	8.0	8.5	-0.26% yr^{-1}	0.310	0.013	-	-	-
25	2	4.6	7.8	-0.19% yr^{-1}	0.281	0.020	-	-	-
25	4	6.1	8.3	-0.22% yr^{-1}	0.279	0.020	-	-	-
25	6	7.5	8.4	-0.19% yr^{-1}	0.215	0.045	9.2×10^3 km^2 yr^{-1}	0.217	0.044
50	2	1.6	4.2	-	-	-	7.1×10^3 km^2 yr^{-1}	0.242	0.032
50	4	2.6	5.1	-	-	-	8.6×10^3 km^2 yr^{-1}	0.282	0.019
50	6	3.7	5.7	-	-	-	10.0×10^3 km^2 yr^{-1}	0.329	0.010

the length of the OW period (*Lewis et al.* 2020). Our analysis indicated that the area of the Arctic Ocean supporting an OW bloom of at least 1 mg Chl m^{-2} increased substantially between 2003 and 2021. However, our analysis, which seeks primarily to understand the relative frequency of UI and MIZ blooms, uses Chl observations from around the time of sea ice retreat that may not represent the maximum Chl concentration achieved during the UI period. Consequently, we could not directly compare the Chl concentrations of UI, MIZ, and OW blooms. Our analysis was further limited by sea ice and cloud cover, which prevented the classification of nearly three quarters of the seasonally ice-free Arctic Ocean (3.3×10^6 km^2) in any given year.

UI phytoplankton blooms have been observed throughout the Arctic Ocean (Figure 5.4a; *Ardyna et al.* 2020a). Our analysis found evidence of UI blooms over an area of 0.5 million km^2, and by using the frequency of UI blooms for each region, we estimate that a total of 2.0 million km^2, or 27.4% of the Arctic Ocean as a whole and nearly 40% of the seasonally ice-free Arctic Ocean, may have supported UI blooms between 2003 and 2021. We found that the Chukchi Sea had the largest area and highest proportion of UI blooms of any region of the Arctic Ocean. This is perhaps not surprising given that the UI blooms observed in the Chukchi Sea have been among the most productive blooms ever observed (*Arrigo et al.* 2012, 2014), as well as the relatively large number of years (1998, 2011, 2013, 2014, 2018) where *in situ* studies found evidence of UI blooms (*Arrigo et al.* 2012; *Hill et al.* 2018a; *Lalande et al.* 2020; *Lowry et al.* 2018; *Yager et al.* 2001). Two previous studies assessed UI bloom prevalence across the Chukchi Sea. Using remote sensing and a minimum Chl threshold of 2.5 mg Chl m^{-3}, *Lowry et al.* (2014) previously found that 72% of the area of the Chukchi Sea showed evidence of producing UI blooms in any given year between 1998 and 2012. A modeling study by *Zhang et al.* (2015) found that UI blooms were generated across 46% of the Chukchi Sea from 1988 to 2013. Our analysis indicated that an average of 56% of classifiable area hosted UI blooms between 2003 and 2021, in line with previous estimates.

The relative ubiquity of UI blooms across the Arctic Ocean in our analysis stands in contrast to the findings of *Perrette et al.* (2011), who used similar satellite-derived estimates of Chl to assess the importance of MIZ blooms. However, the analysis of *Perrette et al.* (2011) was published in the same year that massive UI blooms were first observed in the Chukchi Sea (*Arrigo et al.* 2012) and as a result doesn't differentiate between UI and MIZ blooms. Similar to *Perrette et al.* (2011), our analysis found that MIZ blooms are widespread, with evidence that they cover an area of 0.8 million km^2 and a total estimated extent of 3.2 million km^2 each year from 2003-2021. We found that MIZ blooms are likely generated across 36% of the Arctic as a whole and that they are generated across 60% of the seasonally ice free Arctic Ocean. MIZ blooms were revealed to be particularly widespread in the Kara and Laptev Seas, where they accounted for >60% of the classifiable, seasonally ice free area.

We also evaluated how UI and MIZ blooms changed between 2003 and 2021. On a pan-Arctic scale, we found that the areal coverage of UI blooms did not change substantially, but UI blooms

diminished in their proportional coverage of the seasonally ice free Arctic Ocean by nearly 10% between 2003 and 2021 as the ice-free area of the Arctic Ocean increased. While our analysis cannot be directly related to studies that quantify NPP during the UI period, these findings were qualitatively similar to a previous model inter-comparison study by *Jin et al.* (2016), which found that UI blooms declined in their magnitude across the Arctic from 1980 to 2009. *Jin et al.* (2016) also found that declines in NPP during the UI period coincided with a substantial 3.2 to 8.0 Tg C yr^{-1} increase in total annual NPP across the Arctic Ocean between 1980 and 2009. A similar rate of increase in NPP across the Arctic was observed in a remote sensing study by *Lewis et al.* (2020), which found that annual NPP increased by 6.8 Tg C yr^{-1} between 1998-2018. While changes in NPP during the UI period was not evaluated by *Lewis et al.* (2020), both of these studies found that increases in total NPP were attributable to an increase in the NPP generated during the OW period, not the MIZ period.

The pan-Arctic decline in the proportion of UI bloom area in our analysis appeared to be driven by local processes. *Jin et al.* (2016) hypothesized that, although thinner sea ice cover and an increase in first year ice has increased the light penetration and thus increased UI NPP, reductions in sea ice cover and earlier sea ice retreat has driven an overall reduction in the area of large UI blooms. One might expect that a reduction in the relative importance of UI blooms might be driven by changes in UI bloom frequency at lower latitudes, where sea ice loss happens far earlier in the year. However, we found that the decline in the proportion of UI bloom area was observed over virtually every latitude band (66.5-70°N, 75-85°N) and was greatest in the second northernmost latitude band (75-80°N). Instead of a strong latitudinally dependent reduction in UI bloom frequency, we found that changes in frequency were driven by changes in two regions - the Chukchi Sea (-1.1% yr^{-1}) and Baffin Bay (-0.5% yr^{-1}) - that had the highest areal coverage of UI blooms. This declining trend for UI blooms in the Chukchi Sea contrasts with a modeling study by *Zhang et al.* (2015) which found that UI blooms increased their areal coverage by 2% yr^{-1} between 1988 and 2013. However, two other Chukchi Sea-based studies found evidence of the waning importance of UI blooms in the Chukchi Sea. *Lowry et al.* (2014) found an increase in MIZ blooms (which increased from 13.8% from 1998-2000 to 36.0% from 2010-2012) and a decline in 'probable' UI blooms in the Chukchi Sea from 1998-2012. Similarly, a one-dimensional model implemented in the southern Chukchi Sea by *Payne et al.* (2022) found a large reduction in the magnitude of UI NPP between 1988 and 2018 (with UI blooms generating less than 32% of the NPP between 2009 and 2013 that they did between 1988 and 1992). They attributed this reduction in the importance of UI blooms to earlier sea ice loss and a shorter UI period at their model location (*Payne et al.*, 2022). Further, they found that a reduction in NPP during the UI period did not affect total NPP in the southern Chukchi Sea, which was 22% greater than in the northern Chukchi Sea (*Payne et al.*, 2022). This higher rate of annual NPP was driven most substantially by higher NPP during the OW period, reminiscent of the findings of *Jin et al.* (2016).

Although UI blooms are likely diminishing in their importance, our analysis indicates that nearly 40% of the seasonally ice-free Arctic may presently support these blooms. Because UI blooms can substantially contribute to local annual NPP (*Arrigo et al.*, 2012, 2014; *Mayot et al.*, 2018; *Mundy et al.*, 2009; *Oziel et al.*, 2019), analyses such as ours can be used to identify regions where satellite-based estimates of NPP may represent a substantial underestimate of annual NPP because of the unquantified contributions of UI blooms. Further, UI blooms have been found to have important ecosystem consequences, including reducing zooplankton grazing (*Payne et al.*, 2021), altering the partitioning of organic matter between benthic and pelagic ecosystems (*Arrigo et al.*, 2014), and affecting nitrogen cycling, particularly by changing the rate of sedimentary denitrification (*Payne and Arrigo*, 2022). Critical next steps include leveraging new technologies, such as moorings, floats, and AUVs, to better quantify the importance of UI productivity in relation to total annual NPP, and an increase in *in situ* studies of the impacts of UI productivity on food availability to upper trophic organisms, as well as changes in biogeochemical cycling that may result in areas with UI blooms.

Chapter 6

Determining the functional relationship between co-limiting light and nutrient conditions on phytoplankton growth

Courtney M. Payne, Kevin R. Arrigo
Department of Earth System Science, Stanford University, Stanford, California, USA

Marine phytoplankton growth has long been found to be biochemically co-limited by light and nutrients including iron, nitrogen, and phosphorus. However, despite agreement that nutrient and light co-limitation exists in many places globally, no laboratory study has generated the data required to explicitly quantify how simultaneous light and nutrient limitation interact to control phytoplankton growth. Influential ecosystem models have largely assumed that growth is limited by either the minimum of two limiting factors or a multiplicative relationship between the two, but these functional relationships can produce vastly different predictions of phytoplankton bloom magnitude, influencing the results of ecosystem models. Here, we present a laboratory experiment that aims to determine the functional relationship between light, nutrients, and phytoplankton growth rate. Unfortunately, due to challenges related to quantifying the nitrate concentration and thus in achieving a low nitrate limitation term, we were unable to meaningfully distinguish between these two functional relationships.

6.1 Introduction

Marine phytoplankton account for <1% of the plant biomass on Earth but are responsible for nearly half of the world's net primary production (*Falkowski*, 2012). These single celled organisms both form the base of the oceanic food web and mediate global biogeochemical cycles by drawing down carbon (C) and nutrients from the surface ocean and subsequently sinking to depth (*Volk and Hoffert*, 1985). Because of their ecological and biogeochemical importance, accurately representing growth and primary production rates of phytoplankton in both global climate models as well as regional or one-dimensional models is critical.

The maximum (non-resource limited) rate of phytoplankton growth is controlled by temperature, with higher temperatures corresponding to higher growth rates (*Eppley*, 1972). Phytoplankton growth is further controlled by the interaction between light and nutrient availability. Co-limitation happens when two resources (typically light and one or more nutrients) both impair phytoplankton growth (*Arrigo*, 2005). To alleviate co-limitation, either a simultaneous addition of both resources or an addition of one resource is required before phytoplankton physiology changes and growth is stimulated (*Arrigo*, 2005). Iron availability, for example, directly affects photosynthetic efficiency because of the high iron requirements of portions of the photosynthetic electron transport pathway (*Raven*, 1990; *Strzepek and Harrison*, 2004). When phytoplankton experience low light, the cellular iron requirement increases. This is because photosynthesizing cells require either a larger number (*Raven*, 1990; *Sunda and Huntsman*, 1997, 2011) or greater size (*Strzepek et al.*, 2012) of iron-rich photosynthetic units to fix carbon (C) in low light. Phytoplankton growth has been found to be biochemically co-limited by light and nutrients, including iron (*Boyd et al.*, 1999, 2004, 2007; *Maldonado et al.*, 1999; *Strzepek et al.*, 2012; *Sunda and Huntsman*, 1997; *Timmermans et al.*, 2001), nitrogen (*Carter et al.*, 2005; *Laws and Bannister*, 1980; *Rhee and Gotham*, 1981; *Rosen and Lowe*, 1984), and phosphorus (*Laws and Bannister*, 1980; *Rosen and Lowe*, 1984) in laboratory experiments and in the field.

Despite of widespread agreement that nutrient and light co-limitation exists in many places globally, there is no consensus in the modeling community on how to best constrain phytoplankton growth under co-limiting light and nutrient conditions. While a few complex formulations have been developed to describe nutrient-light interactions on phytoplankton growth (i.e., *Laws and Chalup*, 1990), only two have been widely implemented in ecosystem models. These two functional relationships, developed in the 1970s, both involve calculating a maximum specific growth rate (μ_{max}; d^{-1}), typically based on temperature (*Eppley*, 1972), and then proportionately scaling growth by dimensionless limitation terms for nutrients (N_{lim}) and light (L_{lim}). The first method for adjusting phytoplankton growth, originally hypothesized by *Blackman* (1905), argues that only the minimum limiting term affects growth rate (*Davis*, 1976; *Rodhe*, 1978), such that

$$\mu = [\mu_{max}] \cdot min(L_{lim}, N_{lim}) \tag{6.1}$$

where μ is the instantaneous growth rate (d^{-1}) and *min* is the minimum of the two limitation terms. This minimum or threshold method of addressing the interaction between multiple limits on phytoplankton growth has been used in many ecosystem models (e.g., *Arrigo et al.*, 1998b, 2003; *Franks*, 2002; *Payne et al.*, 2021; *Tett et al.*, 1986; *Varela et al.*, 1992; *Walsh*, 1975). Using this functional relationship, if light and nutrient concentrations were such that they would each independently limit phytoplankton to 50% of their maximum growth rate, phytoplankton would grow at 50% of the maximum growth rate.

The second method, based on laboratory experiments of vitamin B12 limitation in the chrysophyte *Monochrysis lutheri*, assumes that growth scales as a product of light and nutrient limitation (*Droop et al.*, 1982), such that

$$\mu = [\mu_{max}] \cdot L_{lim} \cdot N_{lim} \tag{6.2}$$

This multiplicative limitation term has been adapted into major ecosystem models (e.g., *Besiktepe et al.*, 2003; *Chai et al.*, 2002; *Christian et al.*, 2002; *Fennel et al.*, 2006; *Galbraith et al.*, 2010; *Geider et al.*, 1997, 1998; *Spitz et al.*, 2001), perhaps most notably in the North Atlantic Ocean model by *Fasham et al.* (1990). Using this functional relationship, if light and nutrient concentrations were such that they would each independently limit phytoplankton to 50% of their maximum growth rate, phytoplankton would only grow at 25% of the maximum growth rate, or half the rate of the minimum model given the same light and nutrient limitation terms. Over the course of a hypothetical spring season, the minimum method of modeling phytoplankton growth under co-limiting conditions produces 170% of the primary production that the multiplicative functional relationship would generate (Figure 6.1). These substantial differences in the growth rate produced by the two models under co-limiting conditions demonstrate how critical it is to determine which method of calculating phytoplankton growth under multiple limiting resources is closest to observations.

To determine the functional relationship between simultaneous light and nutrient limitation on phytoplankton growth, we used a laboratory experiment to test the effects of nitrate (NO_3^-) and light co-limitation on rates of phytoplankton growth.

6.2 Methods

6.2.1 Experimental Setup

Nonaxenic cultures of *Thalassiosira weissflogii* (CCMP1049) were obtained from Provasoli-Guillard National Center for Marine Algae and Microbiota at Bigelow (NCMA; East Boothbay, ME, USA). *T. weissflogii* was chosen because of its ecological relevance as a bloom-forming diatom found in many temperate ecosystems (*Van Heurck*, 1882). This culture, originally collected near Amityville, New York, USA, was acquired in September of 2021 and stock cultures were maintained under constant light (from 20-300 μmol photons m^{-2} s^{-1}), at room temperature (23.5 $\pm$ 0.5°C), and in

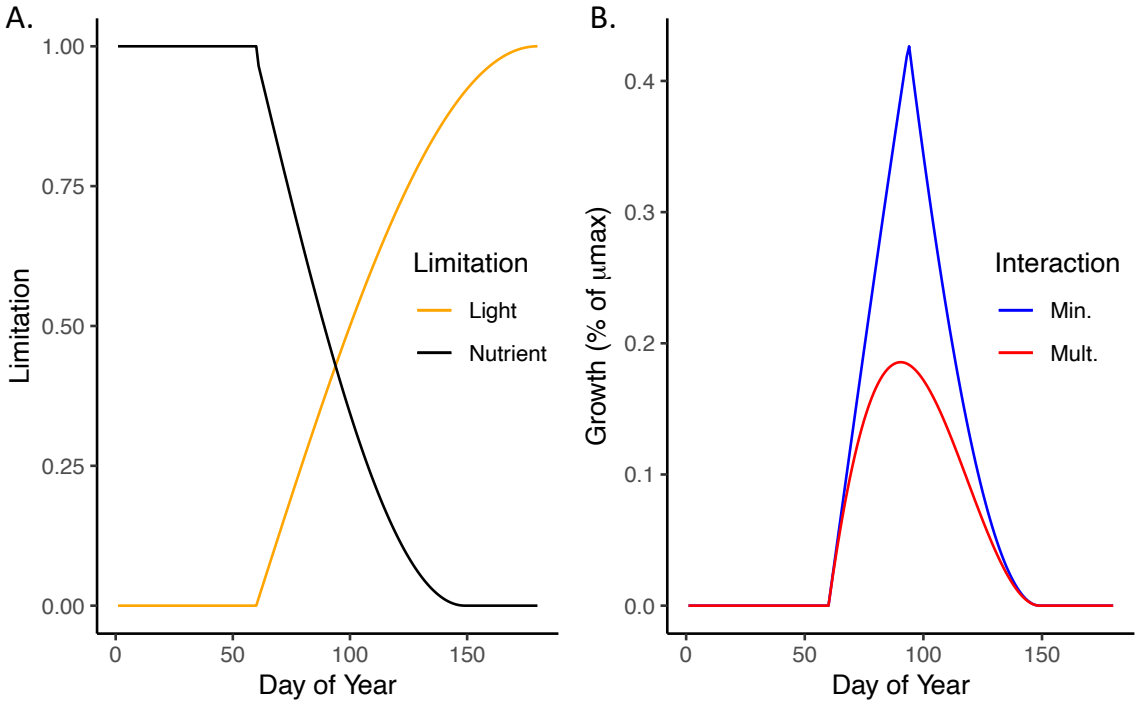

Figure 6.1: An example of the different growth rates predicted by the minimum and multiplicative functional relationships between simultaneous limiting factors and phytoplankton growth rate. A) Light (orange) and nutrient (black) limitation terms during a bloom period. B) Proportion of maximal growth rate produced using the minimum (blue) and multiplicative (red) functional relationships between the two limitation terms.

exponential growth for at least 10 generations before experiments were conducted. Cultures were maintained in synthetic ocean water (*Price et al.*, 1989) enriched with modified F/2 macronutrients, micronutrients, and vitamins (*Guillard and Ryther*, 1962). However, to ensure that nitrate (NO_3^-) concentrations were the most limiting nutrients, the F/2 mixture was modified such that the NO_3^- to phosphate (PO_4^{3-}) ratio was reduced to a 16:1 ratio, rather than the 24:1 ratio used by *Guillard and Ryther* (1962). To confirm that NO_3^- was more limiting than other nutrients, NO_3^-, PO_4^{3-}, or synthetic sea water (control) was added to cultures across a variety of photosynthetically available radiation, or PAR (μmol photons m^{-2} s^{-1}), treatments and initial NO_3^- treatments. Only cultures with high PAR and low initial NO_3^- that received an addition of NO_3^- grew more rapidly than the control, indicating that NO_3^- was the most limiting nutrient.

Algal cultures were maintained in optically dense semi-continuous batch cultures, where new media was dripped in and culture was removed over 3-6 hours each 24 hours. These cultures were maintained at the experimental PAR and non-limiting NO_3^- concentrations (approximately 10 μmol NO_3^- L^{-1}) for 3 days prior to being used for an experimental treatment. To ensure that the cultures were growing exponentially, growth was monitored daily by measuring *in vivo* chlorophyll *a* (Chl)

fluorescence in a Turner Designs fluorometer (model 10-AU). Measurements of NO_3^- concentrations were also conducted periodically using a WestCo SmartChem 200 discrete analyzer. The rate of new media added to the culture was adjusted to maintain cultures at a NO_3^- concentration of around 10 μmol L^{-1}.

Subsequently, optically thin batch cultures were used to conduct 24-hour experimental treatments. The short nature of these experimental treatments was crucial to ensuring that nutrient concentrations remained relatively stable over the entire experimental treatment. Approximately 1 μg Chl L^{-1} of algal culture and concentrations of f/2 equating to 0.5-10 μmol NO_3^- L^{-1} were added to 500 mL polycarbonate Erlenmeyer flasks containing 500 mL of synthetic ocean water. Batch cultures were maintained on magnetic stirring plates for the duration of the experiment. Each experimental treatment was conducted in triplicate between July and December of 2022.

Targeted experimental PAR treatments included 25, 50, 100, 150, 200, 250, and 300 μmol photons m^{-2} s^{-1}. PAR for each experimental treatment was quantified by taking the mean of 10 measurements within each culture by a Biospherical Instruments QSL Quantum Scalar Laboratory Sensor (Biospherical Instruments Inc., San Diego, CA, USA) at the start of each experiment. Targeted experimental NO_3^- concentrations included 0.5, 1, 1.5, 2, 5, and 10 μmol NO_3^- L^{-1}. NO_3^- concentrations were quantified by collecting 5 mL water samples at time zero (t_0), when the experiment was initiated, and at time final (t_f), 24 hours later. These were subsequently measured in triplicate on a WestCo SmartChem 200 discrete analyzer. The NO_3^- concentration for each experimental treatment was calculated as the mean of the NO_3^- concentration at t_0 and t_f. However, to ensure that NO_3^- concentrations didn't change too much over the experiment, treatments where NO_3^- concentrations varied by >1 μmol L^{-1} between t_0 and t_f were excluded from analysis.

6.2.2 Calculated Terms

Growth rate (μ) was quantified by measuring fluorometric Chl concentration in triplicate at both t_0 and t_f such that

$$\mu = \frac{\ln(C_f/C_0)}{t_f - t_0} \tag{6.3}$$

where C_f and C_0 are the Chl concentrations at t_f and t_0, respectively.

Further, to compare the two established functional relationships, light and NO_3^- limitation terms were calculated. A light limitation term (L_{lim}) was quantified for each experimental treatment according to

$$L_{lim} = 1 - e^{-PAR/E_k} \tag{6.4}$$

where E_k is the photoacclimation parameter. E_k was calculated in MATLAB (version 9.12.0) by fitting the Chl-derived growth rate across experimental treatments to the equation of *Platt et al.* (1980). Additionally, a NO_3^- limitation term (N_{lim}) was calculated according to the *Monod* (1942)

equation such that

$$\mathrm{N}_{lim} = \frac{N}{K_S + N} \tag{6.5}$$

where N is the mean NO_3^- concentration of each experimental treatment and K_s is the half saturation constant of NO_3^-. K_s was calculated in R (version 4.1.0) by comparing the Chl-derived growth rate to the NO_3^- concentration across experimental treatments as in *Eppley and Thomas* (1969).

Three parameters - μ_{max} (the maximum growth rate, from eqns. 1 and 2), E_k, and K_s - were fitted to calculate predicted growth rates. A μ_{max} value of 2.14 d^{-1} was determined by using the maximum growth rate observed across all experiments. E_k and K_s values of 76.6 μmol photons m^{-2} s^{-1} and 0.59 μmol L^{-1}, respectively, were calculated using the best parameter fit across all experimental data.

These parameters were used to calculate predicted growth rates according to the minimum and multiplicative functional relationships. Predicted growth rates were calculated for both binned, interpolated data (42 experimental treatments) as well as for all data (224 experimental treatments; Figure 6.2).

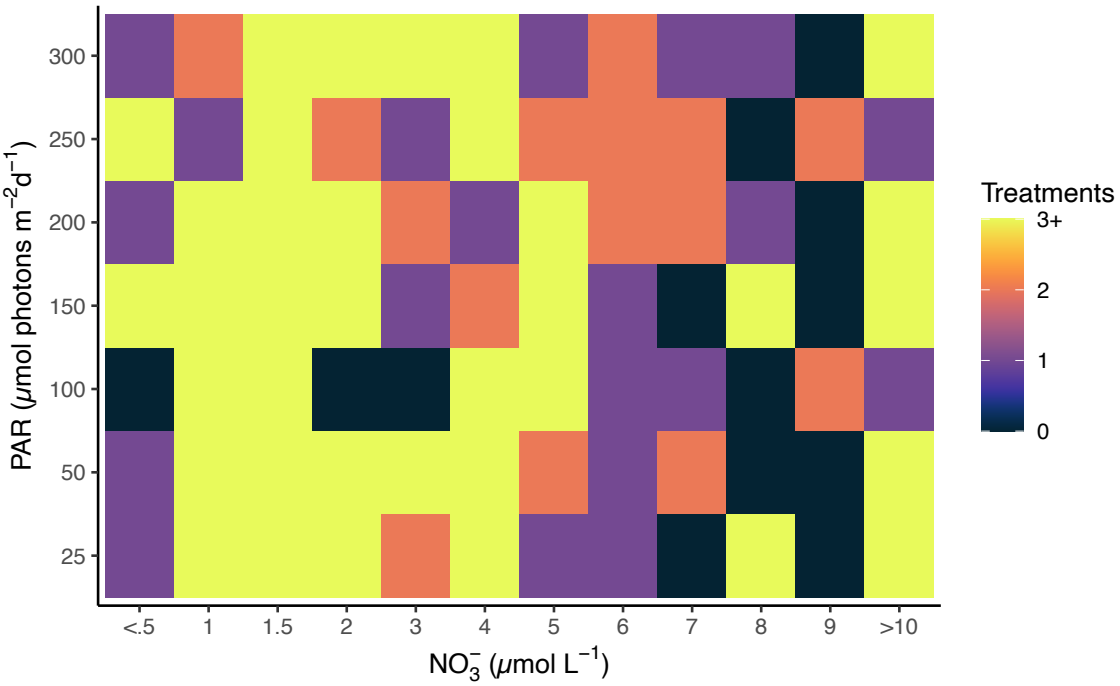

Figure 6.2: Number of experimental treatments, binned by PAR (μmol photons m^{-2} d^{-1}) and NO_3^- concentration (μmol L^{-1}).

6.2.3 Statistical Analyses

To quantify the functional relationship between NO_3^- concentration, light, and growth rate, experimental treatments were first binned into discrete PAR and NO_3^- treatments (Figure 6.2). A bin size of ±12.5 μmol photons m^{-2} s^{-1} was used for PAR treatments of 25 and 50 μmol photons m^{-2} s^{-1}, while a bin size of ±25 μmol photons m^{-2} s^{-1} was used for PAR treatments ≥100 μmol photons m^{-2} s^{-1}. For NO_3^- concentrations, a bin size of ±0.25 μmol L^{-1} was used for NO_3^- treatments of ≤2 μmol L^{-1} and a bin size of ±0.5 μmol L^{-1} was used for treatments of >2 μmol L^{-1}. Bins were further excluded from analysis if there were either fewer than three experimental replicates of the treatment or if the experiment was not experimentally targeted (only NO_3^- concentrations of 0.5-2, 5, and 10 μmol NO_3^- L^{-1} were included). Data were subsequently interpolated linearly using the R 'interp' package.

Linear regressions were used to compare the growth rates predicted by the minimum and multiplicative functional relationships to the observed growth rates, and relationships with p-values of <0.05 considered statistically significant. The functional relationship predictions were evaluated using the R^2, slope, and root mean square error (RMSE) of the linear regressions, computed using the R Metrics package (version 0.1.4). All statistical analyses were conducted in R (version 4.1.0).

6.3 Results

6.3.1 Growth across light and NO_3^- treatments

Over the 224 experimental treatments conducted as a part of this experiment, growth rate varied substantially, from 0.31 to 2.14 d^{-1} (Figure 6.2). Growth was linearly correlated to experimental PAR (R^2=0.289, p<0.001). As PAR increased across the experimental treatments, growth increased, from under 1.0 d^{-1} at PAR of 25 μmol photons m^{-2} s^{-1} to a peak of 1.2-1.8 d^{-1} at 150 μmol photons m^{-2} s^{-1} (Figure 6.3a). At the highest experimental light treatments, 250 and 300 μmol photons m^{-2} s^{-1}, variation between experimental treatments was greatest, with growth rates ranging from 0.7 to 2.1 d^{-1}, indicating photoinhibition among some of the experimental treatments (Figure 6.3a).

Growth rate did not vary predictably as a function of NO_3^- concentration. Growth and NO_3^- concentrations were not linearly correlated (p=0.846). The highest growth rates of >2.0 d^{-1} were achieved at mean NO_3^- concentrations of 2.3-7.1 μmol L^{-1} (Figure 6.3b). The lowest growth rates (<0.5 d^{-1}) were almost exclusively associated with the lowest PAR treatment (25 μmol photons m^{-2} s^{-1}) across a wide range of NO_3^- concentrations (1.0-15.5 μmol L^{-1}; Figure 6.3b). As a result of the weak correlation between NO_3^- concentration and growth rate, growth rates across the experimental light and NO_3^- treatments appear to be most controlled by PAR (Figure 6.3c).

Individual experimental treatments were binned (see section 2.3) and treatments with <3 replicates or with a non-targeted NO_3^- concentration were removed from analysis. Binned data were

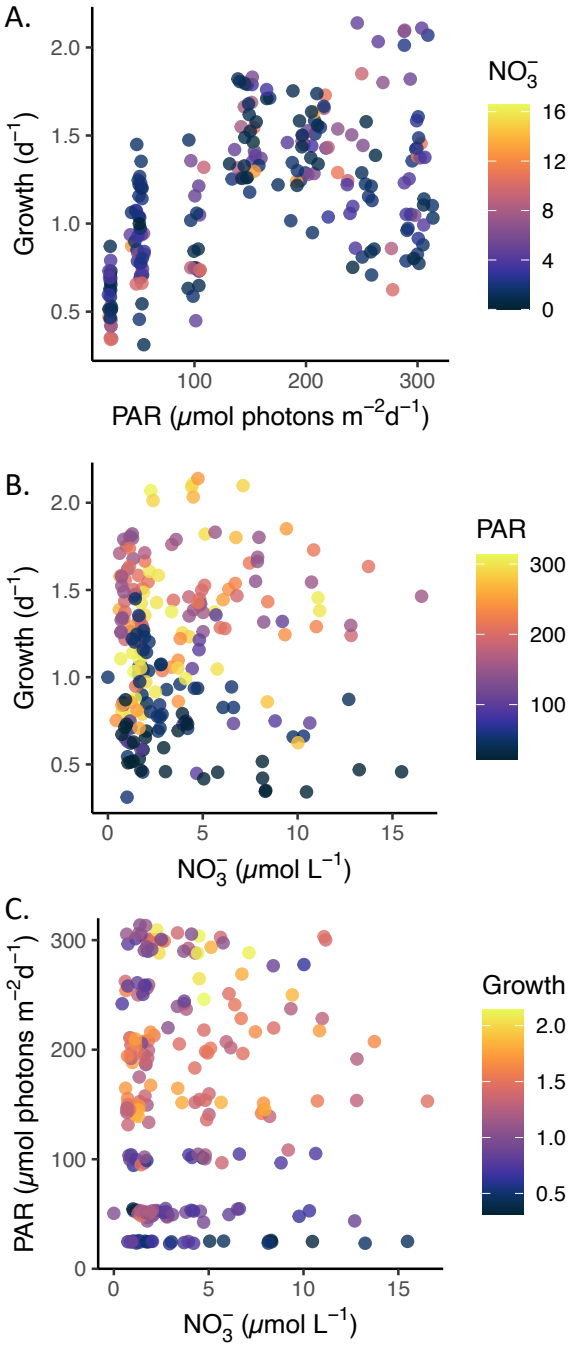

Figure 6.3: A. Growth rate (d^{-1}) as a function of PAR (μmol photons m^{-2} s^{-1}), colored by NO_3^- concentration. B. Growth rate as a function of NO_3^- concentration, colored by PAR. C. PAR vs. NO_3^- concentration, colored by growth rate.

subsequently interpolated so that a contour plot of the relationship between NO_3^- concentration, PAR, and growth rate could be generated (Figure 6.4). If NO_3^- concentration were the dominant factor in controlling growth rate, this contour plot would feature a series of vertical lines, with growth rate increasing as NO_3^- concentration increased. Conversely, if light were the dominant control on growth rate, the contour plot would feature a series of horizontal lines. The contour plot produced through our experiments has some vertical features, but is largely dominated by horizontal contours, demonstrating the importance of light in controlling growth rates across these treatments (Figure 6.4).

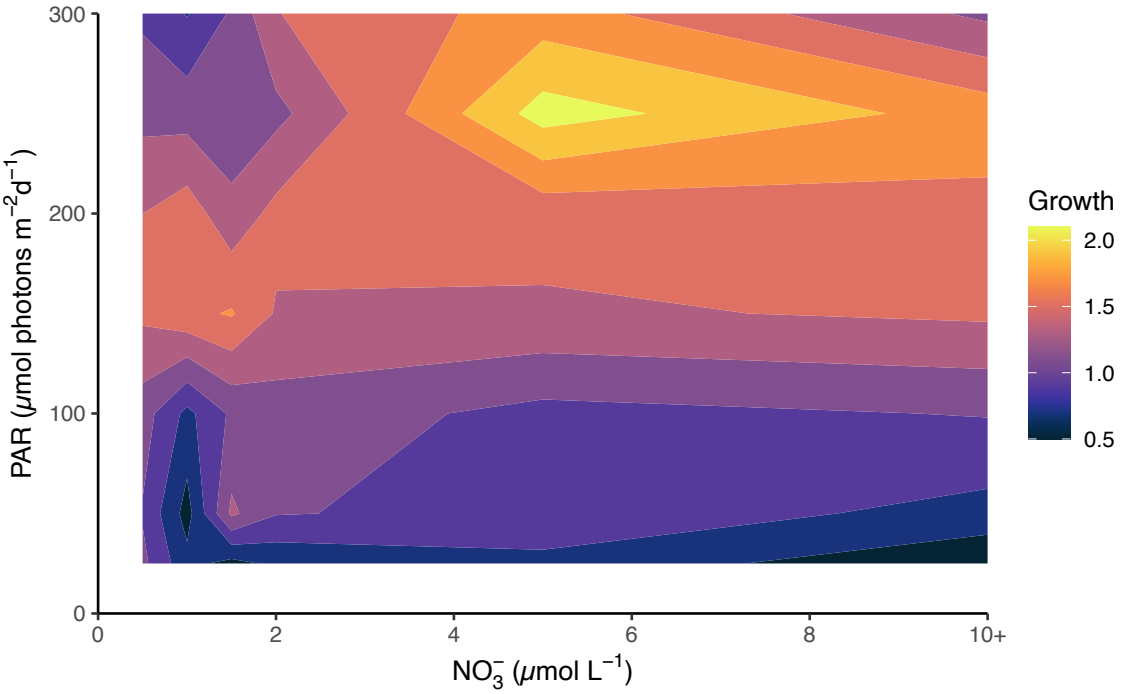

Figure 6.4: Binned, idealized growth rates across a range of NO_3^- concentrations (μmol L^{-1}) and PAR treatments (μmol photons m^{-2} d^{-1}).

6.3.2 Comparison of minimum and multiplicative functional relationships

Predicted growth rates generated by the multiplicative and minimum functional relationships were compared to observed growth rates across binned, interpolated data and all experimental data (Table 6.1). For the binned data, the multiplicative method had a slope closer to 1 and a slightly lower RMSE, but the minimum method had a higher R^2. Among the predicted growth rates generated from all data, the minimum method had a slope closer to 1 and a slightly higher R^2, but the multiplicative method had a lower RMSE. As a result, the minimum and multiplicative functional

relationships appear virtually indistinguishable in their ability to predict growth rates across our experimental treatments.

Table 6.1: A comparison of the growth rates predicted using minimum and multiplicative functional relationships to binned or all observed growth rates, using either parameters calculated from all data or a subset of data. Predicted growth rates are evaluated for fit with observed growth rates by comparing the slope, R^2, p value, and RMSE of linear regressions.

Method	Data type	Slope	R^2	p value	RMSE
Min.	Binned	0.512	0.780	0.002	0.208
Mult.	Binned	0.616	0.693	0.005	0.196
Min.	All	0.590	0.400	<0.001	0.440
Mult.	All	0.546	0.384	<0.001	0.404

6.4 Discussion

Across the 224 experimental treatments conducted as a part of this study, there were no substantial or statistically significant differences between growth rates predicted using the minimum and multiplicative functional relationships (Table 6.1). In the hypothetical growth scenario depicted in Figure 6.1, we demonstrated that if the light and nutrient limitation terms were both 0.5, the multiplicative and minimum functional relationships would produce growth rates of 25% and 50% the maximum growth rate, respectively, a difference substantial enough to allow the methods to be easily distinguished. However, the differences between these two functional relationships are less noticeable if one or both limitation terms are closer to 1. For example, if one of the two limitation terms is 0.8 rather than 0.5, the functional relationships would predict growth rates of 40% and 50% of the maximum growth rate, respectively, making it more challenging to discern the differences between the two functional relationships.

We were not able to observe significant differences between these two functional relationships primarily because of challenges in quantifying the NO_3^- concentration at low NO_3^- values, and thus in experimentally attaining a low NO_3^- limitation term. The NO_3^- limitation term is controlled by the NO_3^- concentration and by the half saturation constant, K_s. K_s values are often 0.2-1.5 μmol L^{-1} for marine phytoplankton (*Carpenter and Guillard* 1971, *Eppley and Thomas* 1969, *Falkowski* 1975), and our study found a K_s value of 0.59 μmol L^{-1}, in line with previously reported values. As a result of this experimentally-derived K_s value, the algal culture used in this study would not experience a NO_3^- limitation term of 0.5 unless NO_3^- concentrations were 0.6 μmol L^{-1}. This NO_3^- concentration, however, was close to the detection limit of the discrete analyzer used to measure NO_3^-, which we quantified at 0.3 μmol L^{-1}. Additionally, triplicate measurements of the NO_3^- concentration of the same sample often revealed standard deviations of >0.5 μmol L^{-1}, impeding our ability to meaningfully differentiate between the 0.5-2.0 μmol L^{-1} NO_3^- treatments. Thus, it was impossible to

accurately determine a functional relationship between growth rate and NO_3^- concentrations, which required accurate measurements of NO_3^- in the 0.1-2.0 μmol L^{-1} range.

Determining the functional relationship between light and nutrient limitation terms and phytoplankton growth rate remains a critical research question. *Haney and Jackson* (1996) drew attention to the lack of experimental efforts to understand this functional relationship, noting that despite extensive efforts to understand the role of nitrogen and light in controlling phytoplankton growth rates individually, there had been no studies seeking to address this fundamental relationship. However, establishing the functional relationship between light and nutrient co-limitation is likely more important in some ecosystems than others. For example, in ecosystems with large boom-bust cycles of phytoplankton, such as the polar and subpolar regions (*Behrenfeld et al.*, 2017; *Ducklow and Harris*, 1993; *Falkowski*, 1994), algal biomass can accumulate to high levels (*Arrigo et al.*, 2014), allowing it to rapidly draw down nutrients. In these systems, nutrient concentrations may rapidly (over a few days) go from non-limiting to scarce (*Palmer et al.*, 2014), indicating that the multiplicative and minimum functional relationships may have little to no effect on predicted growth rates in these systems. On the other hand, in ecosystems where nutrient supply is intermittent and where most primary production is generated in a deep chlorophyll maximum (*Cullen*, 1982; *Huisman et al.* 2006), models will produce drastically different rates and magnitudes of net primary production depending on their choice of functional relationship (e.g., minimum or multiplicative; *Varela et al.* 1992). Thus, our study demonstrates that identifying the functional relationship between light and nutrient limitation terms is likely experimentally challenging, but would have important implications for both regional and global marine ecosystem models, particularly in regions with intermittent nutrient supply.

6.5 Acknowledgments

This work was supported by the National Science Foundation (NSF) grant PLR-2112976 to CMP and KRA.

Chapter 7

Conclusions

In this thesis, I investigated the partitioning of NPP between the under-ice (UI), marginal ice zone (MIZ), and open-water (OW) periods across the Arctic Ocean using a combination of laboratory experiments, ecosystem modeling, and satellite remote sensing. I first developed a one-dimensional ecosystem model, CAOS-GO, which I implemented in the northern (72°N) and southern (68°N) Chukchi Sea to investigate the magnitude of UI blooms across the region, as well as the biogeochemical consequences of these blooms (Chapters 2-4). I found that, while UI blooms were generated frequently between 1988 and 2018 in both the northern and southern Chukchi Sea, the importance of these blooms was strongly dependent on latitude. In the northern Chukchi Sea, UI blooms were responsible for nearly half of total NPP, and the increase over time in annual NPP was driven by the interannual variability of UI blooms. Zooplankton grazing was also depressed in years with large UI blooms in the north, implying that these blooms may result in an increasing mismatch between the timing of zooplankton and phytoplankton blooms (*Conover and Huntley*, 1991). Further, I found that sedimentary denitrification was substantially higher in the northern Chukchi Sea in years with large UI blooms, and that interannual variability in this N loss was driven by increases in particle export in the first half of the year, implying a correlation with UI blooms. In the southern Chukchi Sea, however, UI blooms substantially declined in magnitude between 1988 and 2018, and the years with the highest total NPP were years without UI blooms. At this southern location, total NPP was 22% higher than in the north, driven largely by increases in NPP during the OW period, and both zooplankton grazing and denitrification were also higher as a result. The southern Chukchi Sea has substantially earlier sea ice retreat than the north, implying that, as sea ice continues to retreat earlier in the year in the northern Chukchi Sea, the partitioning of NPP between the UI, MIZ, and OW periods will increasingly resemble the south.

In Chapter 5, I considered the importance of UI blooms on a pan-Arctic scale by using satellite remote sensing data to assess the frequency and distribution of UI bloom generation between 2003 and 2021. My work demonstrated that UI blooms are likely a widespread feature across the Arctic

as a whole, since 40% of the observable seasonally ice-free Arctic Ocean experienced a UI bloom in any given year. However, this analysis also demonstrated that UI blooms are likely waning in their importance across the Arctic Ocean. While sea ice retreat led to an increase in the ice-free area from 2003-2021, there was a nearly 10% decline in the proportion of observable, seasonally ice-free area that hosted UI blooms over time. While my previous modeling work found that the change in UI bloom frequency was driven by declines at lower latitudes, this analysis revealed that the declines in UI bloom prevalence were greatest at relatively high latitudes (75-80°N). Additionally, this analysis determined that certain regions - particularly the Chukchi Sea, where UI blooms were most prevalent - drove most of the changes in UI bloom frequency across the Arctic as a whole.

Finally, in Chapter 6, I sought to use laboratory experiments to determine the functional relationship between phytoplankton growth and co-limiting light and nutrient conditions, which is critical to accurately modeling phytoplankton net primary production (NPP) in the world's oceans. Due to problems in accurately quantifying the nitrogen (N) concentration in my experimental treatments, I was not able to meaningfully distinguish between the two primary functional relationships, the multiplicative and minimum methods, which are typically employed in regional and global ecosystem models. However, these experiments demonstrated that there is little difference between the two functional relationships until N concentrations are very low (<1 μmol L^{-1}), which implies that in regions like the Arctic Ocean, where surface ocean nutrients can be rapidly depleted from being non-limiting to undetectable (e.g., *Arrigo et al.*, 2014), the choice of functional relationship likely has minimal impact on predicted phytoplankton growth rates in this area.

Because of the challenges to quantifying UI NPP, this early period of NPP has often been neglected in estimates of the productivity of Arctic ecosystems. My work demonstrates that UI phytoplankton blooms are an important feature across the Arctic Ocean that can produce half of the NPP generated over the year and drive biogeochemical cycling and food availability within a region. Consequently, there should be an increase in studies aiming to quantify the contributions of these blooms to total NPP. However, this work also demonstrates that UI blooms are likely declining in importance across the Arctic, driven by declines in the Chukchi Sea. As sea ice cover continues to retreat earlier in the year, UI blooms are likely to further decline in importance.

Appendix A

Chapter 2 Supplemental Material

This supplementary material supports the conclusions of Payne et al. (2021). These additional methods describe modifications made to the physical model, GOTM; model equations used for the biogeochemical model, CAOS, introduced in this paper; model forcing; and model performance methods and results.

Payne, C. M., Bianucci, L., van Dijken, G. L., & Arrigo, K. R. (2021). Changes in under-ice primary production in the Chukchi Sea from 1988 to 2018. Journal of Geophysical Research: Oceans, 126. https://doi.org/10.1029/2021JC017483

A.1 Physical Model

A.1.1 Albedo Modifications.

Because GOTM only uses latitude to determine albedo, it was necessary to alter the model's albedo to account for surface type, as in *Perovich and Polashenski* (2012). Albedo of the sea ice prior to snow melt was set to 0.85. Over the snow melt period, albedo declined to 0.6 to reflect the albedo of melting snow. As melt ponds expanded their areal coverage (see A.3.3), albedo diminished as a function of melt pond areal coverage, with an albedo of 0.52 for bare ice and 0.2 for ponded ice. During the ice retreat period, albedo diminished linearly with ice coverage to the open water albedo value of 0.07. When ice advanced in the autumn, albedo was gradually increased by 0.0082 d^{-1}. At the start of each year, albedo was re-set to 0.85 (Figure A.1).

A.1.2 Idealized profiles.

Idealized profiles (Figure A.2a and b) were used to approximate sea ice melt and retreat-drive temperature and salinity changes. Salinity and temperature were relaxed towards these idealized

profiles on a timescale of 5 d and 15 d, respectively. The first idealized profile, reported by *Pacini et al.* (2019) as representative of conditions during the SUBICE cruise in early 2014, was used to represent the well-ventilated winter water conditions present in the winter and spring. The second and third profiles were used to reflect the rapid increase in surface water temperatures following ice retreat. The mixed layer temperatures for these profiles were set using weighted means of maximum and minimum satellite-derived SST (0.6 * (Max - Min) + Min and 0.9 * (Max - Min) + Min for spring and summer, respectively) for each year. Different weights were evaluated by comparing the RMSE and R^2, and the weights that resulted in the best correlation were chosen. Based on observations from the 2011 ICESCAPE cruise, the mixed layer was set to 18 m for the first profile and 23 m for the second profile. Below the mixed layer, there was an exponential reduction in water temperature until 35 m, where winter profile conditions are maintained throughout the year (Figure A.2a).

The first idealized temperature profile for winter/spring was used at the start of sea ice retreat, when satellite-derived ice concentration fell below 90%, and following sea ice advance, when satellite-derived ice concentration rose above 10%. The second idealized temperature profile was used on the first date at which satellite-derived SST exceeds the temperature used in the mixed layer (the 60% weighted mean). The third idealized temperature profile was used on the first and last dates at which SST exceeds the temperature used in the mixed layer (the 90% weighted mean value).

Five idealized profiles were used to approximate the sea ice retreat-driven salinity changes (Figure A.2b). The first salinity profile was adapted from the profile reported by *Pacini et al.* (2019) as representative of conditions during the 2014 SUBICE cruise. The *Pacini et al.* (2019) profile featured a change in salinity of 0.025 between 26 and 33 m. However, the deep-water salinity was fresher (32.7) in 2014 than the water observed in the summer of 2011 (33.1), likely due to the meltwater-driven freshening of the Arctic (*Mauritzen*, 2012; *Woodgate et al.*, 2005). As a result, our winter salinity profile replicated the magnitude and depth of salinity change observed by *Pacini et al.* (2019), but used the higher salinity (33.1) observed in 2011. Although salinity has changed over time in the Chukchi Sea (*Woodgate et al.*, 2012), the modeled winter idealized salinity profile is identical from year to year.

The remaining idealized profiles were created to fit with salinity observations from the 2011 ICESCAPE cruise, with different profiles evaluated by comparing the RMSE and R^2. The profiles that resulted in the best correlation with observations were chosen. To reflect annual differences in fresh water input to the water column due to differences in local ice melting, the salinity in the mixed layer for each year's idealized profiles was scaled linearly from the 2011 profiles depending on the length of the sea ice melt period. In 2011, the second profile had a salinity of 32.8 over a mixed layer of 30 m. The third profile had a salinity of 31.1 over a mixed layer of 12 m. The fourth had a salinity of 32 over a mixed layer of 22 m, and the final profile had a salinity of 32.9 over a mixed layer of 27 m. Each of these profiles had an exponential increase in salinity below the mixed layer

and until 35 m, below which winter profile conditions were maintained throughout the year.

The dates of the idealized salinity profiles were centered around ice melt timing. The first salinity profile is used on the date of sea ice melt, when air temperatures rise above 0°C, and on the date of sea ice advance, when satellite-derived ice concentrations rise above 10%. The second salinity profile is used two-thirds of the way between the date of ice melt onset and the start of sea ice retreat, when ice concentrations reduce below 90%. The third salinity profile is used on the date of sea ice retreat, while the fourth and fifth profiles are used one-third of the length of the ice melt period (ice melt date to start of ice retreat) and the full length of the melt period after sea ice retreat, respectively.

A.2 Biogeochemical Model

A.2.1 Spectral Irradiance.

Spectral irradiance at the air-sea interface was determined using a spectral atmospheric radiative transfer model (*Gregg and Carder*, 1990, as modified by Arrigo et al., 1998a), which was used to calculate direct and diffuse spectral downwelling solar irradiance. Atmospheric inputs were obtained from the National Centers for Environmental Prediction/National Center for Atmospheric Research (NCEP/NCAR) Reanalysis Project 1 (4x daily) and TOMS ozone as described in *Arrigo* (2003). Surface spectral irradiance was corrected for scattering by clouds as in *Dobson and Smith* (1988) - see Figure A.3. Spectral irradiance was binned into 31 wavelengths at 10 nm increments between 400 and 700 nm.

Surface irradiance was specularly reflected depending on one of three surface types - snow, ice, and water/melt pond as in *Arrigo et al.* (1991). For more on how snow, ice, and melt pond timings and thicknesses were established for 1988-2018, see section A.3. When snow-covered, 5% of diffuse and direct light was specularly reflected. For bare ice cover, 5% of diffuse light was specularly reflected, while the reflection of direct light was dependent on sun angle. For melt pond-covered ice, both diffuse and direct light were specularly reflected depending on sun angle, while for open water wind also impacted specular reflection. Light not specularly reflected was assumed to penetrate the surface layer.

Radiative transfer for each wavelength bin was calculated through each layer of snow, ice, and water for each time step using Beer's law such that

$$E_d(z,\lambda) = E_d(z-1,\lambda)e^{-K_d(z,\lambda)z} \tag{A.1}$$

where $E_d(z,\lambda)$ is the spectral irradiance (μmol photons m^{-2} s^{-1} nm^{-1}) at depth z (m) and wavelength λ (nm), $E_d(z\text{-}1,\lambda)$ is the spectral irradiance at the bottom of the previous layer, and $K_d(z, \lambda)$ is the layer-specific spectral diffuse attenuation coefficient (m^{-1}). Different diffuse attenuation coefficients (K_d) were used for dry snow, wet (melting) snow, interior white ice, the scattering layer of white ice,

melting blue ice, and pure water (*Perovich et al.*, 1986). K_d values were further modified by ice algal absorption in the bottom layer of sea ice and water column absorption by phytoplankton, non-algal particles (NAP), and colored dissolved organic matter (CDOM). Absorption spectra for CDOM and NAP vary seasonally in the water column (*Lewis et al.*, 2020), while the chlorophyll-specific phytoplankton absorption spectrum increases over the period of ice retreat each year (*Perovich et al.*, 1986).

Photosynthetically available radiation (PAR; μmol photons m^{-2} s^{-1}) and photosynthetically usable radiation (PUR; μmol photons m^{-2} s^{-1}) were integrated over these wavelength bins for each depth of the water column (*Morel*, 1978), such that

$$PAR(z,t) = \int_{\lambda=400}^{700} E_d(z,\lambda,t)d\lambda \tag{A.2}$$

and

$$PUR(z,t) = \int_{\lambda=400}^{700} E_d(z,\lambda,t)\frac{\alpha^*(\lambda)}{\alpha^*_{max}}d\lambda \tag{A.3}$$

where $\alpha^*{}_{\max}$ is the maximum value attained by the spectral phytoplankton absorption coefficient, $\alpha^*(\lambda)$.

Layer PUR was averaged over the mixed layer and over a 24 hr period to ensure that phytoplankton growing anywhere in the mixed layer were exposed to the same light levels. The depth of the mixed layer was set using the GOTM-derived depth of maximum buoyancy frequency, averaged over a 24 hr period.

A.2.2 Sea Ice Algae

Sea ice algae were modeled prescriptively based on light conditions. Because NH_4^+ made up 0.3% of the total N available during the sea ice algal bloom, algal biomass grew using only the NO_3^- available in the first layer of the water. Once the hourly layer PAR exceeded an algal compensation irradiance (μmol photons m^{-2} s^{-1}; *McMinn et al.* 1999), algae were presumed to grow in the bottom 0.05 m of the sea ice layer (*Selz et al.* 2018). Ice algae (IA) concentrations changed according to

$$\frac{\mathrm{d}IA}{\mathrm{d}t} = \mu_{IA} - loss_{IA} \cdot *IA \tag{A.4}$$

where μ_{IA} represents the growth rate of ice algae and $loss_{IA}$ is the rate of ice algal disassociation (5% of total ice algal biomass). Ice algae grew logistically in an approximation of *Welch and Bergmann* (1989) but using a maximum Chl layer concentration of 30 mg m^{-2} (*Arrigo*, 2017). Layer chlorophyll (Chl) increased according to

$$Chl = \frac{L}{1 + e^{-k(x-x_0)}} \tag{A.5}$$

where k is the logistic growth rate (mg Chl a m^{-2} d^{-1}), x is the date, and x_0 is the x value of the sigmoid midpoint (d). Ice algal Chl a concentration was converted to N to allow for the calculation of μ_{IA} and $loss_{IA}$. However, if there was insufficient NO_3^- to support this growth rate, N-based ice algal growth was set to match available NO_3^-. After the ice melt date, ice algae sloughed off at a rate of 20% d^{-1} of the biomass present on the ice melt date. Ice algae that disassociated or sloughed off at the end of the ice algal period was added to the top layer of the detrital pool.

A.2.3 Phytoplankton.

The two functional groups of phytoplankton represented in this model are large diatoms (*Arrigo et al.* 2012, *Hill and Cota* 2005) and small flagellates (*Hill and Cota* 2005). Phytoplankton functional groups differ in their nutrient utilization, growth rate, and photoacclimation parameters.

The rate of change for each of the two phytoplankton functional groups (Phy) for each timestep and at each depth is calculated as

$$\frac{\mathrm{d}Phy}{\mathrm{d}t} = (\mu_{phy} - mort_{phy})Phy - (g_{zoo \rightarrow phy})Zoo + Diff f_{phy} + Adv_{phy} \tag{A.6}$$

where different phytoplankton (Phy) groups grow as a function of specific relationships with temperature, PUR, and nutrients (μ_{phy}; *Arrigo* 2003) and are lost through mortality ($mort_{phy}$) and grazing by zooplankton ($g_{zoo \rightarrow phy}$), a function of zooplankton biomass (Zoo). Layer concentrations can increase or decrease due to positive or negative transport processes between layers ($Diff_{phy}$ and Adv_{phy} - see section A.2.7).

The phytoplankton growth rate (μ_{phy}) is calculated at each depth and every timestep for both phytoplankton functional groups, such that

$$\mu_{phy} = \mu_{max} \cdot min(L_{lim}, N_{lim}) \tag{A.7}$$

where μ_{max} is the temperature-specific maximum growth rate and phytoplankton grow proportionally to the minimum of two limitation terms, L_{lim} (the light limitation term) and N_{lim} (the nutrient limitation term).

The temperature-specific maximum growth rate (μ_{max}) is calculated at each depth and every timestep for both phytoplankton functional groups, such that

$$\mu_{max} = \mu_0 \cdot e^{(T \cdot r_0)} \tag{A.8}$$

where μ_0 is the specific growth rate at 0°C, T is the temperature, and r_0 is 0.0633, the growth constant for phytoplankton (*Eppley* 1972).

The light limitation term, L_{lim}, is a function of PUR, calculated for each depth and at each

timestep, and of the photoacclimation parameter, E_k, for each phytoplankton functional group:

$$L_{lim} = 1 - e^{-PUR/E_k} \tag{A.9}$$

Large phytoplankton E_k varied between 54.9 and 67.6 μmol photon m^{-2} s^{-1} depending on light history (*Arrigo et al.*, 2014). These E_k values were measured for using photosynthetron-produced PAR on the ICESCAPE 2011 cruise. Since phytoplankton functional groups were modeled using PUR, these values were modified to reflect that only 38.3% of photosynthetron-produced light is usable by phytoplankton. For layer daily mean PUR values below 21.0 or above 25.9, E_k is set to 21.0 and 25.9, respectively. For PUR values between this minimum and maximum value, E_k equals PUR.

N_{lim} is the maximum of the two nutrient sources, such that

$$N_{lim} = max(\mathrm{NO_3^-}_{lim}, \mathrm{NH_4^+}_{lim}) \tag{A.10}$$

where $NO_{3\,lim}^-$ is the NO_3^- limitation term and $NH_{4\,lim}^+$ is the NH_4^+ limitation term.

The NO_3^- limitation term, $NO_{3\,lim}^-$, is a function of the NO_3^- concentration of each depth and each timestep and the half-saturation constant for NO_3^- uptake (K_{s_NO3}) by each phytoplankton functional group (Table 2):

$$\mathrm{NO_3^-}_{lim} = \frac{NO_3^-}{K_{S\_NO3} + NO_3^-} \tag{A.11}$$

The NH_4^+ limitation term, $NH_{4\,lim}^+$, is a function of the NH_4^+ concentration of each depth and each timestep and the half-saturation constant for NH_4^+ uptake (K_{s_NH4}) by each phytoplankton functional group (Table 2):

$$\mathrm{NH_4^+}_{lim} = \frac{NH_4^+}{K_{S\_NH4} + NH_4^+} \tag{A.12}$$

In order to ensure that phytoplankton assimilation of the two dissolved organic nutrient pools ($\mu_{phy \to NO3}$ and $\mu_{phy \to NH4}$) is a function of the nutrient concentration in the layer and the half-saturation constant of the phytoplankton class, assimilation at each timestep and each depth is a function of the $NO_{3\,lim}^-$ and $NH_{4\,lim}^+$ terms, such that

$$\mu_{phy \to NO3} = \mu_{phy} \cdot \frac{\mathrm{NO_3^-}_{lim}}{\mathrm{NO_3^-}_{lim} + \mathrm{NH_4^+}_{lim}} \tag{A.13}$$

and

$$\mu_{phy \to NH4} = \mu_{phy} \cdot \frac{\mathrm{NH_4^+}_{lim}}{\mathrm{NO_3^-}_{lim} + \mathrm{NH_4^+}_{lim}} \tag{A.14}$$

A.2.4 Zooplankton

The two functional groups of zooplankton represented in this model approximate the large copepods (*Ashjian et al.*, 2003; *Sherr et al.*, 2008) and phagotrophic protists (*Sherr et al.*, 2009) common in the Arctic. Small zooplankton graze small phytoplankton, while large zooplankton graze both large phytoplankton and small zooplankton (*Ashjian et al.*, 2003). Zooplankton functional groups are differentiated by different food sources (and can be differentiated using different temperature-dependent growth rates). The rate of change at each timestep and depth for both zooplankton functional groups is calculated as

$$\frac{\mathrm{d}Zoo}{\mathrm{d}t} = (1-\gamma)(g_{zoo})Zoo - mort_{zoo} \cdot Zoo - ex_{zoo} \cdot Zoo + Diff_{zoo} + Adv_{zoo} \tag{A.15}$$

where zooplankton (Zoo) biomass grows through temperature and food availability-dependent grazing rates (g_{zoo}) and is lost through mortality ($mort_{zoo}$, a fraction of zooplankton biomass), excretion (ex_{zoo}, a fraction of zooplankton biomass), and assimilation inefficiency (γ). For large zooplankton, mortality is assumed to add to the biomass of upper trophic levels, while small zooplankton mortality instead contributes to the detrital pool. Layer concentrations can increase or decrease due to positive or negative transport processes between layers ($Diff_{zoo}$ and Adv_{zoo} - see section A.2.7).

The grazing rate is set as a function of temperature and food source limitation, such that

$$g_{zoo} = g_0 F_{lim} \tag{A.16}$$

where g_0 is the temperature-dependent maximum growth rate at a given depth and timestep and F_{lim} is the maximum of the food source limitation terms.

Maximum zooplankton growth rate is calculated based on a relationship between temperature and N-based growth rate (*Campbell et al.*, 2001) such that

$$g_0 = 0.0175T + 0.0443 \tag{A.17}$$

where T is the temperature (°C). The experiments that yielded this relationship were conducted by incubating stage N3 to C5 *Calanus finmarchicus* individuals in tanks with variable temperature treatments (4°C, 8°C, 12°C). The N-based specific growth rate (d^{-1}) over this temperature range increased linearly with temperature. This relationship is used for both zooplankton classes.

Unlike in the *Campbell et al.* (2001) lab experiment, modeled zooplankton growth is often limited by food scarcity. A Monod-style limitation term for each food source i for each zooplankton species, F_{lim}, is used, such that

$$F_{lim}(i) = \frac{F(i) - F(i)_{min}}{K_{S\_F}(i) + F(i) - F(i)_{min}} \tag{A.18}$$

where *F(i)* is the food source, $F(i)_{min}$ is the minimum concentration of the food source (to ensure *F(i)*

never becomes negative - see Table 1) and $K_{s\_F\ (i)}$ is the half-saturation constant for the food source (Table 2). For large zooplankton, which have two food sources, the maximum $F_{lim}(i)$ term modifies the growth rate, while for small zooplankton, F_{lim} is set by the availability of small phytoplankton.

For large zooplankton, which consume both large phytoplankton and small zooplankton functional groups, zooplankton grazing (g_{zoo}) of the two groups is partitioned fractionally by the relative concentration of each to the total food in the layer at that timestep, such that

$$(g_{lzoo \rightarrow lphy}) = g_{lzoo} \frac{Lphy}{Lphy + Szoo} \tag{A.19}$$

and

$$(g_{lzoo \rightarrow szoo}) = g_{lzoo} \frac{Szoo}{Lphy + Szoo} \tag{A.20}$$

where $g_{lzoo \rightarrow lphy}$ and $g_{lzoo \rightarrow szoo}$ are the grazing of large zooplankton on large phytoplankton ($Lphy$) and small zooplankton ($Szoo$), respectively.

A.2.5 Detritus

The model includes a single detrital class. Rates of change for detrital N at each timestep and for each depth are calculated as

$$\begin{aligned} \frac{\mathrm{d}Det}{\mathrm{d}t} &= mort_{IA} + (mort_{phy})Phy + (mort_{szoo})SZoo + \gamma(g_{zoo})Zoo \\ &\quad -(Remin_{det \rightarrow NH4})Det - w\frac{\mathrm{d}Det}{\mathrm{d}z} + Diff_{det} + Adv_{det} \end{aligned} \tag{A.21}$$

where detritus is produced through ice algal or phytoplankton mortality, small zooplankton mortality, and zooplankton assimilation inefficiency (γ), and is lost due to remineralization ($Remin_{Det \rightarrow NH4}$, a fraction of the detrital pool) and sinking (w). Layer concentrations can increase or decrease due to positive or negative transport processes between layers ($Diff_{det}$ and Adv_{det} - see section A.2.7).

A.2.6 Inorganic Nutrients

The model includes both NO_3^- and NH_4^+, the most abundant components of the dissolved inorganic N pool (*Codispoti et al.*, 2005). Other inorganic nutrients, such as phosphate and silicate, do not limit phytoplankton growth in the Chukchi Sea (*Sakshaug*, 2004) and are not included in the model. Rates of change for NO_3^- and NH_4^+ at each timestep and for each depth are calculated as

$$\frac{\mathrm{d}NO_3^-}{\mathrm{d}t} = (Nitr_{NH4 \rightarrow NO3})NH_4^+ - (\mu_{phy \rightarrow NO3})Phy - (\mu_{IA})IA + Diff_{NO3} + Adv_{NO3} \tag{A.22}$$

and

$$\frac{\mathrm{d}NH_4^+}{\mathrm{d}t} = ex_{zoo} + (Remin_{det\rightarrow NH4})Det - (\mu_{phy\rightarrow NH4})Phy \\ -(Nitr_{NH4\rightarrow NO3})NH_4^+ + Diff_{NH4} + Adv_{NH4} \quad \text{(A.23)}$$

where NO_3^- is produced through nitrification ($Nitr_{NH4\rightarrow NO3}$, a linear function of depth and NH_4^+ concentration) and is lost due to assimilation by ice algae and phytoplankton ($\mu_{phy\rightarrow NO3}$). NH_4^+ is produced through zooplankton excretion and detrital remineralization and lost due to phytoplankton assimilation of NH_4^+ ($\mu_{phy\rightarrow NH4}$) and nitrification. Layer concentrations of NO_3^- and NH_4^+ can increase or decrease due to positive or negative transport processes between layers ($Diff_{NO3}$, Adv_{NO3}, $Diff_{NH4}$, and Adv_{NH4} - see section A.2.7).

A.2.7 Diffusion and Advection

In addition to the growth and loss processes described above, all state variables can have their concentrations altered in any given layer due to diffusion and advection.

Diffusion between layers is calculated according to Fick's law at each timestep such that, in the absence of a boundary condition,

$$Diff_X = \frac{X_{(z+1)} - X_{(z)}}{dz^2} \cdot D_{(z+1)} + \frac{X_{(z-1)} - X_{(z)}}{dz^2} \cdot D_{(z)} \quad \text{(A.24)}$$

where $Diff_X$ is the change in any state variable concentration X at depth z and time t due to diffusion and D is the time- and depth-dependent diffusion coefficient ($m^2\ s^{-1}$). This diffusion coefficient is the sum of the GOTM-derived turbulent diffusivity coefficient for salt (ranging between 0 and 0.17 $m^2\ s^{-1}$) and a background turbulent diffusivity ($5 \cdot 10^{-4}\ m^2\ s^{-1}$ - *Rainville and Winsor*, 2008).

The Chukchi Sea is characterized by strong advection. Water enters the sea through the narrow Bering Strait and empties into the Canada Basin. Between 2001 and 2011, advection increased by 50%, with throughflow at the Bering Strait reaching 1.1 Sv per year by 2011 (*Woodgate et al.* 2012). In order to run the model for multiple years without substantially reducing the available N each year, the model must include advection. We simulated advection by relaxing all water column state variables towards prescribed profiles. This was accomplished in the same way that relaxation towards idealized profiles was performed in GOTM (*Burchard et al.* 1999):

$$Adv_X = -\frac{1}{\tau_R(X)} \cdot (X - X_m) \quad \text{(A.25)}$$

where Adv_X is the change in state variable concentration X due to advection, $\tau_R(X)$ is the relaxation timescale (in seconds), and X_m is a prescribed profile of that state variable. Using this formulation, a long relaxation timescale produces a weak forcing of the state variable profile towards the prescribed

profile. As the state variable profile approaches the prescribed profile, the rate of change of the state variable profile towards the prescribed profile diminishes. A relaxation timescale of 30 d for the mixed layer and 60 d for bottom waters was used. This timescale was the weakest relaxation strength that still enabled bottom-water concentrations of NO_3^- to fully restore to the winter concentration before the beginning of the under-ice bloom period the following year.

There are not sufficiently high-quality observational data to provide prescribed profiles of all state variables between 1988 and 2018. To circumvent this issue, we used manipulated model output as the prescribed profiles. This was accomplished by running the model two times. In the first run only, state variables were reset to the initial conditions on January 1st of each year. This first run was then used to produce prescribed profiles, which provided input to the second model run. Because water is advected from the south, sea ice cover of the advecting water diminishes earlier, allowing an earlier start to primary production. Thus, model profiles generated for Day+1 (first run) were used as prescribed profiles for Day+0 (second run), with further modification made to restore NO_3^- concentration in the winter.

NO_3^- prescribed profiles were further manipulated from model data by gradually restoring to the winter NO_3^- concentration of 16 mmol m^{-3} throughout the water column in the standard run. This restoration initiated on the autumn freeze date, the first 24-hr period in the autumn when NCEP-NARR 2 m air temperatures averaged below 0°C at the model location. If air temperatures diminished below 0°C before October 25th (DOY 300) when incident irradiance was still high, nudging the water column NO_3^- concentrations substantially changed the total annual production. As a result, for years with an early autumn freeze date, DOY 300 was used as the starting date for NO_3^- restoration. NO_3^- profiles were restored to the winter concentration using linear interpolation. This interpolation extended between the autumn freeze date and the date when ice concentration exceeded 50% plus 7 days. For example, in 2011, air temperature first fell below 0°C on DOY 294 and ice concentration exceeded 50% on DOY 328. When restoration started on DOY 300, the profiles that the model is relaxing towards had NO_3^- concentrations of 0 - 0.02 mmol m^{-3} in the top 15 m. NO_3^- concentrations in the relaxation profiles increase linearly such that, by DOY 335, the profiles have NO_3^- concentrations of 16 mmol m^{-3} throughout the water column.

A.3 Model Ice Condition Forcing

A.3.1 Sea ice thickness

Modeled sea ice layer thickness for each year was set using remote sensing reanalysis products. Because ice thickness increases with age, an Arctic sea ice age product (*Tschudi et al.*, 2019) was used to approximate ice thickness. This conversion was fit using the *Tschudi et al.* (2016) compilation of average spring (February-March 2004-2008) Ice, Cloud, and land Elevation Satellite (ICESat) ice

thicknesses by age, such that

$$thickness = max \frac{age}{k + age} \tag{A.26}$$

where age is the ice age (d), thickness is the ice thickness (m), and a least squares regression gives k = 155.08 (d^{-1}) and max = 2.90 (m). Ice greater than 5 years old was omitted from the regression because higher age estimates are considered imprecise (*Tschudi et al.* 2019).

For each year between 1988 and 2018, weekly ice age in years (*Tschudi et al.*, 2019) was extracted between March 1st and the ice melt date for the 62.5 by 62.5 km box centering on the model location. The choice of box size (12.5 km, 37.5 km, or 62.5 km) altered the ice thickness within a given year but had no impact on the mean ice thickness over the time series or the lack of trend through time. Ice age in days was calculated as the time between the date when satellite-derived ice concentration surpassed 50% in the previous year and the date of ice melt (when mean air temperatures were above 0°C for at least 24 hrs). For ice >1 yr old, 365 days per year were added to the ice age. Because ice age at the model location was often variable week to week within a given year, ice thickness was computed for each week and a weighted mean of sea ice thickness for the March 1 to ice melt date period was used as the maximum ice thickness input to the model.

Following the ice melt date, ice thickness diminishes linearly until the start of ice retreat. The rate of change in ice thickness was calculated using 50% of the total ice melt necessary to produce the idealized salinity profiles from (see section A.1.2) and assumed to be constant (0.0073 m d^{-1}) between 1988 and 2018 - thus, the longer the ice melt to ice retreat period, the greater the reduction in ice thickness.

A.3.2 Snow and melt pond thickness

Thicknesses for the modeled snow and melt pond layers were set using model results. Two different snow models, SnowModel-LG (*Stroeve et al.* 2020 *Liston et al.* 2020) and CPOM (*Zhou et al.* 2021), were used to set the maximum snow thickness. Both of these models used the European Centre for Medium-Range Weather Forecasts (ECMWF) atmospheric reanalysis products: SnowModel-LG used 5th Generation (ERA5) reanalysis products, while CPOM used the ERA-Interim products. For model location, SnowModel-LG (resolution of 25 km) had consistently thicker snow cover predictions, while for CPOM (12.5 km resolution) the model location predicted thinner snow cover. The snow thickness used as input in the model was a mean of SnowModel-LG and CPOM-computed thicknesses for January 1st to the snow melt date for each year (see section A.3.4).

Final melt pond thickness was derived from snow thickness. Melt ponds concentrate the water formed as snow and the sea ice surface melts, but water is more dense than the snow. As a result, in this model, melt ponds were assumed to grow to 90% of the thickness of the maximum snow depth between melt pond formation and ice breakup date. Between sea ice reduction and break-up, melt ponds are assumed to maintain their maximum thickness.

A.3.3 Melt pond areal coverage

As in *Webster et al.* (2015), melt pond areal coverage increases linearly over time from 0% areal coverage on the day prior to melt pond formation to a maximum of 54% for first-year ice and 38% for multi-year ice. For first-year ice, areal coverage increases at 1.39% per day (reaching maximum extent in 37 days), while for multi-year ice, melt pond coverage increases at 0.64% per day (reaching their maximum extent in 58 days). For years where mean age is between first- and second-year ice, a weighted mean of ice age is used to calculate the maximum and rate of increase for melt pond areal coverage. Between the start of sea ice breakup and retreat, melt ponds are assumed to maintain their maximum areal extent.

A.3.4 Snow melt date

Modeled snow melt date was set for each year using the mean NSIDC snow melt onset date (75 km resolution; *Anderson et al.*, 2019). Following this date, the snow layer K_d changed to melting snow (from dry snow) and snow thickness diminished linearly until the ice melt and melt pond formation date. If snow melted close to or after the ice melt date, the snow melt date was moved to 5 days prior to the ice melt date.

A.4 Model Performance Methods

A.4.1 Comparing modeled and observed data

Modeled NPP was validated using MODIS-derived NPP (*Lewis et al.*, 2020). Surface Chlorophyll *a* (Chl) concentrations were determined from Level 3 MODIS Aqua ocean color data. A modified version of the standard empirical NASA-Chl *a* algorithm was used to reflect the high pigment packaging and chromophoric dissolved organic matter (CDOM) concentrations that make the Arctic Ocean bio-optically unique (*Lewis et al.*, 2020; *Lewis and Arrigo*, 2020). Daily NPP for 2003-2018 was computed for a 125 km by 125 km box centered on the model location from satellite-derived Chl *a*, SST, and sea-ice cover using the algorithm of *Arrigo et al.* (2008) as modified by *Pabi et al.* (2008). This large box size was chosen to reduce data loss due to cloud cover, as a smaller box size greatly reduced the available observations.

Because remote sensing-derived estimates of NPP are computed from observations of ocean color over approximately the top 10 m of the water column, comparisons are restricted to NPP modeled in just the upper 10 m.

Modeled NO_3^- was validated using surface NO_3^- concentrations observed during the ICESCAPE and SUBICE cruises (*Arrigo et al.*, 2017; *Lowry et al.*, 2015) in 2011 and 2014 and from mooring data (*Mordy et al.*, 2020) from 2010 to 2017. These observations were compared to mean daily NO_3^- concentrations across the top 15 m of the water column for 2010-2017.

A.4.2 Sensitivity Analysis

In order to test how sensitive the model was to specific parameter values, the model was run using forcing data for the year 2011. The 27 parameters were then altered one at a time by ± 20%. The impact of each parameter on the model results was evaluated by calculating the change in annual NPP and the change in the date of maximum NPP when compared to the run with standard parameters.

A.5 Model Performance Results

A.5.1 GOTM Performance

Modeled SST between 1988 and 2018 reproduced 83.8% of the variance in the satellite-derived SST (slope=0.805, RMSE=0.9836, p<0.001, n=11313). Modeled SST was most biased in the late summer and autumn (<DOY 200; Figure A.4), when GOTM temperatures tended to diminish earlier than observations. However, this part of the year accounted for a small proportion of total NPP (under 7% on average).

A.5.2 CAOS model

The spectral irradiance model used here was modified from a previously validated model used in the Antarctic (*Arrigo et al.*, 1998a). When using observed ice and melt pond thicknesses from ICESCAPE 2011 (*Light et al.*, 2015), the spectral irradiance model replicates the observed percent transmission of surface irradiance. Transmission ranged from 13% to 58% for ponded ice during ICESCAPE 2011, while the ice model produced transmissions ranging from 16% to 53% (mean transmission was 30.4%). Through un-ponded ice, ICESCAPE observations of transmission ranged and from 5% to 22%, while the model produced transmissions ranging from 3% to 21% (mean transmission was 6.7%). On average, observed ponded ice transmitted 4.4 times more light than bare ice (*Light et al.*, 2015), while modeled melt pond-covered ice transmitted 4.5 times more light than bare ice.

Satellite-derived NPP is unlikely to effectively replicate modeled NPP because of the high proportion of NPP in the UI and MIZ periods. Despite this challenge, satellite-derived NPP in the MIZ and OW periods compared favorably to modeled NPP over the top 10 m for 2003-2018 (Figure A.5a). In one year, 2015, MODIS-derived NPP peaked at 1.2 g C m^{-2} d^{-1} while the model location was still 12% ice-covered, indicating a bloom that was initiated in the under-ice period (*Lowry et al.*, 2014). The slope and timing of declining daily NPP over the open-water period generally matched but was delayed by 1-2 weeks in some years, in part due to the model assuming homogeneity in ice condition timing over an area where ice retreat timing varies. Additionally, in a few years (2007 and 2017, in particular), the model did not replicate an increase in NPP in late September, as was produced

by the satellite-derived record. Because the model assumed very slow advection and restoration of nitrate to the mixed layer, it may under-predict the frequency of autumn blooms.

Modeled surface NO_3^- concentrations also matched well with cruise and mooring-derived observations from 2010-2017 (Figure A.5b), particularly over the spring bloom period. Both observed and modeled wintertime NO_3^- concentrations peaked at 15.8 mmol m^{-3}. Observed and modeled NO_3^- concentrations diminished from 13.04 mmol m^{-3} on day of year (DOY) 138 and 139, respectively, and to 0.04 mmol m^{-3} on DOY 178 and 174, respectively. Observed NO_3^- concentrations at the moorings remained between 0 and 2.2 mmol m^{-3} throughout the summer and autumn, finally increasing from 3 mmol m^{-3} on DOY 309 to 15 mmol m^{-3} by DOY 331. This wintertime increase in NO_3^- concentration was substantially slower in the model due to the slow relaxation simulating advection in the model; modeled surface NO_3^- concentrations increased from 3 to 15 mmol m^{-3} between DOY 322 and DOY 38. This discrepancy in observed and modeled surface NO_3^- concentrations, however, is during the polar night at the model location and as a result does not impact annual NPP values.

A.5.3 Sensitivity Analysis

The model was sensitive to only 3 of the 26 model parameters tested. Altering the large phytoplankton E_k or μ_0 or the winter NO_3^- concentration by ±20% altered bloom magnitude by >5% (Table A.1). The model was most sensitive to the winter NO_3^- concentration, altering by 16-17% when this parameter was altered by 20%. The date of maximum production was altered by 3-6 days when large phytoplankton E_k and μ_0 were altered by 20% (Table A.1).

A.5.4 Annual cycles for different water column bloom types

The three different water column bloom types (UI-dominated, MIZ-dominated, and mixed-dominance blooms) have substantially different annual cycles of NO_3^-, NH_4^+, large and small phytoplankton, and large and small zooplankton (Figures A.6, A.7, and A.8 feature UI-dominated, MIZ-dominated, and mixed-dominance years, respectively). The UI-dominated bloom features large phytoplankton production down to 30 m during the UI period and a small SCM from 30-35 m in the OW period (Figure A.6c). Both the MIZ-dominated and mixed-dominance years featured shallower initial blooms (12 and 15 m, respectively; Figure A.7c and A.8c) and slightly shallower SCMs (< 30 m) than the UI-dominant years. There is also greater NO_3^- drawdown in UI-dominated years than in other years, and lower small phytoplankton NPP and zooplankton concentrations than in MIZ-dominant and mixed dominance years. Years with very low ice algal production, including the year used as an example of a MIZ-dominant year (2010), do not feature a significant increase in surface NH_4^+ concentrations that results due to the remineralization of sinking ice algal biomass.

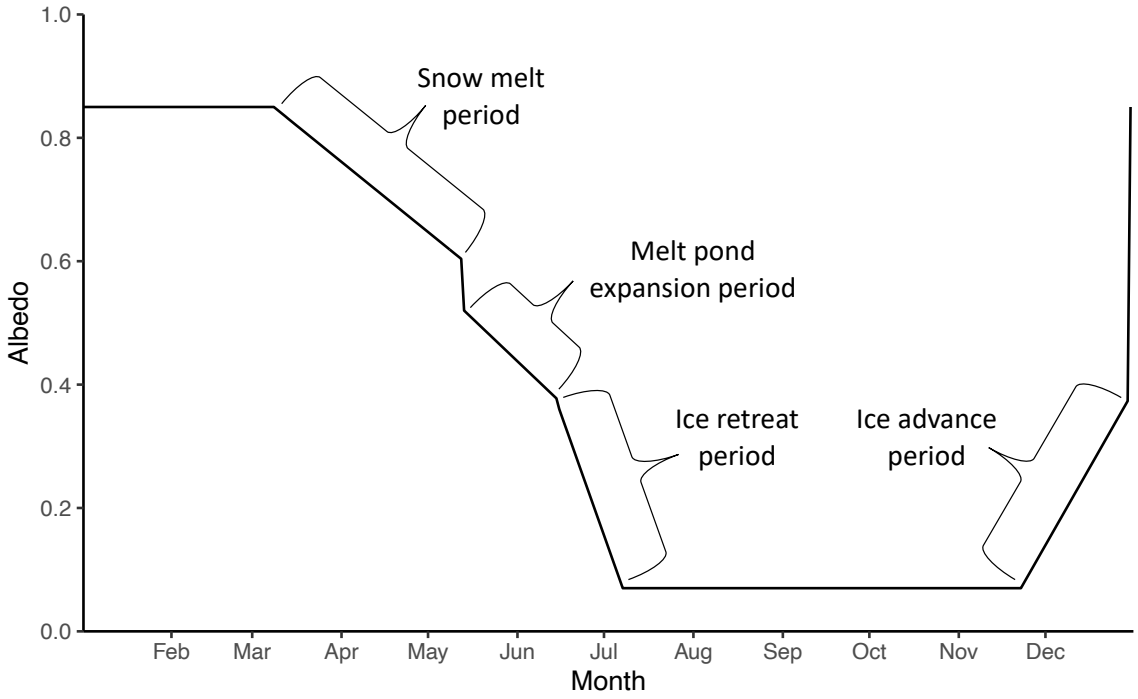

Figure A.1: Albedo used in the standard model run (2011) in GOTM. Periods of changing albedo (labeled brackets) are initiated and terminated based on satellite-derived changes in snow and sea ice conditions. Rates of albedo change during each period are provided by *Perovich and Polashenski* (2012).

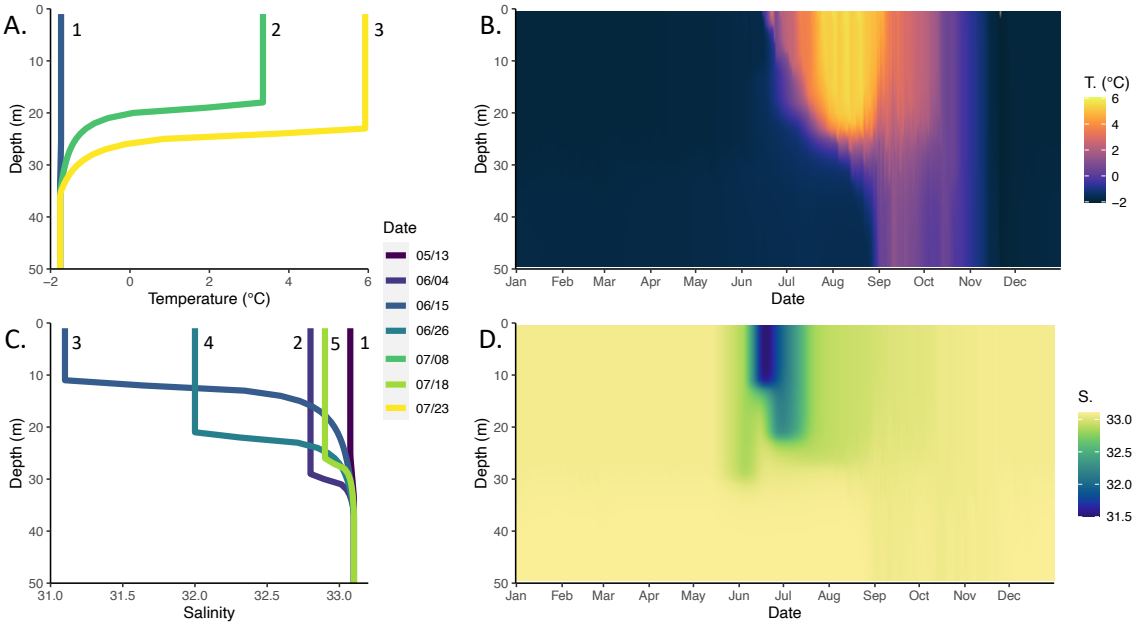

Figure A.2: Idealized profiles for the standard model run for (A) temperature (°C) and (B) salinity, informed by *in situ* observations from the 2011 ICESCAPE campaign. GOTM is relaxed towards these profiles, producing annual (C) temperature (°C) and (D) salinity conditions for the model location between January 1 and December 31, 2011.

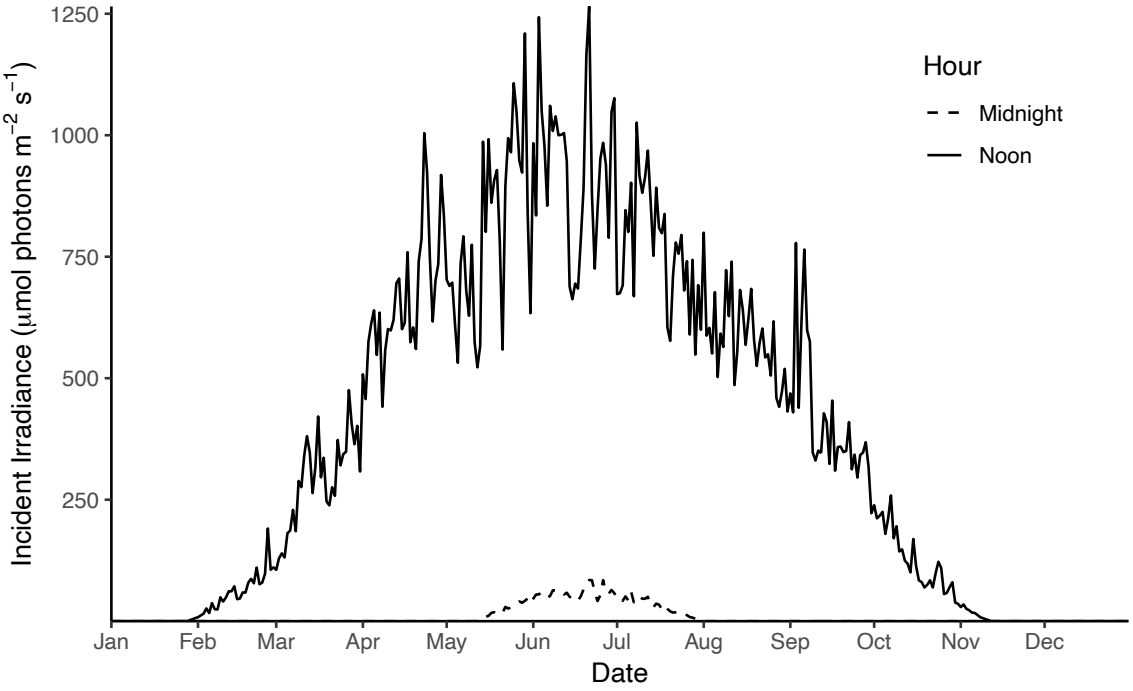

Figure A.3: Cloud-adjusted incident irradiance (μmol photons m^{-2} s^{-1}) at midnight (dashed line) and noon (solid line) for 2011. Direct and diffuse light is computed hourly by *Gregg and Carder* (1990), as modified by *Arrigo et al.* (1998a), for the model location. Irradiance was cloud-adjusted as per *Dobson and Smith* (1988).

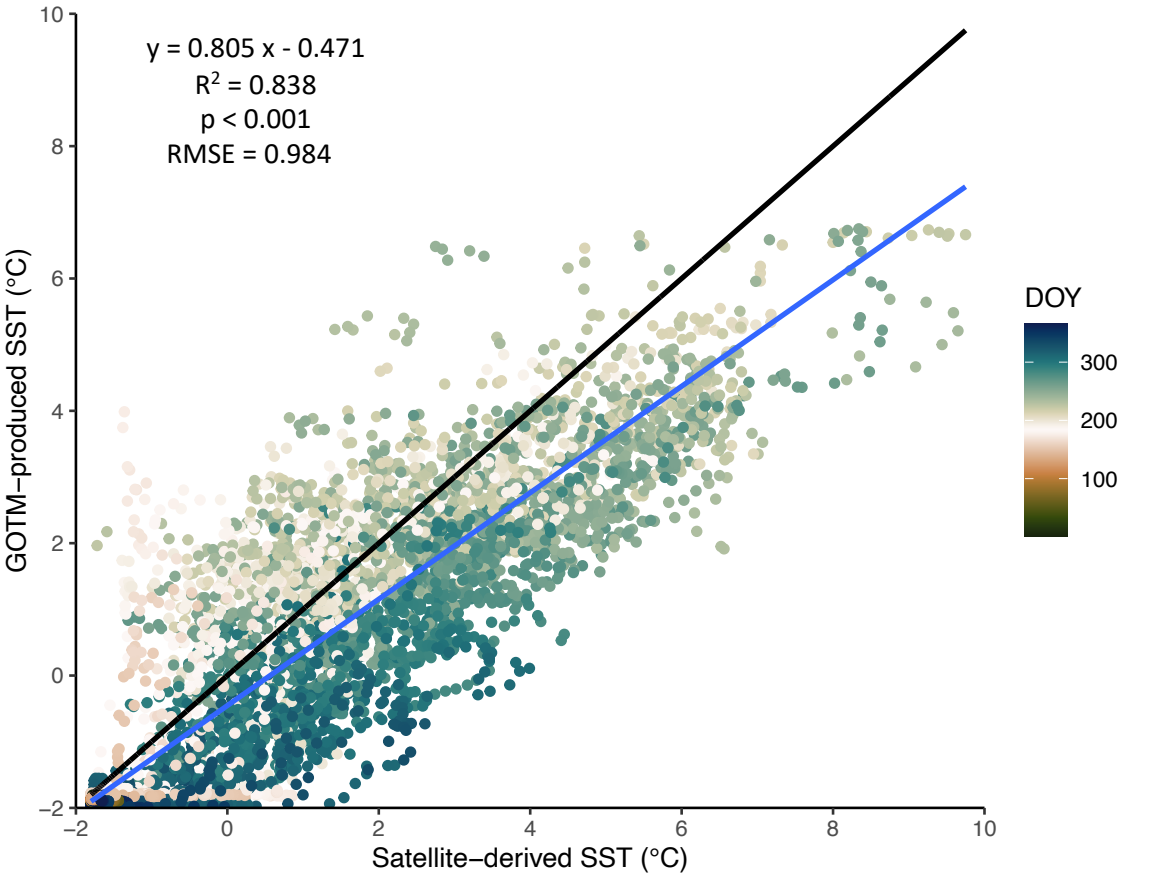

Figure A.4: Scatterplot of daily satellite-derived vs. GOTM-produced sea surface temperature (SST) by DOY (colorbar) for 1988 to 2018. The blue line is the best fit and the black line is the the one-to-one fit line.

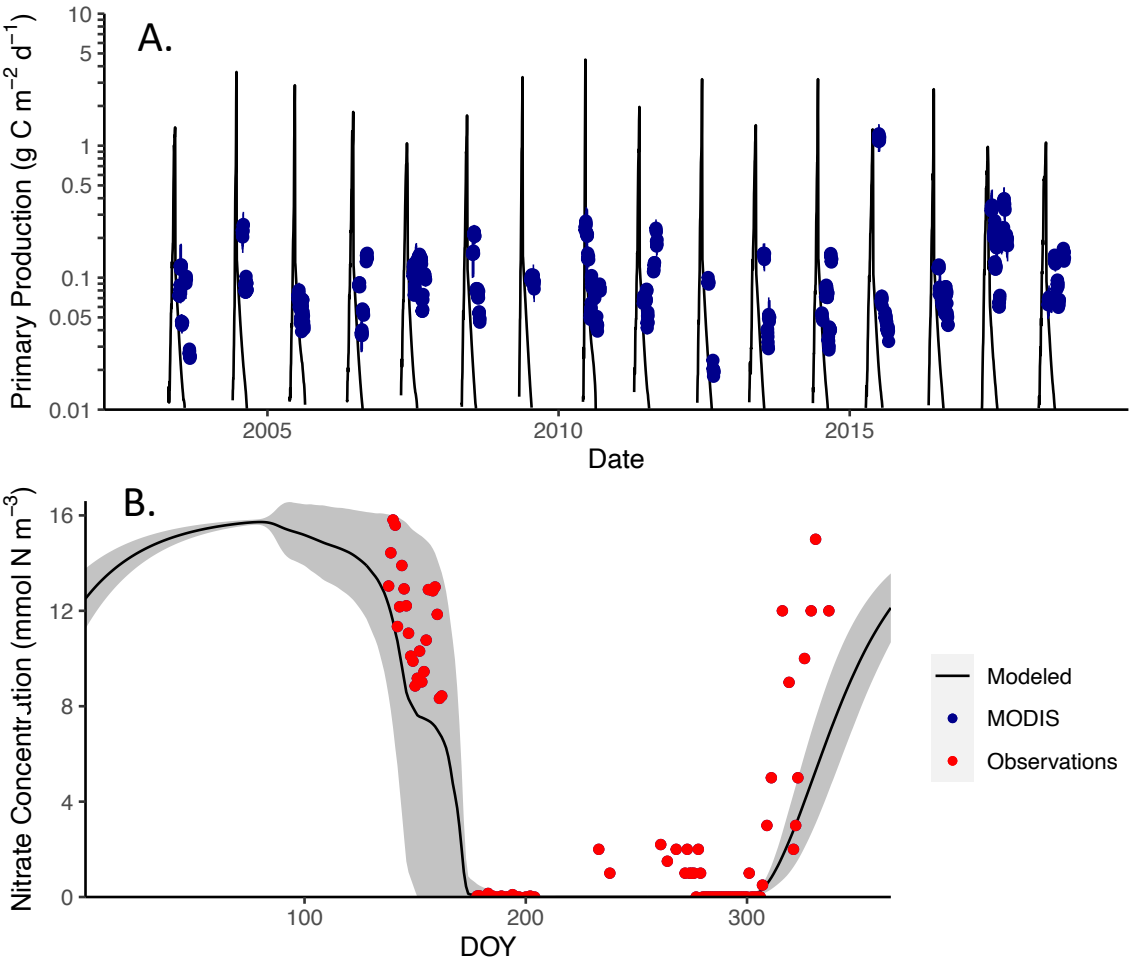

Figure A.5: Comparison of modeled (black lines) to observed (circles) (A) primary production (g C m^{-2} d^{-1}) and (B) surface nitrate concentrations (mmol N m^{-3}). Modeled primary production over the top 10 m (2003-2018) was compared to MODIS-derived production (blue points, with standard deviation lines) computed over the top 10 m. Mean modeled nitrate concentrations over the top 15 m between 2010 and 2017 (black line, with standard deviation in grey) are compared to *in situ* surface observations (*Arrigo et al.* 2017, *Lowry et al.* 2015, *Mordy et al.* 2020) between 2010 and 2017.

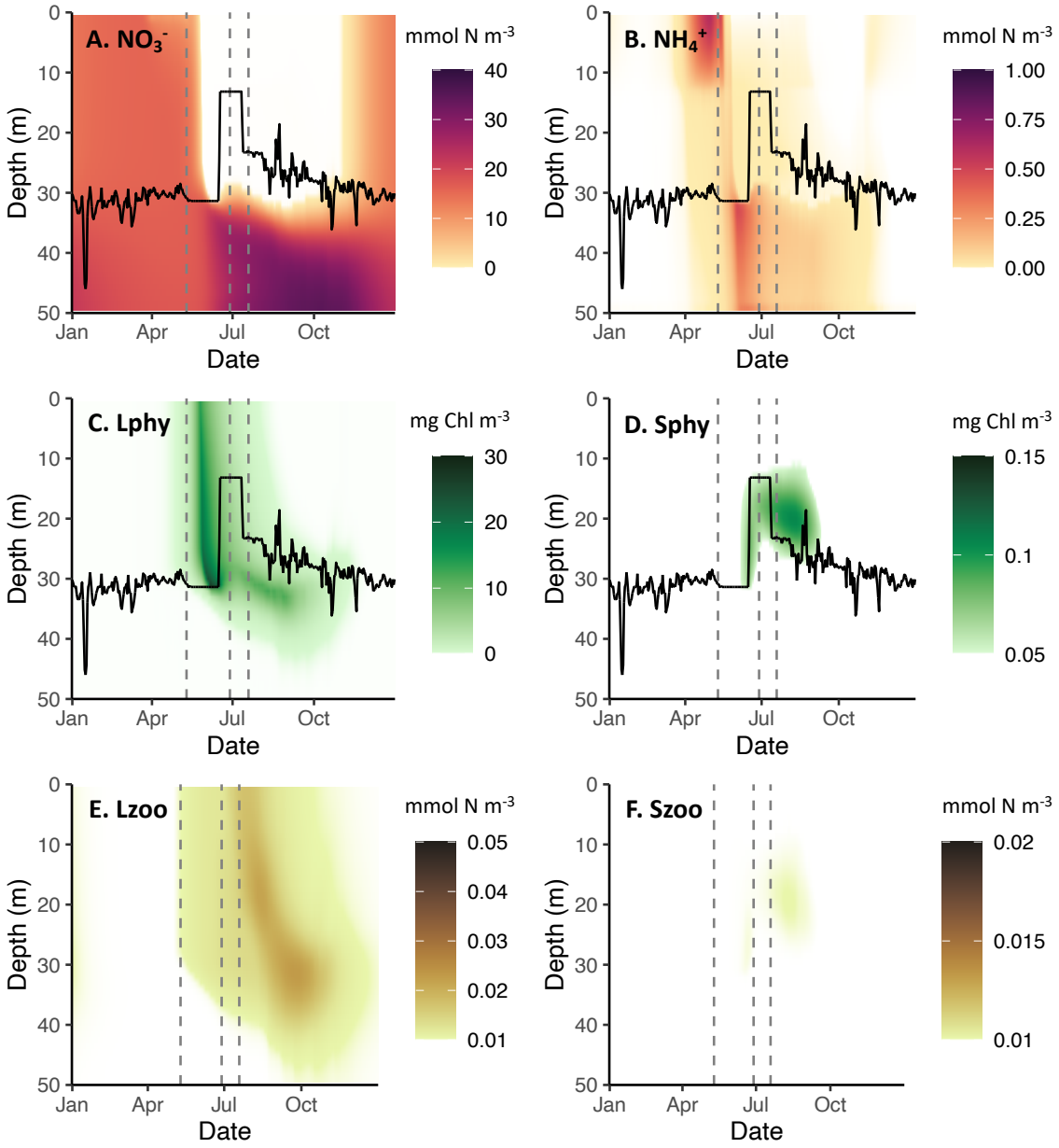

Figure A.6: Annual depth vs. time plots of (A) nitrate (NO_3^-), (B) ammonium (NH_4^+), (C) large phytoplankton (Lphy), (D) small phytoplankton (Sphy), (E) large zooplankton (Lzoo), and (F) small zooplankton (Szoo) for 2013, a UIB-dominant bloom year. Black lines (A-D) represent the mixed layer depth, calculated based on GOTM-derived buoyancy frequency. Grey dashed lines on each subplot represent, from left to right, the date of ice melt, the start of ice retreat (which marks the end of the UI period and start of the MIZ period), and the end of ice retreat (marking the end of the MIZ period and beginning of the OW period).

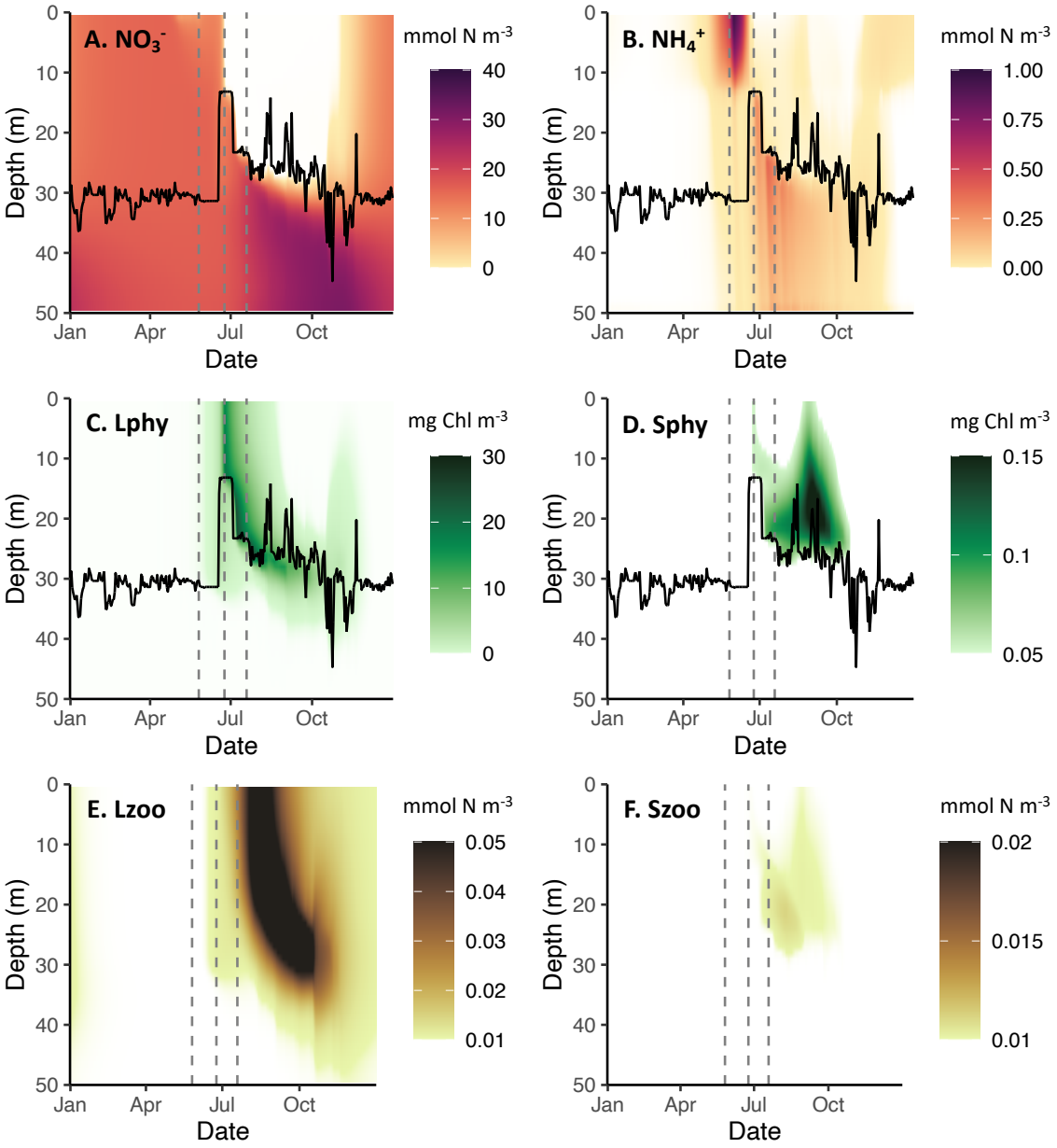

Figure A.7: Annual depth vs. time plots of (A) nitrate (NO_3^-), (B) ammonium (NH_4^+), (C) large phytoplankton (Lphy), (D) small phytoplankton (Sphy), (E) large zooplankton (Lzoo), and (F) small zooplankton (Szoo) for 2005, a mixed-dominance bloom year. Black lines (A-D) represent the mixed layer depth, calculated based on GOTM-derived buoyancy frequency. Grey dashed lines on each subplot represent, from left to right, the date of ice melt, the start of ice retreat (which marks the end of the UI period and start of the MIZ period), and the end of ice retreat (marking the end of the MIZ period and beginning of the OW period).

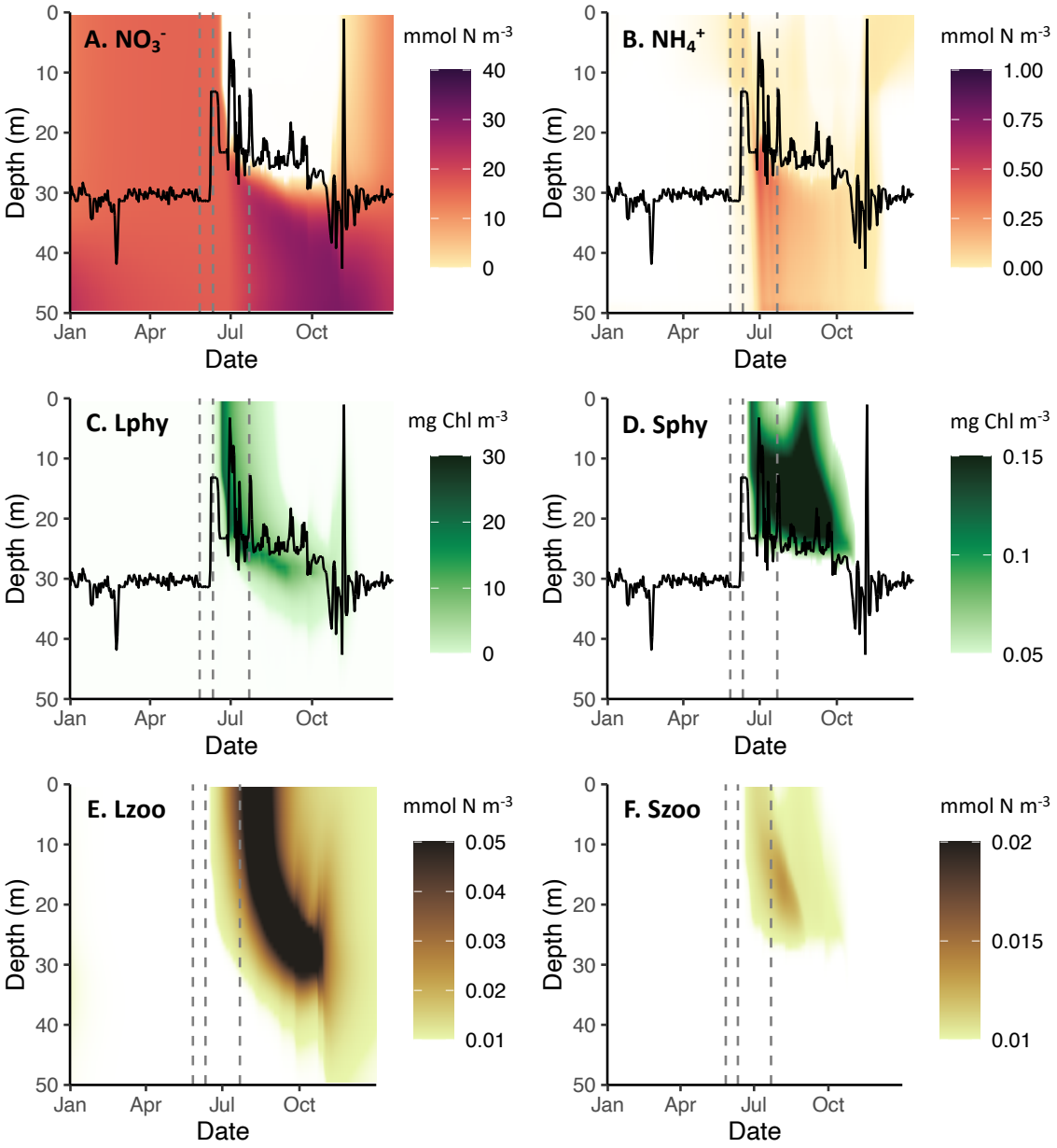

Figure A.8: Annual depth vs. time plots of (A) nitrate (NO_3^-), (B) ammonium (NH_4^+), (C) large phytoplankton (Lphy), (D) small phytoplankton (Sphy), (E) large zooplankton (Lzoo), and (F) small zooplankton (Szoo) for 2010, an MIZ-dominant bloom year. Black lines (A-D) represent the mixed layer depth, calculated based on GOTM-derived buoyancy frequency. Grey dashed lines on each subplot represent, from left to right, the date of ice melt, the start of ice retreat (which marks the end of the UI period and start of the MIZ period), and the end of ice retreat (marking the end of the MIZ period and beginning of the OW period).

Table A.1: Sensitivity analysis. Parameters were increased (Treatment = +) or decreased (Treatment = -) by 20%. Changes in the magnitude (%) of annual NPP, date (d) of maximum production, and depth (m) at which biomass exceeded 1 g C m^{-3} on the date of maximum production are listed. Bold indicates parameters that changed annual NPP by >5%.

Parameter	Treatment	% Δ Magnitude	Δ Max Date
Standard Run	**NA**	**-**	**-**
Winter NO_3^-	**+**	**16.4**	**0**
Winter NO_3^-	**-**	**-17.0**	**-2**
IA_L	+	-0.4	-1
IA_L	-	0.4	0
IA_x_0	+	0.1	0
IA_x_0	-	-0.1	-1
IA_k	+	0	0
IA_k	-	0	0
$IA\_comp.irrad.$	+	0.2	0
$IA\_comp.irrad.$	-	0	0
$mort_{IA}$	+	0.3	0
$mort_{IA}$	-	-0.4	-1
$\boldsymbol{E_{k\_Lphy}}$	**+**	**--5.2**	**3**
$\boldsymbol{E_{k\_Lphy}}$	**-**	**6.2**	**-6**
$\boldsymbol{\mu_{0\_Lphy}}$	**+**	**5.3**	**-4**
$\boldsymbol{\mu_{0\_Lphy}}$	**-**	**-6.8**	**4**
$mort_{Lphy}$	+	0.3	0
$mort_{Lphy}$	-	-0.4	-1
$K_{S\_NO3\_Lphy}$	+	0	0
$K_{S\_NO3\_Lphy}$	-	0	0
$K_{S\_NH4\_Lphy}$	+	0	0
$K_{S\_NH4\_Lphy}$	-	0	0
E_{k_Sphy}	+	0	0
E_{k_Sphy}	-	0	-1
μ_{0_Sphy}	+	0	-1
μ_{0_Sphy}	-	-0.1	0
$mort_{Sphy}$	+	0	0
$mort_{Sphy}$	-	-0	0
$K_{S\_NO3\_Sphy}$	+	0	0
$K_{S\_NO3\_Sphy}$	-	0	0
$K_{S\_NH4\_Sphy}$	+	0	0

$K_{S\_NH4\_Sphy}$	-	0	0
$mort_{Lzoo}$	+	0.1	0
$mort_{Lzoo}$	-	-0.2	0
ex_{Lzoo}	+	-0.2	0
ex_{Lzoo}	-	0.2	-1
γ_{Lzoo}	+	0	-1
γ_{Lzoo}	-	-0.4	0
$K_{S\_Lzoo\_Lphy}$	+	0	0
$K_{S\_Lzoo\_Lphy}$	-	0	0
$K_{S\_Lzoo\_Szoo}$	+	0	0
$K_{S\_Lzoo\_Szoo}$	-	0	0
$mort_{Szoo}$	+	0	0
$mort_{Szoo}$	-	0	0
ex_{Szoo}	+	0	0
ex_{Szoo}	-	-0.1	0
γ_{Szoo}	+	-0.9	0
γ_{Szoo}	-	-0.5	-1
$K_{S\_Szoo\_Sphy}$	+	0	0
$K_{S\_Szoo\_Sphy}$	-	0	0
$Nitr_{NH4\rightarrow\ NO4}$	+	0	0
$Nitr_{NH4\rightarrow\ NO4}$	-	0	0

Table A.2: Modeled ice algal (IA), under ice (UI), marginal ice zone (MIZ), and open water (OW) NPP (g C m^{-2} yr^{-1}) for 1988-2018. Water column NPP is further split into new and regenerated ("Reg.") production.

Year	IA	UI New	UI Reg.	MIZ New	MIZ Reg.	OW New	OW Reg.	Total
1988	0.0	41.5	3.5	20.6	10.8	0.0	0.0	76.3
1989	1.8	48.5	14.3	4.3	5.3	13.2	3.4	90.8
1990	1.5	31.9	3.4	12.0	4.5	21.0	7.8	82.1
1991	0.8	28.3	2.8	20.2	7.7	11.9	3.7	75.4
1992	0.0	26.6	2.1	15.9	5.7	17.0	7.3	74.7
1993	1.9	1.7	0.3	42.0	12.2	21.4	9.9	89.4
1994	3.6	52.6	21.1	5.5	2.2	7.8	1.4	94.2
1995	0.0	50.3	14.2	9.2	5.2	14.6	2.1	95.6
1996	3.2	48.8	17.2	5.7	4.5	17.3	3.4	100.1
1997	1.7	44.3	7.4	3.4	6.3	17.3	6.0	86.4
1998	0.0	1.2	0.0	43.8	11.7	20.0	9.5	86.2
1999	0.0	23.6	0.9	16.4	6.0	28.4	11.9	87.2
2000	0.1	22.8	1.0	23.5	9.9	14.7	5.5	77.4
2001	2.7	44.7	7.9	3.8	6.2	14.4	5.2	84.9
2002	2.6	50.2	18.7	1.4	1.6	17.5	4.7	96.7
2003	3.3	48.2	15.3	6.7	6.0	13.4	2.7	95.6
2004	1.9	4.1	0.6	42.2	13.7	15.4	6.1	84.0
2005	2.4	20.8	1.5	17.7	7.7	25.9	9.9	85.8
2006	0.0	47.3	9.0	4.4	3.3	17.3	4.4	85.6
2007	4.4	45.9	12.8	3.1	4.7	20.9	5.5	97.2
2008	2.2	49.2	16.5	3.9	4.6	13.5	3.4	93.2
2009	0.0	52.4	21.4	6.5	3.5	12.7	2.5	99.0
2010	0.0	0.6	0.0	42.1	12.3	19.3	7.6	81.9
2011	2.8	47.5	15.3	3.5	4.9	19.8	4.8	98.6
2012	0.0	34.7	3.0	14.4	7.5	16.4	5.1	81.2
2013	3.4	50.4	19.4	4.3	2.9	16.1	3.2	99.7
2014	0.0	31.7	3.1	16.2	6.5	19.5	5.1	82.1
2015	3.6	45.2	10.9	4.1	5.7	22.2	5.7	97.4
2016	2.4	30.2	3.3	12.6	5.1	21.7	8.1	83.4
2017	3.8	40.1	5.7	5.1	7.1	28.2	7.0	97.5
2018	3.8	45.0	9.7	5.9	7.3	22.1	4.9	98.8

Table A.3: Modeled ice algal (IA), under ice (UI), marginal ice zone (MIZ), and open water (OW) NPP (g C m^{-2} yr^{-1}) for 1988-2018. Water column primary production is further split into surface ("Surf.") and subsurface ("SCM") NPP.

Year	IA	UI Surf.	UI SCM	MIZ Surf.	MIZ SCM	OW Surf.	OW SCM	Total
1988	0.0	45.4	0.0	10.2	20.8	0.0	0.0	76.3
1989	1.8	61.3	1.9	6.3	3.2	0.8	15.4	90.8
1990	1.5	35.7	0.0	3.5	13.0	0.8	27.6	82.1
1991	0.8	31.4	0.0	2.3	25.6	0.3	14.9	75.4
1992	0.0	29.0	0.0	2.7	18.9	0.8	23.2	74.7
1993	1.9	2.1	0.0	43.5	11.1	3.1	27.6	89.4
1994	3.6	64.8	9.2	1.0	6.8	0.1	8.7	94.2
1995	0.0	64.3	0.6	5.1	9.2	0.2	16.1	95.6
1996	3.2	63.5	2.9	4.2	6.0	0.6	19.8	100.1
1997	1.7	52.2	0.0	8.9	0.7	2.0	20.9	86.4
1998	0.0	1.3	0.0	45.5	10.5	2.8	26.0	86.2
1999	0.0	25.1	0.0	4.5	17.9	1.5	38.4	87.2
2000	0.1	24.2	0.0	4.1	30.5	0.4	18.2	77.4
2001	2.7	53.1	0.0	8.8	1.2	1.6	17.5	84.9
2002	2.6	65.4	3.8	1.8	1.2	1.7	20.1	96.7
2003	3.3	60.8	3.1	6.0	6.7	0.4	15.3	95.6
2004	1.9	5.6	0.0	24.4	31.0	0.6	20.6	84.0
2005	2.4	24.6	0.0	6.0	17.5	1.1	34.3	85.8
2006	0.0	56.6	0.0	3.9	4.0	0.8	20.3	85.6
2007	4.4	56.2	2.9	5.6	2.3	1.1	24.8	97.2
2008	2.2	64.1	1.9	4.8	3.6	1.0	15.5	93.2
2009	0.0	68.1	6.1	2.0	7.9	0.5	14.4	99.0
2010	0.0	0.6	0.0	45.3	9.4	1.9	24.6	81.9
2011	2.8	60.8	2.4	5.8	2.5	0.9	23.4	98.6
2012	0.0	38.2	0.0	5.3	16.8	0.4	20.4	81.2
2013	3.4	64.3	5.8	2.1	5.2	0.7	18.2	99.7
2014	0.0	35.2	0.0	2.5	20.3	0.4	23.7	82.1
2015	3.6	56.5	0.0	7.1	2.7	1.0	26.4	97.4
2016	2.4	34.0	0.0	3.8	14.1	0.7	28.4	83.4
2017	3.8	46.6	0.0	9.2	3.1	1.4	33.5	97.5
2018	3.8	55.2	0.0	8.2	5.0	0.4	26.2	98.8

Appendix B

Chapter 3 Supplemental Material

This supplementary material supports the conclusions of Payne et al (2022). These additional methods describe modifications made to the physical model, GOTM; model equations used for the biogeochemical model, CAOS, introduced in this paper; model forcing; and model performance methods and results.

Payne, C. M., & Arrigo, K. R. (2022). Increases in benthic particulate export and sedimentary denitrification in the northern Chukchi Sea tied to underice primary production. Journal of Geophysical Research: Oceans, 127. https://doi.org/10.1029/2021JC018110.

B.1 Sensitivity analysis

The coupled CAOS-GO model is composed of a biogeochemical model (CAOS, Figure B.1; *Payne et al.* 2021), a physical model (GOTM; *Burchard et al.*, 1999) and a sedimentary chemistry model (OMEXDIA; *Soetaert et al.*, 1996b, a). Water column processes are governed by 31 parameters (Table S1), while OMEXDIA processes are controlled by 14 parameters and 6 variables output by either CAOS or GOTM (Table S2).

To evaluate the sensitivity of our model to these parameters, we conducted a sensitivity analysis. First, 25 CAOS parameters were altered one at a time by ±20% and run for a single representative year, 2011. Model sensitivity to these parameter changes was evaluated by comparing the magnitude in change of total NPP as well as the change in peak bloom date to the run with standard parameters. Next, the most sensitive CAOS parameters (six parameters) and the OMEXDIA parameters were also altered one at a time by ±20% for 2011. Model sensitivity to these parameter changes was evaluated by comparing the change in magnitude of total NPP, C export to the sediments, water column nitrification, and sedimentary nitrification and denitrification to the run with standard parameters.

Additionally, we evaluated our model's sensitivity to the choice in start and end dates for our periods of water column production (UI, MIZ, and OW). In our standard model run, the UI period extended from the initiation of exponential phytoplankton growth (when phytoplankton N assimilation exceeded 0.5 mmol N m^{-2} d^{-1}) and lasted until the start of sea ice retreat, when satellite-derived sea ice concentration diminished below 90%. The MIZ period extended from the start of sea ice retreat until its conclusion, when sea ice concentrations diminished below 10%. Finally, the OW period began at the conclusion of ice retreat and terminated on the earliest date when either ice advanced in the autumn or light diminished below 1% the maximum value reached in the mixed layer, or on DOY 300±6. We altered these choices in a range surrounding the initial value (Table S5) and measured the effect of these changes on the length of the period and on the NPP during that period.

B.2 Sensitivity analysis results

Total NPP was sensitive (altering by >5%) to 3 of the 25 parameters tested. It was most sensitive to the winter NO_3^- concentration, with a 20% change in NO_3^- concentration altering NPP by 16.4-17.0%. Total NPP was also sensitive to two large phytoplankton parameters - E_{k_Lphy} and μ_{0_Lphy}, which both altered annual NPP by 5.2-6.8%. These same parameters led to the largest changes in the timing of peak NPP, with parameters altering the peak bloom date by 0-6 days.

Sediment processes were sensitive (with the magnitude of one or more of POC export to the sediments, water column nitrification, sedimentary nitrification, and sedimentary denitrification altering by >5%) to 7 of the 16 parameters tested (Table B.4). The two tested large phytoplankton parameters (E_{k_Lphy} and μ_{0_Lphy}) altered POC export by ±8.2-10.7%, sedimentary nitrification by ±7.0-9.2%, and denitrification by ±8.9-11.6%. Three of the tested parameters (initial NO_3^- concentration, $Remin_{Det \rightarrow NH4}$, and w_{det}) substantially affected all five metrics of sensitivity, with total annual NPP altered by ±5.4-16.6%, POC export by ±13.2-17.4%, water column nitrification by ±13.1-18.1%, sedimentary nitrification by ±9.9-15.3%, and denitrification by ±11.4-19.6%.

Of the OMEXDIA parameters, only an increase in the proportion of fast-decaying C (p_{fast}) or a change in the bottom-water O_2 concentration (O_2_bw) had a >5% impact on sedimentary nitrification or denitrification, with nitrification changing by ±2.4-5.5% and denitrification changing by ±5.9-6.1%.

Finally, we altered the values used to set the start and end dates for the three water column periods - the UI, MIZ, and OW periods. A few of the larger changes in values resulted in substantial changes in the lengths of these periods. In particular, using a far lower minimum N assimilation threshold (0.1 mmol m_{-2} d_{-1}) caused the UI period to start 19 days earlier, leading to a 36% increase in the length of the UI period (Table S5). Similarly, ending the MIZ period when ice concentration first diminished below 25% led to a MIZ period 9 days (and 41%) shorter than the original model

choice, and choosing higher light thresholds (2%, 5%) to end the OW period led to a decrease in the length of the OW period (10 and 16 days, 9% and 14.3% shorter total period) However, even fairly drastic changes in these parameters resulted in only a small shift in the proportion of NPP that occurred during these periods (with NPP estimates during these periods almost always altering by $<$1.5 g C m^{-2} yr^{-1}). Only substantial changes in the parameter used to set the end of the MIZ period/start of the OW period led to substantial changes in the partitioning of NPP between these two periods (3.3 g C m^{-2} yr^{-1}). However, our original choice of the end of the MIZ period coinciding with the date when ice concentration reached 10% is much closer to the definitions used by other studies (e.g., *Lowry et al.*, 2014; *Perrette et al.*, 2011), which typically define the MIZ period as stretching past the retreat of sea ice and into what we here consider the OW period.

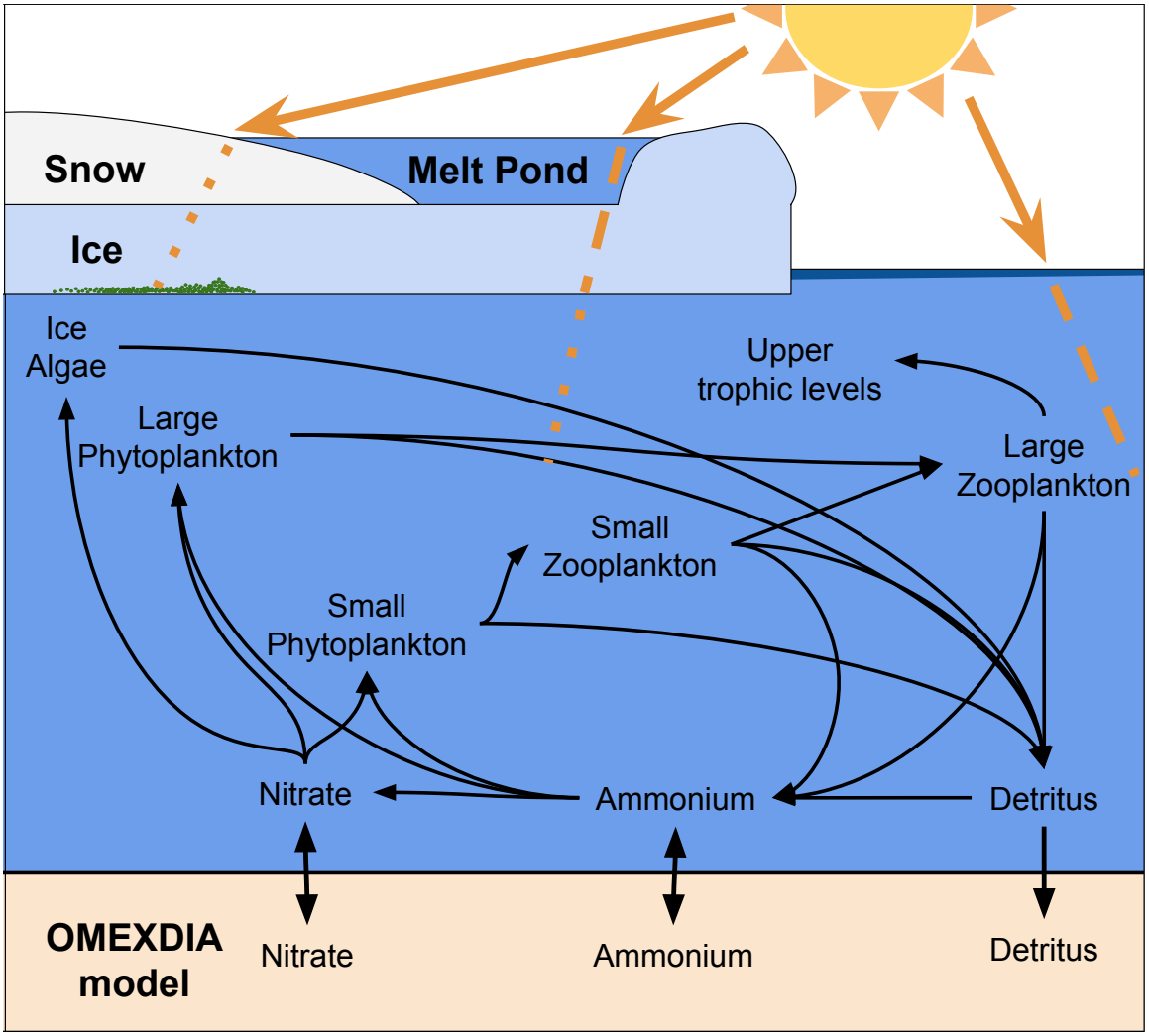

Figure B.1: A diagram of the biogeochemical component of the CAOS-GO model. Light passes through snow, ice, and/or melt ponds depending on ice conditions. Black arrows represent N exchange between state variables (text). Upper trophic levels are not explicitly modeled, but mortality of zooplankton is assumed to contribute to upper trophic levels. Detritus that is exported to the benthos and the bottom layer concentrations of two inorganic nitrogen state variables (nitrate and ammonium) are also used as input for the sediment model, OMEXDIA. From Payne et al. (2021).

Table B.1: CAOS-GO model parameters: parameter descriptions, values, units, and sources of parameters used.

Parameter	Description	Value	Unit	Source
IA_L	Maximum ice algal Chl *a* concentration	30	mg Chl *a* m^{-2}	a
IA_{x_0}	Sigmoid midpoint for logistical curve describing ice algal growth	14	d	b
IA_k	Ice algal logistical growth rate	0.4	mg Chl *a* m^{-2} d^{-1}	b
$IA_{comp.irrad.}$	Compensation irradiance for ice algae	2.0	μmol photons m^{-2} s^{-1}	c
$loss_{IA}$	Disassociation rate of ice algae	0.05	d^{-1}	d
E_{k_Lphy}	Observed photoacclimation parameter, E_k, for large phytoplankton	54.9-67.6	μmol photons m^{-2} s^{-1}	e, *
μ_{0_Lphy}	Specific growth rate for large phytoplankton at 0°C	1.78	d^{-1}	e, **
$mort_{Lphy}$	Death and loss rate of large phytoplankton	0.065	d^{-1}	d
$K_{s\_NO3\_Lphy}$	Half-saturation constant for NO_3^- uptake by large phytoplankton	0.9	mmol N m^{-3}	-
$K_{s\_NH4\_Lphy}$	Half-saturation constant for NH_4^+ uptake by large phytoplankton	0.7	mmol N m^{-3}	-
C/N_{Lphy}	Carbon to nitrogen ratio of large phytoplankton	106/14	mol:mol	f,g
C/Chl_{Lphy}	Carbon to Chl *a* ratio of large phytoplankton	60	g:g	g
E_{k_Sphy}	Observed photoacclimation parameter, E_k, for small phytoplankton	100	μmol photons m^{-2} s^{-1}	h, *
μ_{0_Sphy}	Specific growth rate for small phytoplankton at 0°C	1	d^{-1}	e, **
$mort_{Sphy}$	Death and loss rate of small phytoplankton	0.045	d^{-1}	d
$K_{s\_NO3\_Sphy}$	Half-saturation constant for NO_3^- uptake by small phytoplankton	0.3	d^{-1}	-
$K_{s\_NH4\_Sphy}$	Half-saturation constant for NH_4^+ uptake by small phytoplankton	0.1	mmol N m^{-3}	-
C/N_{Sphy}	Carbon to nitrogen ratio of small phytoplankton	106/16	mol:mol	i
C/Chl_{Sphy}	Carbon to Chl *a* ratio of small phytoplankton	100	g:g	j
$Sphy_{scarce}$	Sphy scarcity threshold: Szoo consumption is adjusted by Sphy/$Sphy_{scarce}$	0.5	mmol N m	-
$mort_{zoo}$	Zooplankton mortality rate	0.05	d^{-1}	d
ex_{zoo}	Zooplankton excretion rate	0.1	d^{-1}	d
γ	Zooplankton unassimilated grazing fraction	0.25	d^{-1}	d
$K_{s\_Sphy\_Szoo}$	Half-saturation constant for small phytoplankton uptake by small zooplankton	0.5	mmol N m^{-3}	-
$K_{s\_Lphy\_Lzoo}$	Half-saturation constant for large phytoplankton uptake by large zooplankton	0.5	mmol N m^{-3}	-
$K_{s\_Szoo\_Lzoo}$	Half-saturation constant for small zooplankton uptake by large zooplankton	0.5	mmol N m^{-3}	-
$Remin_{Det \rightarrow NH4}$	Remineralization rate of detritus to NH_4^+	0.2	mmol N m^{-3}	k
w_{det}	Detrital sinking rate	5	m d^{-1}	b
C/N_{det}	Carbon to nitrogen ratio of detritus	106/15.8	mol:mol	j
$Nitr\_m_{NH4 \rightarrow NO3}$	Slope for the depth-dependent nitrification rate	0.5824	mmol N m^{-4}	l
$Nitr\_b_{NH4 \rightarrow NO3}$	Y-intercept for the depth-dependent nitrification rate (values below 0 = 0)	-3.4313	mmol N m^{-3}	l

a Arrigo (2017), *b* Welch and Bergmann (1989), *c* McMinn et al. (1999), *d* Arrigo et al. (2014), *e* Fasham et al. (1990), *f* Brzezinski (1985); Lomas et al. (2019), *g* ICESCAPE 2011 data, *h* Lewis et al. (2019), *i* Redfield (1958), *j* Sakshaug (2004), *k* Davis and Benner (2007), *l* SUBICE 2014 data

$*$ Reported E_k values were measured for PAR. Since phytoplankton functional groups were modeled using PUR, these values were modified in the model to reflect that only 38.3% of photosynthetron-produced light is usable by phytoplankton.

$**$ Reported growth rates of 0.89 and 1.6 d^{-1} were observed at -1.6 °C. These values were adjusted using the Eppley (1972) temperature/growth relationship to calculate specific growth rates at 0 °C.

Table B.2: Parameters used in the OMEXDIA model that differ from those in *Soetaert et al.* (1996a).

Parameter	**Description**	**Value**	**Unit**	**Source**
F_{fast}	Flux of fast-decaying detritus	(*)	g C m^{-2} yr^{-1}	a
F_{slow}	Flux of slow-decaying detritus	(*)	g C m^{-2} yr^{-1}	a
p_{fast}	Proportion of fast-decaying detritus	0.5	d^{-1}	b
R_{fast}	Decay rate for the fast-decaying detritus	0.18	d^{-1}	c
R_{slow}	Decay rate for the slow-decaying detritus	0.005	d^{-1}	b
$k_{in}(O_2$ denit)	Half saturation conc. for O_2 inhibition in denitrification	15	mmol O_2 m^{-3}	d
$k_{in}(NO_3^-$ anox)	Half saturation conc. for NO_3^- inhibition in anoxic mineralization	1	mmol NO_3^- m^{-3}	d
$k_{in}(O_2$ anox)	Half saturation conc. for O_2 inhibition in anoxic mineralization	1	mmol NO_3^- m^{-3}	d
C/N_{fast}	Carbon to nitrogen ratio of fast-decaying detritus	106/14.18	mol:mol	a
C/N_{slow}	Carbon to nitrogen ratio of slow-decaying detritus	106/12.1	mol:mol	e
ϕ_0	Porosity at the sediment-water interface	0.915	-	d
$coeff_\phi$	Coefficient for exponential porosity changes	4	-	b
Db_0	Constant bioturbation coefficient in the bioturbated layer	2	cm^2 yr^{-1}	f
x_b	Depth below which bioturbation decays exponentially	3	cm	f
O_2_bw	Oxygen concentration of the bottom water NO_3^-	300	mmol N m^{-3}	**
NO_3^-_bw	Daily mean bottom-water NO_3^-	(*)	mmol N m^{-3}	a
NH_4^+_bw	Daily mean bottom-water NH_4^+	(*)	mmol N m^{-3}	a
w	Sedimentation rate	0.35	cm y^{-1}	e, g
Temperature	Daily mean bottom-water temperature	(*)	°C	a
Salinity	Daily mean bottom-water salinity	(*)	-	a

(*) Variable conditions produced by GOTM or the CAOS model.
** Mean oxygen concentration for the stations closest to the model location for ICESCAPE 2011.
a from CAOS model. *b* *Soetaert et al.* (1996a). *c* *Davis and Benner* (2007). *d* *Soetaert et al.* (1996b).
e *Cooper and Grebmeier* (2018). *f* *Teal et al.* (2008). *g* *Darby et al.* (2009).

Table B.3: Sensitivity analysis for water column parameters. Parameters were increased (Treatment = +) or decreased (Treatment = -) by 20%. Changes in the magnitude (%) of annual NPP and date (d) of maximum production are listed. Bold indicates parameters that changed annual NPP by >5%.

Parameter	Treatment	% Δ Magnitude	Δ Max Date
Standard Run	**NA**	**-**	**-**
Winter NO_3^-	**+**	**16.4**	**0**
Winter NO_3^-	**-**	**-17.0**	**-2**
IA_L	+	-0.4	-1
IA_L	-	0.4	0
IA_x_0	+	0.1	0
IA_x_0	-	-0.1	-1
IA_k	+	0	0
IA_k	-	0	0
IA_comp.irrad.	+	0.2	0
IA_comp.irrad.	-	0	0
$mort_{IA}$	+	0.3	0
$mort_{IA}$	-	-0.4	-1
$\boldsymbol{E_{k\_Lphy}}$	+	**--5.2**	**3**
$\boldsymbol{E_{k\_Lphy}}$	-	**6.2**	**-6**
$\boldsymbol{\mu_{0\_Lphy}}$	+	**5.3**	**-4**
$\boldsymbol{\mu_{0\_Lphy}}$	-	**-6.8**	**4**
$mort_{Lphy}$	+	0.3	0
$mort_{Lphy}$	-	-0.4	-1
$K_{S\_NO3\_Lphy}$	+	0	0
$K_{S\_NO3\_Lphy}$	-	0	0
$K_{S\_NH4\_Lphy}$	+	0	0
$K_{S\_NH4\_Lphy}$	-	0	0
E_{k_Sphy}	+	0	0
E_{k_Sphy}	-	0	-1
μ_{0_Sphy}	+	0	-1
μ_{0_Sphy}	-	-0.1	0
$mort_{Sphy}$	+	0	0
$mort_{Sphy}$	-	-0	0
$K_{S\_NO3\_Sphy}$	+	0	0
$K_{S\_NO3\_Sphy}$	-	0	0
$K_{S\_NH4\_Sphy}$	+	0	0

$K_{S\_NH4\_Sphy}$	-	0	0
$mort_{Lzoo}$	+	0.1	0
$mort_{Lzoo}$	-	-0.2	0
ex_{Lzoo}	+	-0.2	0
ex_{Lzoo}	-	0.2	-1
γ_{Lzoo}	+	0	-1
γ_{Lzoo}	-	-0.4	0
$K_{S\_Lzoo\_Lphy}$	+	0	0
$K_{S\_Lzoo\_Lphy}$	-	0	0
$K_{S\_Lzoo\_Szoo}$	+	0	0
$K_{S\_Lzoo\_Szoo}$	-	0	0
$mort_{Szoo}$	+	0	0
$mort_{Szoo}$	-	0	0
ex_{Szoo}	+	0	0
ex_{Szoo}	-	-0.1	0
γ_{Szoo}	+	-0.9	0
γ_{Szoo}	-	-0.5	-1
$K_{S\_Szoo\_Sphy}$	+	0	0
$K_{S\_Szoo\_Sphy}$	-	0	0
$Nitr_{NH4\rightarrow\ NO4}$	+	0	0
$Nitr_{NH4\rightarrow\ NO4}$	-	0	0

Table B.4: Sensitivity analysis. Parameters were increased (Treatment = +) or decreased (Treatment = -) by 20%. Changes in the magnitude (%) of oxic mineralization, anoxic mineralization, nitrification, and denitrification are listed. Bold indicates parameters that changed magnitudes by >5%.

Parameter	Treatment	Δ NPP	Δ C. Exp.	Δ WC. Nitr.	Δ S. Nitr.	Δ S. Denit.
Standard Run	NA	-	-	-	-	-
$\boldsymbol{E_{k\_Lphy}}$	+	**-5.0**	**-8.2**	-1.1	**-7.0**	**-8.9**
$\boldsymbol{E_{k\_Lphy}}$	-	**6.0**	**10.6**	2.2	**8.3**	**10.7**
μ_{0_Lphy}	+	**5.1**	**8.9**	1.3	**7.0**	**9.1**
μ_{0_Lphy}	-	**-6.6**	**-10.7**	-0.3	**-9.2**	**-11.6**
Nitr. rate	+	0	0	0	0	0
Nitr. rate	-	0	0	0	0	0
$\mathbf{NO_3^-}$	+	**15.9**	**13.2**	**18.1**	**10.4**	**19.0**
$\mathbf{NO_3^-}$	-	**-16.6**	**-14.1**	**-17.9**	**-12.4**	**-19.6**
$\boldsymbol{Remin_{Det\rightarrow NH_4}}$	+	**6.3**	**-13.9**	**14.4**	**-12.0**	**-13.8**
$\boldsymbol{Remin_{Det\rightarrow NH_4}}$	-	**-6.6**	**15.5**	**-16.1**	**11.7**	**13.3**
$\boldsymbol{w_{det}}$	+	**-5.4**	**13.0**	**-13.1**	**9.9**	**11.4**
$\boldsymbol{w_{det}}$	-	**7.7**	**-17.4**	**17.4**	**-15.3**	**-17.5**
Db_0	+	0	0	0	1.6	1.8
Db_0	-	0	0	0	-2.2	-2.3
$k_{in}(NO_3^-$ anox)	+	0	0	0	0	-0.4
$k_{in}(NO_3^-$ anox)	-	0	0	0	0	0.5
$k_{in}(O_2$ anox)	+	0	0	0	0	0
$k_{in}(O_2$ anox)	-	0	0	0	0	0
$k_{in}(O_2$ denit)	+	0	0	0	0	3.1
$k_{in}(O_2$ denit)	-	0	0	0	0	-3.4
$\mathbf{p_{fast}}$	+	0	0	0	**-5.5**	**-6.1**
p_{fast}	-	0	0	0	4.7	4.7
por	+	0	0	0	-0.5	-2.2
por	-	0	0	0	-0.7	1.3
R_{fast}	+	0	0	0	-1.3	-2.0
R_{fast}	-	0	0	0	1.5	2.5
R_{slow}	+	0	0	0	-0.6	0.1
R_{slow}	-	0	0	0	0.7	-0.4
$\mathbf{O_2\_bw}$	+	0	0	0	2.4	**-6.0**
$\mathbf{O_2\_bw}$	-	0	0	0	**-5.3**	**5.9**
w	+	0	0	0	0.2	0
w	-	0	0	0	-0.2	0

Table B.5: The sensitivity of the length of and NPP during the UI, MIZ, and OW periods to the choice of start and ending value for 2011 (units: UI start = mmol N m^{-2} d^{-1}, OW end = % of maximum PAR, all others = % satellite-derived sea ice coverage). The values chosen to define these start and end dates were altered (value) and sensitivity was assessed by comparing the change in DOY for the period start/end dates (d), the change in period length, and the change in NPP during the period (g C m^{-2} yr^{-1}).

Parameter	**Value**	**Δ DOY**	**Δ % period length**	**Δ period NPP**
UI start	0.5	-	-	-
UI start	0.1	-19	35.8	0.4
UI start	0.25	-6	11.3	0.2
UI start	0.75	6	-11.3	-0.4
UI start	1	7	-13.2	-0.5
UI end	90%	-	-	-
UI end	95%	-2	-3.8	-0.8
UI end	85%	2	3.8	0.7
UI end	80%	3	5.7	1.1
UI end	75%	4	7.5	1.5
MIZ start	90%	-	-	-
MIZ start	95%	-2	9.1	0.9
MIZ start	85%	2	-9.1	-0.8
MIZ start	80%	3	-13.6	-1.1
MIZ start	75%	4	-18.2	-1.5
MIZ end	10%	-	-	-
MIZ end	5%	1	4.5	0.4
MIZ end	15%	-3	-13.6	-1.1
MIZ end	20%	-3	-13.6	-1.1
MIZ end	25%	-9	-40.9	-3.3
MIZ end	30%	-9	-40.9	-3.3
OW start	10%	-	-	-
OW start	5%	1	-0.9	-0.4
OW start	15%	-3	2.7	1.1
OW start	20%	-3	2.7	1.1
OW start	25%	-9	8	3.3
OW start	30%	-9	8	3.3
OW end	1%	-	-	-
OW end	0.50%	6	5.4	0.4
OW end	2%	-10	-8.9	-1
OW end	5%	-16	-14.3	-1.5

Appendix C

Chapter 4 Supplemental Material

This supplementary material supports the conclusions of Payne et al. (2022). These additional methods describe modifications made to the physical model, GOTM; model performance methods and results; and a description of annual cycles of N, phytoplankton, and zooplankton in the southern Chukchi Sea.

Payne, C. M., van Dijken, G. L., & Arrigo, K. R. (2022). North-south differences in under-ice primary production in the Chukchi Sea from 1988 to 2018. Journal of Geophysical Research: Oceans, 127. https://doi.org/10.1029/2022JC018431

C.1 GOTM Configuration

Several modifications were made to the idealized profiles to implement CAOS-GO at the southern model location. These modifications were made to ensure that GOTM generated profiles as consistent as possible with *in situ* observations. Different methods for generating the mixed layer depth (MLD), thickness of the mixed layer, and the bottom water temperature of profiles were evaluated by comparing the RMSE and R^2 of GOTM-generated profiles with observations, and the mathematical relationships that resulted in the best correlation were chosen.

The first idealized temperature profile, based on observations by *Arrigo et al.* (2014); *Pacini et al.* (2019), was used to represent the well-ventilated winter water conditions present in the winter and spring. This profile was used at the start of sea ice retreat, when satellite-derived ice concentration fell below 90%, and following sea ice advance, when satellite-derived ice concentration rose above 10%. The first profile featured a surface temperature of -1.63°C and a temperature at depth of -1.76°C, with a thermocline between 31 and 38 m *Maslowski et al.* (2004); *Peralta-Ferriz and Woodgate* (2015).

The second and third idealized temperature profiles were used on the first date at which satellite-derived SST exceeded weighted means of maximum and minimum satellite-derived SSTs (0.6 * (Max - Min) + Min and 0.9 * (Max - Min) + Min for the second and third profiles, respectively). The surface temperatures for these profiles were set to the 60% and 90% weighted means of satellite-derived SST values (see *Payne et al.* 2021 supplementary information for more details). The surface temperature for these profiles extended through the top of the mixed layer (ML), which was set such that (D_P - D_{ER})*0.37, where D_P is the day of year (DOY) of the profile and D_{ER} is the DOY of the end of sea ice retreat. For example, if SST reaches 60% of the maximum SST 22 days after the end of ice retreat, the top of the ML of this profile is set to 8 m. Temperature declined exponentially until the bottom of the mixed layer, which was set according to ML_{top} + (D_P - D_{ER})*0.3, where ML_{top} is the the depth of the top of the mixed layer. In the above example, the bottom of the ML would be set to 15 m. Below the mixed layer, observed water temperatures did not remain constant below the MLD through the summer (*Grebmeier* 2017), as it did further to the north (*Arrigo et al.*, 2014; *Payne et al.*, 2021). As a result, the bottom-water temperature for the second and third profiles was set to equal -1.76 + (T_S + 1.76) * 0.59, where T_S is the surface temperature.

Sea ice retreat-driven salinity changes were approximated through the use of five idealized profiles. The first profile, the wintertime profile, featured an increase in salinity from 32.35 to 32.40 over the pycnocline (from 31 to 38 m). The remainder of the profiles had fixed MLDs and varied in their surface salinity depending on the length of the sea ice melt period, as in *Payne et al.* (2021). However, unlike at the northern station featured in *Payne et al.* (2021), seven of the 31 years modeled here featured ice retreat that started prior to ice melt and melt pond formation. In those seven years, salinity was relaxed towards the wintertime profile year-round.

C.2 Comparing modeled and observed NPP

Validation of NPP and N concentrations at the northern model location can be found in the supplement of *Payne et al.* (2021), while a comparison between modeled and observed denitrification rates produced by our model configuration in the northern Chukchi Sea can be found in the discussion section of *Payne and Arrigo* (2022).

For the southern Chukchi Sea location, modeled NPP was validated using MODIS-derived NPP (*Lewis et al.* 2020). Surface Chlorophyll *a* (Chl) concentrations were determined from Level 3 MODIS Aqua ocean color data. A modified version of the standard empirical NASA-Chl *a* algorithm was used to reflect the high pigment packaging and chromophoric dissolved organic matter (CDOM) concentrations that make the Arctic Ocean bio-optically unique (*Lewis et al.* 2020; *Lewis and Arrigo* 2020). Daily NPP for 2003-2018 was computed for a 125 km by 125 km box centered on the model location from satellite-derived Chl *a*, SST, and sea-ice cover using the algorithm of *Arrigo et al.* (2008) as modified by *Pabi et al.* (2008). This large box size was chosen to reduce data loss due to

cloud cover, as a smaller box size greatly reduced the available observations. Remote sensing-derived estimates of NPP were compared to modeled estimates of NPP over the full 50 m water column. While satellite-derived estimates of NPP present numerous challenges in the Arctic, particularly in regions such as the southern Chukchi Sea where there are deep subsurface Chl *a* maxima (SCM), a pan-Arctic estimate of NPP (*Arrigo and Van Dijken*, 2011) found that satellites only underestimated NPP by 8% when an SCM was present, indicating that satellite-derived NPP can act as a reasonable estimate of total NPP.

Further, we validated modeled vertical profiles of mean (and standard deviation) Chl *a* and dissolved inorganic N (DIN; NO_3^- + NO_2^- + NH_4^+) in the southern Chukchi Sea by comparing them to in situ measurements made during two ICESCAPE cruises (June-July 2010 and 2011) and repeated Distributed Biological Observatory (DBO) cruises (July-August 2010-2018). Only observations taken within 0.5°latitude and longitude of our model location were included. Nine ICESCAPE stations met our criteria for comparison, with dates falling between 21 and 30 June 2010 and 2011. Forty-nine DBO cruises stations (stations 3.1-3.8) measured conditions near to the model location between 17 and 20 July 2010 to 2018 (Figure C.3 c and d).

C.3 Model Performance

Modeled SST between 1988 and 2018 reproduced 92.4% of the variance in the satellite-derived SST (slope=0.897, RMSE=0.9878, $p<0.001$, n=11313). Modeled SST had a relative bias of 0.476, with a slight over-prediction of temperature in the spring and an under-prediction of temperature in the fall (Figure C.1).

Due to the much smaller proportion of NPP in the under-ice period in the southern Chukchi Sea, satellite-derived and modeled NPP were very similar between 2003-2018 (Figure C.2). Satellite-derived NPP, for example, averaged 110.1±35.1 g C m^{-2} yr^{-1} while modeled NPP averaged 105.9±5.6 g C m^{-2} yr^{-1} between 2003 and 2018.

Vertical profiles of Chl *a* from the ICESCAPE and DBO cruises demonstrate that in June and July, Chl *a* is highly variable, with concentrations ranging from 0 to 47 mg Chl *a* m^{-3} (Figure C.3 a and c). Modeled Chl *a* concentrations are comparable to observations in surface waters and through the SCM, but are lower than mean Chl *a* concentrations at depth (Figure C.3 a and c). In the surface, both modeled Chl *a* and observed profiles demonstrate that phytoplankton biomass is elevated in June, but that phytoplankton biomass has largely shifted to an SCM by July. Below 40 m, modeled Chl *a* concentrations are less consistent with observations, where the model produces low Chl *a* concentrations. However, phytoplankton observed at depths greater than 40 m in waters where surface Chl *a* concentrations are high are likely not contributing substantially to total NPP. Similarly, observations of DIN during ICESCAPE and DBO cruises demonstrate the high spatial variation. Modeled DIN profiles indicate that DIN is largely unavailable in surface waters during

June and July and that the nitricline diminishes over this period from 23 m to 29 m between June 21-30 and July 17-20, consistent with observations (Figure C.3 b and d). Modeled bottom-water DIN concentrations are somewhat higher than observations but are still within the range of variation (Figure C.3 b and d).

C.4 Annual cycles of N, phytoplankton, and zooplankton

In the southern Chukchi Sea, the phytoplankton bloom began on average in late April, on DOY 111±10. Peak phytoplankton biomass was reached at the end of May (on DOY 151±14), or on average 5.9±12.3 d prior to the end of the MIZ period (Figure C.4c and d). On this peak day, phytoplankton biomass averaged 688.7±96.0 g Chl *a* m^{-2}, and daily NPP rates peaked at 5.3±2.4 g C m^{-2} d^{-1}. These blooms depleted water column N, which featured wintertime concentrations of 16 mmol m^{-3} throughout the water column but diminished below 1 mmol m^{-3} in the mixed layer on average in late May (on DOY 142±9), shortly before the peak in water column phytoplankton biomass (Figure C.4a and b). Through remineralization and nitrification, water-column N inventories rose to 36.4±1.4 mmol N m^{-3} in the bottom 10 m of the water column. Surface N concentrations increased above 1 mmol m^{-3} in the surface of the water column in mid November (on DOY 320±9) as stratification diminished. Zooplankton concentrations also increase following the initiation of the phytoplankton bloom, peaking at 5.0±1.7 mmol N m^{-2} in mid-September (on DOY 259±9; Figure C.4e and f).

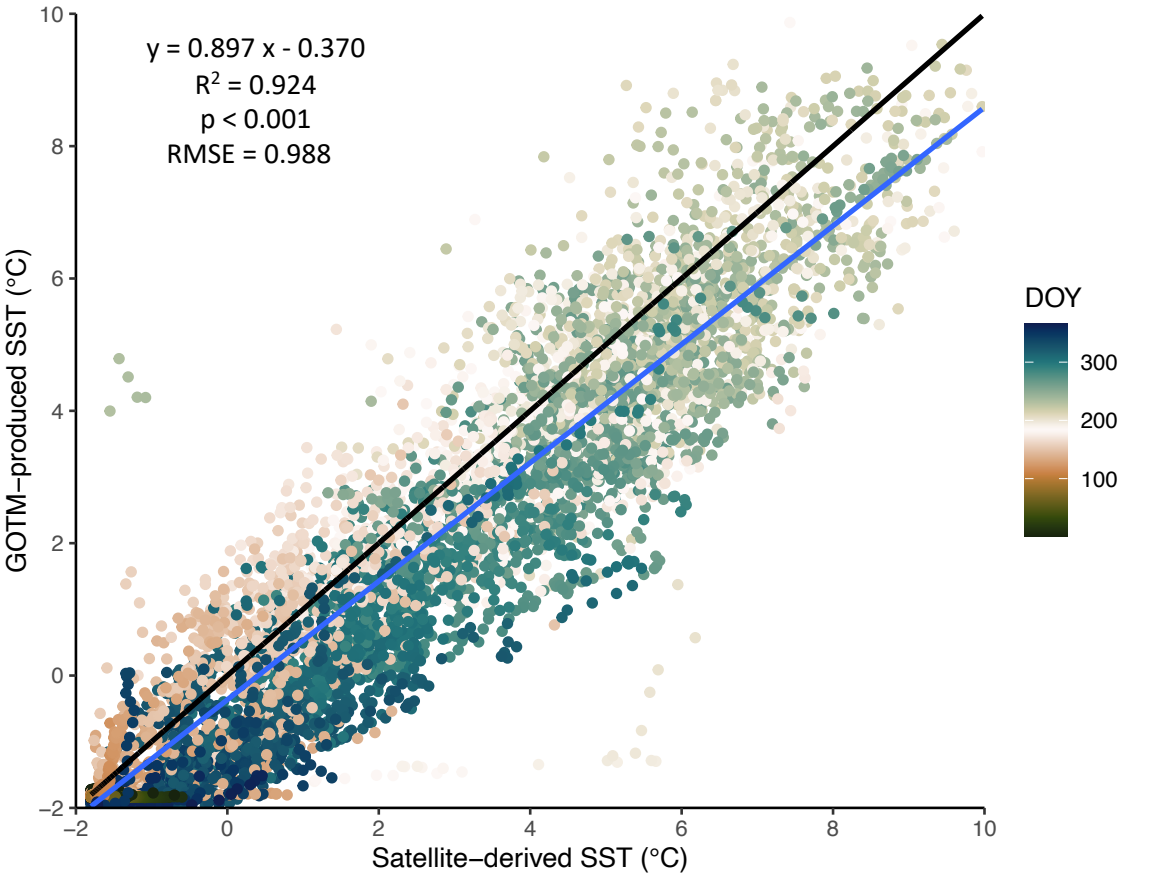

Figure C.1: Scatterplot of daily satellite-derived vs. GOTM-produced sea surface temperature (SST) by DOY (colorbar) for 1988 to 2018. The blue line is the best fit and the black line is the the one-to-one fit line.

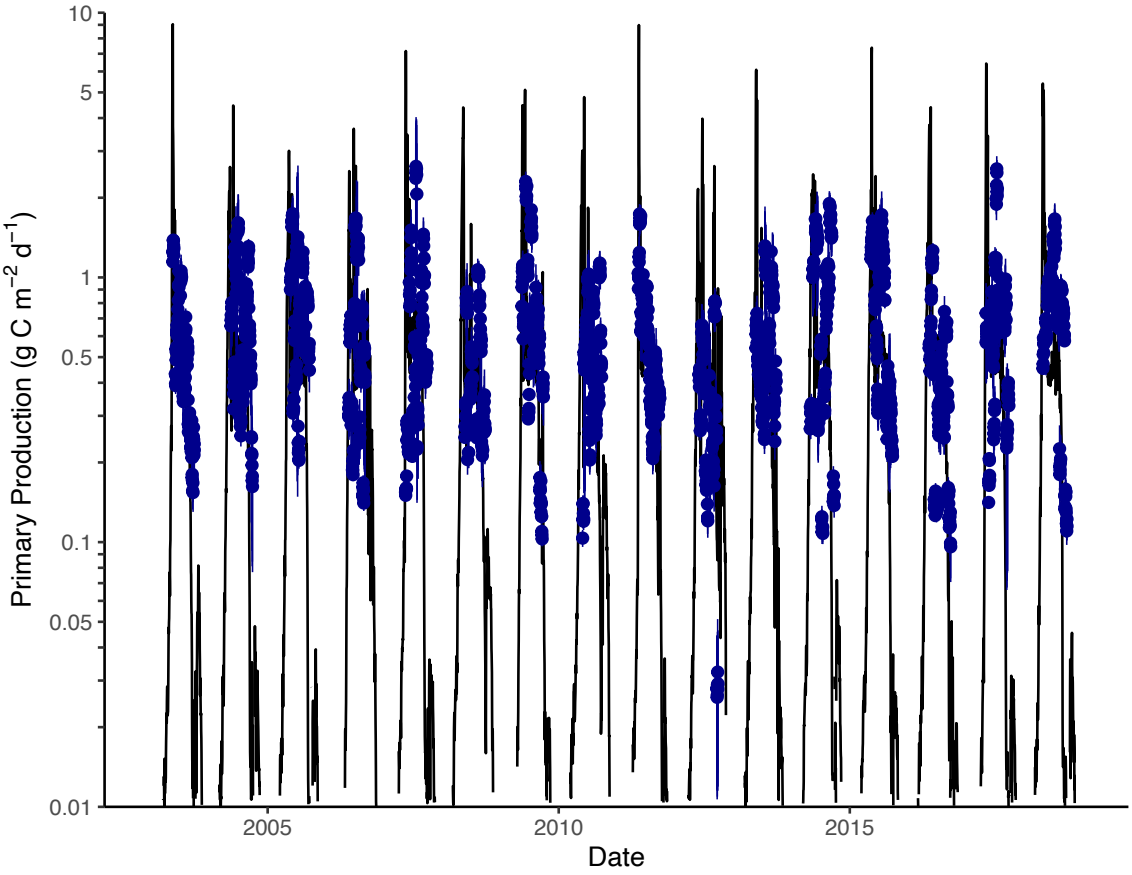

Figure C.2: Comparison of modeled (black lines) to observed MODIS-derived (blue points, with standard deviation lines) net primary production (g C m^{-2} d^{-1}) for 2003 to 2018.

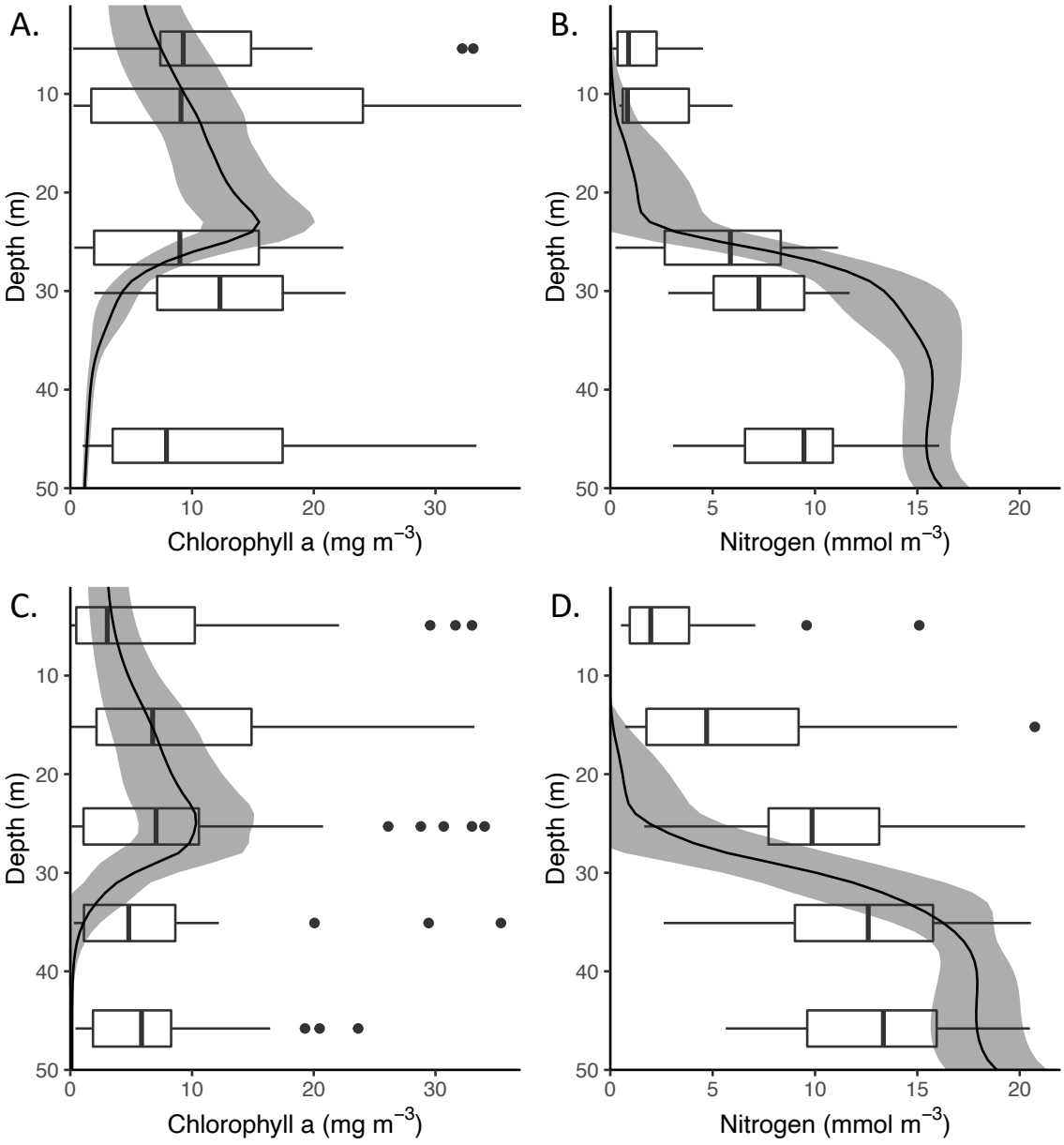

Figure C.3: Comparison of modeled (mean in black lines, standard deviation in grey) to observed ICESCAPE (boxplots in A and B) and DBO (boxplots in C and D) Chl *a* (mg m^{-3}; A, C) and Nitrogen (mmol DIN m^{-3}; B, D) concentrations.

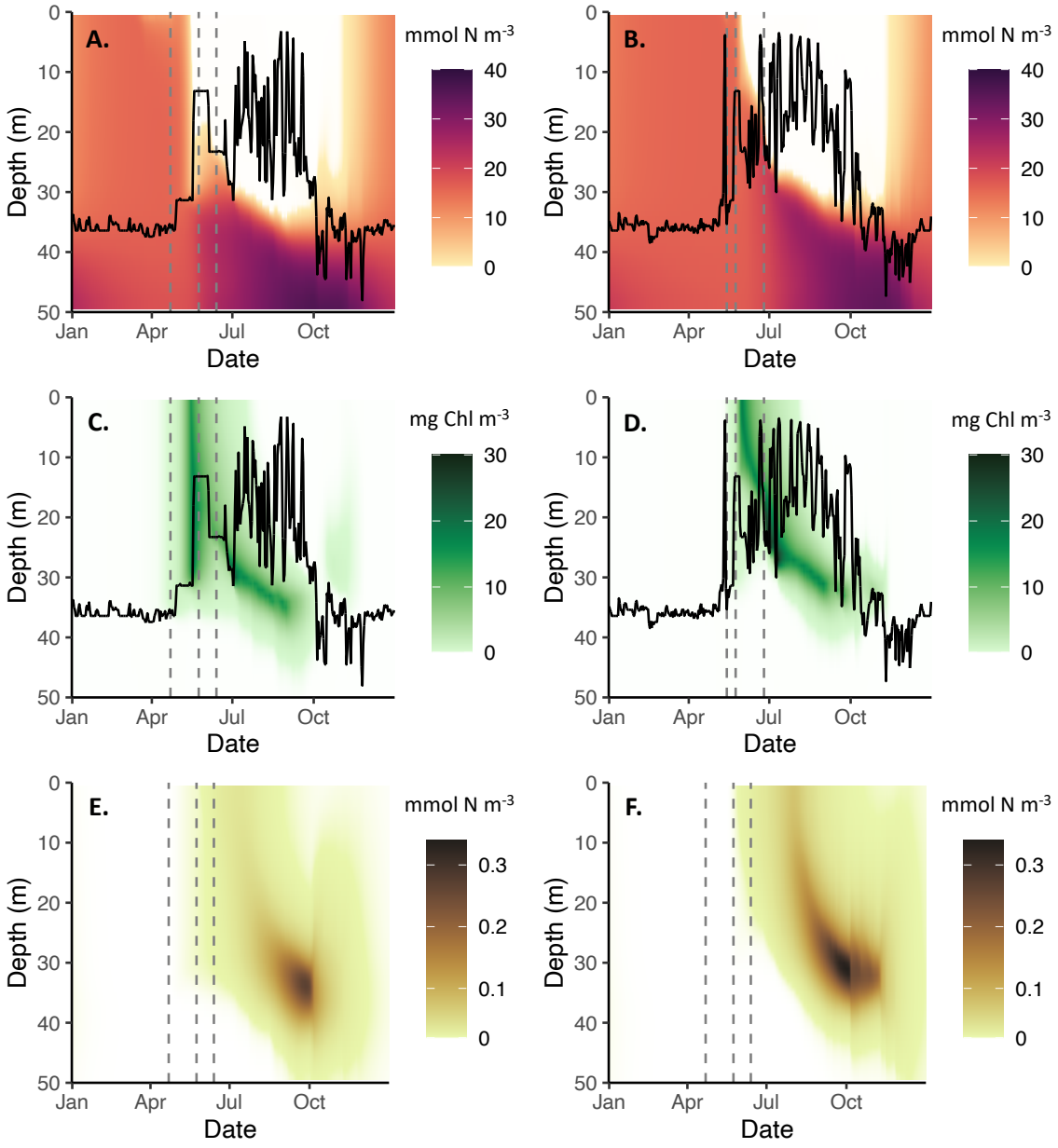

Figure C.4: Annual depth vs. time plots of (A, B) nitrogen (nitrate + ammonium), (C, D) phytoplankton (large + small), and (E, F) zooplankton (large + small) for 2008 (a year with a UIB and a moderate autumn bloom; subplots A, C, and E) and 2006 (a year without a UIB or an autumn bloom; subplots B, D, and F). Black lines (A-D) represent the mixed layer depth, calculated based on GOTM-derived buoyancy frequency. Grey dashed lines on each subplot represent, from left to right, the date of ice melt, the start of ice retreat (which marks the end of the UI period and start of the MIZ period), and the end of ice retreat (marking the end of the MIZ period and beginning of the OW period).Sub

Bibliography

(2019), Arctic Report Card 2019, p. 100.

Anderson, M., AC. Bliss, and S. Drobot (2019), Snow Melt Onset Over Arctic Sea Ice from SMMR and SSM/I-SSMIS Brightness Temperatures, doi:10.5067/A9YK15H5EBHK.

Apollonio, S. (1959), Hydrobiological measurements on IGY Drifting Station Bravo, *National Academy of Sciences IGY Bulletin*, *27*, 16–19.

Apollonio, S., and P. Matrai (2011), Marine primary production in the Canadian Arctic, 1956, 1961–1963, *Polar Biology*, *34*(5), 767–774, doi:10.1007/s00300-010-0928-3.

Ardyna, M., and K. R. Arrigo (2020), Phytoplankton dynamics in a changing Arctic Ocean, *Nature Climate Change*, *10*(10), 892–903, doi:10.1038/s41558-020-0905-y.

Ardyna, M., M. Babin, M. Gosselin, E. Devred, L. Rainville, and J.-É. Tremblay (2014), Recent Arctic Ocean sea ice loss triggers novel fall phytoplankton blooms, *Geophysical Research Letters*, *41*, 6207–6212, doi:10.1002/2014GL061047.

Ardyna, M., C. J. Mundy, N. Mayot, L. C. Matthes, L. Oziel, C. Horvat, E. Leu, P. Assmy, V. J. Hill, P. A. Matrai, M. Gale, I. A. Melnikov, and K. R. Arrigo (2020a), Under-Ice Phytoplankton Blooms: Shedding Light on the "Invisible" Part of Arctic Primary Production, *Frontiers in Marine Science*, *7*, 608,032, doi:10.3389/fmars.2020.608032.

Ardyna, M., C. J. Mundy, M. M. Mills, L. Oziel, P.-L. Grondin, L. Lacour, G. Verin, G. L. Van Dijken, J. Ras, E. Alou-Font, M. Babin, M. Gosselin, J.-É. Tremblay, P. Raimbault, P. Assmy, M. Nicolaus, H. Claustre, and K. R. Arrigo (2020b), Environmental drivers of under-ice phytoplankton bloom dynamics in the Arctic Ocean, *Elementa: Science of the Anthropocene*, *8*, 30, doi:10.1525/elementa.430.

Arrigo, K. R. (2003), Primary Production in Sea Ice, in *Sea Ice: An Introduction to Its Physics, Chemistry, Biology and Geology*, edited by D. N. T. a. G. S. Dieckmann, 1st ed., pp. 143–183, Blackwell Sci., Oxford, UK.

Arrigo, K. R. (2005), Marine microorgansisms and global nutrient cycles, *Nature*, *437*(September), 349–355, doi:10.1038/nature0415.

Arrigo, K. R. (2017), Sea ice as a habitat for primary producers, in *Sea Ice*, edited by D. N. Thomas, pp. 352–369, John Wiley & Sons, Ltd, Chichester, UK, doi:10.1002/9781118778371.ch14.

Arrigo, K. R., and G. L. Van Dijken (2011), Secular trends in Arctic Ocean net primary production, *Journal of Geophysical Research: Oceans*, *116*(9), 1–15, doi:10.1029/2011JC007151.

Arrigo, K. R., and G. L. Van Dijken (2015), Continued increases in Arctic Ocean primary production, *Progress in Oceanography*, *136*, 60–70, doi:10.1016/j.pocean.2015.05.002.

Arrigo, K. R., C. W. Sullivan, and J. N. Kremer (1991), A bio-optical model of Antarctic sea ice, *Journal of Geophysical Research*, *96*(C6), 10,581–10,592, doi:10.1029/91JC00455.

Arrigo, K. R., D. Worthen, A. Schnell, and MP. Lizotte (1998a), Primary production in Southern Ocean waters, *Journal of Geophysical Research*, *103*(C8), 15,587–15,599, doi:10.1029/98JC00930.

Arrigo, K. R., D. H. Robinson, D. L. Worthen, B. Schieber, and M. P. Lizotte (1998b), Bio-optical properties of the southwestern Ross Sea, *Journal of Geophysical Research*, *103*(C10), 683–695.

Arrigo, K. R., D. L. Worthen, and D. H. Robinson (2003), A coupled ocean-ecosystem model of the Ross Sea: 2. Iron regulation of phytoplankton taxonomic variability and primary production, *Journal of Geophysical Research*, *108*(C7), 3231–3231, doi:10.1029/2001JC000856.

Arrigo, K. R., G. L. Van Dijken, and S. Pabi (2008), Impact of a shrinking Arctic ice cover on marine primary production, *Geophysical Research Letters*, *35*(August), 1–6, doi:10.1029/2008GL035028.

Arrigo, K. R., D. K. Perovich, R. S. Pickart, Z. W. Brown, G. L. Van Dijken, K. E. Lowry, M. M. Mills, M. A. Palmer, W. M. Balch, F. Bahr, N. R. Bates, C. Benitez-Nelson, B. Bowler, E. Brownlee, J. K. Ehn, K. E. Frey, R. Garley, S. R. Laney, L. Lubelczyk, J. Mathis, A. Matsuoka, B. G. Mitchell, G. W. K. Moore, E. Ortega-Retuerta, S. Pal, C. M. Polashenski, R. A. Reynolds, B. Schieber, H. M. Sosik, M. Stephens, and J. H. Swift (2012), Massive Phytoplankton Blooms Under Arctic Sea Ice, *Science*, *336*, 1408–1408, doi:10.1126/science.1215065.

Arrigo, K. R., D. K. Perovich, R. S. Pickart, Z. W. Brown, G. L. Van Dijken, K. E. Lowry, M. M. Mills, M. A. Palmer, W. M. Balch, N. R. Bates, C. R. Benitez-Nelson, E. Brownlee, K. E. Frey, S. R. Laney, J. Mathis, A. Matsuoka, B. Greg Mitchell, G. W. Moore, R. A. Reynolds, H. M. Sosik, and J. H. Swift (2014), Phytoplankton blooms beneath the sea ice in the Chukchi sea, *Deep-Sea Research Part II: Topical Studies in Oceanography*, *105*, 1–16, doi:10.1016/j.dsr2.2014.03.018.

Arrigo, K. R., MM. Mills, G. L. Van Dijken, KE. Lowry, RS. Pickart, and R. Schlitzer (2017), Late spring nitrate distributions beneath the ice-covered northeastern Chukchi Shelf, *Journal of Geophysical Research: Biogeosciences*, *122*, 2409–2417, doi:10.1002/2017JG003881.

Ashjian, C. J., R. G. Campbell, H. E. Welch, M. Butler, and D. Van Keuren (2003), Annual cycle in abundance, distribution, and size in relation to hydrography of important copepod species in the western Arctic Ocean, *Deep-Sea Research Part I: Oceanographic Research Papers*, *50*(10-11), 1235–1261, doi:10.1016/S0967-0637(03)00129-8.

Assmy, P., J. K. Ehn, M. Fernández-Méndez, H. Hop, C. Katlein, A. Sundfjord, K. Bluhm, M. Daase, A. Engel, A. Fransson, M. A. Granskog, S. R. Hudson, S. Kristiansen, M. Nicolaus, I. Peeken, A. H. H. Renner, G. Spreen, A. Tatarek, and J. Wiktor (2013), Floating Ice-Algal Aggregates below Melting Arctic Sea Ice, *PLoS ONE*, *8*(10), e76,599, doi:10.1371/journal.pone.0076599.

Assmy, P., M. Fernández-Méndez, P. Duarte, A. Meyer, A. Randelhoff, C. J. Mundy, L. M. Olsen, H. M. Kauko, A. Bailey, M. Chierici, L. Cohen, A. P. Doulgeris, J. K. Ehn, A. Fransson, S. Gerland, H. Hop, S. R. Hudson, N. Hughes, P. Itkin, G. Johnsen, J. A. King, B. P. Koch, Z. Koenig, S. Kwasniewski, S. R. Laney, M. Nicolaus, A. K. Pavlov, C. M. Polashenski, C. Provost, A. Rösel, M. Sandbu, G. Spreen, L. H. Smedsrud, A. Sundfjord, T. Taskjelle, A. Tatarek, J. Wiktor, P. M. Wagner, A. Wold, H. Steen, and M. A. Granskog (2017), Leads in Arctic pack ice enable early phytoplankton blooms below snow-covered sea ice, *Scientific Reports*, *7*(1), 40,850, doi:10.1038/srep40850.

Baer, S. E., R. E. Sipler, Q. N. Roberts, P. L. Yager, M. E. Frischer, and D. A. Bronk (2017), Seasonal nitrogen uptake and regeneration in the western coastal Arctic: Arctic coastal nitrogen dynamics, *Limnology and Oceanography*, *62*(6), 2463–2479, doi:10.1002/lno.10580.

Baumann, M. S., S. B. Moran, M. W. Lomas, R. P. Kelly, and D. W. Bell (2013), Seasonal decoupling of particulate organic carbon export and net primary production in relation to sea-ice at the shelf break of the eastern Bering Sea: Implications for off-shelf carbon export, *Journal of Geophysical Research: Oceans*, *118*(10), 5504–5522, doi:10.1002/jgrc.20366.

Beer, E., I. Eisenman, and T. J. W. Wagner (2020), Polar Amplification Due to Enhanced Heat Flux Across the Halocline, *Geophysical Research Letters*, *47*(4), doi:10.1029/2019GL086706.

Behrenfeld, M. J., Y. Hu, R. T. O'Malley, E. S. Boss, C. A. Hostetler, D. A. Siegel, J. L. Sarmiento, J. Schulien, J. W. Hair, X. Lu, S. Rodier, and A. J. Scarino (2017), Annual boom–bust cycles of polar phytoplankton biomass revealed by space-based lidar, *Nature Geoscience*, *10*(2), 118–122, doi:10.1038/ngeo2861.

Ben Mustapha, S., S. Bélanger, and P. Larouche (2012), Evaluation of ocean color algorithms in the southeastern Beaufort Sea, Canadian Arctic: New parameterization using SeaWiFS, MODIS, and MERIS spectral bands, *Canadian Journal of Remote Sensing*, *38*(5), 535–556, doi:10.5589/m12-045.

Besiktepe, ST., P. F. J. Lermusiaux, and A. R. Robinson (2003), Coupled physical and biogeochemical data-driven simulations of Massachusetts Bay in late summer: Real-time and postcruise data assimilation, *Journal of Marine Systems*, *41*, 171–212, doi:10.1016/S0924-7963(03)00018-6.

Blackman, F. F. (1905), Optima and Limiting Factors, *Annals of Botany*, *os-19*(2), 281–296, doi:10.1093/oxfordjournals.aob.a089000.

Blais, M., J.-É. Tremblay, A. D. Jungblut, J. Gagnon, J. Martin, M. Thaler, and C. Lovejoy (2012), Nitrogen fixation and identification of potential diazotrophs in the Canadian Arctic, *Global Biogeochemical Cycles*, *26*(3), 2011GB004,096, doi:10.1029/2011GB004096.

Boetius, A., S. Albrecht, K. Bakker, C. Bienhold, J. Felden, M. Fernandez-Mendez, S. Hendricks, C. Katlein, C. Lalande, T. Krumpen, M. Nicolaus, I. Peeken, B. Rabe, A. Rogacheva, E. Rybakova, R. Somavilla, F. Wenzhofer, and RV Polarstern ARK27-3-Shipboard Science Party (2013), Export of Algal Biomass from the Melting Arctic Sea Ice, *Science*, *339*(6126), 1430–1432, doi:10.1126/science.1231346.

Boles, E., C. Provost, V. Garçon, C. Bertosio, M. Athanase, Z. Koenig, and N. Sennéchael (2020), Under-Ice Phytoplankton Blooms in the Central Arctic Ocean: Insights From the First Biogeochemical IAOOS Platform Drift in 2017, *Journal of Geophysical Research: Oceans*, *125*(3), doi:10.1029/2019JC015608.

Bopp, L., L. Resplandy, J. C. Orr, S. C. Doney, J. P. Dunne, M. Gehlen, P. Halloran, C. Heinze, T. Ilyina, R. Séférian, J. Tjiputra, and M. Vichi (2013), Multiple stressors of ocean ecosystems in the 21st century: Projections with CMIP5 models, *Biogeosciences*, *10*, 6225–6245, doi:10.5194/bg-10-6225-2013.

Boyd, PW., J. Laroche, M. Gall, R. Frew, R. M. L. Mckay, and A. Phytoplankton (1999), Role of iron, light, and silicate in controlling algal biomass in subantarctic waters SE of New Zealand, *Geo*, *104*(C6), 395–408, doi:10.1029/1999JC900009.

Boyd, PW., A. C. Crossley, G. R. DiTullio, F. B. Griffiths, D. A. Hutchins, B. Queguiner, P. N. Sedwick, and T. W. Trull (2004), Control of phytoplankton growth by iron supply and irradiance in the subantarctic Southern Ocean: Experimental results from the SAZ Project, *Journal of Geophysical Research: Oceans*, *106*(C12), 31,573–31,583, doi:10.1029/2000jc000348.

Boyd, PW., T. Jickells, C. S. Law, S. Blain, E. A. Boyle, K. O. Buesseler, K. H. Coale, J. J. Cullen, H. J. De Baar, M. Follows, M. Harvey, C. Lancelot, M. Levasseur, N. P. Owens, R. Pollard, R. B. Rivkin, J. Sarmiento, V. Schoemann, V. Smetacek, S. Takeda, A. Tsuda, S. Turner, and A. J. Watson (2007), Mesoscale iron enrichment experiments 1993-2005: Synthesis and future directions, *Science*, *315*(5812), 612–617, doi:10.1126/science.1131669.

Bradstreet, M. S., and W. E. Cross (1982), Trophic Relationships at High Arctic Ice Edges, *ARCTIC*, *35*(1), 1–12, doi:10.14430/arctic2303.

Bricaud, A., M. Babin, A. Morel, and H. Claustre (1995), Variability in the chlorophyll-specific absorption coefficients of natural phytoplankton: Analysis and parameterization, *Journal of Geophysical Research*, *100*(C7), 13,321–13,332, doi:10.1029/95JC00463.

Brown, Z. W., K. L. Casciotti, R. S. Pickart, J. H. Swift, and K. R. Arrigo (2015a), Aspects of the marine nitrogen cycle of the Chukchi Sea shelf and Canada Basin, *Deep-Sea Research Part II: Topical Studies in Oceanography*, *118*, 73–87, doi:10.1016/j.dsr2.2015.02.009.

Brown, Z. W., K. E. Lowry, M. A. Palmer, G. L. Van Dijken, M. M. Mills, R. S. Pickart, and K. R. Arrigo (2015b), Characterizing the subsurface chlorophyll a maximum in the Chukchi Sea and Canada Basin, *Deep-Sea Research Part II: Topical Studies in Oceanography*, *118*, 88–104, doi:10.1016/j.dsr2.2015.02.010.

Brzezinski, M. A. (1985), The Si:C:N ratio of marine diatoms: Interspecific variability and the effect of some environmental variables, *Journal of Phycology*, *21*(3), 347–357.

Burchard, H., K. Bolding, and M. Ruiz-Villarreal (1999), *GOTM, a General Ocean Turbulence Model. Theory, Implementation and Test Cases*, Space Applications Institute.

Cabré, A., I. Marinov, and S. Leung (2015), Consistent global responses of marine ecosystems to future climate change across the IPCC AR5 earth system models, *Climate Dynamics*, *45*(5-6), 1253–1280, doi:10.1007/s00382-014-2374-3.

Campbell, R. G., M. Wagner, G. Teegarden, C. Boudreau, and E. Durbin (2001), Growth and development rates of the copepod *Calanus finmarchicus* reared in the laboratory, *Marine Ecology Progress Series*, *221*, 161–183, doi:10.3354/meps221161.

Campbell, R. G., E. B. Sherr, C. J. Ashjian, S. Plourde, B. F. Sherr, V. J. Hill, and D. A. Stockwell (2009), Mesozooplankton prey preference and grazing impact in the western Arctic Ocean, *Deep Sea Research Part II: Topical Studies in Oceanography*, *56*(17), 1274–1289, doi:10.1016/j.dsr2.2008.10.027.

Carmack, E., and D. C. Chapman (2003), Wind-driven shelf/basin exchange on an Arctic shelf: The joint roles of ice cover extent and shelf-break bathymetry: WIND-DRIVEN SHELF/BASIN EXCHANGE, *Geophysical Research Letters*, *30*(14), doi:10.1029/2003GL017526.

Carpenter, E. J., and R. R. L. Guillard (1971), Intraspecific Differences in Nitrate Half-Saturation Constants for Three Species of Marine Phytoplankton, *Ecology*, *52*(1), 183–185, doi:10.2307/1934753.

Carter, C. M., A. H. Ross, D. R. Schiel, C. Howard-Williams, and B. Hayden (2005), In situ microcosm experiments on the influence of nitrate and light on phytoplankton community composition, *Journal of Experimental Marine Biology and Ecology*, *326*(1), 1–13, doi: 10.1016/j.jembe.2005.05.006.

Chai, F., R. C. Dugdale, T. Peng, F. P. Wilkerson, and R. T. Barber (2002), One-dimensional ecosystem model of the equatorial Pacific upwelling system . Part I : Model development and silicon and nitrogen cycle, *Deep Sea Research Part II: Topical Studies in Oceanography*, *49*, 2713–2745.

Chang, B. X., and A. H. Devol (2009), Seasonal and spatial patterns of sedimentary denitrification rates in the Chukchi sea, *Deep-Sea Research Part II: Topical Studies in Oceanography*, *56*(17), 1339–1350, doi:10.1016/j.dsr2.2008.10.024.

Christian, J. R., M. A. Verschell, R. Murtugudde, and A. J. Busalacchi (2002), Biogeochemical modelling of the tropical Pacific Ocean . I : Seasonal and interannual variability, *Deep-Sea Research Part II*, *49*, 509–543.

Clement Kinney, J., W. Maslowski, R. Osinski, M. Jin, M. Frants, N. Jeffery, and Y. J. Lee (2020), Hidden Production: On the Importance of Pelagic Phytoplankton Blooms Beneath Arctic Sea Ice, *Journal of Geophysical Research: Oceans*, *125*(9), doi:10.1029/2020JC016211.

Codispoti, L. A., C. Flagg, V. Kelly, and J. H. Swift (2005), Hydrographic conditions during the 2002 SBI process experiments, *Deep-Sea Research Part II: Topical Studies in Oceanography*, *52*(24-26), 3199–3226, doi:10.1016/j.dsr2.2005.10.007.

Codispoti, L. A., C. N. Flagg, and J. H. Swift (2009), Hydrographic conditions during the 2004 SBI process experiments, *Deep-Sea Research II*, *56*, 1144–1163, doi:10.1016/j.dsr2.2008.10.013.

Comiso, J. C. (2012), Large decadal decline of the arctic multiyear ice cover, *Journal of Climate*, *25*(4), 1176–1193, doi:10.1175/JCLI-D-11-00113.1.

Conover, R., and M. Huntley (1991), Copepods in ice-covered seas—Distribution, adaptations to seasonally limited food, metabolism, growth patterns and life cycle strategies in polar seas, *Journal of Marine Systems*, *2*(1-2), 1–41, doi:10.1016/0924-7963(91)90011-I.

Cooper, L. W., and J. M. Grebmeier (2018), Deposition patterns on the Chukchi shelf using radionuclide inventories in relation to surface sediment characteristics, *Deep Sea Research Part II: Topical Studies in Oceanography*, *152*, 48–66, doi:10.1016/j.dsr2.2018.01.009.

Corlett, W. B., and R. S. Pickart (2017), Progress in Oceanography The Chukchi slope current, *Progress in Oceanography*, *153*, 50–65, doi:10.1016/j.pocean.2017.04.005.

Cota, G., and E. Home (1989), Physical control of arctic ice algal production, *Marine Ecology Progress Series*, *52*, 111–121, doi:10.3354/meps052111.

Coyle, K., B. Konar, A. Blanchard, R. Highsmith, J. Carroll, M. Carroll, S. Denisenko, and B. Sirenko (2007), Potential effects of temperature on the benthic infaunal community on the southeastern Bering Sea shelf: Possible impacts of climate change, *Deep Sea Research Part II: Topical Studies in Oceanography*, *54*(23-26), 2885–2905, doi:10.1016/j.dsr2.2007.08.025.

Crawford, A. D., K. M. Krumhardt, N. S. Lovenduski, G. L. Dijken, and K. R. Arrigo (2020), Summer High-Wind Events and Phytoplankton Productivity in the Arctic Ocean, *Journal of Geophysical Research: Oceans*, *125*(9), doi:10.1029/2020JC016565.

Cullen, J. J. (1982), The Deep Chlorophyll Maximum: Comparing Vertical Profiles of Chlorophyll *a*, *Canadian Journal of Fisheries and Aquatic Sciences*, *39*(5), 791–803, doi:10.1139/f82-108.

Darby, D., J. Ortiz, L. Polyak, S. Lund, M. Jakobsson, and R. Woodgate (2009), The role of currents and sea ice in both slowly deposited central Arctic and rapidly deposited Chukchi–Alaskan margin sediments, *Global and Planetary Change*, *68*(1-2), 58–72, doi:10.1016/j.gloplacha.2009.02.007.

Davis, CO. (1976), Continuous culture of marine diatoms under silicate limitation. Effect of light intensity on growth and nutrient uptake of Skeletonema Costatum, *Journal of Phycology*, *12*, 291–300.

Davis, J., and R. Benner (2007), Quantitative estimates of labile and semi-labile dissolved organic carbon in the western Arctic Ocean: A molecular approach, *Limnology and Oceanography*, *52*(6), 2434–2444, doi:10.4319/lo.2007.52.6.2434.

De Robertis, A., K. Taylor, C. D. Wilson, and E. V. Farley (2017), Abundance and distribution of Arctic cod (Boreogadus saida) and other pelagic fishes over the U.S. Continental Shelf of the Northern Bering and Chukchi Seas, *Deep Sea Research Part II: Topical Studies in Oceanography*, *135*, 51–65, doi:10.1016/j.dsr2.2016.03.002.

Deutsch, C., and T. Weber (2012), Nutrient Ratios as a Tracer and Driver of Ocean Biogeochemistry, *Annual Review of Marine Science*, *4*(1), 113–141, doi:10.1146/annurev-marine-120709-142821.

Devol, A. H., L. A. Codispoti, and J. P. Christensen (1997), Summer and winter denitrification rates in western Arctic shelf sediments, *Continental Shelf Research*, *17*(9).

Díez, B., B. Bergman, C. Pedrós-Alió, M. Antó, and P. Snoeijs (2012), High cyanobacterial nifH gene diversity in Arctic seawater and sea ice brine: Arctic nifH gene diversity, *Environmental Microbiology Reports*, *4*(3), 360–366, doi:10.1111/j.1758-2229.2012.00343.x.

Dobson, F. W., and S. D. Smith (1988), Bulk models of solar radiation at sea, *Quarterly Journal of the Royal Meteorological Society*, *114*(479), 165–182, doi:10.1002/qj.49711447909.

Droop, MR., M. J. Mickelson, J. M. Scott, and M. F. Turner (1982), Light and nutrient status of algal cells, *Journal of the Marine Biological Association of the United Kingdom*, *62*(2), 403–434, doi:10.1017/S0025315400057362.

Ducklow, H. W., and R. P. Harris (1993), Introduction to the JGOFS North Atlantic bloom experiment, *Deep Sea Research Part II: Topical Studies in Oceanography*, *40*(1-2), 1–8, doi:10.1016/0967-0645(93)90003-6.

Dupont, F. (2012), Impact of sea-ice biology on overall primary production in a biophysical model of the pan-Arctic Ocean: ARCTIC ICE-OCEAN BIO-PHYSICAL MODEL, *Journal of Geophysical Research: Oceans*, *117*(C8), n/a–n/a, doi:10.1029/2011JC006983.

English, T. (1961), Some Biological Observations in the Central North Polar Sea Drift Station Alpha, 1957-1958, *Scientific Reports No. 15*, pp. 1–80.

Eppley, R. W. (1972), Temperature and Phytoplankton Growth in the Sea, *Fishery Bulletin*, *70*(4), 1063–1085.

Eppley, R. W., and W. H. Thomas (1969), COMPARISON OF HALF-SATURATION CONSTANTS FOR GROWTH AND NITRATE UPTAKE OF MARINE PHYTOPLANKTON, *Journal of Phycology*, *5*(4), 375–379, doi:10.1111/j.1529-8817.1969.tb02628.x.

Ershova, E., R. Hopcroft, K. Kosobokova, K. Matsuno, R. J. Nelson, A. Yamaguchi, and L. Eisner (2015), Long-Term Changes in Summer Zooplankton Communities of the Western Chukchi Sea, 1945–2012, *Oceanography*, *28*(3), 100–115, doi:10.5670/oceanog.2015.60.

Fahl, K., and E.-M. Nöthig (2007), Lithogenic and biogenic particle fluxes on the Lomonosov Ridge (central Arctic Ocean) and their relevance for sediment accumulation: Vertical vs. lateral transport, *Deep Sea Research Part I: Oceanographic Research Papers*, *54*(8), 1256–1272, doi:10.1016/j.dsr.2007.04.014.

Falkowski, P. G. (1975), Nitrate uptake in marine phytoplankton: Comparison of half-saturation constants from seven species1: NOs˜ ATPase in phytoplankton, *Limnology and Oceanography*, *20*(3), 412–417, doi:10.4319/lo.1975.20.3.0412.

Falkowski, P. G. (1994), The role of phytoplankton photosynthesis in global biogeochemical cycles, *Photosynthesis Research*, *39*(3), 235–258, doi:10.1007/BF00014586.

Falkowski, P. G. (2012), Ocean Science: The power of plankton, *Nature*, *483*, S17–S20.

Fasham, M. J. R., H. W. Ducklow, and S. M. McKelvie (1990), A nitrogen-based model of plankton dynamics in the oceanic mixed layer, *Journal of Marine Research*, *48*(3), 591–639, doi:10.1357/002224090784984678.

Fennel, K. (2010), The role of continental shelves in nitrogen and carbon cycling: Northwestern North Atlantic case study, *Ocean Science*, *6*(2), 539–548, doi:10.5194/os-6-539-2010.

Fennel, K., J. Wilkin, J. Levin, J. Moisan, J. O'Reilly, and D. Haidvogel (2006), Nitrogen cycling in the Middle Atlantic Bight: Results from a three-dimensional model and implications for the North Atlantic nitrogen budget, *Global Biogeochemical Cycles*, *20*(3), n/a–n/a, doi:10.1029/2005GB002456.

Fennel, K., D. Brady, D. Di Toro, WF. Robinson, WS. Gardner, A. Giblin, M. J. McCarthy, A. Rao, S. Seitzinger, M. Thouvenot-Korppoo, and C. Tobias (2009), Modeling denitrification in aquatic sediments, *Biogeochemistry*, *93*, 159–178, doi:10.1007/s10533-008-9270-z.

Fernández-Méndez, M., K. A. Turk-Kubo, P. L. Buttigieg, J. Z. Rapp, T. Krumpen, J. P. Zehr, and A. Boetius (2016), Diazotroph Diversity in the Sea Ice, Melt Ponds, and Surface Waters of the Eurasian Basin of the Central Arctic Ocean, *Frontiers in Microbiology*, *7*, doi:10.3389/fmicb.2016.01884.

Fichot, C. G., K. Kaiser, S. B. Hooker, R. M. W. Amon, M. Babin, S. Bélanger, S. A. Walker, and R. Benner (2013), Pan-Arctic distributions of continental runoff in the Arctic Ocean, *Scientific Reports*, *3*(1), 1053, doi:10.1038/srep01053.

Field, C. B., M. J. Behrenfeld, J. T. Randerson, and P. G. Falkowski (1998), Primary Production of the Biosphere: Integrating Terrestrial and Oceanic Components, *Science*, *281*, 237–240.

Fortier, M., L. Fortier, C. Michel, and L. Legendre (2002), Climatic and biological forcing of the vertical flux of biogenic particles under seasonal Arctic sea ice, *Marine Ecology Progress Series*, *225*, 1–16, doi:10.3354/meps225001.

Franks, PJ. (2002), NPZ models of phytoplankton dynamics: Their construction, coupling to physics, and application, *Journal of Oceanography*, *58*, 379–387.

Frey, K. E., D. K. Perovich, and B. Light (2011), The spatial distribution of solar radiation under a melting Arctic sea ice cover, *Geophysical Research Letters*, *38*(November), 1–6, doi:10.1029/2011GL049421.

Fu, W., J. T. Randerson, and J. K. Moore (2016), Climate change impacts on net primary production (NPP) and export production(EP) regulated by increasing stratification and phytoplankton communitystructure in the CMIP5 models, *Biogeosciences*, *13*(18), 5151–5170, doi:10.5194/bg-13-5151-2016.

Galbraith, E. D., A. Gnanadesikan, J. P. Dunne, and M. R. Hiscock (2010), Regional impacts of iron-light colimitation in a global biogeochemical model, *Biogeosciences*, *7*, 1043–1064.

Geider, R. J., H. L. MacIntyre, and T. M. Kana (1998), A dynamic regulatory model of phytoplanktonic temperature acclimation to light , nutrients , and, *Limnology and Oceanography*, *43*(4), 679–694.

Geider, RJ., HL. MacIntyre, and TM. Kana (1997), Dynamic model of phytoplankton growth and acclimation: Responses of the balanced growth rate and the chlorophyll a:carbon ratio to light , nutrient-limitation and temperature, *Marine Ecology Progress Series*, *148*, 187–200.

Gosselin, M., M. Levasseur, P. A. Wheeler, R. A. Horner, and B. C. Booth (1997), New measurements of phytoplankton and ice algal production in the Arctic Ocean, *Deep Sea Research Part II: Topical Studies in Oceanography*, *44*(8), 1623–1644, doi:10.1016/S0967-0645(97)00054-4.

Gradinger, R. (1996), Occurrence of an algal bloom under Arctic pack ice, *Marine Ecology Progress Series*, *131*(1-3), 301–305, doi:10.3354/meps131301.

Gradinger, R. (2009), Sea-ice algae: Major contributors to primary production and algal biomass in the Chukchi and Beaufort Seas during May/June 2002, *Deep Sea Research Part II: Topical Studies in Oceanography*, *56*(17), 1201–1212, doi:10.1016/j.dsr2.2008.10.016.

Granger, J., M. G. Prokopenko, D. M. Sigman, C. W. Mordy, Z. M. Morse, L. V. Morales, R. N. Sambrotto, and B. Plessen (2011), Coupled nitrification-denitrification in sediment of the eastern Bering Sea shelf leads to15N enrichment of fixed N in shelf waters, *Journal of Geophysical Research: Oceans*, *116*(11), 1–18, doi:10.1029/2010JC006751.

Granger, J., D. M. Sigman, J. Gagnon, J.-E. Tremblay, and A. Mucci (2018), On the Properties of the Arctic Halocline and Deep Water Masses of the Canada Basin from Nitrate Isotope Ratios, *Journal of Geophysical Research: Oceans*, *123*(8), 5443–5458, doi:10.1029/2018JC014110.

Grebmeier, J. M. (2006), A Major Ecosystem Shift in the Northern Bering Sea, *Science*, *311*(5766), 1461–1464, doi:10.1126/science.1121365.

Grebmeier, J. M. (2012), Shifting Patterns of Life in the Pacific Arctic and Sub-Arctic Seas, *Annual Review of Marine Science*, *4*, 63–78, doi:10.1146/annurev-marine-120710-100926.

Grebmeier, J. M. (2017), The Distributed Biological Observatory (DBO) Conductivity-Temperature-Depth (CTD) data from 2011, doi:10.18739/A29Z90C7B.

Grebmeier, J. M., C. McRoy, and H. Feder (1988), Pelagic-benthic coupling on the shelf of the northern Bering and Chukchi Seas. I. Food supply source and benthic bio-mass, *Marine Ecology Progress Series*, *48*, 57–67, doi:10.3354/meps048057.

Grebmeier, J. M., B. Bluhm, L. Cooper, S. Denisenko, K. Iken, M. Kedra, and C. Serratos (2015), Time-Series Benthic Community Composition and Biomass and Associated Environmental Characteristics in the Chukchi Sea During the RUSALCA 2004–2012 Program, *Oceanography*, *28*(3), 116–133, doi:10.5670/oceanog.2015.61.

Gregg, W. W., and K. L. Carder (1990), A simple spectral solar irradiance model for cloudless maritime atmospheres, *Limnology and Oceanography*, *35*(8), 1657–1675, doi:10.4319/lo.1990.35.8.1657.

Grömping, U. (2006), Relative Importance for Linear Regression in *R* : The Package **relaimpo**, *Journal of Statistical Software*, *17*(1), doi:10.18637/jss.v017.i01.

Gruber, N., and J. L. Sarmiento (1997), Global patterns of marine nitrogen fixation and denitrification, *Global Biogeochemical Cycles*, *11*(2), 235–266, doi:10.1029/97GB00077.

Guillard, R. R. L., and J. H. Ryther (1962), STUDIES OF MARINE PLANKTONIC DIATOMS: I. CYCLOTELLA NANA HUSTEDT, AND DETONULA CONFERVACEA (CLEVE) GRAN., *Canadian Journal of Microbiology*, *8*(2), 229–239, doi:10.1139/m62-029.

Hameedi, M. J. (1978), Aspects of water column primary productivity in the Chukchi Sea during summer, *Marine Biology*, *48*(1), 37–46, doi:10.1007/BF00390529.

Hamilton, C., C. Lydersen, J. Aars, M. Biuw, A. Boltunov, E. Born, R. Dietz, L. Folkow, D. Glazov, T. Haug, M. Heide-Jørgensen, L. Kettemer, K. Laidre, N. Øien, E. Nordøy, A. Rikardsen, A. Rosing-Asvid, V. Semenova, O. Shpak, S. Sveegaard, F. Ugarte, Ø. Wiig, and K. Kovacs (2021), Marine mammal hotspots in the Greenland and Barents Seas, *Marine Ecology Progress Series*, *659*, 3–28, doi:10.3354/meps13584.

Haney, J. D., and G. A. Jackson (1996), Modeling phytoplankton growth rates, *Journal of Plankton Research*, *18*(1), 23.

Hansell, D. A., T. E. Whitledge, and J. J. Goering (1993), Patterns of nitrate utilization and new production over the Bering-Chukchi shelf, *Continental Shelf Research*, *13*(5-6), 601–627, doi:10.1016/0278-4343(93)90096-G.

Henley, S. F., M. Porter, L. Hobbs, J. Braun, R. Guillaume-Castel, E. J. Venables, E. Dumont, and F. Cottier (2020), Nitrate supply and uptake in the Atlantic Arctic sea ice zone: Seasonal cycle, mechanisms and drivers, *Philosophical Transactions of the Royal Society A: Mathematical, Physical and Engineering Sciences*, *378*(2181), 20190,361, doi:10.1098/rsta.2019.0361.

Hill, V. J., and G. Cota (2005), Spatial patterns of primary production on the shelf, slope and basin of the Western Arctic in 2002, *Deep-Sea Research Part II: Topical Studies in Oceanography*, *52*(24-26), 3344–3354, doi:10.1016/j.dsr2.2005.10.001.

Hill, V. J., B. Light, M. Steele, and R. C. Zimmerman (2018a), Light Availability and Phytoplankton Growth Beneath Arctic Sea Ice: Integrating Observations and Modeling, *Journal of Geophysical Research: Oceans*, *123*(5), 3651–3667, doi:10.1029/2017JC013617.

Hill, V. J., M. Ardyna, S. H. Lee, and D. E. Varela (2018b), Decadal trends in phytoplankton production in the Pacific Arctic Region from 1950 to 2012, *Deep Sea Research Part II: Topical Studies in Oceanography*, *152*, 82–94, doi:10.1016/j.dsr2.2016.12.015.

Honjo, S., R. A. Krishfield, T. I. Eglinton, S. J. Manganini, J. N. Kemp, K. Doherty, J. Hwang, T. K. McKee, and T. Takizawa (2010), Biological pump processes in the cryopelagic and hemipelagic Arctic Ocean: Canada Basin and Chukchi Rise, *Progress in Oceanography*, *85*(3-4), 137–170, doi:10.1016/j.pocean.2010.02.009.

Horak, R. E., H. Whitney, D. H. Shull, C. W. Mordy, and A. H. Devol (2013), The role of sediments on the Bering Sea shelf N cycle: Insights from measurements of benthic denitrification and benthic DIN fluxes, *Deep-Sea Research Part II: Topical Studies in Oceanography*, *94*, 95–105, doi:10.1016/j.dsr2.2013.03.014.

Horvat, C., D. R. Jones, S. Iams, D. Schroeder, D. Flocco, and D. Feltham (2017), The frequency and extent of sub-ice phytoplankton blooms in the Arctic Ocean, *Science Advances*, *3*(3), doi:10.1126/sciadv.1601191.

Huisman, J., N. N. Pham Thi, D. M. Karl, and B. Sommeijer (2006), Reduced mixing generates oscillations and chaos in the oceanic deep chlorophyll maximum, *Nature*, *439*(7074), 322–325, doi:10.1038/nature04245.

Huntley, M., and MDG. Lopez (1992), Temperature-Dependent Production of Marine Copepods : A Global Synthesis, *The American Naturalist*, *140*(2), 201–242.

Huot, Y., B. A. Franz, and M. Fradette (2013), Estimating variability in the quantum yield of Sun-induced chlorophyll fluorescence: A global analysis of oceanic waters, *Remote Sensing of Environment*, *132*, 238–253, doi:10.1016/j.rse.2013.01.003.

Jin, M., C. Deal, S. H. Lee, S. Elliott, E. Hunke, M. Maltrud, and N. Jeffery (2012), Investigation of Arctic sea ice and ocean primary production for the period 1992–2007 using a 3-D global ice–ocean ecosystem model, *Deep Sea Research Part II: Topical Studies in Oceanography*, *81–84*, 28–35, doi:10.1016/j.dsr2.2011.06.003.

Jin, M., E. E. Popova, J. Zhang, R. Ji, D. Pendleton, Ø. Varpe, A. Yool, and Y. J. Lee (2016), Ecosystem model intercomparison of under-ice and total primary production in the Arctic Ocean, *Journal of Geophysical Research: Oceans*, *121*(1), 934–948, doi:10.1002/2015JC011183.

Joiris, C. R. (2011), A major feeding ground for cetaceans and seabirds in the south-western Greenland Sea, *Polar Biology*, *34*(10), 1597–1607, doi:10.1007/s00300-011-1022-1.

Kondo, J. (1975), Air-sea bulk transfer coefficients in diabatic conditions, *Boundary-Layer Meteorology*, *9*(1), 91–112, doi:10.1007/BF00232256.

Krisch, S., T. J. Browning, M. Graeve, K.-U. Ludwichowski, P. Lodeiro, M. J. Hopwood, S. Roig, J.-C. Yong, T. Kanzow, and E. P. Achterberg (2020), The influence of Arctic Fe and Atlantic fixed N on summertime primary production in Fram Strait, North Greenland Sea, *Scientific Reports*, *10*(1), 15,230, doi:10.1038/s41598-020-72100-9.

Krumhardt, K. M., N. S. Lovenduski, M. C. Long, and K. Lindsay (2017), Avoidable impacts of ocean warming on marine primary production: Insights from the CESM ensembles, *Global Biogeochemical Cycles*, *31*(1), 114–133, doi:10.1002/2016GB005528.

Kuletz, K. J., M. C. Ferguson, B. Hurley, A. E. Gall, E. A. Labunski, and T. C. Morgan (2015), Seasonal spatial patterns in seabird and marine mammal distribution in the eastern Chukchi and western Beaufort seas: Identifying biologically important pelagic areas, *Progress in Oceanography*, *136*, 175–200, doi:10.1016/j.pocean.2015.05.012.

Kwok, R. (2018), Arctic sea ice thickness, volume, and multiyear ice coverage: Losses and coupled variability (1958-2018), *Environmental Research Letters*, *13*, 105,005–105,005, doi:10.1088/1748-9326/aae3ec.

Lalande, C., J. M. Grebmeier, P. Wassmann, L. W. Cooper, M. V. Flint, and V. M. Sergeeva (2007), Export fluxes of biogenic matter in the presence and absence of seasonal sea ice cover in the Chukchi Sea, *Continental Shelf Research*, *27*(15), 2051–2065, doi:10.1016/j.csr.2007.05.005.

Lalande, C., E.-M. Nöthig, R. Somavilla, E. Bauerfeind, V. Shevchenko, and Y. Okolodkov (2014), Variability in under-ice export fluxes of biogenic matter in the Arctic Ocean: Under-ice fluxes in the Arctic Ocean, *Global Biogeochemical Cycles*, *28*(5), 571–583, doi:10.1002/2013GB004735.

Lalande, C., J. M. Grebmeier, R. R. Hopcroft, and S. L. Danielson (2020), Annual cycle of export fluxes of biogenic matter near Hanna Shoal in the northeast Chukchi Sea, *Deep Sea Research Part II: Topical Studies in Oceanography*, p. 104730, doi:10.1016/j.dsr2.2020.104730.

Laney, S. R., and H. M. Sosik (2014), Phytoplankton assemblage structure in and around a massive under-ice bloom in the Chukchi Sea, *Deep Sea Research Part II: Topical Studies in Oceanography*, *105*, 30–41, doi:10.1016/j.dsr2.2014.03.012.

Laurent, A., K. Fennel, R. Wilson, J. Lehrter, and R. Devereux (2016), Parameterization of biogeochemical sediment–water fluxes using in situ measurements and a diagenetic model, *Biogeosciences*, *13*(1), 77–94, doi:10.5194/bg-13-77-2016.

Laws, E. A., and T. T. Bannister (1980), Nutrient- and light-limited growth of Thalassiosira fluviatilis in continuous culture, with implications for phytoplankton growth in the ocean, *Limnology and Oceanography*, *25*(3), 457–473, doi:10.4319/lo.1980.25.3.0457.

Laws, E. A., and M. S. Chalup (1990), A microalgal growth model, *Limnology and Oceanography*, *35*(3), 597–608, doi:10.4319/lo.1990.35.3.0597.

Laxon, S. W., K. A. Giles, A. L. Ridout, D. J. Wingham, R. Willatt, R. Cullen, R. Kwok, A. Schweiger, J. Zhang, C. Haas, S. Hendricks, R. Krishfield, N. Kurtz, S. Farrell, and M. Davidson (2013), CryoSat-2 estimates of Arctic sea ice thickness and volume, *Geophysical Research Letters*, *40*(4), 732–737, doi:10.1002/grl.50193.

Lee, S. H., T. E. Whitledge, and S.-H. Kang (2007), Recent carbon and nitrogen uptake rates of phytoplankton in Bering Strait and the Chukchi Sea, *Continental Shelf Research*, *27*(17), 2231–2249, doi:10.1016/j.csr.2007.05.009.

Leu, E., J. Søreide, D. Hessen, S. Falk-Petersen, and J. Berge (2011), Consequences of changing sea-ice cover for primary and secondary producers in the European Arctic shelf seas: Timing, quantity, and quality, *Progress in Oceanography*, *90*(1-4), 18–32, doi:10.1016/j.pocean.2011.02.004.

Lewis, K. M., and K. R. Arrigo (2020), Ocean Color Algorithms for Estimating Chlorophyll *a* , CDOM Absorption, and Particle Backscattering in the Arctic Ocean, *Journal of Geophysical Research: Oceans*, *125*(6), doi:10.1029/2019JC015706.

Lewis, K. M., A. E. Arntsen, P. Coupel, H. Joy-Warren, K. E. Lowry, A. Matsuoka, M. M. Mills, G. L. Van Dijken, V. Selz, and K. R. Arrigo (2019), Photoacclimation of Arctic Ocean phytoplankton to shifting light and nutrient limitation, *Limnology and Oceanography*, *64*(1), 284–301.

Lewis, K. M., G. L. Van Dijken, and K. R. Arrigo (2020), Changes in phytoplankton concentration now drive increased Arctic Ocean primary production, *Science*, *369*(6500), 198–202, doi:10.1126/science.aay8380.

Li, W. K., F. A. McLaughlin, C. Lovejoy, and E. C. Carmack (2009), Smallest algae thrive as the Arctic Ocean freshens, *Science*, *326*(5952), 539–539, doi:10.1126/science.1179798.

Light, B., D. K. Perovich, M. A. Webster, C. Polashenski, and R. Dadic (2015), Optical properties of melting first-year Arctic sea ice, *Journal of Geophysical Research: Oceans*, *120*(11), 7657–7675, doi:10.1002/2015JC011163.

Liston, G. E., P. Itkin, J. Stroeve, M. Tschudi, J. S. Stewart, S. H. Pedersen, A. K. Reinking, and K. Elder (2020), A Lagrangian Snow-Evolution System for Sea-Ice Applications (SnowModel-LG): Part I—Model Description, *Journal of Geophysical Research*, p. 43.

Loeng, H., K. Brander, E. Carmack, S. Denisenko, K. Drinkwater, B. Hansen, K. Kovacs, P. Livingston, F. McLaughlin, and E. Sakshaug (2005), *Marine Systems. Arctic Climate Impact Assessment*.

Logerwell, E., M. Busby, C. Carothers, S. Cotton, J. Duffy-Anderson, E. Farley, P. Goddard, R. Heintz, B. Holladay, J. Horne, S. Johnson, B. Lauth, L. Moulton, D. Neff, B. Norcross, S. Parker-Stetter, J. Seigle, and T. Sformo (2015), Fish communities across a spectrum of habitats in the western Beaufort Sea and Chukchi Sea, *Progress in Oceanography*, *136*, 115–132, doi:10.1016/j.pocean.2015.05.013.

Lomas, M. W., S. E. Baer, S. Acton, and J. W. Krause (2019), Pumped Up by the Cold: Elemental Quotas and Stoichiometry of Cold-Water Diatoms, *Frontiers in Marine Science*, *6*, 286, doi:10.3389/fmars.2019.00286.

Lowry, K. E., G. L. Van Dijken, and K. R. Arrigo (2014), Evidence of under-ice phytoplankton blooms in the Chukchi Sea from 1998 to 2012, *Deep-Sea Research Part II: Topical Studies in Oceanography*, *105*, 105–117, doi:10.1016/j.dsr2.2014.03.013.

Lowry, K. E., R. S. Pickart, M. M. Mills, Z. W. Brown, G. L. Van Dijken, N. R. Bates, and K. R. Arrigo (2015), The influence of winter water on phytoplankton blooms in the Chukchi Sea, *Deep-Sea Research Part II*, *118*, 53–72, doi:10.1016/j.dsr2.2015.06.006.

Lowry, K. E., R. S. Pickart, V. Selz, M. M. Mills, A. Pacini, K. M. Lewis, H. L. Joy-Warren, C. Nobre, G. L. Van Dijken, P.-L. Grondin, J. Ferland, and K. R. Arrigo (2018), Under-Ice Phytoplankton Blooms Inhibited by Spring Convective Mixing in Refreezing Leads, *Journal of Geophysical Research: Oceans*, *123*(1), 90–109, doi:10.1002/2016JC012575.

Maldonado, M. T., P. W. Boyd, P. J. Harrison, and N. M. Price (1999), Co-limitation of phytoplankton growth by light and Fe during winter in the NE subarctic Pacific Ocean, *Deep-Sea Research Part II: Topical Studies in Oceanography*, *46*(11-12), 2475–2485, doi:10.1016/S0967-0645(99)00072-7.

Martin, J., J.-É. Tremblay, J. Gagnon, G. Tremblay, A. Lapoussière, C. Jose, M. Poulin, M. Gosselin, Y. Gratton, and C. Michel (2010), Prevalence, structure and properties of subsurface chlorophyll maxima in Canadian Arctic waters, *Marine Ecology Progress Series*, *412*, 69–84, doi:10.3354/meps08666.

Maslowski, W., D. Marble, W. Walczowski, U. Schauer, J. L. Clement, and A. J. Semtner (2004), On climatological mass, heat, and salt transports through the Barents Sea and Fram Strait from a pan-Arctic coupled ice-ocean model simulation: MASS AND PROPERTY FLUXES INTO THE ARCTIC, *Journal of Geophysical Research: Oceans*, *109*(C3), doi:10.1029/2001JC001039.

Matsuoka, A., Y. Huot, K. Shimada, S.-I. Saitoh, and M. Babin (2007), Bio-optical characteristics of the western Arctic Ocean: Implications for ocean color algorithms, *Canadian Journal of Remote Sensing*, *33*(6), 16.

Matsuoka, A., V. Hill, Y. Huot, M. Babin, and A. Bricaud (2011), Seasonal variability in the light absorption properties of western Arctic waters: Parameterization of the individual components of absorption for ocean color applications, *Journal of Geophysical Research*, *116*(C2), C02,007, doi:10.1029/2009JC005594.

Matsuoka, A., E. Boss, M. Babin, L. Karp-Boss, M. Hafez, A. Chekalyuk, C. W. Proctor, P. J. Werdell, and A. Bricaud (2017), Pan-Arctic optical characteristics of colored dissolved organic matter: Tracing dissolved organic carbon in changing Arctic waters using satellite ocean color data, *Remote Sensing of Environment*, *200*(August), 89–101, doi:10.1016/j.rse.2017.08.009.

Mauritzen, C. (2012), Arctic freshwater, *Nature Geoscience*, *5*(3), 162–164, doi:10.1038/ngeo1409.

Mayot, N., P. Matrai, I. H. Ellingsen, M. Steele, K. Johnson, S. C. Riser, and D. Swift (2018), Assessing Phytoplankton Activities in the Seasonal Ice Zone of the Greenland Sea Over an Annual Cycle, *Journal of Geophysical Research: Oceans*, *123*(11), 8004–8025, doi:10.1029/2018JC014271.

McLaughlin, F. A., and E. C. Carmack (2010), Deepening of the nutricline and chlorophyll maximum in the Canada Basin interior, 2003-2009, *Geophysical Research Letters*, *37*(24), n/a–n/a, doi: 10.1029/2010GL045459.

McMinn, A., C. Ashworth, and K. Ryan (1999), Growth and Productivity of Antarctic Sea Ice Algae under PAR and UV Irradiances, *Botanica Marina*, *42*(4), doi:10.1515/BOT.1999.046.

McTigue, N. D., W. S. Gardner, K. H. Dunton, and A. K. Hardison (2016), Biotic and abiotic controls on co-occurring nitrogen cycling processes in shallow Arctic shelf sediments, *Nature Communications*, *7*(1), 13,145, doi:10.1038/ncomms13145.

Meier, W. N., F. Fetterer, M. Savoie, S. Mallory, R. Duerr, and J. Stroeve (2019), NOAA/NSIDC Climate Data Record of Passive Microwave Sea Ice Concentration, Version 3, *NSIDC: National Snow and Ice Data Center*, *Boulder, Colorado, USA*, doi:10.7265/N59P2ZTG.

Meier, W. N., F. Fetterer, A. K. Windnagel, and S. Stewart (2021), NOAA/NSIDC Climate Data Record of Passive Microwave Sea Ice Concentration, version 4, *NSIDC: National Snow and Ice Data Center*, *Boulder, Colorado, USA*, doi:10.7265/efmz-2t65.

Mills, M. M., Z. W. Brown, K. E. Lowry, G. L. Van Dijken, S. Becker, S. Pal, C. R. Benitez-Nelson, M. M. Downer, A. L. Strong, J. H. Swift, R. S. Pickart, and K. R. Arrigo (2015), Impacts of low phytoplankton NO3-:PO43- utilization ratios over the Chukchi Shelf, Arctic Ocean, *Deep Sea Research Part II: Topical Studies in Oceanography*, *118*, 105–121, doi:10.1016/j.dsr2.2015.02.007.

Mills, M. M., Z. W. Brown, S. R. Laney, E. Ortega-Retuerta, K. E. Lowry, G. L. Van Dijken, and K. R. Arrigo (2018), Nitrogen Limitation of the Summer Phytoplankton and Heterotrophic Prokaryote Communities in the Chukchi Sea, *Frontiers in Marine Science*, *5*, 362, doi:10.3389/fmars.2018.00362.

Moisander, P. H., R. A. Beinart, I. Hewson, A. E. White, K. S. Johnson, C. A. Carlson, J. P. Montoya, and J. P. Zehr (2010), Unicellular Cyanobacterial Distributions Broaden the Oceanic N2 Fixation Domain, *Science*, *327*(5972), 1512–1514, doi:10.1126/science.1185468.

Monod, J. (1942), Recherches sur la croissance des cultures bacteriennes, *Actualite's Scientifique et Industrielles*, *911*, 1–215.

Moore, S. E., and J. M. Grebmeier (2018), The Distributed Biological Observatory: Linking Physics to Biology in the Pacific Arctic Region + Supplementary File (See Article Tools), *ARCTIC*, *71*(5), doi:10.14430/arctic4606.

Moore, S. E., and K. J. Kuletz (2019), Marine birds and mammals as ecosystem sentinels in and near Distributed Biological Observatory regions: An abbreviated review of published accounts and recommendations for integration to ocean observatories, *Deep Sea Research Part II: Topical Studies in Oceanography*, *162*, 211–217, doi:10.1016/j.dsr2.2018.09.004.

Mordy, C. W., S. Bell, E. D. Cokelet, C. Ladd, G. Lebon, P. Proctor, P. Stabeno, D. Strausz, E. Wisegarver, and K. Wood (2020), Seasonal and interannual variability of nitrate in the eastern Chukchi Sea: Transport and winter replenishment, *Deep Sea Research Part II: Topical Studies in Oceanography*, p. 104807, doi:10.1016/j.dsr2.2020.104807.

Morel, A. (1978), Available, usable, and stored radiant energy in relation to marine photosynthesis, *Deep Sea Research*, *25*(8), 673–688, doi:10.1016/0146-6291(78)90623-9.

Mulholland, M. R., P. W. Bernhardt, J. L. Blanco-Garcia, A. Mannino, K. Hyde, E. Mondragon, K. Turk, P. H. Moisander, and J. P. Zehr (2012), Rates of dinitrogen fixation and the abundance of diazotrophs in North American coastal waters between Cape Hatteras and Georges Bank, *Limnology and Oceanography*, *57*(4), 1067–1083, doi:10.4319/lo.2012.57.4.1067.

Mundy, C. J., M. Gosselin, J. Ehn, Y. Gratton, A. Rossnagel, D. G. Barber, J. Martin, J.-É. Tremblay, M. Palmer, K. R. Arrigo, G. Darnis, L. Fortier, B. Else, and T. Papakyriakou (2009), Contribution of under-ice primary production to an ice-edge upwelling phytoplankton bloom in the Canadian Beaufort Sea, *Geophysical Research Letters*, *36*(17), L17,601, doi:10.1029/2009GL038837.

Mundy, C. J., M. Gosselin, Y. Gratton, K. Brown, V. Galindo, K. Campbell, M. Levasseur, D. Barber, T. Papakyriakou, and S. Bélanger (2014), Role of environmental factors on phytoplankton bloom initiation under landfast sea ice in Resolute Passage, Canada, *Marine Ecology Progress Series*, *497*, 39–49, doi:10.3354/meps10587.

Munk, P. (2003), Changes in plankton and fish larvae communities across hydrographic fronts off West Greenland, *Journal of Plankton Research*, *25*(7), 815–830, doi:10.1093/plankt/25.7.815.

Neukermans, G., L. Oziel, and M. Babin (2018), Increased intrusion of warming Atlantic water leads to rapid expansion of temperate phytoplankton in the Arctic, *Global Change Biology*, *24*, 2545–2553, doi:10.1111/gcb.14075.

Niebauer, H. (1991), Bio-physical oceanographic interactions at the edge of the Arctic ice pack, *Journal of Marine Systems*, *2*(1-2), 209–232, doi:10.1016/0924-7963(91)90025-P.

Nishino, S., T. Kikuchi, A. Fujiwara, T. Hirawake, and M. Aoyama (2016), Water mass characteristics and their temporal changes in a biological hotspot in the southern Chukchi Sea, *Biogeosciences*, *13*(8), 2563–2578, doi:10.5194/bg-13-2563-2016.

Nummelin, A., C. Li, and LH. Smedsrud (2015), Response of Arctic Ocean stratification to changing river runoff in a column model, *Journal of Geophysical Research: Oceans*, *120*, 2655–2675, doi:10.1002/2014JC010571.Received.

Nummelin, A., M. Ilicak, C. Li, and L. H. Smedsrud (2016), Consequences of future increased Arctic runoff on Arctic Ocean stratification, circulation, and sea ice cover, *Journal of Geophysical Research: Oceans*, *121*(1), 617–637, doi:10.1002/2015JC011156.

Osborne, E., J. Richter-Menge, and M. Jeffries (2018), Arctic Report Card 2018, *Tech. rep.*

Oziel, L., P. Massicotte, A. Randelhoff, J. Ferland, A. Vladoiu, L. Lacour, V. Galindo, S. Lambert-Girard, D. Dumont, Y. Cuypers, P. Bouruet-Aubertot, C. J. Mundy, J. Ehn, G. Bécu, C. Marec, M.-H. Forget, N. Garcia, P. Coupel, P. Raimbault, M.-N. Houssais, and M. Babin (2019), Environmental factors influencing the seasonal dynamics of spring algal blooms in and beneath sea ice in western Baffin Bay, *Elementa: Science of the Anthropocene*, *7*, 34, doi:10.1525/elementa.372.

Oziel, L., A. Baudena, M. Ardyna, P. Massicotte, A. Randelhoff, J.-B. Sallée, R. B. Ingvaldsen, E. Devred, and M. Babin (2020), Faster Atlantic currents drive poleward expansion of temperate phytoplankton in the Arctic Ocean, *Nature Communications*, *11*(1), 1705, doi:10.1038/s41467-020-15485-5.

Pabi, S., G. L. Van Dijken, and K. R. Arrigo (2008), Primary production in the Arctic Ocean, 1998-2006, *Journal of Geophysical Research: Oceans*, *113*(8), 1–22, doi:10.1029/2007JC004578.

Pacini, A., G. W. K. Moore, R. S. Pickart, C. Nobre, F. Bahr, K. Våge, and K. R. Arrigo (2019), Characteristics and Transformation of Pacific Winter Water on the Chukchi Sea Shelf in Late Spring, *Journal of Geophysical Research: Oceans*, *124*(10), 7153–7177, doi:10.1029/2019JC015261.

Palmer, M. A. (2013), Primary Productivity and Biogeochemical Carbon Cycling in the Beaufort and Chukchi Seas, Arctic Ocean, *Stanford University Dissertation*.

Palmer, M. A., B. T. Saenz, and K. R. Arrigo (2014), Impacts of sea ice retreat, thinning, and melt-pond proliferation on the summer phytoplankton bloom in the Chukchi Sea, Arctic Ocean, *Deep-Sea Research Part II: Topical Studies in Oceanography*, *105*, 85–104, doi:10.1016/j.dsr2.2014.03.016.

Payne, C. M., and K. R. Arrigo (2022), Increases in Benthic Particulate Export and Sedimentary Denitrification in the Northern Chukchi Sea Tied to Under-Ice Primary Production, *Journal of Geophysical Research: Oceans*, *127*(2), doi:10.1029/2021JC018110.

Payne, C. M., L. Bianucci, G. L. Van Dijken, and K. R. Arrigo (2021), Changes in Under-Ice Primary Production in the Chukchi Sea From 1988 to 2018, *Journal of Geophysical Research: Oceans*, *126*(9), doi:10.1029/2021JC017483.

Payne, C. M., G. L. van Dijken, and K. R. Arrigo (2022), North-South Differences in Under-Ice Primary Production in the Chukchi Sea From 1988 to 2018, *Journal of Geophysical Research: Oceans*, *127*(7), doi:10.1029/2022JC018431.

Peng, G., W. N. Meier, D. J. Scott, and M. H. Savoie (2013), A long-term and reproducible passive microwave sea ice concentration data record for climate studies and monitoring, *Earth System Science Data*, p. 8.

Peralta-Ferriz, C., and R. A. Woodgate (2015), Seasonal and interannual variability of pan-Arctic surface mixed layer properties from 1979 to 2012 from hydrographic data, and the dominance of stratification for multiyear mixed layer depth shoaling, *Progress in Oceanography*, *134*, 19–53, doi:10.1016/j.pocean.2014.12.005.

Peralta-Ferriz, C., and R. A. Woodgate (2017), The Dominant Role of the East Siberian Sea in Driving the Oceanic Flow Through the Bering Strait—Conclusions From GRACE Ocean Mass Satellite Data and In Situ Mooring Observations Between 2002 and 2016, *Geophysical Research Letters*, *44*(22), doi:10.1002/2017GL075179.

Perovich, D. K., and C. Polashenski (2012), Albedo evolution of seasonal Arctic sea ice, *Geophysical Research Letters*, *39*(8), n/a–n/a, doi:10.1029/2012GL051432.

Perovich, D. K., G. A. Maykut, and T. C. Grenfell (1986), Optical Properties Of Ice And Snow In The Polar Oceans. I: Observations, in *1986 Technical Symposium Southeast*, edited by M. A. Blizard, p. 232, Orlando, doi:10.1117/12.964238.

Perrette, M., A. Yool, G. D. Quartly, and E. E. Popova (2011), Near-ubiquity of ice-edge blooms in the Arctic, *Biogeosciences*, *8*(2), 515–524, doi:10.5194/bg-8-515-2011.

Platt, TC., C. Gallegos, and W. Harrison (1980), Photoinhibition of photosynthesis in natural assemblages of marine phytoplankton in the Arctic, *Deep-Sea Research*, *29*, 1159–1170.

Polyakov, I. V., M. B. Alkire, B. A. Bluhm, K. A. Brown, E. C. Carmack, M. Chierici, S. L. Danielson, I. Ellingsen, E. A. Ershova, K. Gårdfeldt, R. B. Ingvaldsen, A. V. Pnyushkov, D. Slagstad, and P. Wassmann (2020), Borealization of the Arctic Ocean in Response to Anomalous Advection From Sub-Arctic Seas, *Frontiers in Marine Science*, *7*, 491, doi:10.3389/fmars.2020.00491.

Price, N. M., G. I. Harrison, J. G. Hering, R. J. Hudson, P. M. V. Nirel, B. Palenik, and F. M. M. Morel (1989), Preparation and Chemistry of the Artificial Algal Culture Medium Aquil, *Biological Oceanography*, *6*(5-6), 443–461, doi:10.1080/01965581.1988.10749544.

Rainville, L., and P. Winsor (2008), Mixing across the Arctic Ocean: Microstructure observations during the Beringia 2005 Expedition, *Geophysical Research Letters*, *35*(8), L08,606, doi:10.1029/2008GL033532.

Rainville, L., and R. A. Woodgate (2009), Observations of internal wave generation in the seasonally ice-free Arctic, *Geophysical Research Letters*, *36*(23), L23,604, doi:10.1029/2009GL041291.

Randelhoff, A., M. Reigstad, M. Chierici, A. Sundfjord, V. Ivanov, M. Cape, M. Vernet, J.-É. Tremblay, G. Bratbak, and S. Kristiansen (2018), Seasonality of the Physical and Biogeochemical Hydrography in the Inflow to the Arctic Ocean Through Fram Strait, *Frontiers in Marine Science*, *5*, 224, doi:10.3389/fmars.2018.00224.

Randelhoff, A., L. Oziel, P. Massicotte, G. Bécu, M. Galí, L. Lacour, D. Dumont, A. Vladoiu, C. Marec, F. Bruyant, M.-N. Houssais, J.-É. Tremblay, G. Deslongchamps, and M. Babin (2019), The evolution of light and vertical mixing across a phytoplankton ice-edge bloom, *Elementa: Science of the Anthropocene*, *7*, 20, doi:10.1525/elementa.357.

Randelhoff, A., J. Holding, M. Janout, M. K. Sejr, M. Babin, J.-É. Tremblay, and M. B. Alkire (2020), Pan-Arctic Ocean Primary Production Constrained by Turbulent Nitrate Fluxes, *Frontiers in Marine Science*, *7*, 150, doi:10.3389/fmars.2020.00150.

Rantanen, M., A. Y. Karpechko, A. Lipponen, K. Nordling, O. Hyvärinen, K. Ruosteenoja, T. Vihma, and A. Laaksonen (2022), The Arctic has warmed nearly four times faster than the globe since 1979, *Communications Earth & Environment*, *3*(1), 168, doi:10.1038/s43247-022-00498-3.

Raven, J. A. (1990), Predictions of Mn and Fe use efficiencies of phototrophic growth as a function of light availability for growth and of C assimilation pathway, *New Phytol.*, *116*(1), 1–18, doi:10.1111/j.1469-8137.1990.tb00505.x.

Redfield, A. C. (1958), The biological control of chemical factors in the environment, *American Scientist*, *46*(3), 230A–221.

Reeve, J. L., R. C. Hamme, and W. J. Williams (2019), Tracing denitrification in the Canada Basin: N2 loss to the atmosphere on the Chukchi Shelf and benthic inputs in deep waters, *Deep Sea Research Part I: Oceanographic Research Papers*, *143*, 127–138, doi:10.1016/j.dsr.2018.11.003.

Reynolds, RR., TM. Smith, D. B. Chelton, K. S. Casey, and MG. Schlax (2007), Daily High-Resolution-Blended Analyses for Sea Surface Temperature, *Journal of Climate*, *20*(22), 5473–5496, doi:10.1175/2007jcli1824.1.

Rhee, G.-y., and I. J. Gotham (1981), The effect of environmental factors on phytoplankton growth : Light and the interactions of light with nitrate limitation, *Limnology and Oceanography*, *26*(4), 649–659.

Rodhe, W. (1978), Algae in culture and nature, *SIL Communications, 1953-1996*, *21*(1), 7–20, doi:10.1080/05384680.1978.11903945.

Rosen, B. H., and R. L. Lowe (1984), Physiological and Ultrastructural Responses of Cyclotella Meneghiniana (Bacillariophyta) To Light Intensity and Nutrient Limitation, *Journal of Phycology*, *20*(2), 173–183, doi:10.1111/j.0022-3646.1984.00173.x.

Rysgaard, S., T. Nielsen, and B. Hansen (1999), Seasonal variation in nutrients, pelagic primary production and grazing in a high-Arctic coastal marine ecosystem, Young Sound, Northeast Greenland, *Marine Ecology Progress Series*, *179*, 13–25, doi:10.3354/meps179013.

Sakshaug, E. (2004), Primary and Secondary Production in the Arctic Seas, in *The Organic Carbon Cycle in the Arctic Ocean*, pp. 57–81, Springer, Berlin, Heidelberg, doi:10.1007/978-3-642-18912-8_3.

Sakshaug, E., and H. R. Skjoldal (1989), Life at the ice edge, *Ambio (Sweden)*.

Schulze, L. M., and R. S. Pickart (2012), Seasonal variation of upwelling in the Alaskan Beaufort Sea: Impact of sea ice cover, *Journal of Geophysical Research: Oceans*, *117*(C6), doi:10.1029/2012JC007985.

Screen, J. A., and I. Simmonds (2010), The central role of diminishing sea ice in recent Arctic temperature amplification, *Nature*, *464*, 1334–1337, doi:10.1038/nature09051.

Selz, V., B. T. Saenz, G. L. Van Dijken, and K. R. Arrigo (2018), Drivers of Ice Algal Bloom Variability Between 1980 and 2015 in the Chukchi Sea, *Journal of Geophysical Research: Oceans*, *123*(10), 7037–7052, doi:10.1029/2018JC014123.

Serreze, M. C., and J. Stroeve (2015), Arctic sea ice trends, variability and implications for seasonal ice forecasting, *Philosophical transactions of the Royal Society of London*, pp. 20140,159–20140,159.

Serreze, M. C., A. D. Crawford, J. C. Stroeve, A. P. Barrett, and R. A. Woodgate (2016), Variability, trends, and predictability of seasonal sea ice retreat and advance in the Chukchi Sea, *Journal of Geophysical Research: Oceans*, *121*(10), 7308–7325, doi:10.1002/2016JC011977.

Sherr, B. F., V. J. Hill, S. Plourde, D. A. Stockwell, C. J. Ashjian, E. B. Sherr, and R. G. Campbell (2008), Mesozooplankton prey preference and grazing impact in the western Arctic Ocean, *Deep Sea Research Part II: Topical Studies in Oceanography*, *56*(17), 1274–1289, doi:10.1016/j.dsr2.2008.10.027.

Sherr, E. B., and B. F. Sherr (2009), Capacity of herbivorous protists to control initiation and development of mass phytoplankton blooms, *Aquatic Microbial Ecology*, *57*(3), 253–262, doi:10.3354/ame01358.

Sherr, E. B., B. F. Sherr, and A. J. Hartz (2009), Microzooplankton grazing impact in the Western Arctic Ocean, *Deep Sea Research Part II: Topical Studies in Oceanography*, *56*(17), 1264–1273, doi:10.1016/j.dsr2.2008.10.036.

Shimada, K., T. Kamoshida, M. Itoh, S. Nishino, E. Carmack, F. McLaughlin, S. Zimmermann, and A. Proshutinsky (2006), Pacific Ocean inflow: Influence on catastrophic reduction of sea ice cover in the Arctic Ocean, *Geophysical Research Letters*, *33*(8), L08,605, doi:10.1029/2005GL025624.

Sipler, R. E., D. Gong, S. E. Baer, M. P. Sanderson, Q. N. Roberts, M. R. Mulholland, and D. A. Bronk (2017), Preliminary estimates of the contribution of Arctic nitrogen fixation to the global nitrogen budget, *Limnology and Oceanography Letters*, *2*(5), 159–166, doi:10.1002/lol2.10046.

Smetacek, V. (1999), Diatoms and the Ocean Carbon Cycle, *Protist*, *150*(1), 25–32, doi:10.1016/S1434-4610(99)70006-4.

Soetaert, K., and F. Meysman (2012), Reactive transport in aquatic ecosystems: Rapid model prototyping in the open source software R, *Environmental Modelling & Software*, *32*, 49–60, doi:10.1016/j.envsoft.2011.08.011.

Soetaert, K., P. M. Herman, and J. J. Middelburg (1996a), A model of early diagenetic proceses from the shelf ot abyssal depths, *Geochimica et Cosmochimica Acta*, *60*(6), 1019–1040.

Soetaert, K., P. M. J. Herman, and J. J. Middelburg (1996b), Dynamic response of deep-sea sediments to seasonal variations: A model, *Limnology and Oceanography*, *41*(8), 1651–1668, doi:10.4319/lo.1996.41.8.1651.

Soetaert, K., T. Petzoldt, and R. W. Setzer (2010), Solving Differential Equations in *R* : Package **deSolve**, *Journal of Statistical Software*, *33*(9), doi:10.18637/jss.v033.i09.

Sohm, J. A., E. A. Webb, and D. G. Capone (2011), Emerging patterns of marine nitrogen fixation, *Nature Reviews Microbiology*, *9*(7), 499–508, doi:10.1038/nrmicro2594.

Søreide, J. E., E. V. Leu, Jør. Berge, M. Graeve, and S. Falk-Petersen (2010), Timing of blooms, algal food quality and Calanus glacialis reproduction and growth in a changing Arctic, *Global Change Biology*, *16*(11), 3154–3163, doi:10.1111/j.1365-2486.2010.02175.x.

Spitz, Y. H., J. R. Moisan, and M. R. Abbott (2001), Configuring an ecosystem model using data from the Bermuda Atlantic Time Series (BATS), *Deep-Sea Research II*, *48*, 1733–1768.

Stabeno, P. J., C. W. Mordy, and M. F. Sigler (2020), Seasonal patterns of near-bottom chlorophyll fluorescence in the eastern Chukchi Sea: 2010–2019, *Deep Sea Research Part II: Topical Studies in Oceanography*, *177*, 104,842, doi:10.1016/j.dsr2.2020.104842.

Stocker, T. F., D. Qin, G.-K. Plattner, M. M. B. Tignor, S. K. Allen, J. Boschung, A. Nauels, Y. Xia, V. Bex, and P. M. Midgley (2013), Climate change 2013: The physical science basis, *Cambridge university press Cambridge, United Kingdom and New York, NY, USA*, *1535*, 14.

Strass, V. H., and E. M. Nöthig (1996), Seasonal shifts in ice edge phytoplankton blooms in the Barents Sea related to the water column stability, *Polar Biology*, *16*(6), 409–422, doi:10.1007/BF02390423.

Stroeve, J., T. Markus, L. Boisvert, J. Miller, and A. Barrett (2014), Changes in Arctic melt season and its implications for sea ice loss, *Geophysical Research Letters*, *41*, 1216–1225, doi:10.1002/2013GL058951.Received.

Stroeve, J., G. E. Liston, S. Buzzard, L. Zhou, R. Mallett, A. Barrett, M. Tschudi, M. Tsamados, P. Itkin, and J. S. Stewart (2020), A Lagrangian Snow Evolution System for Sea Ice Applications (SnowModel-LG): Part II—Analyses, *Journal of Geophysical Research: Oceans*, *125*(10), doi:10.1029/2019JC015900.

Strzepek, R. F., and P. J. Harrison (2004), Photosynthetic architecture differs in coastal and oceanic diatoms, *Nature*, *431*(7009), 689–692, doi:10.1038/nature02954.

Strzepek, R. F., K. A. Hunter, R. D. Frew, P. J. Harrison, and P. W. Boyd (2012), Iron-light interactions differ in Southern Ocean phytoplankton, *Limnology and Oceanography*, *57*(4), 1182–1200, doi:10.4319/lo.2012.57.4.1182.

Sunda, W. G., and S. A. Huntsman (1997), Interrelated influence of iron, light and cell size on marine phytoplankton growth, *Nature*, *390*(6658), 389–392, doi:10.1038/37093.

Sunda, W. G., and S. A. Huntsman (2011), Interactive effects of light and temperature on iron limitation in a marine diatom: Implications for marine productivity and carbon cycling, *Limnology and Oceanography*, *56*(4), 1475–1488, doi:10.4319/lo.2011.56.4.1475.

Szymanski, A., and R. Gradinger (2016), The diversity, abundance and fate of ice algae and phytoplankton in the Bering Sea, *Polar Biology*, *39*(2), 309–325, doi:10.1007/s00300-015-1783-z.

Tagliabue, A., A. R. Bowie, P. W. Boyd, K. N. Buck, K. S. Johnson, and M. A. Saito (2017), The integral role of iron in ocean biogeochemistry, *Nature*, *543*(7643), 51–59, doi:10.1038/nature21058.

Tagliabue, A., L. Kwiatkowski, L. Bopp, M. Butenschön, W. Cheung, M. Lengaigne, and J. Vialard (2021), Persistent Uncertainties in Ocean Net Primary Production Climate Change Projections at Regional Scales Raise Challenges for Assessing Impacts on Ecosystem Services, *Frontiers in Climate*, *3*, 738,224, doi:10.3389/fclim.2021.738224.

Teal, L., M. Bulling, E. Parker, and M. Solan (2008), Global patterns of bioturbation intensity and mixed depth of marine soft sediments, *Aquatic Biology*, *2*(3), 207–218, doi:10.3354/ab00052.

Tett, P., A. Edwards, and K. Jones (1986), A model for the growth of shelf-sea phytoplankton in summer, *Estuarine, Coastal and Shelf Science*, *23*(5), 641–672, doi:10.1016/0272-7714(86)90104-6.

Timmermans, K. R., M. S. Davey, B. V. D. Wagt, J. Snoek, R. J. Geider, M. J. W. Veldhuis, L. J. A. Gerringa, and H. J. W. D. Baar (2001), Co-limitation by iron and light of Chaetoceros brevis , C . dichaeta and, *Marine Ecology Progress Series*, *217*(Raven 1990), 287–297.

Townsend, D. W., and L. M. Cammen (1988), Potential Importance of the Timing of Spring Plankton Blooms to Benthic-Pelagic Coupling and Recruitment of juvenile demersal fishes, *Biological Oceanography*, *5*(13), 215–228.

Tremblay, J.-É., and J. Gagnon (2009), The effects of irradiance and nutrient supply on the productivity of Arctic waters: A perspective on climate change, in *Influence of Climate Change on the Changing Arctic and Sub-Arctic Conditions*, edited by J. C. J. Nihoul and A. G. Kostianoy, pp. 73–93, Springer Netherlands, Dordrecht, doi:10.1007/978-1-4020-9460-6_7.

Tremblay, J.-É., S. Bélanger, D. G. Barber, M. Asplin, J. Martin, G. Darnis, L. Fortier, Y. Gratton, H. Link, P. Archambault, A. Sallon, C. Michel, W. J. Williams, B. Philippe, and M. Gosselin (2011), Climate forcing multiplies biological productivity in the coastal Arctic Ocean, *Geophysical Research Letters*, *38*(18), n/a–n/a, doi:10.1029/2011GL048825.

Tschudi, M., J. Stroeve, and J. Stewart (2016), Relating the Age of Arctic Sea Ice to its Thickness, as Measured during NASA's ICESat and IceBridge Campaigns, *Remote Sensing*, *8*(6), 457, doi:10.3390/rs8060457.

Tschudi, M., W. N. Meier, J. S. Stewart, C. Fowler, and J. Maslanik (2019), EASE-Grid Sea Ice Age, Version 4.

Tsujii, K., M. Otsuki, T. Akamatsu, I. Matsuo, K. Amakasu, M. Kitamura, T. Kikuchi, K. Miyashita, and Y. Mitani (2016), The migration of fin whales into the southern Chukchi Sea as monitored with passive acoustics, *ICES Journal of Marine Science*, *73*(8), 2085–2092, doi:10.1093/icesjms/fsv271.

Van Heurck, H. (1882), Types du synopsis des diatomées de belgique. Séries I-XXII. [slides nr. 1-550], *Anvers*.

Vancoppenolle, M., L. Bopp, G. Madec, J. Dunne, T. Ilyina, P. R. Halloran, and N. Steiner (2013), Future Arctic Ocean primary productivity from CMIP5 simulations: Uncertain outcome, but consistent mechanisms: FUTURE ARCTIC OCEAN PRIMARY PRODUCTIVITY, *Global Biogeochemical Cycles*, *27*(3), 605–619, doi:10.1002/gbc.20055.

Varela, R. A., A. Cruzado, J. Tintore, and E. García Ladona (1992), Modelling the deep-chlorophyll maximum: A coupled physical-biological approach, *Journal of Marine Research*, *50*, 441–463, doi:10.1357/002224092784797638.

Volk, T., and M. I. Hoffert (1985), Ocean Carbon Pumps: Analysis of Relative Strengths and Efficiencies in Ocean-Driven Atmospheric CO2 Changes, in *The Carbon Cycle and Atmospheric CO2: Natural Variations Archean to Present*, *Geophysical Monograph Series*, vol. 32, edited by E. Sundquist and W. Broecker, pp. 99–110, American Geophysical Union, Washington, D. C., doi:10.1029/GM032p0099.

Waga, H., and T. Hirawake (2020), Changing Occurrences of Fall Blooms Associated With Variations in Phytoplankton Size Structure in the Pacific Arctic, *Frontiers in Marine Science*, *7*, 209, doi:10.3389/fmars.2020.00209.

Walsh, J. J. (1975), A spatial simulation model of the Peru upwelling ecosystem, *Deep-Sea Research and Oceanographic Abstracts*, *22*(4), 201–236, doi:10.1016/0011-7471(75)90028-5.

Wang, M., and J. E. Overland (2015), Projected future duration of the sea-ice-free season in the Alaskan Arctic, *Progress in Oceanography*, *136*, 50–59, doi:10.1016/j.pocean.2015.01.001.

Webster, M. A., I. G. Rigor, D. K. Perovich, J. A. Richter-Menge, C. M. Polashenski, and B. Light (2015), Seasonal evolution of melt ponds on Arctic sea ice, *Journal of Geophysical Research: Oceans*, *120*(9), 5968–5982, doi:10.1002/2015JC011030.

Welch, H. E., and M. A. Bergmann (1989), Seasonal Development of Ice Algae and its Prediction from Environmental Factors near Resolute, N.W.T., Canada, *Canadian Journal of Fisheries and Aquatic Sciences*, *46*(10), 1793–1804, doi:10.1139/f89-227.

Woodgate, R. A. (2018), Increases in the Pacific inflow to the Arctic from 1990 to 2015, and insights into seasonal trends and driving mechanisms from year-round Bering Strait mooring data, *Progress in Oceanography*, *160*, 124–154, doi:10.1016/j.pocean.2017.12.007.

Woodgate, R. A., K. Aagaard, and T. J. Weingartner (2005), A year in the physical oceanography of the Chukchi Sea: Moored measurements from autumn 1990–1991, *Deep Sea Research Part II: Topical Studies in Oceanography*, *52*(24-26), 3116–3149, doi:10.1016/j.dsr2.2005.10.016.

Woodgate, R. A., T. J. Weingartner, and R. Lindsay (2012), Observed increases in Bering Strait oceanic fluxes from the Pacific to the Arctic from 2001 to 2011 and their impacts on the Arctic Ocean water column, *Geophysical Research Letters*, *39*(24), 2012GL054,092, doi: 10.1029/2012GL054092.

Yager, P. L., T. L. Connelly, B. Mortazavi, K. E. Wommack, N. Bano, J. E. Bauer, S. Opsahl, and J. T. Hollibaugh (2001), Dynamic bacterial and viral response to an algal bloom at subzero temperatures, *Limnology and Oceanography*, *46*(4), 790–801, doi:10.4319/lo.2001.46.4.0790.

Yamamoto-Kawai, M., E. Carmack, and F. McLaughlin (2006), Nitrogen balance and Arctic throughflow, *Nature*, *443*(7107), 43–43, doi:10.1038/443043a.

Yang, J. (2004), Storm-driven mixing and potential impact on the Arctic Ocean, *Journal of Geophysical Research*, *109*(C4), C04,008, doi:10.1029/2001JC001248.

Zhang, J., Y. H. Spitz, M. Steele, C. Ashjian, R. Campbell, L. Berline, and P. Matrai (2010), Modeling the impact of declining sea ice on the Arctic marine planktonic ecosystem, *Journal of Geophysical Research*, *115*(C10), C10,015, doi:10.1029/2009JC005387.

Zhang, J., C. Ashjian, R. G. Campbell, Y. H. Spitz, M. Steele, and V. J. Hill (2015), The influence of sea ice and snow cover and nutrient availability on the formation of massive under-ice phytoplankton blooms in the Chukchi Sea, *Deep-Sea Research Part II*, *118*, 122–135, doi: 10.1016/j.dsr2.2015.02.008.

Zhang, X., J. E. Walsh, and J. Zhang (2004), Climatology and Interannual Variability of Arctic Cyclone Activity: 1948–2002, *JOURNAL OF CLIMATE*, *17*, 18.

Zhou, L., J. Stroeve, S. Xu, A. Petty, R. Tilling, M. Winstrup, P. Rostosky, I. R. Lawrence, G. E. Liston, A. Ridout, M. Tsamados, and V. Nandan (2021), Inter-comparison of snow depth over Arctic sea ice from reanalysis reconstructions and satellite retrieval, *The Cryosphere*, *15*(1), 345–367, doi:10.5194/tc-15-345-2021.